DISSERTATION

QUANTITATIVE EVALUATION OF RADIATION FIELD BEHAVIOR IN SUBTERRANEAN TUNNEL ENVIRONMENTS USING MONTE CARLO MODELING

Submitted by

Sarah M. Sublett

Department of Environmental and Radiological Health Sciences

In partial fulfillment of the requirements

For the Degree of Doctor of Philosophy

Colorado State University

Fort Collins, Colorado

Spring 2026

Doctoral Committee:

Advisor: Alexander Brandl

Ellison Carter
Sheryl Magzamen
Ralf Sudowe

ABSTRACT

QUANTITATIVE EVALUATION OF RADIATION FIELD BEHAVIOR IN SUBTERRANEAN TUNNEL ENVIRONMENTS USING MONTE CARLO MODELING

Subterranean transportation and utility tunnel systems present unique radiological response challenges due to restricted geometry, limited ventilation, and complex photon scattering environments. In the event of an accidental or deliberate radiological release, accurate characterization of the radiation fields within these environments is critical for first responder protection and risk-informed decision-making. However, conventional open-air dose-rate assumptions may not adequately represent radiation transport behavior in confined tunnel geometries.

This research quantifies gamma radiation transport and effective dose rates in representative subterranean tunnel configurations using Monte Carlo N-Particle (MCNP) simulations. Photon-emitting radionuclides of operational relevance, including Cs-137, Co-60, Ir-192, and Ra-226 (with progeny in equilibrium), were modeled under varying source strengths and spatial configurations. Fluence-to-dose conversion was performed using established gamma dose rate constants and the International Commission on Radiological Protection (ICRP)-based dose conversion methodologies. Dose fields were evaluated as a function of distance, geometry, and material composition to assess deviations from inverse-square behavior observed in free-field environments.

Results demonstrate that tunnel geometry significantly alters photon fluence distribution through enhanced scattering and wall backscatter effects, resulting in spatial dose profiles that differ measurably from open-air assumptions. In certain configurations, dose rates at extended distances were sustained above free-field expectations, indicating potential underestimation of responder risk

when applying standard outdoor models. The magnitude of deviation was radionuclide-dependent and influenced by photon energy spectra and tunnel material composition.

These findings support the need for geometry-specific modeling in subterranean radiological response planning and provide quantitative insight for operational health physics assessments. The work contributes to improved dose prediction accuracy in confined environments and informs emergency response doctrine for underground radiological incidents.

ACKNOWLEDGEMENTS

I would like to express my sincere gratitude to my dissertation advisor, Dr. Alexander Brandl, for his guidance, mentorship, and unwavering support throughout this research. His expertise and thoughtful feedback were instrumental in shaping both the direction and quality of this work.

I also extend my appreciation to my dissertation committee members, Dr. Ellison Carter, Dr. Sheryl Magzamen, and Dr. Ralf Sudowe, for their valuable insights and constructive critiques that strengthened this study.

I am grateful to Dr. Brandl's research group, especially Dave Oertli, whose efforts in conducting the numerous simulations formed the foundation of this research. I also thank Justin Bell, Noah Blair, and Paige Witter for their support, technical expertise, and collaboration throughout this process.

This research was made possible through the support of Colorado State University and collaborating research partners who provided access to facilities, modeling resources, and technical expertise. I am particularly appreciative of colleagues within the radiation protection and subterranean operations research communities whose prior work provided an essential foundation for this effort.

I would also like to express my sincere appreciation to the United States Army for providing the time, funding, and professional opportunity to pursue doctoral studies. The trust and support I received made it possible to undertake and complete this long-standing personal and professional goal.

I am also sincerely grateful for the friendship and steadfast support of Olivia, Rachel, Sarah, Lisa, Carol and John. Their encouragement, perspective, and willingness to stand beside me through both challenges and successes have been a constant source of strength. Their presence in my life has been a reminder that meaningful support can come from the family we build along the way.

Most importantly, I am profoundly grateful to my husband for his unwavering support, patience, and encouragement throughout this journey. His belief in me, steady perspective, and willingness to shoulder additional responsibilities made it possible for me to dedicate the time and focus required to complete this work.

I am also deeply thankful for my daughter, whose curiosity, resilience, and joy have been a constant source of motivation and inspiration. She has reminded me daily of the importance of perseverance and balance, and her pride in this achievement means more to me than words can express.

Finally, I wish to honor the memory of my mother and my mother-in-law. Their love, strength, and enduring examples of dedication and compassion continue to guide me. Although they are not here to witness this milestone, their influence remains woven into every success I achieve.

This dissertation is dedicated to my family and friends.

TABLE OF CONTENTS

LIST OF FIGURES

LIST OF TABLES

Chapter 1 - Introduction:

1.1 - Background and Motivation:

Since the discovery of ionizing radiation, protection frameworks have evolved to balance the beneficial use of ionizing radiation with exposure risk. Modern health physics integrates measurement, modeling, and operational response to evaluate both planned and accidental exposures. Understanding radiation transport behavior in confined tunnel systems is critical for rapid dose assessment, responder protection, and infrastructure risk evaluation.

Health physicists are armed with the knowledge of how radiation acts in biological entities and the environment to determine the associated risk with exposure to a radiation source. A key component in determining risk is correctly determining the type and dose of radiation the individual was exposed to, which can be determined using radiation detectors. Health physicists are often charged with being both proactive and reactive, forecasting potential exposure when the exposure is planned in instances like the operation of a nuclear power plant, and in emergency response scenarios such as recovering a lost source. Planning and preparing for potential exposures can be achieved using modeling software, such as Monte Carlo N-Particle (MCNP), to determine the potential radiation dose rates being emitted for a specific radiation source in a particular situation without anyone being exposed. Conducting research in this manner aligns with one of the defining Health Physics principles, As Low As Reasonably Achievable (ALARA), which aims to balance time, distance, and shielding to reduce individual exposure as much as possible while still achieving the desired effect. (Johnson, 2017)

Ionizing radiation is typically classified by its transformation mechanism, specifically what is emitted from the radioactive source to deexcite it, whether through the emission of alpha particles, beta particles, gamma-rays, or X-rays. (Johnson, 2017) Alternatively, we can categorize radiation into the following four types: charged particles, either fast electrons or heavy charged particles, and uncharged radiation, either electromagnetic radiation or neutrons. (Knoll, 2010) Generally speaking, each of these mechanisms requires a different type of radiation detector to characterize it best, so it is essential to know the type of transformation being measured. The range of energies emitted varies from 10 eV to 20 MeV (20,000,000 eV), further complicating selecting the proper detector. (Knoll, 2010) Having a pure radiation sample with only one radiation source is very rare. Radiation sources decay and produce daughter products, each with its own energy signature. A single radiation source may emit multiple types and energies of radiation. (Knoll, 2010)

1.2 - The Threat:

About 3 million shipments containing radioactive materials are shipped annually in the United States by ship, plane, train, or truck, with most on the highway. (US Nuclear Regulatory Commission, 2023) (US Environmental Protection Agency, 2024) This transportation is regulated by the US Nuclear Regulatory Commission (NRC) and the US Department of Transportation (DOT), where the NRC sets the “requirements for the design and manufacture of packages for radioactive materials” (US Nuclear Regulatory Commission, 2023). The DOT sets the requirements for packages in transit and the criteria for labeling. (US Nuclear Regulatory Commission, 2023) Depending on the nature and activity of the radioactive material being shipped and the mode of transport, there are different requirements for its shipment, all designed to keep those working with the radioactive material and any member of the public safe from unnecessary radiation exposure and keep the source from being released to the environment. The packaging for shipping the radioactive material undergoes rigorous testing, including the ability to withstand fire, water, and accidents. Specific packaging testing for casks, which are designed to transport high-level radioactive material, includes: “Collisions with objects that cannot move, like being dropped from 30 feet in the air. Being dropped 40 inches onto a steel spike. Being burned in a gasoline fire for 30 minutes. Submersion in water for eight hours” (US Environmental Protection Agency, 2024b).

While every effort is made in the US to maintain the safety and security of all radioactive materials, sources can still be lost or stolen. Radioactive sources exist worldwide, and many nations also have robust systems to ensure the safety and security of their radioactive materials; however, there are instances in which these sources could be acquired and used for nefarious purposes.

According to the International Atomic Energy Agency's (IAEA) 2024 Incident and Trafficking Database (ITDB), there were 4243 confirmed incidents during the timeframe of 1993-2023 (International Atomic Energy Agency, 2024). The ITDB noted a 22% increase in incidents between 2022 and 2023, with the rise potentially related to a return to normal activities following the COVID-19 pandemic, during which the IAEA reported a decline in incidents. (International Atomic Energy Agency, 2024) The ITDB categorizes incidents into three groups: "Group I: are incidents that are, or are likely to be, connected with trafficking or malicious use; Group II: incidents of undetermined intent; and Group III: incidents that are not, or are unlikely to be, connected with trafficking or malicious use" (International Atomic Energy Agency, 2024, p. 2). The IAEA points out that Group I incidents involving the sale of radioactive material are often discovered through sting operations, and the number of such incidents is unknown. (International Atomic Energy Agency, 2024) Furthermore, the IAEA reports that, historically, 52% of thefts of radioactive material occurred during authorized transport; over the last ten years, that statistic has risen to 65%, underscoring the need to increase attention to the reinforcement of the transport security of radioactive materials. (International Atomic Energy Agency, 2024)

Potential uses of a stolen radioactive source would be as a Radiological Dispersal Device (RDD) or a Radiological Exposure Device (RED). An RDD or "dirty bomb" is defined as taking a large quantity of radioactive material and using conventional explosives or other means to disperse the radioactive material, contaminating the area or property and causing harm to those around it, both through the radiological hazard and potentially from the conventional explosion. (Bland et al.,

2018) Both RDD and RED aim to cause “massive disruption and panic but would not be expected to cause significant morbidity and mortality from the effects of radiation” (Chao, 2007). There are no known instances of an RDD being employed, but the threat is of concern. There are several known instances of an RED being used to harm others; in most cases, it was used by an individual with access to radioactive materials with the intent to harm a specific individual.

One historical RED instance recently declassified was the ionizing radiation exposure at a significant level of then US Vice President Richard Nixon and his wife, Pat, in July 1959 on their famous visit to Moscow. (Burr & Kornbluh, 2022) There is no evidence of any significant health effects from this exposure, as the supporting Secret Service Agents used a Radiac meter to detect the exposure in the Nixons’ sleeping quarters and responded appropriately. The most recent RED case was the 2006 homicide of former KGB Agent Alexander Litvinenko, where he drank tea laced with five millicuries of polonium-210, an alpha-emitting radionuclide, resulting in his death due to Acute Radiation Syndrome. (Bland et al., 2018)

An RED is defined as exposing individuals to a sealed radioactive source, generally without intentionally dispersing that source and causing harm maliciously, often in public places where unsuspecting individuals would be exposed. (Bland et al., 2018) “The RED assailant would be attempting to avoid detection both of the material theft and of the material while the act is in progress” (Bland et al., 2018, p. 8). The Litvinenko case is considered a RED from the perspective of the individual who perished; it is noted that the contamination from this incident was spread throughout Europe due to the nature of the contaminant and was not the intention of the actors. With an RED, the threat of it lies in a radioactive source being placed in a public place like under a bench in a park, or under a seat in a train, bus, or subway car, or under a table in a restaurant. An RED would cause the most significant biological harm to humans in locations where individuals remain near the source. (Bland et al., 2018) For an RDD, the radioactive material would be dispersed, contaminating the individual and the area.

The IAEA defines a dangerous quantity of radioactive material as "one 'that could, if not under control, give rise to exposure sufficient to cause severe deterministic effects'" (International Atomic Energy Agency, 2006). Furthermore, Sandia National Lab's Threat Profile for REDs lists specific criteria for use as an RED the following:

- "Dose rate equal to 100 rad (1 Gy) per hour at one meter from the source
- Mass less than or equal to 10 kg
- Half-life greater than or equal to one week" (Bland et al., 2018, p. 11).

The theory behind these criteria is that the quantity used must be able to produce the desired biological impact, be of a size that may be acquired so as not to cause too much alarm or be noticed easily when stolen or placed, and have a long enough half-life to get to its intended location and cause enough harm to meet the intent.

The use of an RED in a tunnel is a potential scenario that could create high enough dose rates to meet the criteria for an act of terrorism; due to the high density of their structure, the fixed distance they create between an RED and anyone traveling through the tunnel, and their ability to provide locations where an RED could inconspicuously be placed.

According to Merriam-Webster online, a tunnel is a "covered passageway specifically: a horizontal passageway through or under an obstruction, a subterranean gallery (as in a mine). [or] burrow" (Merriam-Webster, 2024). Tunnels are widespread worldwide, enabling travel from one side of a mountain to the other without going up and over it, whether by automobile or train. Tunnels and underground structures enable mass transit in large cities like New York and London, where underground railways cross from one side of the city to the other, transporting hundreds of thousands of people daily. This high incidence leads to another potential target for terrorists, aiming to cause the most destruction with the least effort. Despite increasing reliance on subterranean infrastructure worldwide, quantitative characterization of radiation transport behavior in such environments remains limited, particularly at infrastructure-representative scales.

Sixty miles west of Denver, Colorado, on Interstate 70, lies the 1.7-mile Eisenhower-Johnson Memorial Tunnel (Colorado Department of Transportation, 2023). An average of 35,000 vehicles pass through it daily, and it takes approximately 2 minutes to travel from one end of the tunnel to the other (Colorado Department of Transportation, 2023). This tunnel allows the public to bypass over nine miles of treacherous mountain terrain, connecting east and west Colorado. The tunnel enables the vital transport of goods and people year-round, especially in winter when mountain passes become more challenging to navigate.

Imagine a terrorist hiding a large radiation source in one of the pedestrian passages between the two bores of an automobile or train tunnel, exposing those passing through the tunnel. Or suppose an Iridium-192 source, often used in industrial radiography, is orphaned and lost in a commuter train tunnel, again exposing the public to a large dose of ionizing radiation. Several incidents have occurred in recent history where both unintentional and intentional CBRNE incidents involving railways have occurred, including the 1995 Tokyo Subway incident involving the intentional release of sarin gas into the trains and stations (Petersen et al., 2023). As of 5 July 2024, the University of Maryland Global Terrorism Database (GTD) listed 822 incidents worldwide from 1970-2020, including the key term "tunnel" (University of Maryland, 2024). The GTD listed 747 of the 822 total incidents in which bombing or explosives were used as the attack type (University of Maryland, 2024). While none of them are listed as being nuclear or radiological, it is known that the use of a radiation source with explosives to create a dirty bomb is a potential threat.

In either scenario, once the radiation is detected, a specialized team must locate and secure the source to prevent future exposure to others. The challenge in a well-shielded tunnel is that ionizing radiation does not behave the same there as in free space or less-dense environments, producing higher radiation levels where no source exists. (Parker, 2022) This phenomenon is known but needs to be better characterized, making the team's task of locating the radiation source more difficult and increasing the dose for the responding members.

One key element in the preparedness and response of Chemical Biological Radiological Nuclear Explosive (CBRNE) teams is the detailed modeling of potential threats to better support team response planning (Norman Coleman et al., 2019). Modeling ahead of time is critical to training, and modeling during an event helps the team adapt to each situation. Real-time modeling includes mapping the radiation dose heat map onto the geographical map, providing the on-site commander and team members with a visual representation of the hazard (Norman Coleman et al., 2019). When an incident occurs, every moment counts, making the accuracy of the modeling crucial.

Another tool in the health physicist's toolkit is the use of robust transport modeling, such as Monte Carlo N-Particle (MCNP) software, in conjunction with additional coding and visualization software to view results and assist in interpreting findings. Using a series of specialized software packages, including SpaceClaim, Attila4MC, and Monte Carlo N-Particle (MCNP), earlier research (Parker, 2022) provided a baseline for more precisely defining and characterizing ionizing radiation in a subterranean environment. This increased characterization enables the process of taking as few measurements as possible to predict the radiation field faced by first responders or CBRNE response teams and their command elements.

The overall aim of this research was to utilize specialized software to construct various geometries, evaluating both the location of the radiation source and the actual physical characteristics of the tunnels. These geometries served as the basis for creating a repository of standard or possible underground or dense environment geometries, providing the technical foundation for responding to Chemical, Biological, Radiological, Nuclear, and Explosive (CBRNE) response team scenarios worldwide. The tunnels evaluated were designed in SpaceClaim using a computer-aided design (CAD) file, which was then loaded into another computer program called Attila4MC to create the MCNP file and run in MCNP to determine the resulting radiation field. An iterative process was employed to create a repository of scenarios by evaluating each tunnel geometry individually with different radioactive sources and various source locations within the tunnel, including on the tunnel ground, near the tunnel walls, and at tunnel intersections. The goal was to determine which of these characteristics had the greatest impact on the resulting radiation field and which had a lesser effect.

1.3 - Problem Statement:

The limitations of the current subterranean radiation assessment are foundational: little is known about the radiation field in dense environments, and most first responders, including highly specialized CBRNE teams, assume that the radiation field in a dense environment mimics that in free air. When a radiation source is missing or a suspected RED/RDD is present in a tunnel, understanding the radiation field in a dense environment is critical. The basic radiation safety principles of time, distance, and shielding remain valid; however, assuming a radiation source is within line of sight, based on radiation detection measurements, is unsupported and warrants further investigation.

1.4 - Research Objectives:

This research investigates photon dose behavior in confined tunnel geometries using validated Monte Carlo transport modeling. The aim of this research is to explore the radiation field in a dense tunnel environment, with particular attention to regions and conditions in which it deviates from the inverse square law. There were two primary components to this research: one was to build a large repository of subterranean radiation fields using particle-transport simulation software, and the other was to analyze and interpret the modeled radiation field results. Future collaborative work will bridge the gap between what is currently used to evaluate the basic environmental hazards of a subterranean environment, taking as few radiation measurements as possible to determine the overall radiation field using an artificial intelligence (AI) platform to provide the on-scene commander in an emergency response involving a radiological hazard on the different zones of radiation to protect life and property best. A 2020 study aimed at assessing the efficacy of AI in reducing patient and provider radiation exposure found that AI significantly reduced the dose compared to traditional methods. (Bang et al.) Although the present research does not directly implement AI, the development of high-fidelity radiation field datasets in confined environments may support future data-driven modeling approaches.

Despite extensive characterization of gamma radiation transport in open-air environments, comparatively little peer-reviewed work has quantitatively evaluated dose-rate behavior within confined subterranean tunnel systems under radiological release conditions. Many emergency response models assume inverse-square attenuation without explicitly accounting for wall scatter and backscatter effects, introducing uncertainty in dose assessment and risk characterization during subterranean incidents.

1.5 - Research Hypotheses:

This research aims to quantify mesh dependence in F4 tallies and to validate photon dose predictions in confined tunnel geometries using International Commission on Radiological Protection (ICRP) 116 AP response functions.

A set of standard tunnel geometries and radiation sources will enable a better understanding and prediction of the radiation field in previously uncharted subterranean environments. The three aims of this research centered around the following hypotheses:

1. Geometric Convergence: Photon dose rates in sufficiently large tunnel geometries converge to inverse square law behavior within ±5% of gamma constant predictions.

2. Material Influence: Tunnel wall composition significantly alters photon dose distributions compared to an air-filled free-field geometry.
3. Scatter Enhancement: Confined geometries produce measurable scattered photon enhancement beyond direct line-of-sight relative to free-field conditions.

Each hypothesis was tested through controlled variation of:

- Tunnel geometry
- Wall material
- Source location
- Radionuclide energy spectrum

1.6 - Significance of the Research:

This research supports health physics and emergency response planning by providing quantitative dose-rate characterization in confined tunnel environments. Subterranean radiological scenarios remain underexplored despite their operational plausibility. The modeling framework developed herein provides a transferable methodology for evaluating radiation transport in other complex geometries.

Chapter 2 - Literature Review and Technical Background:

The literature review identified limited peer-reviewed research addressing radiation transport in dense subterranean environments. Prior studies largely focus on open-field geometries, shielding design, or contamination dispersion, with few quantitative analyses of operationally relevant tunnel configurations using Monte Carlo transport methods. This work addresses that gap by systematically evaluating photon transport behavior under controlled geometric and material variations relevant to emergency response.

2.1 - Radiation Interaction with Matter:

Ionizing radiation interacts with matter predominantly by transferring energy to the matter with which it interacts, specifically the atomic nuclei, the extranuclear electrons, or both, through excitation and ionization processes. Ionization is when "a sufficient amount of energy is imparted to raise the electron to an infinitely great orbit, that is, to remove it from the electrical field of the nucleus" (Johnson, 2017, p. 62). Excitation is similar to ionization; however, the electron does not leave the atom; instead, it moves to a higher orbit, and energy is released when it returns to a stable state. The type and energy of the incident radiation and the absorbing material dictate the probability and nature of the interaction. The energy transferred to the absorbing material results in the excitation and ionization of the absorbing material, resulting in heat. (Johnson, 2017)

"The probability of occurrence of any particular category of interaction, and hence the penetrating power of the several radiations, depends on the type and energy of the radiation as well as on the nature of the absorbing medium" (Johnson, 2017. p. 141).

The nature of the absorbing material affects how the radiation interacts. For gamma-rays of energies ranging between 0.75 and 5 MeV, how effective a material is at shielding the energy of an incident gamma-ray is approximately proportional to the density of the material. (Johnson, 2017) The denser a material is, the better it is at shielding than a less dense material. Gamma-ray interactions include three different mechanisms: photoelectric absorption, Compton scattering, and pair production. These three interactions end in the complete or partial transfer of the gamma-ray's energy to electron energy, and the photon either completely disappears or is scattered. (Knoll, 2010)

Charged particles like alpha and beta are more easily shielded and pose less of an external radiation exposure hazard than electromagnetic radiation and neutrons. Electromagnetic radiation, such as gamma and X-rays, is more easily detected and generally requires more shielding. Considering the risk to human health due to external exposure to electromagnetic radiation is a more significant biological concern and will be the focus of this research.

2.2 - Radiation Dosimetry Frameworks:

A radiation field is defined by the number of particles, their energy, direction, and sequential or temporal distributions. (ICRP, 2010) This description requires defining both scalar and vector quantities. Fluence is the term used for the scalar quantity in this research. Fluence is constructed on the notion of counting the number of particles incident or passing through a small sphere or point in the irradiated area. Fluence, F, is defined mathematically as the quotient of the number of particles, dN, incident on a sphere of cross-sectional area dA with units of per square m. (ICRP, 2010)

International Commission on Radiological Protection Publication 116: Conversion Coefficients for Radiological Protection Quantities for External Radiation Exposures (ICRP 116) effective dose conversion coefficients were used to calculate the effective dose from the fluence determined for each F4 and F5 tally. Specifically, the Anteroposterior (AP) dose conversion coefficients from Table A.1 for photons were used. See Appendix A for Excerpt from Table A.1 ICRP Publication 116. The AP effective dose conversion coefficients were used instead of the isotropic (ISO) effective dose conversion coefficients because the individual is most likely facing the radiation source, rather than being fully immersed in it, which is what the ISO effective dose conversion coefficient is designed to calculate. Still, it would also be less accurate or representative of real-world scenarios. The ICRP 116 AP effective dose conversion coefficients were applied to the energy deposited in each sectioned energy bin per particle, and the results were converted to dose in units of pSv cm^2 for monoenergetic particles. Effective dose conversion coefficients were selected to ensure consistency between fluence-based tallies and operational dose-equivalent metrics relevant to responder exposure assessment.

2.3 - Radiation Detection:

Humans cannot detect radiation with any of our senses and rely upon instruments called radiation detectors. (Johnson, 2017) There are a variety of radiation detectors with a few basic qualities in common. For a radiation detector to respond to or detect the presence of radiation, the radiation must undergo an interaction that the detector can measure. There is not one radiation detector that can measure and characterize all types and energies of radiation. Radiation detector application varies based on the type of radiation and the energy range. The main types of effects used in the detection of radiation are electrical, chemical, light, thermoluminescence, optical luminescence, and heat. (Johnson, 2017) The types of detectors commonly used are gas-filled, semiconductor, crystal, solid, and liquid. (Johnson, 2017) Further classification of common instruments used includes ionization chamber, proportional counter, Geiger-Mueller counter, solid-state detector, scintillation counter, Cerenkov counter, semiconductor diode detector, and calorimeter. (Johnson, 2017)(Knoll, 2010)

Valuable considerations to address with all detectors are their efficiency and energy resolution. Efficiency is how well a detector or instrument can measure or detect radiation. Knoll describes absolute efficiency as the ratio of the number of radiation events measured divided by the number of radiation events emitted by the source. (2010) Knoll further describes intrinsic efficiency as the ratio of the number of radiation events measured divided by the number of radiation events incident on the detector. (2010) So, if the event gets to the detector, how efficient is the detector at determining that a radiation event did indeed occur? (Knoll, 2010) These definitions highlight the importance of geometry in radiation detection. Geometry is a term used to refer to the distance and angle or orientation of a radiation source from a detector. The efficiency must be known or determined to calculate the activity of the radiation source. Each type of detector varies in their efficiency. For example, sodium-iodide scintillation detectors have an accepted efficiency of around 13% for gamma-emitting sources and may be almost 100% efficient for measuring alphas and betas. Gas-filled counters, where the radiation source is placed inside the detector, result in up to 100% efficiency for alpha and beta emitters but their efficiency may be as low as 1% for gamma-emitting sources. (Knoll, 2010) (Johnson, 2017) Note that detectors require calibration and efficiency determination for radiation type and energy, as that varies.

The radiation source's physical characteristics also impact its detection efficiency, specifically size and shape. The most straightforward shape for calculating a rough dose rate is a point source, where the source is concentrated into one uniform sphere or point. Other common shapes or orientations that have been explored are line and plane sources. An example of a line source would be a pipe filled with radioactively contaminated water that runs the length of a wall or space. A plane source could be where radioactively contaminated water spills on the floor and makes a puddle or the wall of a container filled with a uniform radioactive material.

A health physicist or experienced CBRNE Team member using a radiation detector to determine the risk associated with radiation exposure know how to use their detectors, including any limitations, not just the efficiency and which types and energies of radiation it is capable of measuring or detecting, but also the upper and lower limits of detection inherent in their detector or the geometry needed to trust the measurements given. An experienced health physicist or a Certified Health Physicist (CHP) needs to not only know how to use the tools properly but also be able to relate dose rates and determine the associated risk to that exposure. Part of detector maintenance includes periodic calibration, usually annually, which confirms that the detector works as specified and provides a calibration curve showing how it responds to different energies. (Johnson, 2017) Detectors need periodic calibration to ensure they measure radiation accurately, as they may over- or underrepresent the actual radiation present. The reliance on what the detector reads is so significant that verifying it is working correctly is not only accepted in the scientific community but also required by regulatory bodies such as the Nuclear Regulatory Commission (NRC). The NRC also requires that a survey instrument be calibrated "before first use, annually, and following a repair that affects the calibration" (Calibration of Survey Instruments, 2017) and that instruments that differ more than 20 percent between the indicated and calculated measurement may not be used.

A detector type is selected based on the inherent characteristics of the measured radiation source, the knowledge sought, and the environment in which the radiation source exists. Some radiation detectors are designed to measure quantities in fixed laboratories, while others are battery-operated, handheld, vehicle-mounted, or aircraft-mounted. Radiation detectors can also be passive monitors, as seen in hospitals, transport centers, waste disposal facilities, and scrap metal collection facilities.

The German nuclear emergency response organization, Kerntechnischer Hilfsdienst GmbH (KHG), has a remote detection group with an array of specialized remotely operated radiation measurement systems or robots capable of operating in high radiation fields. (Friedrich et al., 2024) The KHG's systems can transmit data and video through radio or cable connection. It is noted by the KHG that for optimal data collection, transmission should be conducted by use of a cable, rather than a radio signal. (Friedrich et al., 2024)

Another piece of the radiation detection and characterization puzzle is understanding how radiation acts in the environment being studied. It is well understood how ionizing radiation acts in open or free space, where radiation intensity is not easily scattered or absorbed. The dose rate of a gamma point source is characterized by the inverse square law, which states that the intensity of that radiation "in free space varies inversely with the square of the distance from the point" (Johnson, 2017). Another way to consider this concept is that doubling the distance from a point source reduces the intensity by a factor of four. Since the inverse square law only applies to point sources and not to other source geometries, like a line or plane source, it is helpful in application to know the following "rule of thumb: as long as the distance away from the source is at least three times the longest dimension of the source, then inverse square law calculations will give the correct answer to within one percent" (Gollnick, 2018). This is helpful when measuring the radiation dose rate for a source contained within a pipe, liquid spilled on the floor, or a generally irregular shape and using that dose rate to more easily calculate the dose rate emitted from the source's surface.

The radiation field surrounding gamma sources is well-characterized and understood above ground or in free space, but not in the highly shielded, dense environment found in tunnels or the subterranean environment. With the ever-expanding system of tunnels used for a variety of modes of transportation throughout the world and the presence of nefarious entities aiming to terrorize and wreak havoc on the unsuspecting public, it is vital to delve into this environment to aid in CBRNE response teams when that scenario plays out. CBRNE teams are specialized to respond to various threats, each with unique hazards and response protocols.

It is important to distinguish between detecting and mapping a radiation source or field. Detection is the process of determining the presence of a radiation source and distinguishing it from naturally occurring or background radiation. Mapping of a radiation source or field is intended to show the radiation dose rates created by the source or field. Given the survey's purpose, there are roles for both processes. Detection can be performed relatively quickly, whereas mapping takes more time, depending on several factors, including the detector used and whether it is handheld and manually recorded or connected to an automated system, an autonomous device, or a robot. (Zavala, 2016)

Subterranean geometries introduce a radiation transport phenomenon commonly referred to as tunneling or streaming. In radiation transport analysis, tunneling describes the axial streaming of photons through an elongated confined cavity where lateral boundaries limit geometric dispersion and reduce shielding interception. Unlike free-field conditions, where dose decreases primarily according to inverse-square behavior, tunnel geometries allow forward-directed photons and scattered components to propagate over extended distances, producing sustained fluence and dose rates relative to open-air environments. (IAEA, 2006)

2.4 - Radiation Detection in Subterranean Environments:

There are several distinct differences in radiation detection in subterranean environments compared with other environments. Some of these differences are related to the detection and characterization of the radiation, which is the subject of this research, and others are specific to the environment inherent to subterranean. One of the bigger concerns is communication. The same dense environment that modifies the radiation field also poses communication challenges, whether for an individual in the tunnel or for a robot evaluating the environment. If a traditional wireless radio or data transmission is used, it often relies on line-of-sight or wall penetration. This creates a challenge because tunnels typically have a limited line of sight, and dense walls impede the transmission of communication waves. Planning for these challenges is an important part of preparation. Whatever form is used to relay communication between the robot or team members in the tunnel and the team outside the subterranean environment, such as the command center, can also relay the radiation dose reported by the detectors used for this application. This is a tested method used for other applications, such as monitoring the vital signs of response teams.

While the repository characterizes radiation fields of defined tunnel geometries, given the large variety of tunnel shapes, the future application of this research must also consider the location of a radiation source in an unknown or unmapped tunnel. There are several options for achieving this, including light detection and ranging (LiDAR) and photogrammetry. LiDAR works well in poor light or no light since it uses lasers to determine the space and does not require ambient light to function properly. LiDAR generally requires a few minutes to hours or days, depending upon the complexity of the space being measured. The equipment used in LiDAR is comparatively expensive to that used in photogrammetry. Photogrammetry can be completed relatively quickly, but for more accurate rendering, it requires the space to be lit. This could be accomplished using powerful lights to illuminate the space. Photogrammetry relies on 40-50 photographs taken with a simple digital camera, then uploaded to software to compile the 3D map. Each technology has its advantages and disadvantages. LiDAR is an established technology for mapping mining tunnels. Still, it may not be within the responding team's capabilities but to use photogrammetry instead, which can be easily applied with existing equipment, as another viable option to determine the tunnel's geometry. Another consideration when choosing between these two mapping technologies is time. LiDAR can take quite a bit of time and may not be optimal in high-radiation environments or when time is of concern. Alternatively, existing design or building documents, such as maps or blueprints, could be consulted by the first response or incident command team to better understand tunnel layouts and dimensions.

The ideal situation for obtaining both radiation dose measurements and tunnel geometry or a map would be an autonomous driving robot equipped with LiDAR and radiation detection (gamma spectrometry and dose rate measurements). Pairing radiation detection with precise tunnel location improves the accuracy of estimating radiation source strength and location, while also providing a radiation heat map to equip the on-scene commander with the most effective information on radiation hazard zones.

The training tunnels at the Eisenerz Training Facility in Zentrum am Berg (ZAB), Austria, are used as a standardized example for tunnel geometries. Many agencies use the ZAB tunnels to train on emergency response techniques in the event of tunnel fires, large-scale accidents, and CBRNE scenarios without needing to shut down actual transportation modes to provide these essential training opportunities. The attention placed on building these tunnels provides an excellent example for modeling other tunnel systems worldwide.

Earlier research (Parker, 2022) demonstrated the presence of enhanced photon scatter and apparent radiation streaming in small-scale subterranean tunnel analogs through combined measurement and Monte Carlo modeling. The present study extends that foundational work by examining full-scale roadway tunnel geometries, implementing a hypothesis-driven statistical evaluation framework, and quantifying confinement effects using effective-dose metrics relevant to operational radiation protection. This progression enables systematic assessment of geometry scale, material composition, and transport methodology in determining spatial dose behavior in complex underground infrastructure.

2.5 - Zentrum am Burg Tunnel System:

The inspiration for and foundational tunnel system used in this research is the Zentrum am Berg Tunnel System in Eisenerz, Austria. This tunnel system is used for training both military and civilian response teams. This innovative training site enables first responders to gain valuable experience working in tunnels without necessitating the shutdown or diversion of active tunnels. To facilitate this research, a Computer-Aided Design (CAD) file of the tunnel system at ZAB, provided by COL Hofer of the Theresian Military Academy of the Austrian Armed Forces, served as the foundational blueprint for standardized tunnel design. The ZAB tunnel system consists of roughly four kilometers of tunnels, with four major transportation tunnels comprised of two parallel road tunnels and two parallel train tunnels, as well as various geometries within each to model and gain insight to the interaction of radiation in the highly dense environment. (Montan-Universität - Leoben, n.d.) Figure *2-1* shows the ZAB tunnel system. The provided CAD file is highly detailed, with over 200 individual components, enabling extraction of each tunnel or tunnel section for focus. The ability to select only portions of the tunnel system for modeling assisted in ensuring the geometry remained representative and the model ran efficiently.

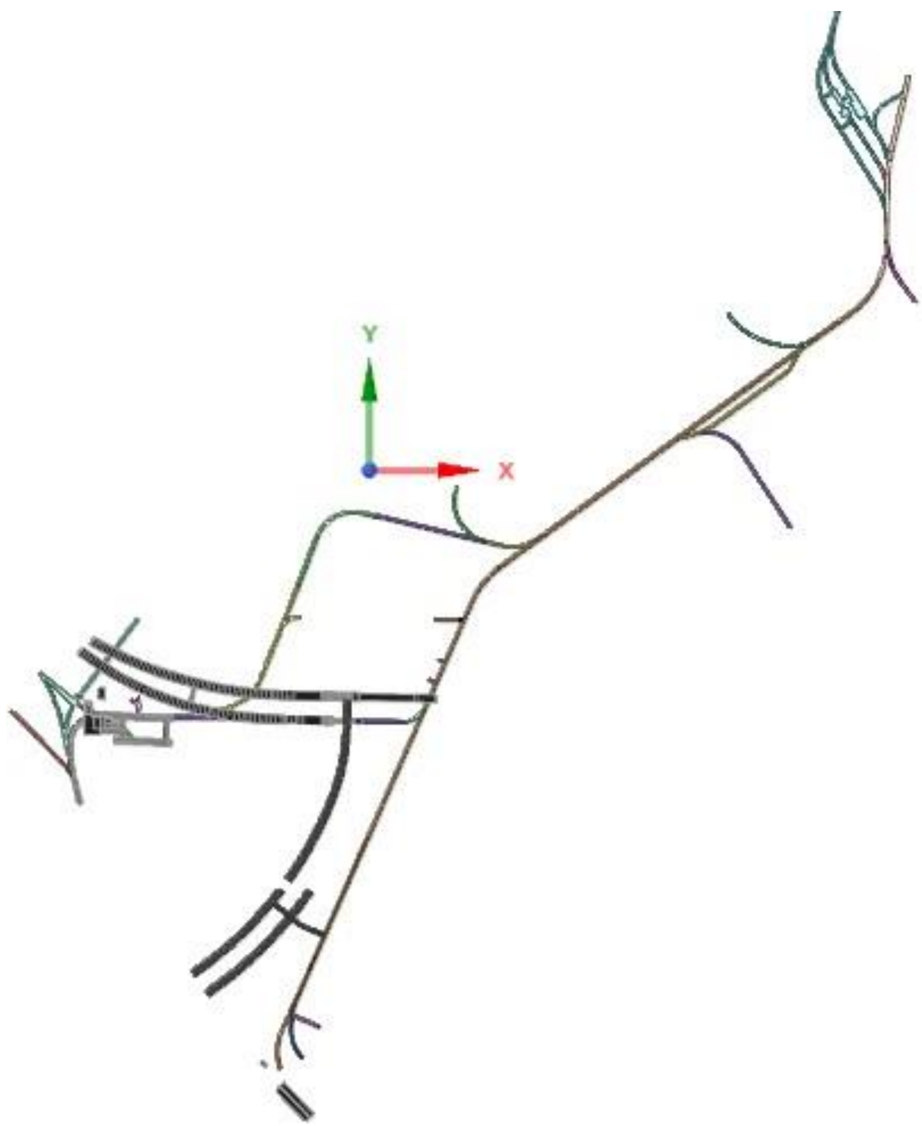

Figure 2-1 Zentrum Am Berg Tunnel Map.

2.6 - Monte Carlo Radiation Transport in Confined Geometries:

2.6.1 Photon Transport Physics:

Photon transport in matter is governed by stochastic interactions, including the photoelectric effect, Compton scattering, and pair production. For the photon energy range investigated in this work (primarily 0.186–2.2 MeV corresponding to Ir-192, Ra-226 progeny, Cs-137, and Co-60 emissions), Compton scattering dominates in low- to medium-Z materials, while the photoelectric effect contributes more significantly at lower energies.

The total linear attenuation coefficient μ_t is defined by the following equation:

Equation 1: Total linear attenuation coefficient.

$$\mu_t = \mu_{pe} + \mu_{cs} + \mu_{pp}$$

Where:

- μ_t is the total linear attenuation coefficient
- μ_{pe} is the Photoelectric Effect linear attenuation coefficient
- μ_{cs} is the Compton scattering linear attenuation coefficient
- μ_{pp} is the Pair Production linear attenuation coefficient (Johnson, 2017)

The attenuation of an uncollided photon beam in homogeneous media follows (Johnson, 2017):

Equation 2: Attenuation of an uncollided photon beam.

$$I(x) = I_0 e^{-\mu x}$$

Where:

- $I(x)$ is the intensity of the photon beam after attenuation by absorbing media of x thickness
- μ is the attenuation coefficient
- I_o is the initial intensity of the photon beam
- x is the thickness of the absorbing media

However, in confined geometries such as tunnels, the radiation field is not governed solely by exponential attenuation. Multiple scattering events produce a build-up of scattered photons, modifying both spatial dose gradients and angular distributions.

2.6.2 Inverse Square Law and Its Assumptions:

The inverse square law (ISL) is derived from geometric divergence of radiation in an unbounded medium and can be represented by the following equation (Turner, 2010):

Equation 3: Inverse Square Law

$$X(r) = \frac{\Gamma A}{r^2}$$

Where:

- $X(r)$ is the dose rate from a point source at distance r
- Γ is the gamma dose rate constant
- A is the source activity
- r is the radial distance

This relationship assumes:

- No scattering
- No shielding
- Isotropic emission
- Infinite free field

In confined tunnel geometries, scattering from walls, floor, and ceiling introduces secondary photon contributions. Therefore, deviation from ideal inverse square law behavior is expected. This work quantifies that deviation.

2.6.3 Monte Carlo Radiation Transport:

Monte Carlo radiation transport simulates individual particle histories by probabilistically sampling interaction cross-sections. Each particle is tracked through:

- Emission from the source
- Transport through materials
- Interaction sampling based on evaluated nuclear data libraries
- Scoring in defined tally regions

Monte Carlo N-Particle (MCNP) is an export-controlled software developed by the Department of Energy at Los Alamos National Laboratory as a general-purpose particle transport code that models three-dimensional space or geometry. (Los Alamos National Laboratory, 2024) MCNP is used to determine the radiation field produced by a defined radiation source, accounting for the physical properties of the radioactive particle's interaction with the material. Radioactive decay and interactions are statistical in nature, and increasing the number of particles simulated in the software improves statistical accuracy in predicting how a given radiation source will affect each environment. This allows modifications to the environment to be made during design and before construction, ensuring exposure to the environment and individuals is kept as low as reasonably achievable (ALARA). It can also allow for increasing shielding or changing the entry or exit path in cases where a radiation source needs to be secured.

While Monte Carlo radiation transport methods are mathematically rigorous, their practical value lies in their ability to simulate complex, real-world radiation environments that cannot be solved analytically. Conceptually, the Monte Carlo method tracks a large number of individual photons as they are emitted from a source and undergo probabilistic interactions with surrounding materials, including scattering and absorption. Each interaction is governed by known physical cross sections, allowing the aggregate behavior of many particles to approximate the true radiation field.

In the context of subterranean tunnel environments, this approach is particularly well-suited because photon transport is strongly influenced by geometry, material composition, and repeated scattering interactions. Unlike free-field conditions, where radiation behavior can be approximated using simple inverse-square relationships, tunnel environments introduce boundary-driven effects that require explicit simulation of particle trajectories. The Monte Carlo method therefore provides a physically grounded means of resolving how confinement, wall interactions, and structural features modify the resulting dose field in ways that are directly relevant to operational radiation protection.

2.6.4 Tallies in MCNP:

MCNP is a particle transport modeling software package. Tally cards are used to inform MCNP what the user would like to know or what they would like calculated. The two types of tally cards used in this research are F4 and F5:

F4 – Cell Fluence Tally

One note on the terminology between fluence and flux in the context of this research and published MCNP guidance. The MCNP F4 tally provides a track-length estimate of photon fluence (particles$\cdot$cm^{-2} per source particle) within the defined cell volume. Although the MCNP manual refers to this quantity as "volume flux," it is formally equivalent to scalar fluence in radiation protection terminology. After scaling by source activity, the resulting quantity represents photon fluence rate (particles$\cdot$cm$^{-2}\cdot$s^{-1}), which was subsequently converted to effective dose rate using energy-dependent fluence-to-dose conversion coefficients. The F4 tally computes the track-length averaged fluence within a cell in the following equation (Werner, 2017, p.1-11):

Equation 4: Track-length average fluence.

$$\Phi = \frac{1}{V}\sum \text{track length}$$

Because the tally is volume averaged, spatial gradients within a large cell may reduce peak values.

F5 – Point Detector Tally

The F5 tally estimates fluence at a specific point using next-event estimation, reducing variance for localized measurements. (Werner, 2017, pp. 1–11) Unlike F4, F5 does not average over a finite volume and therefore more closely represents an idealized detector at a point in space. This distinction becomes critical in confined geometries with strong spatial gradients.

MCNP tallies provide different ways of estimating radiation quantities depending on how particle interactions are sampled and recorded. In this work, two complementary tallies were used: the F4 tally (track-length fluence estimator) and the F5 tally (point detector). The F4 tally estimates the average photon fluence within a defined volume by summing the total path length traveled by particles within that region. This makes it particularly well-suited for evaluating spatially distributed radiation fields, such as those present in tunnel environments, where dose varies continuously across space. In contrast, the F5 tally estimates fluence at a single point using an analytical next-event estimator, effectively bypassing some of the stochastic variability associated with particle transport. This makes the F5 tally highly efficient and precise for point-specific comparisons. The combined use of F4 and F5 tallies in this research serves both a practical and validation purpose: the F4 tally enables spatial mapping of effective dose throughout the tunnel geometry, while the F5 tally provides an independent point-based reference to verify the accuracy of the volume-averaged results. Agreement between these two approaches increases confidence that the modeled radiation fields accurately represent the underlying physical transport processes.

2.6.5 Fluence-to-Dose Conversion:

Photon fluence was converted to effective dose using ICRP 116 fluence-to-effective-dose coefficients. The AP (anteroposterior) geometry was selected as it most closely represents forward irradiation conditions relevant to tunnel response scenarios.

The effective dose was calculated as:

Equation 5: Effective dose.

$$D = \Phi \times \text{DCF}$$

where DCF is the fluence-to-effective-dose coefficient (pSv·cm²).

The AP geometry was selected over ISO geometry because ISO coefficients led to an overestimation in preliminary modeling. Specifically, when comparing the ICRP 116 ISO effective dose conversion coefficient, the resulting effective dose was approximately 30% above the calculated dose. When using the ICRP 116 AP effective dose conversion coefficient, the average percent difference between the F4 tally effective dose, and the calculated dose using ICRP 38 was 7%-10%. Additionally, isotropic geometry "approximates the radiation field to which a body is subjected, if suspended in a large cloud of radioactive gas or placed in a highly scattered radiation field" (ICRP, 2010) and thus does not fit the description of the research conducted. Whereas when considering the definition for AP geometry is when "the ionizing radiation is incident on the front of the body in a direction orthogonal to its long axis," (ICRP, 2010), which is a stronger correlation to the radiation environment core to this research.

2.7 - Other Specialized Software:

While MCNP is the most widely used software and provides the basis for the research, other specialized software was also instrumental in this research. The following additional specialized software was used for modeling and analysis of the results: Attila4MC, SpaceClaim, and Tecplot. A brief description of each software package and its use follows. Note that Microsoft Excel and Python were also used but are not described in detail below due to their widespread familiarity.

2.7.1 SpaceClaim:

Ansys's SpaceClaim software is a three-dimensional modeling and rendering tool that can import geometry from other modeling and rendering software to create an Attila4MC-compatible geometry file needed to replicate the physical space modeled in MCNP. This software streamlines the transport modeling process using MCNP by generating the necessary Attila4MC input files through an intuitive user interface. (Ansys, 2024) SpaceClaim enhances the accuracy of the model by allowing the input of more precise renderings of actual spaces, such as a LiDAR-created file, which can provide a more accurate representation of the real-life geometry. SpaceClaim was also used because the provided tunnel geometry file required additional modification to ensure compatibility with the complexity of radiation transport modeling in MCNP.

SpaceClaim can be used to either modify existing files, like the ZAB CAD file, or create geometries from scratch. Additional tunnels were created in SpaceClaim to simulate tunnels of varying dimensions, allowing for an investigation into the impact that tunnel diameter has on the radiation field. Part of the aim of this research is to identify parameters where a radiation field in a dense environment mimic the free-space field to allow for a better understanding of this environment.

Space Claim allows for measuring distances and determining coordinates for radiation source locations. Given that most of the research focused on the ZAB tunnel system, utilizing this functionality was crucial to ensure the source was correctly assigned within the tunnel and to identify the coordinates for potential locations for additional sources, thereby expanding the repository of radiation heat maps.

Using the SpaceClaim measuring tools helped determine the coordinates for the optimal placement of radiation sources, which were then input into Atilla4MC. There are virtually an infinite number of locations that the source could be placed, so the goal was to focus on the most likely locations. Radiation sources were modeled to be on the ground, near walls, on the ceiling, near entryways between one tunnel and another, centered between tunnel walls on the ground, centered between tunnel walls, and at a height of one meter.

2.7.2 Attila4MC:

Once the geometry file was created in SpaceClaim, it was uploaded into Attila4MC to be the basis of the MCNP input file. The geometry file was further modified in Attila4MC via meshing. This process took each solid body in the three-dimensional geometry and divided it into hundreds of thousands of unique shapes, called tetrahedrons. During the meshing process, the maximum length of each side of a tetrahedron in each solid body can be set or left undefined. The smaller the tetrahedron, the more precise the resulting radiation field or heat map. Additional parameters were added to include the specific radiation source, generate the MCNP input file, which the MCNP modeling software will execute to determine the radiation field. Attila4MC creates a mesh and allows the user to assign physical properties to each component. An example of this is indicating that the chemical composition of the floor is concrete and that the shipping container is made of steel. Once all parameters are selected, including the number of particles and the radiation source location and source properties, Attila4MC produces the necessary MCNP input file. According to Silver Fir, the software engineering company behind Attila4MC, MCNP "relies on command line input for defining model geometry, calculation input, and variance reduction, which can often create significant bottlenecks limiting calculation throughput" (Silver Fir, n.d.). Attila4MC streamlines the modeling process.

2.7.3 Tecplot:

Tecplot is an additional software package embedded within Attila4MC. Tecplot provides key data visualization and extraction capabilities, using the eeout file produced by MCNP.

2.8 - Foundational Work:

Earlier research conducted as part of a Colorado State University Master of Science thesis titled *Characteristics of Gamma Radiation Fields in Subterranean Structures for Radiation Protection and Decision Making* investigated photon transport behavior in confined tunnel environments using a combination of Monte Carlo modeling and controlled experimental measurements (Parker, 2022). This work established a proof-of-concept framework by demonstrating consistent agreement between simulated and measured radiation fields within small-scale subterranean geometries. The study utilized the Zentrum am Berg (ZAB) tunnel system in Eisenerz, Austria, as a representative environment for evaluating radiation transport under high-scatter conditions.

Results from this earlier investigation demonstrated that radiation fields in confined, high-scattering environments deviate from classical inverse-square behavior. Dose rates were observed to exceed free-field predictions in both near-field and far-field regions, indicating the presence of scatter-mediated transport and radiation streaming effects (Parker, 2022). The study further showed that tunnel geometry plays a significant role in shaping radiation field distributions, with distinct spatial patterns observed in straight, curved, and intersecting tunnel configurations. In straight tunnel geometries, dose rates were reported to be up to approximately 33% higher than free-field values, while T-intersection configurations exhibited variations of approximately 65%–77% depending on detector position relative to the source.

Additionally, earlier research identified strong spatial dependence in dose behavior within confined environments. Scattered photon interactions contributed to elevated dose rates near the source, while the angular distribution of scattered photons limited propagation along the tunnel axis, resulting in more rapid attenuation in certain shielded regions despite enhanced near-field dose. These findings collectively demonstrate that confined geometries produce complex, spatially structured radiation fields that are not adequately described by simple geometric attenuation models.

This prior work established a validated foundation for applying Monte Carlo methods to subterranean radiation transport problems and demonstrated that confinement effects produce measurable and operationally relevant deviations from free-field expectations.

Key methodological differences between this earlier work and the present study include the selection of dose conversion coefficients and irradiation geometry. Earlier research employed the International Commission on Radiation Units and Measurements (ICRU) Report 57 dose conversion coefficients with an ISO irradiation geometry, whereas the present study uses the ICRP Publication 116 dose conversion coefficients with an anterior–posterior (AP) geometry. ICRP 116 represents an updated dosimetric framework with revised computational methodology and improved anatomical modeling (ICRU, 1998). The implications of ISO versus AP geometry selection were discussed previously in this dissertation.

2.9 - Research Gap and Contribution:

This research addresses two scenarios: the accidental loss of a radioactive source in a tunnel and the purposeful placement of a radioactive source in a tunnel, such as a Radiological Exposure Device (RED). The more likely scenario is the RED, at least in areas where transportation and management of radioactive sources are highly regulated, such as in the United States.

Currently, detecting ionizing radiation in free air is well characterized and follows the inverse square law. Still, due to several factors, radiation detection behaves differently than we would conventionally expect underground. This is problematic when a radiation source needs to be found or threatens the lives of emergency or military personnel called in to respond to an emergency or in a potential terrorist attack involving a radiation source in tunnels or another underground structure.

While there is a clear gap this research addresses from an application, emergency response, and preparedness standpoint, the scientific gap it addresses concerns radiation characterization and detection in dense and confined spaces. There is a wealth of knowledge on the inverse-square law and on the radiation dose map for different radiation geometries, including line sources, area sources, and air plumes. Still, there is minimal research on how radiation sources behave in highly dense areas such as mines and tunnels.

2.10 - Assumptions:

For this research, it is assumed that the measured dose rates were obtained by a qualified individual using a calibrated detector capable of accurately measuring the radiation source of concern.

Chapter 3 - Methodology:

This chapter details the methodology employed to model, simulate, and analyze gamma radiation fields in subterranean tunnel environments. The approach integrates high-fidelity geometric modeling in SpaceClaim, unstructured mesh generation in Attila, and radiation transport simulations using MCNP. Multiple tunnel geometries, construction materials, and radiation-source configurations were evaluated to quantify deviations from the inverse-square law (ISL) and to assess the influence of scattering and streaming effects.

The MCNP code was selected for its validated photon-transport physics, established use in radiation protection analysis, and ability to accurately simulate coupled scattering phenomena within complex geometries. Photon histories were simulated to achieve relative statistical uncertainties (1σ) below 0.05 in regions of operational interest. Convergence was evaluated using the MCNP-reported relative standard deviation (R) of tally estimates, along with standard Monte Carlo diagnostic parameters and variance reduction performance metrics.

3.1 - Operational Radiation-Field Terminology:

For clarity in interpretation of confinement-modified transport behavior, several descriptive terms are used throughout this dissertation.

Structural photon streaming refers to preferential radiation transport pathways created by connected tunnel segments, openings, or geometric discontinuities that allow photon propagation beyond direct line-of-sight conditions.

Scatter-mediated dose persistence describes sustained effective-dose levels at distances or locations where geometric attenuation alone would predict substantially lower dose. This persistence arises primarily from Compton scattering interactions with tunnel boundaries.

Anisotropic dose field behavior denotes spatial variation in effective-dose magnitude that depends on geometric orientation and structural connectivity rather than radial distance alone.

The operational domain refers to the spatial region within which responder movement, measurement activities, or hazard-zone decisions are expected to occur, and corresponds to the analysis interval used for integrated dose metrics.

These terms are introduced to support consistent interpretation of hypothesis-driven statistical results and their application to radiation-protection decision making in confined environments.

3.2 - Overall Research Framework:

The research plan was organized to first determine how the specialized software functioned, interpret its results, and optimize its functionality, with the aim of addressing knowledge gaps in this field. Once a model was developed that balanced strong agreement across benchmarks and provided sufficient data to support future work in statistical machine learning and AI, variations were introduced to evaluate the hypotheses. Specifically varying the shielding material, tunnel geometry, and radiation source modeled to respond to all three hypotheses.

The study included systematic variations in tunnel geometry, tunnel size, mountain material, radiation source, and radiation-source placement within the tunnel. Throughout the experimental process, detailed notes and a standardized methodology, including following a regimented model naming nomenclature, were maintained to ensure that variations between runs could be compared and their impact assessed.

One key element of keeping these variations discernible was the use of a naming convention and a run log to document the specifics of each model. One of the names of the final set of models is run10ac137. Note that all models started with "run." The next element in the naming was a number that was used to signify the iteration of the model (starting with 1, and the final set was 10).

The next digit in the model's name referred to the alphabetic code assigned to the radiation source location, in this example, "a." The next item was the mountain material, in this example, "c" referring to concrete. For iterations in which an isotope other than Co-60 was used, the three-digit numerical value for that isotope was used; thus, this example was for a Cs-137 radiation source.

The selection of Monte Carlo N-Particle (MCNP) modeling for this research is driven by the need to accurately represent radiation transport in geometrically complex and materially heterogeneous environments. Subterranean tunnels introduce conditions in which analytical solutions are insufficient due to the combined effects of confinement, multiple scattering, and structural discontinuities. Monte Carlo methods allow these effects to be explicitly modeled by simulating particle interactions at the level of individual photon histories. This enables direct evaluation of how tunnel geometry, material composition, and source placement influence the resulting radiation field. As a result, MCNP provides a physically robust and flexible framework for addressing the central research question: how radiation dose behavior in confined tunnel environments deviates from idealized free-field assumptions.

3.3 - Conceptual Tunnel Geometry Definition:

Using SpaceClaim and the ZAB CAD file, the structures were identified and labeled with numbered labels and a diagram to determine which of the over 7,000 structures was optimal for use in this research. Specific tunnels were isolated from the tunnel system to reduce the overall file size, enabling more precise modeling of the desired geometries. This was accomplished by selecting and deleting the unnecessary tunnels in SpaceClaim, creating a new file with only the desired tunnel geometry. The focus was on solid structures because the follow-on software is designed to model radiation most effectively using solids. There are 64 solid structures, and the remaining 6,936 structures are surfaces that could be combined with other surfaces or modified as is to create a solid structure for modeling.

The primary tunnel evaluated was the road tunnel, as shown in Figure *3-1*. This tunnel featured several notable geometric characteristics, including straight and curved sections, three distinct tunnel diameters, and a pedestrian tunnel connecting the two adjacent road tunnels, thereby enabling investigation of the line-of-sight phenomenon explored by earlier research (Parker, 2022). Additional tunnels were created in SpaceClaim to simulate a much smaller and a much larger tunnel, to examine the impact of tunnel size. Representative tunnel dimensions and configurations were selected to reflect operationally realistic subterranean infrastructure rather than idealized radiation transport test geometries.

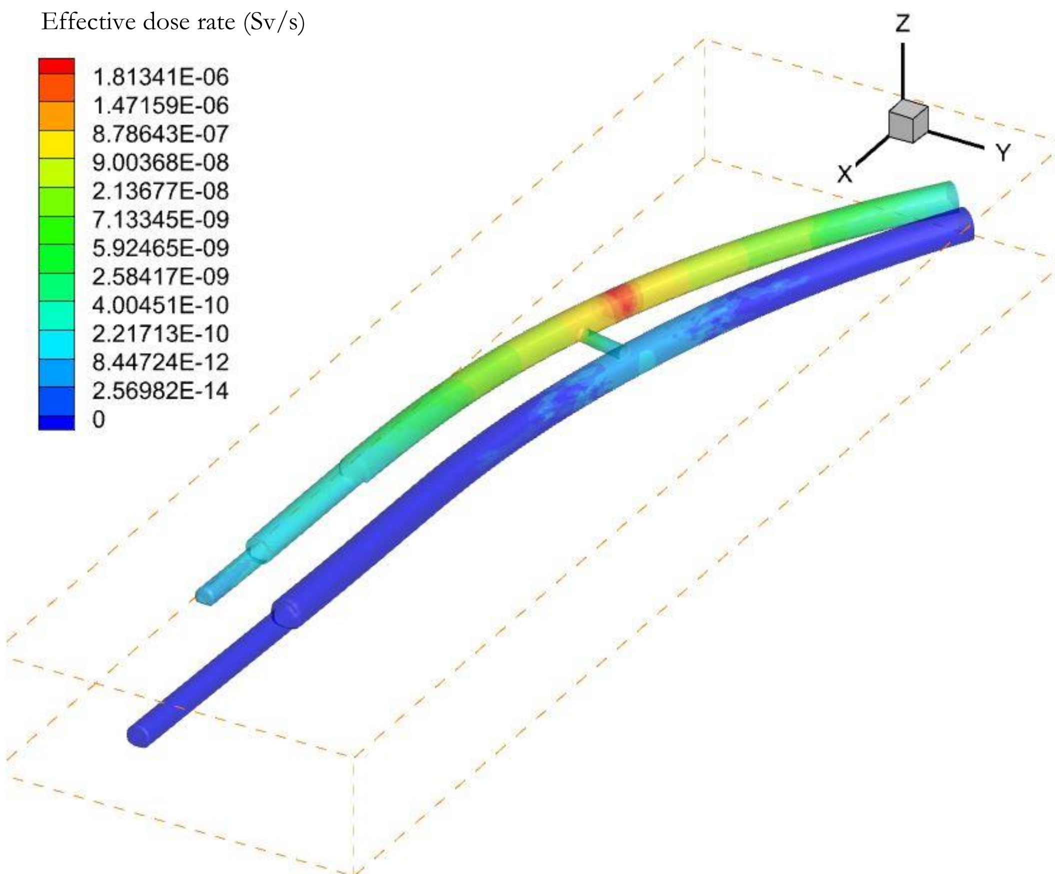

Figure 3-1 Spatial distribution of effective dose rate ($Sv \cdot s^{-1}$) in the ZAB road tunnel for a 1 Bq Co-60 source, calculated using MCNP F4 tallies with ICRP 116 AP conversion coefficients. The figure illustrates the baseline radiation field geometry used for subsequent quantitative analyses.

The materials chosen for mountain or tunnel material in this research include concrete, basalt, limestone, sandstone, granite, lead, and an average of five common rocks. Table *3.1* shows their densities in grams per cubic centimeter (g/cc). Note that lead is the densest material evaluated in this research, which is roughly four times denser than the following dense material. These materials were chosen based on their prevalence in mountain materials where tunnels may be, as well as using lead as a standard reference material, often used in ionizing radiation shielding. The aim of evaluating these materials was to assess the relative impact of the mountain or tunnel material on the resulting radiation heat map.

Table 3.1: Displays the materials used in this research and their associated density in units of grams per cubic centimeter. (Williams et al., 2006).

Material	Density (g/cc)
Air	0.001205
Rock, Limestone	2.278
Concrete	2.3
Rock, Sandstone	2.3
Rock, Average of Five Types	2.55
Rock, Granite	2.729
Rock, Basalt	2.9
Lead	11.35

3.4 - Source Term Modeling:

Another characteristic of the selected isotopes that affects this research is the energy and associated decay probability. Note that Table 3.2 lists each of the investigated isotopes and some of the more notable energies emitted from each. This is not an exhaustive list.

Table 3.2: Depicts select gamma and x-ray energy and probability of decay for the select isotopes, from the Health Physics and Radiological Health Handbook, fourth edition. The bolded values represent the energies and associated probabilities of greatest interest to a health physicist. (Johnson & Birky, 2012)

Isotope	Probability per decay	Energy (MeV)
Barium-137m (for Cs-137)	0.010381	0.004470
	0.020703	0.031817
	0.038197	0.032194
	0.013900	0.036400
	0.899800	**0.661650**
Cobalt-60	**1.000000**	**1.173200**
	1.000000	**1.332500**
	0.000163	0.693820
Iridium-192	**0.040934**	**0.009440**
	0.019555	**0.063001**
	0.290150	**0.295960**
	0.296780	0.308460
	0.828530	0.316510
	0.480550	0.468070
Radium-226	0.008023	0.011700
	0.001802	0.081070
	0.002994	0.083780
	0.001357	0.094900
	0.032800	**0.186210**
	0.000067	0.309700

Note that there are three known possible energies emitted from Co-60: 1.1732 MeV and 1.3325 MeV, each with a probability per decay of 1 (meaning each decay of Co-60 results in the emission of one of these photon energies), and 0.693820 MeV with a probability per decay of 0.000163. In MCNP, each modeled radiation source is defined using the SDEF card, which does not include all possible energy emissions or their associated decay probabilities. The SDEF card is user-defined and driven by data such as that in Table 3.2.

3.5 - MCNP Simulation Setup:

Monte Carlo particle transport is particularly well-suited to modeling radiation behavior in confined tunnel environments because it explicitly accounts for stochastic photon interactions with complex geometries and heterogeneous materials. Unlike analytic approaches, which assume idealized conditions such as unbounded space or uniform attenuation, the Monte Carlo method tracks individual photon histories as they undergo scattering, absorption, and energy loss. This enables direct quantification of boundary scattering, material-dependent attenuation, and structural photon streaming—phenomena central to radiation transport in confined geometries. This capability is particularly critical in subterranean tunnel environments, where repeated boundary interactions and geometric confinement fundamentally alter photon transport behavior relative to free-field conditions.

In this study, F4 (volume-averaged track-length fluence) tallies were used to estimate spatially distributed dose rate across the tunnel geometry, while F5 (point detector) tallies provided an independent reference for verification. The combined use of these tally methods supports both physically realistic dose estimation and internal validation of simulation fidelity.

MCNP Version 6 was used for this research. The user interface in Attila4MC was used to take the SpaceClaim geometry file and create a mesh geometry file. MCNP can use external structured and unstructured meshes to define problem geometry in a hybrid mode by embedding a mesh within a constructive solid geometry cell, providing an alternate path to defining complex geometries (Los Alamos National Laboratory, 2024).

The MCNP input file was produced in Attila4MC, which included the geometry file from SpaceClaim and the associated input deck. These files were then executed in MCNP. The computational time required for each simulation varied depending on model complexity and the number of transported particles. MCNP produced two files for each run: an output file with an Elemental Edit OUTput (.eeout) extension and a standard text output file containing the input file and simulation results. See Appendix B for a sample input file and Appendix C for a sample output file.

The .eeout file was subsequently converted to a .plt file for visualization in Tecplot using Attila4MC's built-in file conversion utility, facilitating post-processing, data extraction, and evaluation.

3.6 - Tally and Dose Conversion Methodology:

This research included two MCNP tally types: F4 and F5.

The F4 tally represents the track-length estimate of fluence averaged over a cell, computed using the track-length method and applying the ICRP 116 AP effective dose conversion coefficient in MCNP. The unit of measure for the F4 tally is cm^-2 per source particle emitted. The effective dose conversion coefficient has units of pSv * cm^2. The unit for the F4 tally is particles cm^-2, so for every particle that enters or passes through the area, it is related to the number of particles emitted from the radiation source. The radiation dose for the ICRP 38 and Health Physics and Radiation Health Handbook gamma dose rate constants represents the air-kerma rate in free air at a distance from a point source, per unit activity. Air kerma is the energy transferred from the photons to the air. ICRP 38 gamma dose rate constants assume that the source is a point source, no shielding, no buildup, no scatter, and that the geometry is free-air. (ICRP, 1983) This is not an effective dose or an absorbed dose in tissue.

The F4 tally in MCNP computes the average particle fluence in a cell and assigns each particle entering that cell to its corresponding energy bin. The specific energy bins are applied using a DE/DF card in MCNP. The energy bins and associated conversion coefficients used are from Table A.1 of ICRP 116 and are shown in Appendix A.

Photon fluence values obtained from F4 track-length tallies were converted to effective dose rates using energy-dependent fluence-to-dose conversion coefficients consistent with ICRP methodology. Effective dose was selected as the primary comparison quantity because it enables direct evaluation of operational relevance for responder exposure scenarios.

In the present study, external photon dose quantities were derived using energy-dependent fluence-to-dose conversion coefficients from ICRP Publication 116, which provide operationally relevant effective dose estimates for reference irradiation geometries. Earlier methodology presented in ICRU Report 57 was considered for historical and conceptual context in the development of ambient dose equivalent conversion approaches. Radionuclide-specific dose conversion factors described in ICRP Publication 38 were not directly applied, as those factors relate activity intake to committed internal dose rather than external photon transport fields modeled in this research.

Following application of these conversion coefficients, dose results were normalized to source activity and analyzed to evaluate geometric attenuation trends and material-dependent transport behavior.

The main source used for evaluation of the model, specific to variations in mountain material and radiation source placement, was Co-60. The Co-60 source was modeled as discrete photon emissions at 1.17 and 1.33 MeV, with one photon sampled per source history. Application of ICRP 116 AP fluence-to-effective dose conversion coefficients via DE/DF cards yielded effective dose per emitted photon ($Sv \cdot photon^{-1}$). For normalization to physical units, results were scaled to a source activity of 1 Bq, corresponding to approximately two photons per second, and converted to effective dose rate ($Sv \cdot s^{-1}$).

Gamma dose rate constants (Γ) were used to compute a free-field reference air kerma rate at the node location using the point-source inverse-square formulation, $\dot{K}_{air} = \Gamma A / r^2$, where A is activity and $r$is the source-to-node distance. This calculation provides an unbounded-air baseline that excludes confinement, wall scattering, and buildup effects. In contrast, MCNP results extracted at the corresponding node represent ICRP 116 AP effective dose rate derived from photon fluence tallies using DE/DF conversion, thereby incorporating geometry- and material-dependent scattering contributions. Accordingly, Γ-based estimates were used as a free-field reference rather than as a direct validation of effective dose, enabling quantification of deviations attributable to tunnel confinement and material composition.

Data extracted from Tecplot were organized in Excel workbooks for each simulation case. Calculations included source-to-node distance, effective dose rate from F4 tallies, air kerma rate from ICRP-38 and Radiation Health Handbook gamma dose rate constants, and symmetric percent difference comparisons. Because gamma constants yield air kerma rate under free-field assumptions while DE/DF tallies yield effective dose rate under AP geometry, the two quantities were compared as physically interpretable benchmarks rather than identical dosimetric measures.

The gamma dose rate constant is a radionuclide-specific scaling parameter that expresses free-field air kerma rate per unit activity at a defined distance, incorporating photon emission energies and yields. In contrast, fluence-to-effective dose conversion coefficients are energy-dependent protection quantities that convert simulated photon fluence into biologically weighted effective dose. The use of transport-based effective dose conversion in this study was necessary because tunnel boundaries introduce scattering and backscatter effects that alter photon angular and energy distributions, conditions under which inverse-square gamma-constant scaling alone is insufficient.

Conceptually, the modeling approach used in this study can be understood as a three-step process:

(1) Particle transport simulation: MCNP tracks photon histories as they interact with the modeled tunnel geometry and materials.

(2) Fluence estimation: Tallies such as F4 and F5 quantify the resulting photon fluence either over volumes or at specific points.

(3) Dose conversion: Fluence values are converted to effective dose using ICRP 116 conversion coefficients to produce quantities directly relevant to radiation protection.

This framework provides a transparent link between fundamental radiation physics and operational dose metrics, enabling the results to be interpreted in a manner that is both physically rigorous and practically meaningful for responder exposure assessment.

3.7 - Data Analysis and Management:

Once the data were extracted from Tecplot, they were entered into Excel files, with each run or model in its own workbook. Each Excel workbook was composed of sheets for the coordinates used to extract precise line data, the full raw data extracted from the entire mesh, the F5 tally data, and a sheet for each precise line. The Precise Line (PL) represents a predefined spatial sampling pathway along the tunnel axis or structural corridor used to extract continuous effective dose estimates from the transport solution. This construct enables standardized comparison of spatial dose behavior across geometry and material configurations. This organization enabled comparison of the baseline and variations to assess the impact of each variation. Calculations were performed in Excel to include calculating the distance from the node or F5 tally and the source location, determining the committed dose based upon ICRP 38 and the Health Physics and Radiation Health Handbook gamma dose rate constant conversion factors based upon the specific isotope, percent uncertainty between the reported F4 tally effective dose rate from Tecplot, and the two different gamma dose rate constants. Percent uncertainty was used to compare the two values as a benchmark. It should be noted that these two values represent different things. An example of the Excel file is in Appendix C

3.8 - Software-Based Geometry Preparation:

Section 3.2 defined the conceptual and physical tunnel representation. Section 3.7 describes the implementation of that geometry within SpaceClaim and Attila4MC.

Tunnel geometries were modeled in SpaceClaim based on standard cross-sectional dimensions for road, pedestrian, and train tunnels, supplemented by scaled variants to explore geometric thresholds. CAD references include the Zentrum am Berg (ZAB) tunnel system. Each geometry was exported as a Parasolid file to ensure compatibility with Attila. Boolean operations and geometric separation were performed to maintain distinct solids for meshing.

3.9 - Source Placement and Definition:

Radiation sources were placed at defined coordinates corresponding to operationally relevant locations, such as tunnel midpoints or offsets from intersections. Isotopes included Co-60 for initial baseline determination, and Cs-137, Ir-192, and Ra-226 for additional exploration into the impact the specific isotope has in the dense mountain environment. Source strengths were normalized for comparative analysis across scenarios.

Table 3.3 presents the investigated isotopes and their half-value layers for two of the investigated materials: lead and concrete. The half-value layer is the thickness of a specific material needed to reduce the transmission of the emitted energy from the specified isotope by half. Comparing the half-value layer thicknesses of lead and concrete indicates that, for the same radiation source, a greater concrete thickness is required to achieve the same shielding.

Table 3.3: The half-value layer (HVL) for each of the investigated isotopes for lead and concrete in millimeters and inches. This table compares the transmission of each isotope for two of the investigated materials, as reported in Table 6.13 of the Fourth edition of the Health Physics and Radiological Health Handbook. *(Johnson & Birky, 2012)*.

Isotope	HVL - Lead	HVL - Concrete
Cesium-137	6 mm (0.25 in)	48 mm (1.9 in)
Cobalt-60	12 mm (0.49 in)	66 mm (2.6 in)
Iridium-192	6 mm (0.24 in)	41 mm (1.6 in)
Radium-226	16 mm (0.65 in)	69 mm (2.7 in)

Figure *3-2* illustrates the modeled radiation source locations within the road tunnel geometry. Although the figure presents a plan (bird's-eye) view, each source location was also varied vertically within the tunnel cross-section to evaluate the influence of source height in addition to horizontal position.

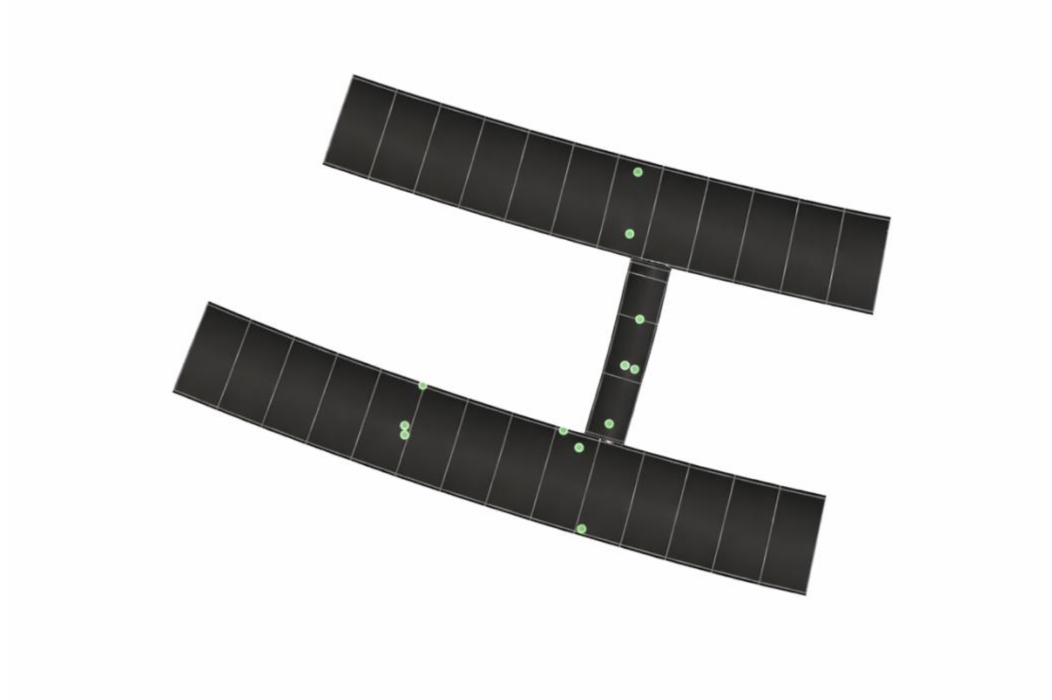

Figure 3-2 Radiation source locations in the road tunnel are represented by green circles. Image created in SpaceClaim.

3.10 - Mesh Generation and Material Assignment:

Attila4MC was used to create unstructured tetrahedral meshes, with element sizes chosen to balance computational fidelity and runtime. Material cards were assigned based on tunnel wall composition: concrete, granite, basalt, limestone, sandstone, and lead. Air was modeled as the fill medium within tunnels. Material definitions utilized validated PNNL cross-section libraries.

The process of taking the file from SpaceClaim into Attila4MC and dividing it into unstructured tetrahedral meshes proved to be challenging. The sheer size of the tunnel system competed with the percent difference associated with tetrahedra that were too large to accurately represent the dose, especially in the near field. To overcome this challenge, the tunnels were further subdivided into smaller sections in SpaceClaim, allowing the assignment of a smaller max edge length in the tunnel sections closest to the radiation source, thereby yielding smaller tetrahedra where a larger variation in radiation strength exists. The more tetrahedra in a geometry, the longer the run time and the more computing resources needed to conduct the computation of the particle transport.

The spatial discretization of the tunnel geometry into a tetrahedral mesh is a critical component of the Monte Carlo modeling framework. The mesh defines the regions over which radiation quantities are averaged and directly influences the resolution of spatial dose gradients.

In this study, mesh refinement was applied in regions near the radiation source and along expected transport pathways to ensure accurate capture of steep dose gradients and localized scattering effects. Coarser mesh regions were used in areas farther from the source to maintain computational efficiency without sacrificing accuracy. This balance between resolution and computational cost is particularly important in subterranean environments, where complex geometry and repeated photon interactions can produce highly nonuniform dose distributions. An appropriately designed mesh ensures that the model captures physically meaningful variations in the radiation field while maintaining tractable simulation times.

To visually demonstrate the complex tetrahedral mesh produced in this process, the next three figures depict an example of the mesh for this research, including the mountain, the tunnel, and a magnified portion of the tunnel with the radiation heat map. Figure *3-3* depicts a representative portion of the road tunnel with the mesh visible for both the tunnel and the surrounding mountain layer. Figure *3-4* depicts the mesh of one of the evaluated tunnels with the heat map giving the tunnel the gradient color associated with the effective dose. Figure *3-5* shows a zoomed-in portion of the mesh.

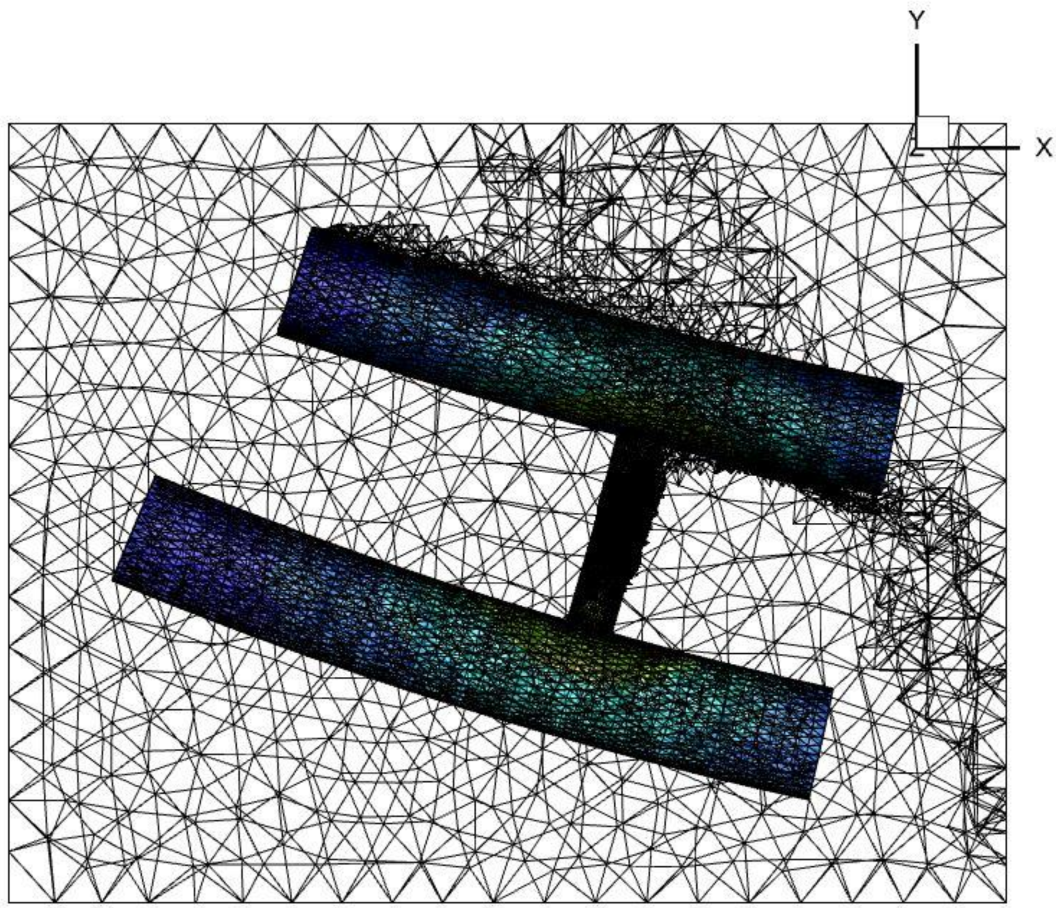

Figure 3-3: Full tetrahedral mesh of the road tunnel and surrounding mountain layer as generated in Attila4MC and visualized in Tecplot. Mesh refinement near the source region enables accurate resolution of steep spatial dose gradients.

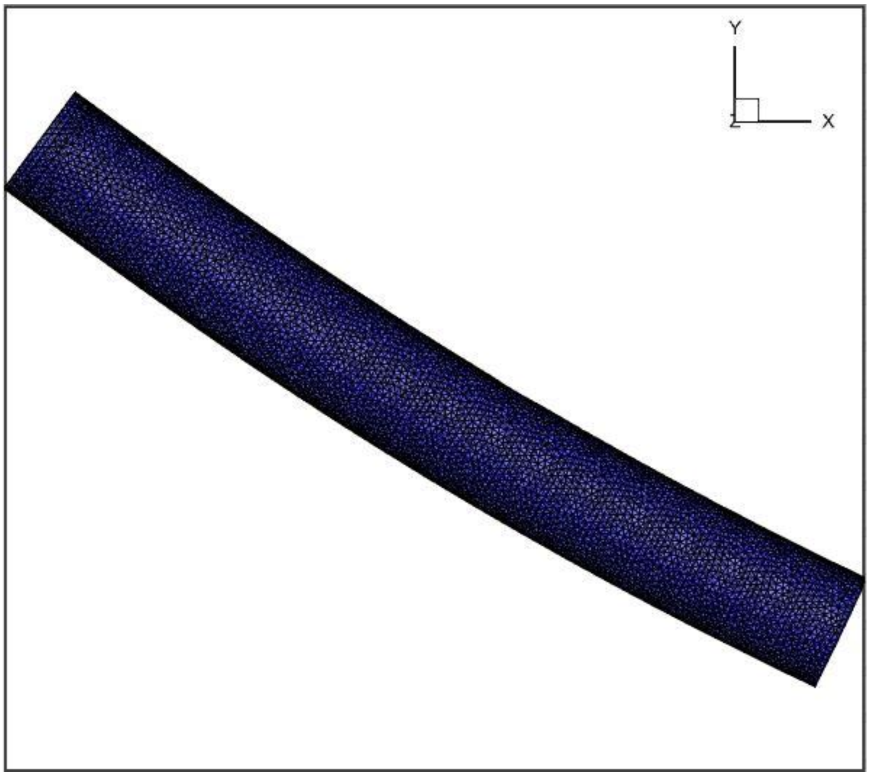

Figure 3-4: Representative meshed tunnel geometry with overlaid effective dose contour. The visualization illustrates spatial dose gradients resolved by the nonuniform tetrahedral discretization strategy.

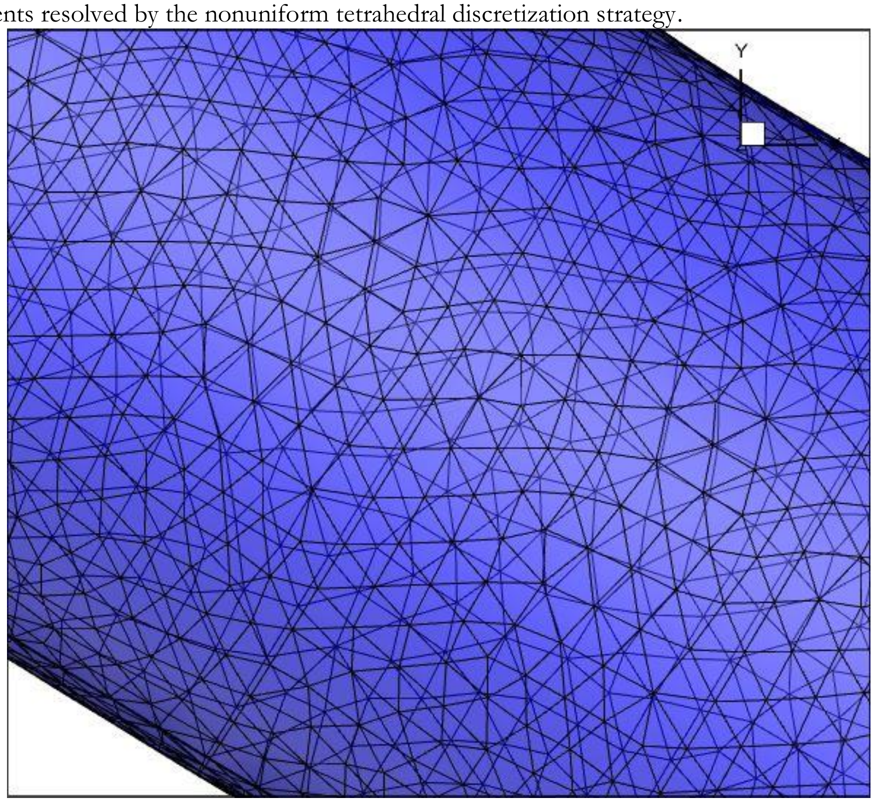

Figure 3-5: Zoomed in view of the meshed tunnel from Figure 3-4. Mesh created in Attila4MC and visualized in Tecplot.

3.11 - MCNP Simulation Framework:

Simulations were executed with 10 million particle histories per run to reduce the relative standard deviation while balancing computational time with adherence to strong statistical principles. Both F4 (track length estimate) and F5 (point detector) tallies were employed. The F4 tallies were implemented using Attilla4MC's software, and the F5 tallies were added manually later. Tallies were binned using ICRP-116 anterior-posterior (AP) geometry effective dose conversion coefficients to enable direct dose rate estimation in Gy/s. Calculated values using gamma constants were generated for comparison.

Anterior–posterior (AP) ICRP 116 effective dose conversion coefficients were selected to represent a scenario in which an individual approaches a localized radiation source, with photon incidence predominantly on the anterior surface of the body. Alternative geometries include lateral (LAT) and isotropic (ISO) irradiation conditions. LAT irradiation may approximate certain operational exposures but underestimates dose relative to AP geometry for frontal approach scenarios. ISO geometry is appropriate for spatially uniform radiation fields. Given the directional nature of the modeled sources, AP coefficients were conservatively selected. (ICRP, 2010)

Attila4MC was used to create the MCNP input files, relying on the SpaceClaim generated base geometry. The geometry was meshed using a nonuniform tetrahedral discretization strategy, with refined element sizing in the near-field region surrounding the radiation source to capture steep spatial dose gradients. If time and computer power were not constraints, then the tetrahedron sizes could have been substantially smaller. However, the decision was made to allow for congruence between a select number of manually input F5 tallies placed at specified F4 tally node locations within the near field of the radiation source. Mesh refinement was iteratively adjusted until agreement between F4 mesh tallies and collocated F5 point detector tallies met the predefined ±5% convergence criterion.

For each variation of tunnel geometry and radiation source location, a unique geometry mesh was produced in Attila4MC. This allowed for unique optimization aligning with each model. This geometry mesh served as the basis for the MCNP input file, also created in Attila4MC, and included assigning materials to each geometry mesh component, including the mountain and the tunnel. The material used for the tunnel was air in all models evaluated in this research. All MCNP items were created using the Attila4MC user interface, except the F5 tally, which was added manually in a later step.

Once the output files for each MCNP run were obtained, there were two files: the basic MCNP output text file and the eeout file, which contained the data for Tecplot visualization of the radiation heat map and extraction of the F4 tally node data. The extraction process will be discussed in a later section.

3.12 - Experimental Variations:

Hundreds of different variations were attempted during the process of developing the final set of models, of which forty different variations were included in the results of this research. The aim of the variation was to make incremental changes to the working model, which could then be compared with a benchmark to demonstrate their impact. The base model used air for both the tunnel and the mountain material, as shown in Figure *3-6*.

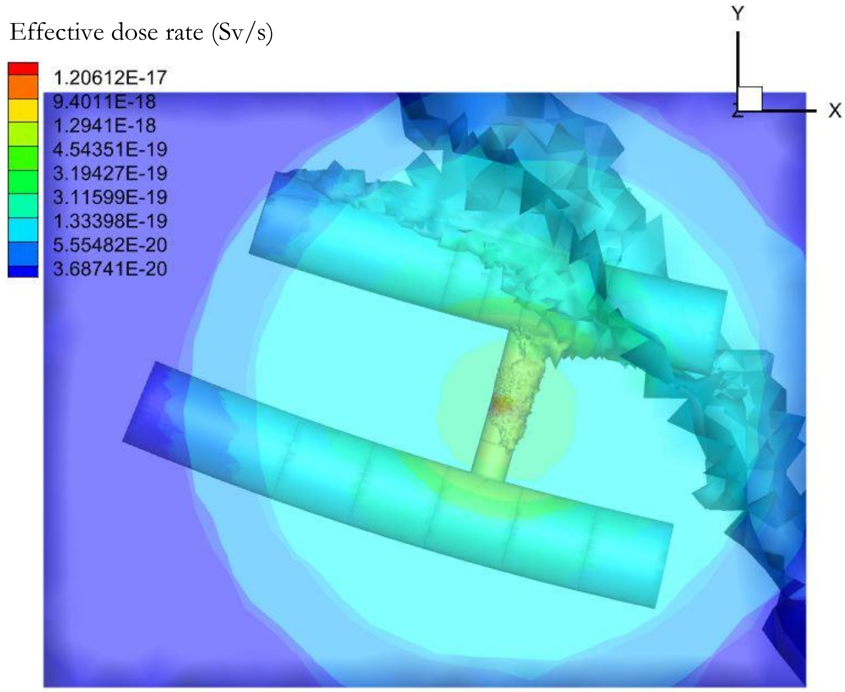

Figure 3-6: Spatial distribution of effective dose rate (Sv·s⁻¹) within the modeled road tunnel geometry for a 1 Bq Co-60 source located in the center of the pedestrian tunnel connecting the two road tunnels, computed using MCNP F4 tallies with ICRP 116 AP conversion coefficients. Values represent steady-state effective dose rate normalized per unit source activity. Air is assigned to both the mountain and the tunnel material cards. The spatial pattern illustrates anisotropic dose attenuation resulting from boundary scatter and structural transport pathways, with localized persistence of effective dose beyond direct line-of-sight regions. As depicted in Tecplot.

Note the circular radiation heat map pattern shown. Since all sections of the tunnel were filled with air and no other materials, including the mountain structure, with the radiation source at the center of the pedestrian tunnel, it provided a standard for comparing the impact of the mountain material. The jagged line running from the top center of the image to the bottom right is an artifact of the meshing and MCNP packing process. This process required that each section be broken into smaller sections, with no more than 50,000 cells, to increase computer efficiency and reduce processing time. This step broke the mesh into these smaller chunks. This increased the data extraction time because each chunk of 50,000 cells needed to be extracted independently and compiled in the Excel workbook. Previously, each section of the mesh (mountain and tunnel) could be extracted as one file from Tecplot. This proved time-consuming and a place where human error could affect the data collection process. Careful attention was taken to ensure that the exact number of nodes was extracted for each model. This further division of the sections affected the visual effect, as seen more prominently in Figure *3-6*, but did not affect the modeling results. Another view of the tunnel depicted in Figure *3-6*, with the mountain layer removed from view, is seen in Figure *3-7*; both images have the source located in the center of the pedestrian tunnel between the road tunnels with air for the mountain material.

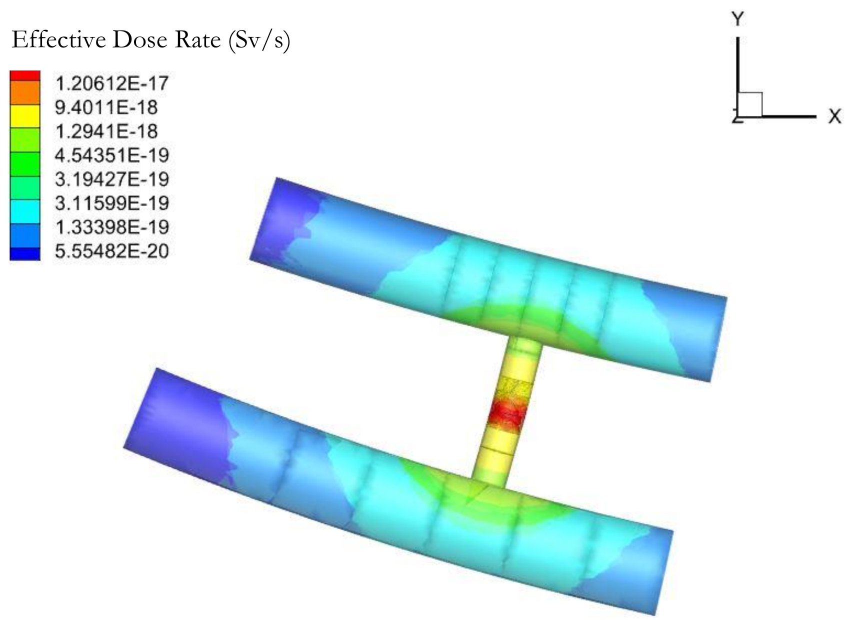

Figure 3-7: Spatial distribution of effective dose rate ($Sv \cdot s^{-1}$) within the modeled road tunnel geometry for a 1 Bq Co-60 source located in the center of the pedestrian tunnel connecting the two road tunnels, computed using MCNP F4 tallies with ICRP 116 AP fluence-to-effective dose conversion coefficients. Values represent steady-state effective dose rate normalized per unit source activity. Air is assigned to both the mountain and the tunnel material cards. Mountain layer visually removed. The spatial pattern illustrates anisotropic dose attenuation resulting from boundary scatter and structural transport pathways, with localized persistence of effective dose beyond direct line-of-sight regions As depicted in Tecplot.

Note that in the mountain with air for the material, there is no scattering or tunneling observed. The radiation heat map radiates outward from the radiation source, with each outer ring representing a lower, banded radiation dose.

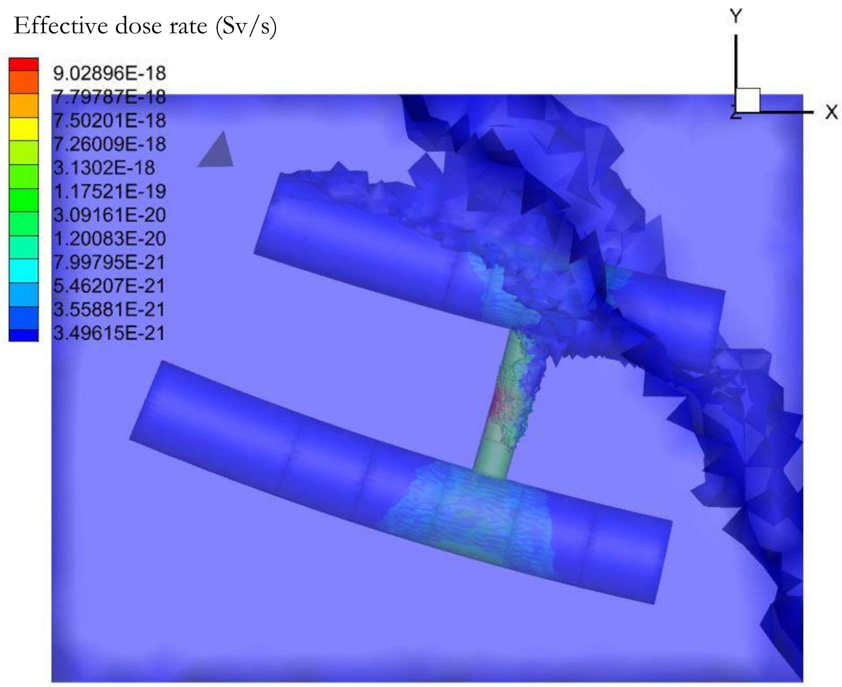

Figure 3-8: Spatial distribution of effective dose rate ($Sv \cdot s^{-1}$) within the modeled road tunnel geometry for a 1 Bq Co-60 source located in the center of the pedestrian tunnel connecting the two road tunnels, computed using MCNP F4 tallies with ICRP 116 AP fluence-to-effective dose conversion coefficients. Values represent steady-state effective dose rate normalized per unit source activity. Air is assigned to the tunnel material card, and concrete to the mountain material card. As depicted in Tecplot.

In Figure *3-8*, the mountain is made of concrete, and just like in Figure *3-6* and 3.5, the radiation source is in the center of the pedestrian tunnel. Also, as shown in Figure *3-6*, the visual artifact does not affect the modeling results but shows how the mesh was divided for processing efficiency.

Figure, 3.7, shows figure 3.6 without its concrete mountain, highlighting visually the streaming and scattering effect of the concrete material on the radiation heat map.

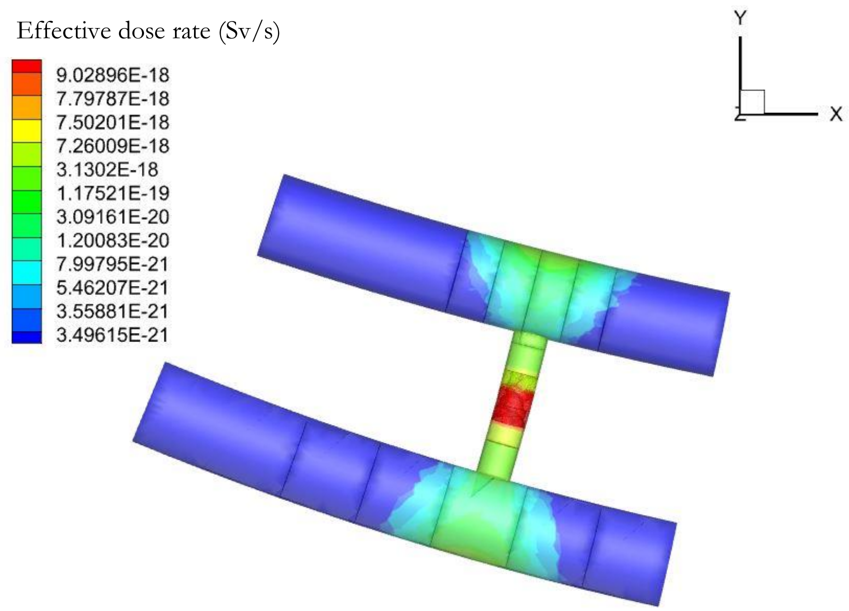

Figure 3-9: Spatial distribution of effective dose rate (Sv·s⁻¹) within the modeled road tunnel geometry for a 1 Bq Co-60 source located in the center of the pedestrian tunnel connecting the two road tunnels, computed using MCNP F4 tallies with ICRP 116 AP fluence-to-effective dose conversion coefficients. Values represent steady-state effective dose rate normalized per unit source activity. Air is assigned to the tunnel material card, and concrete to the mountain material card. The mountain layer has been removed to improve visualization. The spatial pattern illustrates anisotropic dose attenuation resulting from boundary scatter and structural transport pathways, with localized persistence of effective dose beyond direct line-of-sight regions As depicted in Tecplot.

Comparison of the air-filled (Figure *3-7*) and concrete-bounded tunnel (Figure *3-9*) configurations demonstrates that structural boundary interactions modify photon transport pathways. In the concrete configuration, increased Compton scattering within the surrounding material redistributes photon fluence into adjacent tunnel volumes, producing anisotropic attenuation patterns and localized downstream dose persistence. These spatial features are not numerical artifacts but reflect confinement-mediated transport processes that alter the angular distribution of scattered photons.

With the various mountain materials applied, using the same underlying mesh and node locations, the differences observed among the variations were attributable solely to the material. Additionally, the radiation source was placed at 9 locations within the road tunnel, 2 within the large tunnel, and 2 within the small tunnel. Each location was selected to highlight differences in the model's overall geometry: the tunnel's shape, size, or the placement of the source relative to the tunnel wall, floor, or ceiling. Having a comparable air tunnel allowed a direct correlation between the two.

3.13 - Tecplot Visualization and Data Extraction:

Tecplot is an additional software package that is nested inside of Attila4MC. Tecplot provides key data visualization and extraction capabilities, using the eeout file produced by MCNP. A simple command in the computer's Command Prompt converts the eeout file type to a .plt file type, which can be loaded into Attila4MC and viewed in Tecplot. The eeout file contains the F4 tally data for each tetrahedron specified in the meshing process. The F4 tally is the average dose for the area and is assigned to the node. Each node is assigned a location with three-dimensional coordinates (x, y, z). This coordinate enables assigning a dose to a precise location, which can then be used to measure the exact distance from the source to the node by generating a heat map and a large volume of data. The heat map produced in Tecplot depicts the radiation field, which can then be analyzed to examine radiation interactions in space. One drawback of extracting the F4 tally data from the eeout file is that it depends on the tetrahedron size.

The dose assigned to a node is based on the average dose within the tetrahedra to which it is assigned; the larger the area it represents, the less accurate the reported dose, particularly near the radiation source. Radiation energy responds to the inverse square law in free air, so the closer to the source of radiation, the more impactful the distance is for the dose.

The F4 mesh tally was selected because it enables efficient extraction of spatially resolved dose data across large geometries. The final MCNP model produced approximately 850,000 nodal values per simulation, providing high-resolution characterization of the radiation field. In contrast, discrete F5 point detector tallies would require prohibitively large arrays to achieve comparable spatial coverage and are therefore less practical for full-field evaluation in complex tunnel geometries.

Tecplot was used to visualize and extract spatial dose results generated by MCNP F4 mesh tallies. The contour function enabled three-dimensional rendering of effective dose rate distributions within the modeled tunnel geometries. These visualizations provided qualitative confirmation of confinement effects, including measurable dose in geometrically shadowed regions consistent with photon scattering from tunnel boundaries. An example contour rendering is shown in Figure 3-10, illustrating effective dose rate ($Sv \cdot s^{-1}$) for a representative tunnel configuration.

In all contour visualizations, effective dose rate values were normalized per unit source activity. Material assignments correspond to those defined in the MCNP material cards, with outer structural layers selectively hidden when necessary to improve visualization of internal dose distributions. As shown in Figure 3-10 measurable dose extends beyond direct line-of-sight regions, reflecting the contribution of scattered photons within confined geometries.

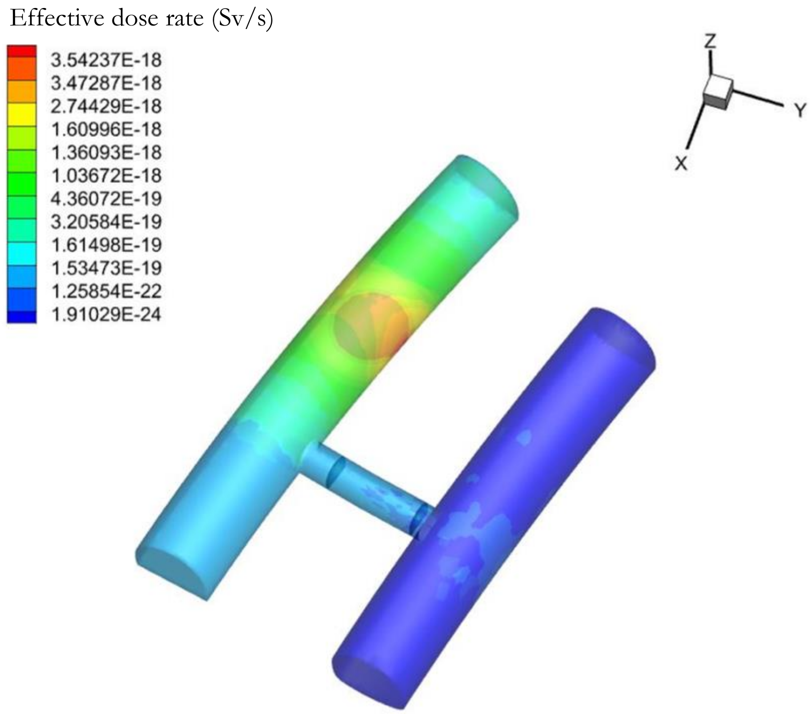

Figure 3-10: Spatial distribution of effective dose rate (Sv·s⁻¹) within the modeled road tunnel geometry for a 1 Bq Co-60 source located in the one of two road tunnels, computed using MCNP F4 tallies with ICRP 116 AP conversion coefficients. Values represent steady-state effective dose rate normalized per unit source activity. Air is assigned to the tunnel material card, and concrete to the mountain material card. The spatial pattern illustrates anisotropic dose attenuation resulting from boundary scatter and structural transport pathways, with localized persistence of effective dose beyond direct line-of-sight regions. The mountain layer has been removed to improve visualization. As depicted in Tecplot.

Beyond qualitative visualization, Tecplot was used for quantitative data extraction. The software enabled export of three-dimensional Cartesian coordinates, F4-derived effective dose values, and associated relative standard deviations for each mesh node. The final simulations produced approximately 850,000 nodal data points per iteration, providing high-resolution spatial characterization of the radiation field.

To enable structured evaluation of dose behavior, the Precise Line (PL) extraction tool was employed. This tool allowed extraction of dose values along defined linear paths within the geometry. PLs were positioned along the tunnel centerline, near structural boundaries, parallel to the source location, and within adjacent tunnels to evaluate both line-of-sight and non-line-of-sight dose behavior. The placement of these lines is illustrated in Figure *3-11*, which shows the extracted PL paths superimposed on the radiation contour map.

All extracted PL datasets were exported to Microsoft Excel for subsequent statistical analysis and comparison with analytic gamma dose rate constant calculations.

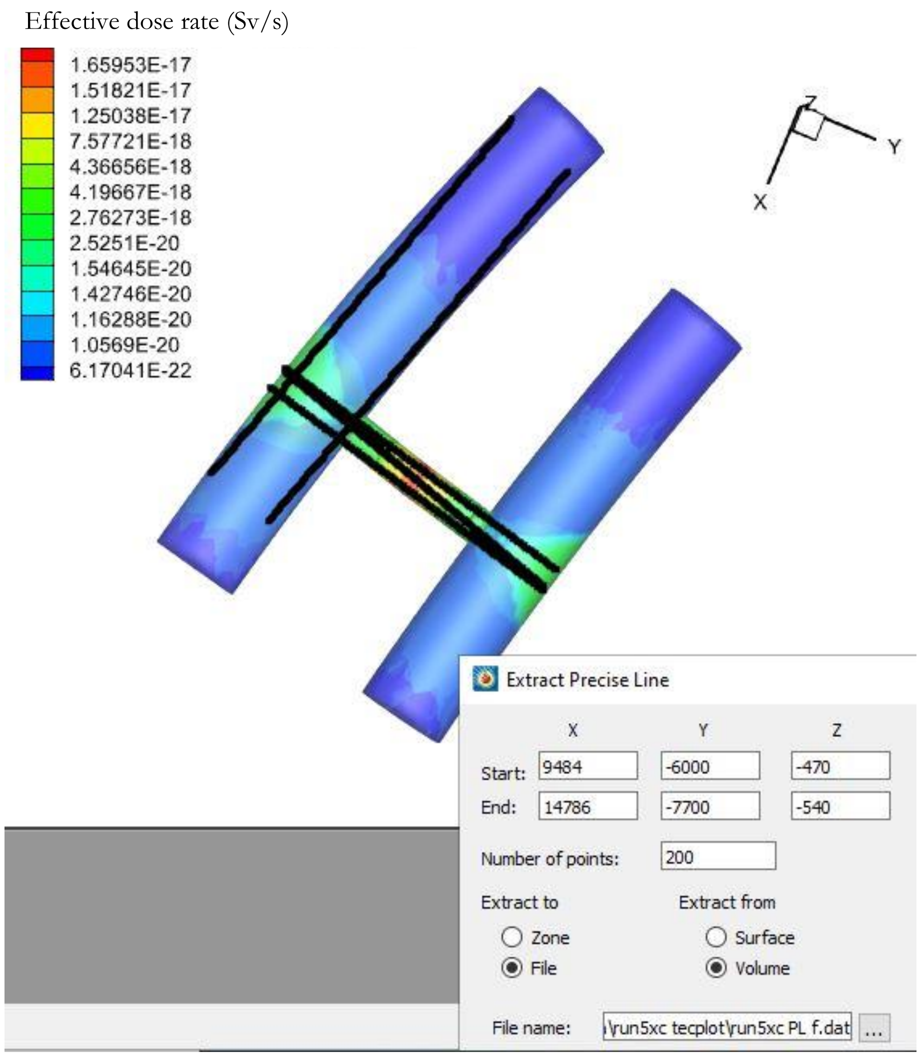

Figure 3-11: Tecplot-derived radiation heat map with precise lines (PL) drawn to show their locations. The radiation source is in the center of the pedestrian tunnel.

The data extraction capabilities of Tecplot included the ability to retrieve the three-dimensional Cartesian coordinates, the F4 dose, and the relative standard deviation for each node in the results, and to import these data into an Excel spreadsheet for further evaluation. The F4 dose node data, while providing the exact location of that node in the tunnel, are useful for statistical machine learning and artificial intelligence applications; they exceed the scope of what can be reasonably and meaningfully evaluated within the confines of this research. Additionally, the over 850,000 data points are not necessarily organized in a meaningful way; therefore, another tool was used to extract more meaningful data to further explore and assess the findings.

The Precise Line (PL) extraction tool in Tecplot was used to obtain dose values along user-defined linear paths within the geometry. Lines were positioned along the tunnel centerline, near boundaries, parallel to the source, and within adjacent tunnels to evaluate both line-of-sight and non-line-of-sight dose behavior. Figure *3-11* shows the PLs, drawn as black lines on the contour, for a model with the source at the center of the pedestrian tunnel, with the red color indicating the higher radiation dose at that point.

Output tallies were post-processed in Tecplot. Precise line functions extracted spatially resolved dose rates. Data were exported to Excel for percent difference calculations between F4, F5, gamma dose rate constant-calculated values based on distance from the source using two different gamma dose rate constants described in Table *3.4*, and ISL-predicted values.

The percent difference was calculated as follows:

Equation 6: Percent difference.

$$Percent\ difference = \frac{|A - B|}{\frac{B + A}{2}}$$

Where A is the dose for the F4 tally, and B is the gamma dose rate constant calculated value in both equations.

The gamma dose rate constants from Table 6.5 of the Health Physics and Radiological Health Handbook, fourth edition, were used for the isotopes modeled to calculate the free-air dose rates expected for each node, point detector, and precise line point measurement. The specific dose rate constants are depicted in Table *3.4*.

Table 3.4: Isotopes investigated in this research, their associated gamma dose rate constants, and half-lives.

Isotope	Health Physics and Radiation Health Handbook Dose Rate Constant (Gy m^2/Bq-S)	ICRP 38 Dose Rate Constant (Gy m^2/Bq-S)	Half-life
Cesium-137 (Ba-137m)	2.27E-17	2.26E-17	30.07 years
Cobalt-60	8.5E-17	8.5E-17	5.2714 years
Iridium-192	3.18E-17	3.18E-17	74.02 days
Radium-226	5.08E-19	4.65E-19	1600 years

Note that the dose rate constant for barium-137m, the daughter of cesium-137, was used for cesium-137, since the gamma dose contribution comes from barium, not cesium. (Johnson & Birky, 2012)

3.14 - Statistical Analysis:

Given the vast amount of data generated in this research, Python code to compare the 40 Excel spreadsheets, each with at least 7 sheets per workbook, was essential. Portions of the Python scripts used for data parsing and visualization were initially drafted with assistance from a generative artificial intelligence (AI) tool (OpenAI ChatGPT). All generated code was independently reviewed, validated against expected outputs, and modified as necessary to ensure methodological accuracy and reproducibility. Final implementation, debugging, statistical validation, and interpretation were performed by the author.

Variability in model results was characterized using the standard deviation across configurations. This approach reflects the spread of outcomes across modeled scenarios rather than uncertainty in the estimated mean and is therefore more directly relevant for interpreting configuration-dependent effects in radiation transport behavior. Accordingly, summary statistics are reported using mean values and standard deviation, and variability is represented as mean ± 2 standard deviations as a descriptive measure of configuration-level spread. Confidence intervals are not used, as the objective of this analysis is to characterize variability across modeled configurations rather than uncertainty in the estimate of a population mean. This convention is applied consistently throughout all tables and figures unless otherwise noted.

3.15 - Hypothesis Evaluation Metrics:

To ensure methodological clarity and statistical consistency, each hypothesis was evaluated using a single primary quantitative metric selected to directly reflect the underlying physical mechanism under investigation. These metrics were defined a priori and applied consistently across all modeled configurations.

3.15.1 Hypothesis 1: Inverse-Square Convergence

Hypothesis 1: Photon dose rates in sufficiently large tunnel geometries converge toward inverse-square law behavior within a defined tolerance.

Primary Metric: Log–Log Attenuation Slope

For each configuration, the effective dose rate $\dot{E}(r)$ along the Precise Line (PL) was evaluated as a function of source-to-point distance r. Inverse-square behavior was assessed using a log–log linear regression of the form:

$$\log_{10}\left(\dot{E}(r)\right) = m \log_{10}(r) + b$$

where:

- m is the attenuation slope,
- b is the intercept.

Under ideal free-field conditions, the theoretical expectation is:

$$m = -2$$

For each configuration, the estimated slope m_i was calculated over the operational domain beyond the near-field region. The primary summary statistic was the mean slope across configurations, reported with the standard deviation. Variability across configurations is represented as mean ± 2 standard deviations to provide an approximate 95% range of dispersion.

The inverse-square law represents a geometric scaling relationship. Evaluating convergence, therefore, requires assessing the exponent governing spatial attenuation rather than pointwise percent differences. The log–log slope directly tests whether the modeled radiation field approaches the expected $1/r^2$ behavior at increasing distances. This metric isolates geometric transport behavior from material-dependent modifications, providing a physically interpretable measure of inverse-square convergence.

3.15.2 Hypothesis 2: Material-Dependent Modification

Hypothesis 2: Tunnel wall composition significantly modifies photon dose distributions relative to air-filled free-field conditions.

Primary Metric: Integrated Effective Dose Along the Precise Line (0–20 m)

To quantify overall material influence on the dose field, the effective dose rate (paired by isotope, geometry, and source location) was integrated along the Precise Line from 0 to 20 meters:

$$\mathrm{ID}_{0-20} = \int_{0}^{20\,\mathrm{m}} \dot{E}\,(r)\,dr$$

The 0–20 m domain was selected to represent the primary operational region of interest for pedestrian-accessible tunnel segments while excluding far-field geometric dominance beyond modeled tunnel extents. In practice, this integral was evaluated numerically using trapezoidal integration of the discretized F4-derived effective dose values:

$$\mathrm{ID}_{0-20} \approx \sum_{j=1}^{k-1} \frac{\dot{E}(r_j) + \dot{E}(r_{j+1})}{2}\,(r_{j+1} - r_j)$$

For each configuration, the percent change relative to the matched air baseline was computed as:

$$\Delta_{\mathrm{ID}}(\%) = \left(\frac{\mathrm{ID}_{\mathrm{material}} - \mathrm{ID}_{\mathrm{air}}}{\mathrm{ID}_{\mathrm{air}}}\right) \times 100$$

The primary reported statistic was the mean percent change across configurations, reported with the standard deviation. Variability across configurations is represented as mean $\pm$ 2 standard deviations to describe the spread of configuration-dependent behavior. This integrated metric provides a stable representation of cumulative spatial dose modification across the operational domain.

Hypothesis 2 concerns modification of the entire dose distribution, not behavior at a single point. Pointwise percent comparisons can become unstable at large distances where denominators approach zero. Integrating dose along the PL provides a physically meaningful measure of cumulative spatial exposure modification within the operational region of interest. This approach preserves distance-dependent behavior while yielding a stable scalar metric for statistical comparison. Because the integral reflects total spatial dose response along the tunnel axis, it directly captures material-induced changes to photon transport and scattering behavior.

3.15.3 Hypothesis 3: Scatter Enhancement in Confined Geometry

Hypothesis 3: Confined geometries produce measurable scatter enhancement beyond direct line-of-sight regions.

Primary Metric: Non-Line-of-Sight (NLOS) Enhancement Index

To isolate confinement-induced scattering effects, spatial regions lacking direct line-of-sight to the source were identified geometrically within each tunnel configuration. For these regions, the effective dose rate was compared to the corresponding air-reference configuration at matched distances.

The enhancement index was defined as:

$$\mathrm{NLOS}_{\mathrm{Enh}}(\%) = \left(\frac{\dot{E}_{\mathrm{confined,NLOS}} - \dot{E}_{\mathrm{air,NLOS}}}{\dot{E}_{\mathrm{air,NLOS}}}\right) \times 100$$

Mean enhancement values were computed across all identified non-line-of-sight (NLOS) points within the operational domain for each configuration. These configuration-level means were then aggregated to produce overall summary statistics and associated standard deviations. Variability is represented as mean $\pm$ 2 standard deviations, reflecting the spread of results across modeled configurations.

Scatter enhancement is a spatially localized phenomenon associated with boundary interactions and photon redirection. Evaluating this hypothesis, therefore, requires isolating regions where direct geometric attenuation does not dominate. The NLOS enhancement index directly quantifies confinement-induced deviations from free-field expectations and provides a targeted metric for assessing streaming and scatter persistence beyond line-of-sight.

Grammar, punctuation, and sentence clarity were reviewed using the Grammarly writing assistance tool during preparation of this manuscript. The software was used solely to improve readability and language mechanics. All technical analysis, modeling methodology, interpretation of results, and conclusions presented in this dissertation are the independent work of the author.

Chapter 4 - Model Verification and Validation:

The modeling workflow described herein enables reproducibility of results within the expected stochastic variability inherent to Monte Carlo particle transport simulations. Minor numerical variation between independent reproductions is expected due to random number sampling and differences in mesh discretization; however, this variation remains consistent with the configuration-level variability observed across modeled scenarios.

Procedural validation was conducted by replicating the benchmark modeling framework established by earlier research using the ZAB tunnel geometry (Parker, 2022). The original SpaceClaim representations of the three reference tunnel configurations were reconstructed and implemented under equivalent source definition, transport parameters, and tally methodology. Agreement between the reproduced simulations and the attenuation trends reported in the benchmark study confirmed correct implementation of geometry construction, source modeling, and effective-dose calculation within the present computational workflow.

These findings are consistent with earlier subterranean transport modeling and benchmark comparisons reported by earlier research (Parker, 2022), who demonstrated measurable deviation from free-field attenuation behavior in straight tunnel configurations. The present research extends that foundational work by incorporating statistically structured hypothesis testing, larger-scale tunnel geometries, and effective-dose-based operational interpretation. Agreement in observed confinement-mediated dose persistence across both investigations strengthens confidence that the identified transport behaviors represent physical phenomena rather than modeling artifacts.

This validation lineage supports extension of confined-geometry radiation transport interpretation from laboratory-scale tunnel analogs to infrastructure-scale response environments.

Variability in F4–F5 agreement was quantified using standard deviation, calculated directly from the distribution of percent-difference values across modeled configurations (run-level, N = 40) and pooled point comparisons (N = 400).

Standard deviation was selected as the primary statistical metric to represent variability in model behavior, as it reflects the spread of results across configurations rather than uncertainty in the estimated mean. Mean ± 2 standard deviations is reported as an approximate representation of the expected range of variation.

Table *4.1* summarizes the primary statistical metrics used to evaluate numerical agreement, geometric attenuation behavior, and material influence. These metrics establish quantitative confidence in the modeling framework prior to formal hypothesis testing. The standard deviation values reported in Table 4.1 were calculated directly from the distribution of run-level (N = 40) and pooled (N = 400) percent-difference values, rather than derived from analytical approximations.

Table 4.1: Summary statistics for F4–F5 agreement and inverse-square convergence. Values represent mean and standard deviation, with mean ± 2 standard deviations provided as an approximate representation of variability across modeled configurations.

Metric	N	Mean	Std Dev	Mean ± 2 SD
F4 vs F5 Mean Absolute % Difference – Run Level	40	4.76%	1.66%	1.44% - 8.08%
F4 vs F5 Mean Absolute % Difference - Pooled	400	4.74%	4.55%	-4.36% - 13.84%
Log–Log Slope (All Materials Pooled)	40	-1.980	0.140	−2.260 – −1.700

Note: The lower bound of the ±2 SD range may extend below zero due to variability in percent-difference calculations and does not imply negative absolute differences.

The standard deviation values reported in Table 4.1 were calculated directly from the distribution of percent-difference values across modeled configurations (run-level) and pooled point comparisons, rather than derived from analytical approximations. These values characterize variability in model behavior across configurations and provide a basis for assessing consistency in F4–F5 agreement.

The observed effect was consistent across modeled configurations. While geometric attenuation dominates overall dose behavior, boundary-induced scattering and material-dependent photon interactions introduce systematic amplification relative to free-field conditions. The magnitude of this effect is modest but reproducible, supporting the second hypothesis that tunnel wall composition measurably modifies dose distributions.

4.1 - F4 vs F5 Comparison:

As shown in Figure *4-1*, agreement between the F4 mesh tally and F5 point detector tally was evaluated across all modeled configurations. The mean absolute percent difference was 4.76%, with a standard deviation of 1.66% at the run level (N = 40).

Agreement was consistent across configurations, as evidenced by the close correspondence between run-level and pooled statistics (Table 4.1), indicating that no individual configuration disproportionately influenced the overall behavior. The pooled dataset (N = 400), representing all F4–F5 comparison points across configurations, is provided in Appendix E.

Variability across configurations is visualized in Figure 4-1. The spread of configuration-level mean absolute percent differences is shown relative to the overall mean, with a mean ± 2 standard deviation band illustrating variability across modeled scenarios. The distribution demonstrates consistent agreement within a narrow range across configurations, with no evidence of systematic deviation.

This level of agreement indicates strong numerical consistency between the spatially averaged (F4) and point-based (F5) estimators. Despite fundamentally different sampling approaches—volume-averaged track-length estimation versus point detection—the results show that spatial averaging does not introduce meaningful bias in the modeled effective dose field at the scales evaluated.

Each model was evaluated across approximately ten reference distances spanning ~10 cm to 500 cm from the source. Due to geometric discretization and mesh-based spatial sampling, extracted distances vary slightly from nominal values but remain consistent with intended detector placement locations.

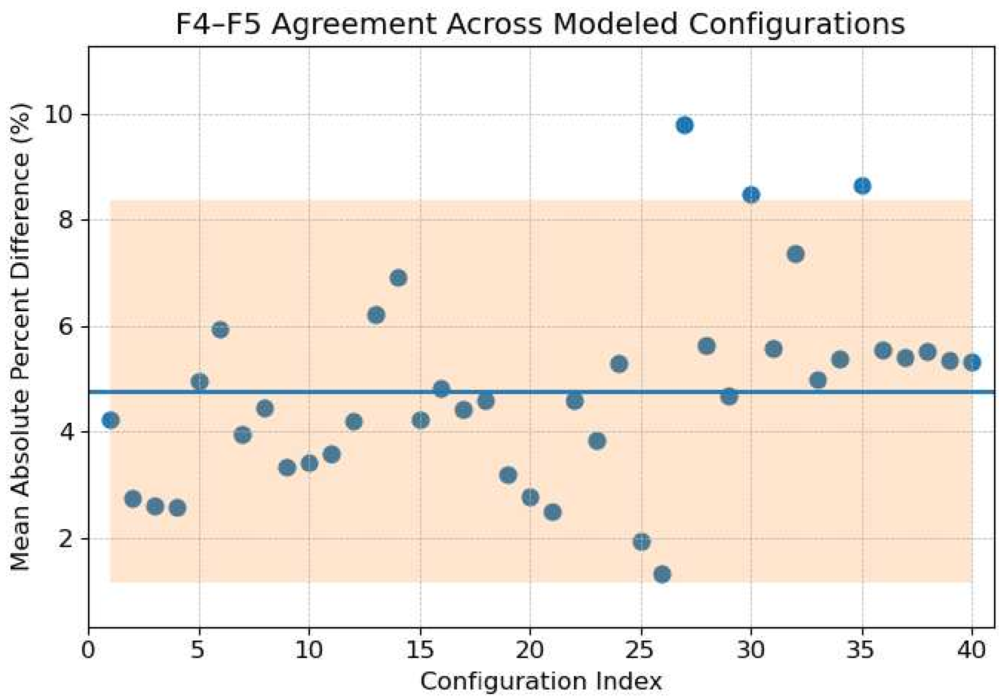

Figure 4-1: F4–F5 agreement across 40 modeled configurations. Points represent configuration-level mean absolute percent differences. The solid line indicates the overall mean, and the shaded region represents mean ± 2 standard deviations, illustrating variability across modeled configurations.

A ±5% agreement threshold is well within practical detector uncertainty. Typical handheld NaI(Tl) scintillation detectors (2"–3" crystals) exhibit intrinsic efficiencies of approximately 10–40% at Co-60 photon energies (1.17–1.33 MeV), with substantially lower full-energy peak efficiency due to dominant Compton interactions (ALMisned et al., 2022)(Sen et al., 2013). These values represent intrinsic efficiency and do not account for geometry-dependent detection probability. Accordingly, the observed F4–F5 agreement falls well within accepted experimental uncertainty bounds, reinforcing the reliability of the modeling framework.

4.2 - Inverse Square Law Convergence:

As shown in Figure *4-2*, the log–log slope of F4-derived effective dose versus distance yielded a mean value of −1.98 with a standard deviation of approximately 0.04 across air-reference configurations. As summarized in Table 4.1, the reported slope represents the mean of configuration-level log–log regression slopes rather than a single pooled regression. No statistical outliers were identified based on interquartile range (IQR) analysis.

The observed mean slope is in close agreement with the theoretical inverse-square value (−2), demonstrating convergence toward geometric attenuation behavior under air reference conditions. The relatively small standard deviation indicates low variability across configurations and consistent attenuation behavior. This agreement is consistent with expected physical transport and confirms that the modeling framework accurately reproduces free-field geometric attenuation in sufficiently large tunnel geometries.

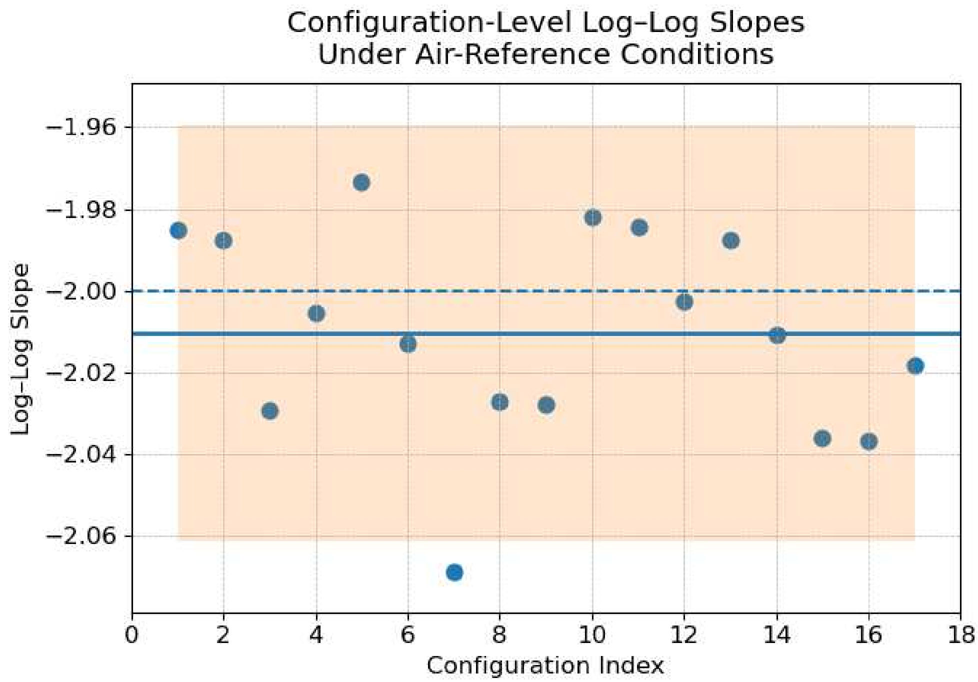

Figure 4-2: Configuration-level log–log regression slopes of effective dose versus distance under air-reference conditions. Points represent individual configuration-level log-log regression slopes. The solid line indicates the overall mean, the shaded region represents mean ± 2 standard deviations, and the dashed line indicates the theoretical inverse-square slope (−2).

This result demonstrates that the modeling framework achieves consistent agreement with expected free-field inverse-square attenuation behavior, establishing confidence in the physical accuracy of the transport solution. Consequently, deviations observed in confined tunnel configurations can be attributed to boundary interactions and material effects rather than numerical instability or implementation error. Establishing this baseline geometric fidelity is essential before interpreting confinement-induced dose modifications in subsequent analyses.

From an operational perspective, this validation supports the use of Monte Carlo transport modeling to interpret radiation measurements in confined infrastructure, where analytic assumptions alone may be insufficient. The deviation of the mean slope from −2 remains small relative to the observed variability across configurations, indicating that the modeled attenuation behavior is consistent with geometric expectations.

4.3 - Material Influence Relative to Air Baseline:

The influence of tunnel wall material was assessed using percent change relative to matched air-reference configurations across Precise Line (PL) evaluations. Using the integrated effective dose along the 0–20 m Precise Line, percent change relative to air was quantified and summarized statistically. For the operational concrete configuration, the mean percent change was +8.60% relative to matched air baselines (SD = 21.54%, N = 14). Although the mean indicates a modest increase relative to air, the large standard deviation reflects substantial variability across configurations, indicating that material effects are strongly influenced by configuration-specific transport conditions.

These results demonstrate that structural materials can modify effective-dose distribution through competing attenuation and scatter processes, producing spatial dose behavior that differs from free-field expectations. From a radiation-protection perspective, this indicates that responder exposure assessment in confined infrastructure must account for environmental composition rather than relying solely on distance-based estimation approaches.

4.4 - Mesh Sensitivity Study:

Mesh sensitivity analysis demonstrated that larger tetrahedral elements produced increased deviation between modeled F4 dose and analytical gamma-constant–derived expectations, whereas refined local meshing substantially reduced this variance. Optimal results were achieved when maximum tetrahedral edge length was constrained to approximately 5–10% of the largest global geometry dimension, with local refinement to ≤10 cm within 2 meters of the source region. This effect is particularly important in confined geometries where steep spatial dose gradients are expected near structural interfaces.

Because global refinement at this scale was computationally prohibitive for the full tunnel domain, the geometry was partitioned into subregions containing fewer than 50,000 cells, enabling localized refinement in source-proximal regions. This strategy reduced average variance from approximately 20% to approximately 2% in critical regions, confirming that near-source mesh resolution strongly influences F4 volume-averaged tallies. These results support the selected discretization strategy as both computationally feasible and numerically stable.

In this work, model verification and validation are treated as distinct but complementary processes. Verification refers to ensuring that the numerical implementation of the Monte Carlo model is internally consistent and free of computational error, while validation refers to demonstrating that the model accurately represents the underlying physical radiation transport processes relevant to the problem domain.

4.5 - Model Verification and Validation:

In this work, model verification and validation are treated as distinct but complementary processes. Verification refers to ensuring that the numerical implementation of the Monte Carlo model is internally consistent and free of computational bias, while validation refers to demonstrating that the model accurately represents the underlying physical radiation transport processes relevant to the problem domain.

Model verification was established through agreement between independent estimators of the radiation field, specifically the F4 volume-averaged fluence tally and the F5 point-detector tally. Consistent agreement within approximately 5% across reference distances indicates numerical stability and absence of significant estimator bias.

Model validation was evaluated using multiple criteria. First, under air-reference conditions, the model demonstrated attenuation behavior consistent with the theoretical inverse-square relationship, with configuration-level log–log slopes tightly clustered around −2. Second, material-dependent deviations from this baseline were physically interpretable and consistent with known photon interaction mechanisms, including attenuation and scattering. Third, observed non-line-of-sight dose persistence exhibited spatial behavior consistent with expected boundary interaction and scattering effects in confined geometries.

Collectively, these results demonstrate that:

1) the Monte Carlo transport solution is numerically stable,
2) geometric attenuation behavior is physically consistent with free-field expectations under air-reference conditions, and
3) deviations observed in confined tunnel environments arise from physical boundary interactions and material effects rather than numerical artifacts.

Satisfaction of these criteria supports the conclusion that the model is both numerically verified and physically validated for the evaluation of photon transport in subterranean tunnel environments. It is recognized that model validation is context-dependent; therefore, the criteria applied here are specific to photon transport behavior and operational dose assessment in confined environments.

Collectively, these verification and validation results demonstrate that the modeling framework provides consistent, physically realistic, and quantitatively reliable estimates of effective dose across the range of configurations investigated. Agreement between F4 and F5 tallies, convergence toward inverse-square behavior under air-reference conditions, and consistency with analytic dose-rate expectations establish confidence that the simulation approach accurately represents photon transport processes.

With this validation established, the following chapter presents the application of the model to characterize radiation field behavior in confined subterranean tunnel environments.

Chapter 5 - Radiation Field Characterization in Subterranean Environment Results:

The verification and validation results presented in Chapter 4 establish the reliability of the modeling framework, including agreement between independent tally methods, convergence toward expected geometric behavior under air-reference conditions, and stability with respect to mesh resolution. Building on this validated framework, Chapter 5 presents the quantitative characterization of radiation field behavior in confined subterranean geometries.

In contrast to free-field conditions, photon transport in confined tunnel geometries is influenced by geometric confinement, boundary interactions, and material-dependent scattering processes. These mechanisms produce measurable deviations from classical inverse-square attenuation behavior, particularly in near-field and non-line-of-sight regions. The following sections quantify these effects using precise-line (PL) evaluations and configuration-level statistical analysis

Because the modeling framework has been independently verified and validated, the deviations and trends identified in this chapter are interpreted as physical radiation transport behavior rather than numerical or methodological artifacts. These findings provide quantitative confirmation and extension of earlier confined-geometry radiation transport observations reported in small-scale tunnel studies, demonstrating that similar scatter-mediated persistence and structural streaming behavior occur in infrastructure-scale subterranean environments.

This chapter evaluates the three hypotheses defined in Section 1.5 using quantitative statistical metrics derived from 40 Monte Carlo configurations. Results are presented sequentially: (1) convergence toward inverse-square behavior, (2) material-dependent deviation relative to air baseline conditions, and (3) confined-geometry scatter and streaming effects. For each hypothesis, statistical conclusions are stated explicitly based on configuration-level variability characterized using mean values and standard deviation (mean $\pm$ 2 standard deviations).

Table *5.1* summarizes the principal quantitative metrics used to evaluate the three study hypotheses. Metrics are reported as mean estimates with accompanying standard deviation–based descriptors to reflect variability across configurations rather than uncertainty in the estimated mean. Hypothesis 1 is evaluated using log–log slope convergence toward the theoretical inverse-square exponent under air reference conditions. Hypothesis 2 is assessed using integrated effective dose change along the 0–20 m Precise Line (PL), comparing material configurations to their matched air baselines. Hypothesis 3 is quantified through non-line-of-sight persistence and structural streaming ratios.

Collectively, these results demonstrate convergence toward inverse-square geometric attenuation behavior under air-reference conditions, including measurable material-dependent dose modification and scatter-mediated dose persistence within confined tunnel environments. Variability is reported as mean ± 2 standard deviations, representing configuration-level spread rather than uncertainty in an estimated population mean.

Table 5.1: Summary of key quantitative metrics supporting study hypotheses. Values are reported as mean estimates with standard deviation–based variability descriptors; where shown, mean ± 2 standard deviations is used as a descriptive representation of configuration-level variability.

Metric	N	Mean	Variability (Mean ± 2 SD)	Supporting statistics
Mean absolute % diff (F4 vs F5) (workflow agreement)	40 runs	4.67%	± 3.60%	Median = 4.72%; 3 outliers identified using the IQR method
Log–log slope (Air) (Hypothesis 1 baseline inverse-square)	17 runs	−2.010	± 0.026	Mean R^2 = 0.9997
Log–log slope (All materials pooled) (departure under confinement/material)	40 runs	−1.980	± 0.280	Systematic flattening relative to the theoretical inverse-square exponent (−2)
Integrated effective dose change vs Air (0–20 m, PL) (Hypothesis 2 material influence, pooled configurations)	14 configs	+8.60%	±43.08%	High variability (SD = 21.54%) indicates strong geometry dependence
NLOS persistence ratio (PL c, d vs PL a, b, g) (Hypothesis 3 scatter persistence)	28 runs	0.285	± 0.166	Sustained scatter-mediated dose beyond line-of-sight regions
Streaming ratio (PL e vs PL f) (Hypothesis 3 structural streaming)	32 runs	2.92	± 3.80	Strong entrance-driven transport with substantial configuration-dependent variability

As summarized in Table 5.1, workflow agreement between F4 and F5 tallies yielded a mean absolute percent difference of 4.67% with low variability across configurations. Under air-reference conditions, the mean log–log attenuation slope was −2.010, tightly clustered around the theoretical inverse-square value. When material configurations were pooled, the mean slope shifted to −1.980, indicating systematic flattening under confinement. Material-dependent effects exhibited substantial configuration-level variability, reflecting strong dependence on geometry and spatial position. Non-line-of-sight persistence and structural streaming metrics further demonstrate sustained dose beyond line-of-sight and preferential transport through tunnel features, consistent with scatter-mediated redistribution and geometry-driven transport pathways.

Variability in model results is characterized using standard deviation across configurations, consistent with the statistical framework established in Chapter 4. This approach reflects the spread of outcomes across modeled scenarios rather than uncertainty in an estimated population mean and is used throughout Chapter 5 to support interpretation of configuration-dependent effects.

5.1 - Model-to-Model Agreement:

Across 40 modeled configurations, the mean absolute percent difference between F4 and F5 tallies was 4.67%, with low variability across configurations (±3.60%, mean ± 2 SD). The median was 4.72%, indicating minimal skew. Only three of forty configurations were identified as statistical outliers using the interquartile range (IQR) method, and inclusion of these cases did not materially alter the mean.

This level of agreement confirms numerical consistency between the spatially averaged F4 estimator and the point-based F5 estimator, supporting the use of F4 for full-field spatial characterization while retaining F5 as an internal verification reference.

5.2 - Hypothesis 1: Convergence Toward the Inverse Square Law:

Air-reference configurations represent conditions with negligible material interaction, providing a geometric attenuation baseline for comparison. For these configurations, the mean F4 log–log slope was −2.010, with low variability across configurations (±0.026, mean ± 2 SD) and mean $R^2 \approx 0.9997$ (range 0.9987–0.99998). These results indicate strong agreement with expected inverse-square attenuation behavior and confirm geometric fidelity under air-reference conditions.

Figure *5-1* separates the dominant Co-60 air-reference dataset from the single-run reference isotopes to improve the interpretability of the air-benchmark attenuation behavior. Panel A shows the Co-60 mean normalized effective dose with variability represented as ±2 standard deviations across configurations, while Panel B shows the corresponding single-run air-reference trends for Cs-

137, Ir-192, and Ra-226. Across all air-reference configurations, the mean configuration-level log–log slope was −2.010 (N = 17), closely aligned with the theoretical inverse-square value of −2.

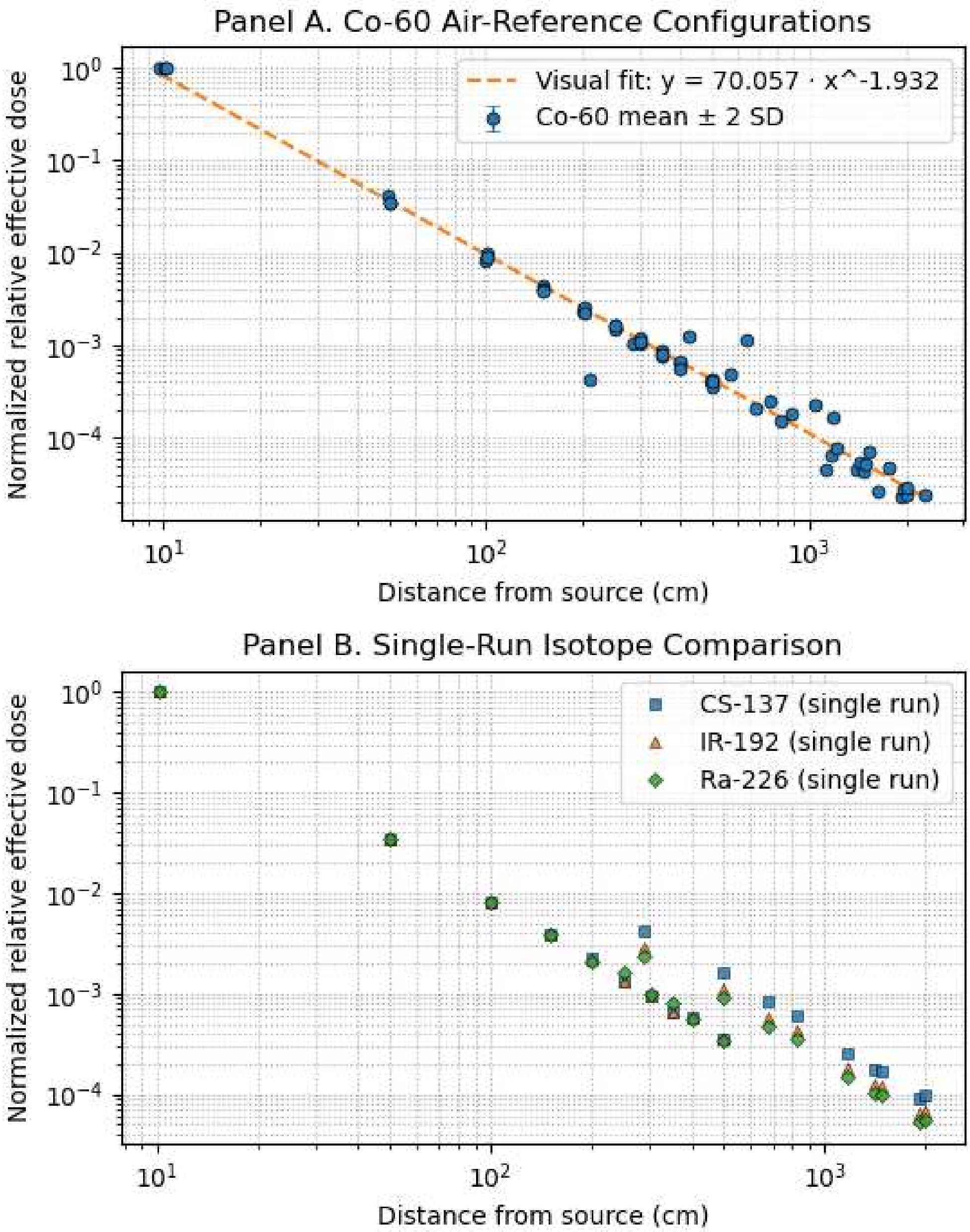

Figure 5-1: Air-reference attenuation behavior shown in a two-panel format. Panel A presents the normalized relative effective dose as a function of distance for Co-60 configurations. Points represent mean values across configurations, and error bars indicate ±2 standard deviations, illustrating variability rather than uncertainty in the estimated mean. The dashed line shows a representative power-law fit to the data, demonstrating near inverse-square attenuation behavior under air-reference conditions. Panel B shows single-run isotope comparisons (Cs-137, Ir-192, and Ra-226) under identical geometric conditions. Markers represent normalized effective dose values as a function of distance without connecting lines to avoid implying continuous interpolation between sampled points. Results illustrate consistent attenuation trends across isotopes while highlighting subtle differences in spectral-dependent behavior.

As shown in Figure *5-1*, normalized dose exhibits near–inverse-square behavior under air-reference conditions, with fitted slopes approaching −2. Log–log scaling reveals attenuation behavior consistent with geometric expectations, with power-law regression of the form $y = ar^b$ confirming the expected distance dependence. The fitted exponents approach −2 in the absence of significant material interaction, while small deviations from ideal inverse-square behavior reflect energy-dependent scattering and spectral differences among isotopes. The high coefficients of determination (R^2) indicate strong conformity to geometric attenuation trends, supporting the physical validity of the Monte Carlo transport modeling. Differences in slope between isotopes illustrate the influence of photon energy on effective attenuation and scatter contribution within the modeled environment.

Collectively, these results support convergence toward inverse-square attenuation behavior in sufficiently large air-filled tunnel geometries, consistent across configurations and isotopes.

5.3 - Hypothesis 2: Material Influence:

Material-dependent modification was evaluated using integrated effective dose along the Precise Line from 0–20 m, as defined in section 3.15.2. For the operational concrete tunnel configuration, the mean integrated dose change relative to air was +8.60% (SD = 21.54%, N = 14). While configuration-level variability was observed, systematic departures from air-reference behavior were evident across materials, confirming that boundary composition modifies the cumulative spatial dose distribution within the tunnel environment. These results demonstrate that tunnel wall composition modifies effective dose distributions relative to free-field conditions, with the magnitude and direction of the effect dependent on material properties and geometric configuration.

5.3.1 By Material

Material-dependent modification of the cumulative dose field was evaluated using the integrated effective dose along the Precise Line from 0–20 m, as defined in Section 3.15.2. The results demonstrate that photon transport in confined geometries is strongly influenced by boundary composition through energy-dependent scattering and attenuation mechanisms governed by material density (ρ) and effective atomic number (Z_{eff}).

For the operational concrete tunnel configuration (N = 14), the mean integrated dose change relative to air was +8.60%, with a standard deviation of 21.54%, corresponding to a variability range of approximately −34.48% to +51.68% (mean ± 2 SD). Concrete possesses moderate density (≈2.3 $g \cdot cm^{-3}$) and an intermediate effective atomic number. At the dominant photon energies modeled (0.662–1.33 MeV), Compton scattering is the primary interaction mechanism. Concrete's density is sufficient to increase the probability of multiple scatter events while not being so absorptive as to strongly attenuate photon fluence. The net result is partial backscatter and lateral redistribution of photon fluence into regions that would otherwise experience geometric falloff under air-reference conditions. This produces a modest increase in integrated dose along the Precise Line (PL).

In contrast, higher-density and/or higher-Z materials demonstrated reductions in cumulative dose relative to air within the 0–20 m domain:

- Granite: −15.46%
- Sandstone: −15.32%
- Basalt: −14.90%
- Limestone: −14.70%
- Lead: −19.37%

For silicate-based materials (granite, sandstone, basalt, limestone), increased bulk density relative to air raises the macroscopic attenuation coefficient, thereby increasing the probability of both Compton scatter and photon removal from the forward fluence field. Although scattering remains dominant in this energy regime, higher effective electron density increases the likelihood of photon redirection out of the PL path, producing a net attenuation effect in the integrated metric.

The strongest attenuation was observed for lead (−19.37%), consistent with its high density (≈11.3 $g \cdot cm^{-3}$) and high atomic number (Z = 82). At MeV energies, Compton scattering remains significant; however, the increased photoelectric absorption contribution at lower energy components and the greater overall linear attenuation coefficient substantially reduce transmitted and redistributed photon fluence. Consequently, integrated effective dose along the PL decreases relative to air.

Collectively, these results are consistent with fundamental photon transport theory:

- Air (low ρ, low Z_{eff}): minimal scattering and attenuation → near-geometric behavior
- Moderate-density materials (e.g., concrete): enhanced multiple scattering → localized fluence redistribution and possible cumulative dose enhancement
- Higher-density and/or higher-Z materials: increased attenuation dominance → net integrated dose reduction

Although results are based on a finite set of modeled configurations, the observed trends are consistent with energy-dependent interaction cross sections and macroscopic attenuation behavior in the 0.6–1.3 MeV photon energy range. These findings confirm that boundary composition exerts a predictable, physics-governed influence on confined photon transport, supporting Hypothesis 2 and reinforcing the necessity of incorporating realistic material properties in subterranean radiological exposure modeling.

To examine the spatial structure of material-dependent dose modification, distance-resolved percent change relative to matched air configurations was evaluated along the full Precise Line (0–20 m). At each distance increment, the percent deviation was computed as:

$$\Delta(r) = \frac{D_{\text{material}}(r) - D_{\text{air}}(r)}{D_{\text{air}}(r)} \times 100\%$$

where $D(r)$represents F4-derived effective dose rate at distance r. Figure *5-2* shows the mean percent deviation curves for representative materials and the pooled material set, illustrating how confinement effects evolve with increasing standoff distance. Shaded regions represent variability across configurations, shown as mean ± 2 standard deviations.

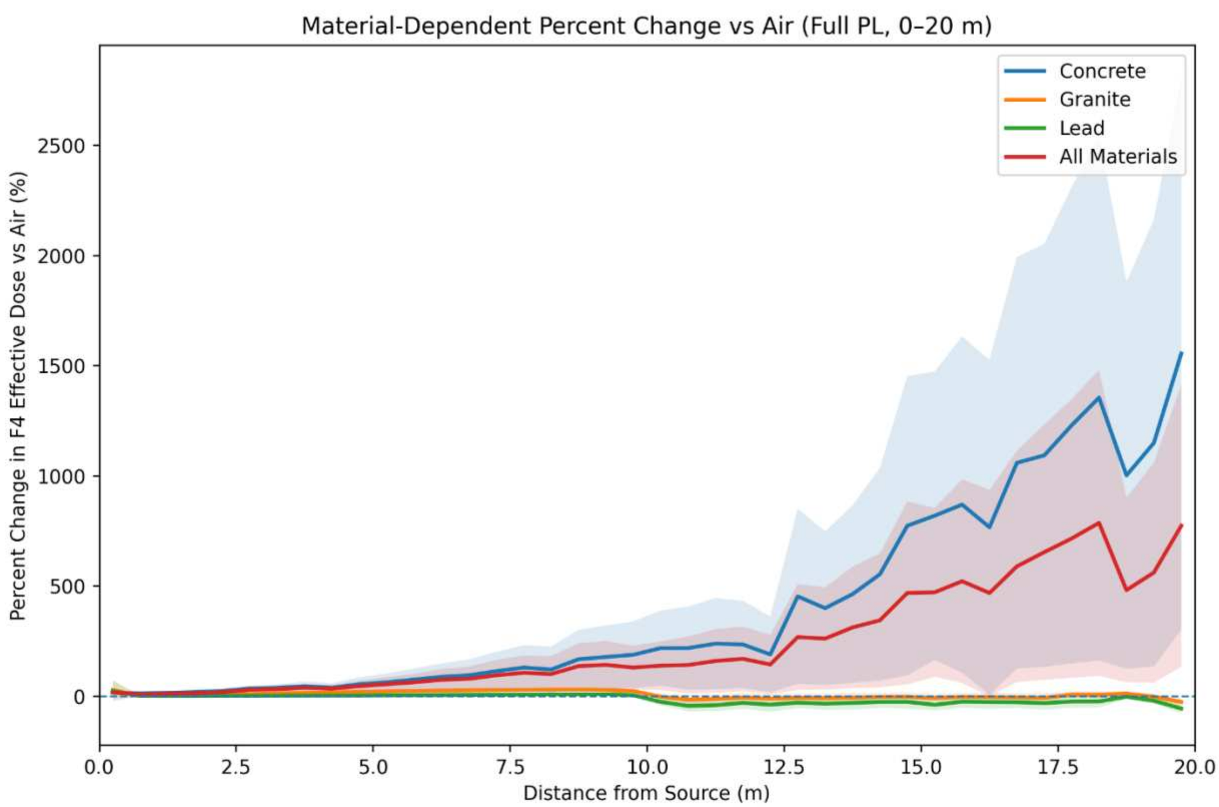

Figure 5-2: Material-dependent percent change in F4-derived effective dose relative to matched air configurations along the full Precise Line (0–20 m). Curves represent distance-binned mean percent deviation (0.5 m bins) with shaded regions indicating variability across configurations (±2 standard deviations). The dashed horizontal line denotes parity with air (0%). Concrete exhibits monotonic amplification with distance, while lead demonstrates near-field attenuation followed by partial downstream convergence toward inverse-square behavior. The pooled curve summarizes aggregate material effects. Divergence of the curves with distance reflects the coupled influence of attenuation and scattering, demonstrating that material-dependent modifications become increasingly evident beyond the near-source region.

The distance-resolved curves in Figure *5-2* demonstrate that material influence is strongly geometry- and distance-dependent rather than uniform across the tunnel domain. Concrete exhibits progressive amplification of percent deviation with increasing distance, consistent with cumulative scatter contributions and boundary-mediated photon redirection under confined conditions. In contrast, higher-density and higher-atomic-number materials such as lead show near-field attenuation relative to air, followed by partial downstream convergence toward inverse-square behavior as multiply scattered photons contribute to the dose field. Intermediate-density silicate materials (e.g., granite) demonstrate comparatively modest deviation, reflecting the balance between Compton scattering and attenuation processes at the photon energies evaluated.

The increasing spread at larger distances reflects increasing variability driven by spectral softening, angular redistribution, and geometric shadowing effects. While these curves provide mechanistic insight into spatial dose evolution, hypothesis testing for material influence is based on the integrated effective dose metric (0–20 m), which captures the net operational impact of these distance-dependent behaviors. Percent change increases with distance because scattered photon contributions remain significant while the free-field reference dose decreases more rapidly due to geometric attenuation.

Collectively, these results demonstrate that material composition exerts a systematic and physically predictable influence on photon transport within confined tunnel geometries, supporting the role of boundary interactions in modifying effective dose distributions.

5.4 - Hypothesis 3: Non-Line-of-Sight Enhancement:

Non-line-of-sight (NLOS) dose behavior was evaluated using Precise Line extractions in the pedestrian tunnel (PL c and d), which represent regions lacking direct geometric line-of-sight to the source. For each eligible configuration, mean effective dose along these NLOS paths was compared to a line-of-sight (LOS) reference defined by road-tunnel paths (PL a, b, and g). Analysis was restricted to configurations containing the full PL set required for this comparison, excluding straight-tunnel geometries and source-location cases lacking complete LOS reference paths.

Dose values were evaluated over the 100–4500 cm distance window to ensure consistent comparison across configurations. Across the 28 eligible configurations, the mean NLOS-to-LOS dose ratio was 0.285 with a standard deviation of 0.083, corresponding to 0.118 to 0.451 (mean $\pm$ 2 SD). These results demonstrate substantial dose persistence in NLOS regions relative to LOS reference magnitudes.

This behavior is consistent with confinement-driven angular redistribution via Compton scattering and boundary interactions within the tunnel system, which sustain photon transport beyond direct line-of-sight pathways.

Streaming effects at the pedestrian tunnel opening were evaluated by comparing effective dose along the entrance-adjacent road-tunnel wall (PL e) to the opposing wall without an opening (PL f). Across 32 eligible configurations, the mean streaming ratio was 2.92 with a standard deviation of 1.90, indicating substantial but highly variable dose enhancement along the entrance-adjacent wall. Observed ratios ranged from values near unity to greater than 6, reflecting strong dependence on geometry, material composition, and source placement.

Despite this variability, the majority of configurations exhibited ratios greater than unity, confirming preferential photon transport through the structural opening. This behavior is consistent with geometric channeling of scattered photons and localized amplification of dose along connected pathways within confined tunnel systems.

Collectively, these findings provide quantitative support for Hypothesis 3 and demonstrate that confined geometries produce measurable non-line-of-sight dose persistence beyond direct line-of-sight attenuation behavior. The observed NLOS-to-LOS ratio remains consistently non-zero across all evaluated configurations, indicating that scattering and boundary interactions sustain a non-negligible effective dose in geometrically shadowed regions.

The variability observed across configurations reflects differences in geometry, material composition, and source placement, but does not alter the overall conclusion that confinement-mediated transport produces persistent NLOS dose fields. These findings demonstrate that confined geometries produce measurable non-line-of-sight dose persistence beyond direct line-of-sight attenuation behavior. Table *5.2* provides summarizes the quantitative metrics supporting Hypothesis 3.

Table 5.2: Quantitative evidence for non-line-of-sight persistence and streaming (PL extractions, 100–4500 cm window).

Metric (supports Hypothesis 3)	Definition	N	Mean	Standard Deviation	Mean ± 2SD	Interpretation
NLOS persistence ratio	(PL c, d) / (PL a, b, g)	28	0.285	0.083	0.118–0.451	NLOS dose is ~28% of LOS magnitude
Streaming ratio (entrance effect)	(PL e) / (PL f)	32	2.92	1.90	-0.88 – 6.72	Strong but variable streaming

Across 32 eligible configurations, the mean streaming ratio was 2.92 with a standard deviation of 1.90, indicating substantial but highly variable dose enhancement along the entrance-adjacent wall. Observed ratios ranged from values near unity to greater than 6, reflecting strong dependence on geometry, material composition, and source placement.

Despite this variability, the majority of configurations exhibited ratios greater than unity, confirming preferential photon transport through the structural opening. This behavior is consistent with geometric channeling of scattered photons and localized amplification of dose along connected pathways within confined tunnel systems.

The larger variability observed in the streaming ratio relative to the NLOS persistence metric reflects the sensitivity of streaming behavior to geometric alignment and structural connectivity, rather than indicating inconsistency in the underlying physical process.

Collectively, these findings demonstrate that confined geometries produce measurable non-line-of-sight dose persistence beyond direct line-of-sight attenuation behavior. The observed NLOS-to-LOS ratio remains consistently non-zero across all evaluated configurations, indicating that scattering and boundary interactions sustain a non-negligible effective dose in geometrically shielded regions. Variability across configurations reflects differences in geometry, material composition, and source placement, but does not alter the overall conclusion that confinement-mediated transport produces persistent NLOS dose fields.

5.5 - Summary and Conclusions

From an operational radiation-protection perspective, the results of this study demonstrate that responder exposure assessment in confined infrastructure must account for geometry-dependent transport effects rather than relying solely on distance-based estimation or visual line-of-sight assumptions. Structural features such as corridor intersections, transitions in tunnel cross-section, and access openings can facilitate scatter-enhanced dose persistence and streaming-mediated photon transport, resulting in measurable exposure even in geometrically shielded locations. Consequently, survey strategies should prioritize measurements along anticipated movement pathways and near structural transition regions to support accurate hazard-zone delineation and reduce the potential for systematic underestimation of effective dose during subterranean response operations.

Collectively, the results provide quantitative support for all three study hypotheses. Under air-reference conditions, effective dose attenuation demonstrated tight convergence toward inverse-square behavior, confirming geometric fidelity of the modeling framework. When realistic tunnel materials were introduced, integrated effective dose along the 0–20 m Precise Line exhibited measurable deviation from matched air baselines, demonstrating that boundary composition systematically modifies photon transport behavior. Although geometric attenuation remains the dominant mechanism at extended distances, material-dependent attenuation and scattering introduce bounded but operationally meaningful departures from free-field expectations. Finally, consistently observed non-line-of-sight persistence and structural streaming confirm that confined geometries sustain dose fields beyond direct line-of-sight regions and preferentially channel photons through structural discontinuities.

Together, these findings demonstrate that subterranean dose distributions are governed by predictable geometric principles that are systematically modulated by material composition and confinement effects, underscoring the necessity of geometry-specific modeling for accurate operational dose assessment in underground environments. From an operational perspective, reliance on simplified free-field assumptions may lead to systematic misestimation of responder dose in confined environments.

Chapter 6 - Discussion:

6.1 - Operational Interpretation Framework

For responder-focused interpretation, the findings of this study can be organized into three practical radiation-field behavior categories:

(1) near-field scatter-enhanced dose conditions,

(2) transitional attenuation regions influenced by structural geometry, and

(3) far-field geometric attenuation approaching free-field expectations.

These categories provide a simplified conceptual framework for interpreting radiation measurements in confined infrastructure. By linking observed dose behavior to underlying photon transport mechanisms, this framework supports improved assessment of exposure conditions and operational risk in subterranean environments.

6.2 - Overview of Study Objectives and Key Findings:

This research investigated photon dose behavior in confined tunnel geometries using Monte Carlo radiation transport modeling. The primary objective was to determine how tunnel geometry, wall material composition, and source characteristics influence photon dose distributions relative to classical inverse-square law (ISL) expectations. This work extends prior subterranean radiation transport studies by providing a physically grounded characterization of effective-dose attenuation behavior across large-scale tunnel geometries.

Three hypotheses were evaluated:

1. Photon dose rates in sufficiently large tunnel geometries converge toward inverse-square law behavior.
2. Tunnel wall composition modifies photon dose distributions relative to air-filled free-field conditions.

3. Confined geometries produce measurable non-line-of-sight dose persistence beyond direct line-of-sight regions.

The principal findings of this work are:

• Volume-averaged F4 tallies are sensitive to mesh resolution in regions of strong spatial gradients.

• Point-detector F5 tallies provide dose estimates that agree with gamma constant calculations within approximately 1–10% when properly implemented.

• The use of ICRP 116 AP fluence-to-effective-dose coefficients improves agreement with expected dose behavior compared to ISO geometry coefficients.

• Tunnel confinement produces measurable deviation from idealized inverse-square attenuation behavior, particularly at increased distances and in the presence of realistic wall materials.

• Scatter contributions within confined geometries alter spatial dose gradients in ways not captured by simplified analytic models.

Collectively, these findings demonstrate that confined tunnel environments require transport-based modeling to produce reliable dose estimates. Reliance on simplified inverse-square law assumptions alone may introduce systematic bias in responder exposure assessment within subterranean infrastructure. These findings provide the basis for the operational interpretations and responder-focused guidance developed in the following sections.

6.3 - Interpretation of Hypothesis 1 –Convergence Toward Inverse Square Behavior:

6.3.1 Agreement in Air-filled Geometries:

The air-filled tunnel configuration served as a baseline case approximating free-field conditions. For centrally located point sources, modeled dose rates followed a log–log slope near −2 over short to intermediate distances from the source. Comparison with gamma constant calculations demonstrated agreement within approximately 1–10%, depending on mesh refinement and distance.

These results confirm that, in sufficiently open geometries with minimal boundary interaction, Monte Carlo–derived dose distributions converge toward classical inverse-square attenuation behavior.

6.3.2 Deviation at Larger Distances:

At greater distances within the tunnel, deviations from idealized inverse-square behavior became measurable. Two primary mechanisms contribute to this behavior:

1. Wall scatter accumulation
2. Finite geometric boundary effects

In a confined tunnel, photons that would otherwise escape in a free-field environment interact with surrounding boundaries and re-enter the air volume as scattered radiation. This scattered component modifies the radial fluence gradient and introduces departures from purely geometric attenuation. The magnitude of this deviation increases with distance and varies with material composition.

These observations demonstrate that inverse-square behavior represents an idealized limit, and its applicability depends on the relative scale of the geometry compared to the photon mean free path.

6.3.3 Threshold Behavior:

Although a single universal geometric threshold cannot be defined across all materials and photon spectra, the results indicate that as tunnel cross-sectional dimensions become large relative to the photon mean free path of the dominant energy, attenuation behavior increasingly approaches inverse-square scaling within practical engineering tolerance. This observation is consistent with photon transport theory, in which reduced boundary interaction frequency diminishes scatter-mediated deviation from geometric attenuation.

From an operational perspective, this provides practical guidance for identifying conditions under which simplified inverse-square–based dose estimation methods may be appropriate in large subterranean spaces.

Collectively, these findings demonstrate that while geometric attenuation remains the dominant governing mechanism at extended distances, localized deviations arise from boundary interactions that modify angular photon flux distributions. This combined influence highlights the importance of evaluating both distance and structural context when interpreting radiation behavior in confined environments.

6.4 - Interpretation of Hypothesis 2 – Material Influence:

6.4.1 Mechanisms of Material Impact:

Material composition influences photon transport through fundamental interaction properties, including linear attenuation coefficient, scattering cross section, atomic number (Z dependence), and material density. Higher-density materials increase the probability of photon interaction; however, the net effect on dose within the tunnel air volume is not purely attenuative.

Two competing processes govern the resulting dose field:

• Increased absorption reduces the direct beam contribution

• Increased Compton scattering enhances redistribution of photon fluence

The balance between these processes determines whether material presence produces net attenuation or localized dose enhancement within the confined geometry.

6.4.2 Distance-Dependent Material Effects:

Material-dependent effects were evaluated as a function of distance along the Precise Line to distinguish near-field and far-field behavior. As shown in Figure 5-2, differences between materials are minimal within approximately 1 m of the source, where photon transport occurs predominantly in air and geometric attenuation governs dose behavior.

Beyond this near-field region, material-dependent divergence becomes increasingly pronounced, reflecting the cumulative influence of scattering and attenuation along tunnel boundaries. These results indicate that material effects are secondary to geometric transport near the source but become increasingly important with distance as scattered photon contributions accumulate.

Material influence is further enhanced under conditions that increase boundary interaction, including larger source-to-detector distances, off-center source placement, and reduced tunnel cross-sectional dimensions. These findings demonstrate that material-dependent effects are inherently context-dependent rather than universally dominant, reflecting the combined influence of geometry, source position, and scattering processes on confined photon transport.

6.4.3 Observed Material Trends:

Comparisons between air, concrete, basalt, limestone, sandstone, and lead demonstrate consistent material-dependent behavior:

• Air-filled configurations show the closest agreement with inverse-square attenuation

• Moderate-density materials (e.g., concrete) produce measurable but modest deviations

• Higher-density and higher-Z materials (e.g., lead) produce stronger attenuation and greater modification of dose gradients

However, the magnitude of deviation is smaller than might be expected for centrally located sources, indicating that geometry and source position often exert a stronger influence on dose behavior than material composition alone.

6.4.4 Integrated Interpretation:

Taken together, Figures 5-1 and 5-2 illustrate the transition from geometric attenuation behavior to confinement- and material-driven transport effects within the tunnel environment. Figure 5-1 establishes the baseline spatial behavior under air-reference conditions, demonstrating near–inverse-square attenuation with minor isotope-dependent variation. Figure 5-2 builds on this foundation by quantifying the influence of confinement and material composition, revealing distance-dependent deviation from the air-reference baseline, including both enhancement and attenuation of effective dose relative to geometric expectations.

Collectively, these results demonstrate that while geometric attenuation remains the dominant mechanism governing dose behavior, material-dependent scattering and attenuation introduce systematic, distance-dependent modifications. This highlights the importance of incorporating realistic boundary conditions and material properties when evaluating photon transport in confined subterranean environments.

6.5 - Interpretation of Hypothesis 3 – Scatter Enhancement Beyond Line-of-Sight:

6.5.1 Non-Line-of-Sight Regions:

Precise line-extraction analyses demonstrated measurable dose in regions lacking direct geometric line-of-sight to the source due to tunnel curvature or structural obstruction. This behavior arises from Compton-scattered photons originating from tunnel boundaries, along with subsequent secondary scattering cascades that redistribute photon fluence throughout the confined environment.

As a result, effective dose is sustained in geometrically shielded regions, even in the absence of a direct path between the source and detector location. Such behavior is not captured by direct-line analytic models and highlights the importance of accounting for scatter-mediated transport in confined geometries.

6.5.2 Operational Relevance:

From an operational health physics perspective, these findings indicate that standard outdoor standoff distance guidelines do not directly translate to subterranean response scenarios. Enhanced photon scattering within tunnel geometries can sustain dose fields beyond expected geometric attenuation profiles, influencing time-to-dose calculations and personnel rotation strategies.

In practical terms, radiation may be detectable in geometrically shielded or non-line-of-sight regions, and dose gradients may be less steep than those predicted by inverse-square behavior alone. Additionally, localized dose amplification can occur due to geometric channeling and boundary-driven photon transport along connected structural pathways.

These effects have important implications for radiation survey strategy, detector interpretation, and hazard-zone delineation in confined environments, where reliance on line-of-sight assumptions may lead to underestimation of exposure risk. These findings reinforce that confined photon transport must be evaluated using geometry-aware approaches rather than relying solely on simplified free-field assumptions.

6.6 - Mesh Sensitivity and Volume Averaging Effects:

6.6.1 Volume Averaging Mechanism:

One of the most significant findings of this work was the strong dependence of F4 cell-based tallies on mesh resolution. The dose assigned to each node represents a volume-averaged value over its associated tetrahedral cell. Larger tetrahedra reduce spatial resolution and introduce averaging error, particularly near steep dose gradients adjacent to the source.

Because dose in free air follows inverse-square behavior, small positional differences near the source correspond to large dose differences, making mesh resolution especially critical in this region.

6.6.2 Quantified Impact of Mesh Resolution:

Model development demonstrated substantial differences between F4 and F5 tallies when tetrahedral elements were large, particularly in the near-field region. In some cases, reducing the maximum tetrahedron edge length decreased the mean absolute F4–F5 percent difference from approximately 20% to approximately 2%.

This behavior is consistent with the volume-averaging nature of the F4 tally. Larger cells near the source average dose over a wider spatial region, leading to underestimation of peak dose values. In contrast, the F5 point-detector tally provides a localized estimate of dose that is independent of mesh discretization and is therefore less sensitive to spatial averaging effects.

Under air-reference conditions, F5 results were observed to agree closely with gamma constant–based dose estimates, typically within 1–2%, supporting its use as a verification reference for evaluating mesh-dependent effects in F4 tallies.

6.6.3 Implications for Future Modeling:

Researchers using embedded mesh tallies must consider:

- Local refinement near high-gradient regions
- Volume-averaging bias in large cells
- Trade-offs between mesh resolution and computational time.

Failure to account for this may result in systematic underestimation of peak dose, particularly in near-source regions where dose gradients are steep.

6.7 - Validation Through F5 and Gamma Dose Rate Constant Comparison:

The F5 point-detector tally provided a critical mechanism for independent validation of the modeled dose field.

6.7.1 Agreement with Gamma Dose Rate Constant:

When implemented with appropriate dose-response coefficients and careful normalization, F5 tallies demonstrated agreement with gamma dose rate constant–based calculations within approximately 1–10%.

This level of agreement confirms the internal consistency of the modeling framework, including accurate source definition, appropriate energy binning, correct application of fluence-to-dose conversion coefficients, and proper geometric representation. The close correspondence between F5 results and analytical dose estimates under air-reference conditions supports the validity of the simulation approach and provides confidence in the use of F4 tallies for spatial dose characterization.

6.7.2 Multiplier Correction:

Initial discrepancies between modeled and analytical dose estimates were traced to the unintended double application of scaling factors between the SDEF source definition and the F5 tally. Correction of this issue resulted in substantial improvement in agreement between simulation results and gamma constant–based calculations.

This finding highlights the importance of carefully tracking normalization and multiplier application in Monte Carlo simulations, particularly when combining source definition parameters with tally-based scaling factors. Even minor inconsistencies in multiplier application can produce systematic deviations in reported dose values. Together, these results demonstrate that the modeling framework is both physically consistent and numerically reliable for evaluating photon transport in confined tunnel environments.

6.8 - Impact of Dose Conversion Coefficient Selection:

Interpretation of modeled dose behavior depends on the selection of the dosimetric conversion framework used to translate photon fluence into operational protection quantities. The use of fluence-to-dose conversion coefficients from ICRP Publication 116 in this work reflects the need to represent external photon exposure under complex irradiation geometries characteristic of confined subterranean environments

While earlier recommendations in ICRU Report 57 established the basis for operational dose quantities such as ambient dose equivalent, modern coefficient sets provide improved energy resolution and compatibility with Monte Carlo transport modeling. In contrast, the radionuclide intake dose conversion factors presented in ICRP Publication 38 are intended for internal exposure assessment and are not applicable to external field characterization. Maintaining this distinction is essential to ensure dosimetric consistency when interpreting deviations from idealized inverse-square attenuation behavior in confined geometries. Within a consistent dosimetric framework, observed departures from free-field attenuation can be attributed to geometric confinement and material-dependent scattering processes rather than methodological artifacts.

Comparison of anterior–posterior (AP) and isotropic (ISO) dose conversion coefficients demonstrated that modeled dose values using AP coefficients differed by up to approximately 20% from free-air gamma-constant estimates, whereas ISO-based results differed by up to approximately 50%. This indicates that the selection of an inappropriate irradiation geometry can introduce larger discrepancies than the transport modeling itself.

The ISO geometry assumes isotropic irradiation of the human body and therefore does not represent the directional exposure conditions typical of tunnel environments. In contrast, the AP geometry provides a more appropriate representation of forward-facing exposure scenarios and reduces systematic overestimation of effective dose. Accordingly, the selection of AP-oriented conversion coefficients is justified for modeling confined, directionally biased radiation fields.

These findings demonstrate that accurate dose assessment in subterranean environments requires careful selection of dosimetric conversion coefficients in addition to physically accurate transport modeling. This reinforces that both transport modeling and dosimetric interpretation must be aligned to ensure reliable prediction of responder exposure in confined environments.

6.9 - Isotope Energy Dependence:

Comparisons among Co-60, Cs-137, Ir-192, and Ra-226 progeny demonstrate the influence of photon energy on transport behavior within confined tunnel geometries. Differences observed in attenuation trends and spatial dose distributions across isotopes are consistent with energy-dependent interaction mechanisms governing photon transport.

Higher-energy photons exhibit longer mean free paths and undergo scattering with smaller angular deflection, resulting in broader spatial dose distributions and greater persistence of photon fluence at extended distances. In contrast, lower-energy photons experience increased attenuation and more pronounced interaction with surrounding materials, leading to steeper dose gradients and greater sensitivity to material composition.

These observations are consistent with established photon transport theory and confirm that energy-dependent scattering and attenuation processes contribute to the variation in dose behavior observed across isotopes in confined environments. This energy dependence further reinforces that both material properties and photon energy must be considered when interpreting dose behavior in confined radiation fields.

6.10 - Limitations:

This study assumes idealized tunnel geometries and homogeneous material composition. Although a real-world tunnel geometry was used as the modeling basis, the simulated environment was represented as empty, with smooth and uniform wall surfaces. In practice, subterranean environments may include structural irregularities, ventilation flow, partial shielding, equipment, vehicles, and heterogeneous surface materials that could modify scattering behavior and localized dose distributions.

The modeling framework was steady-state and did not incorporate transient plume transport, source movement, or time-dependent radioactive decay during exposure. While steady-state assumptions are appropriate for isolating geometric and material transport effects, operational response scenarios may involve dynamic aerosol dispersion and evolving source terms. Additionally, only photon-emitting radionuclides were evaluated; beta contributions and aerosolized particulate transport were outside the scope of this investigation.

Several additional methodological limitations define the interpretive bounds of this work. Human body modeling was not explicitly incorporated, and effective dose was calculated using standardized fluence-to-dose conversion coefficients. Detector response functions were not instrument-specific and therefore do not account for individual detector efficiency or energy-dependent response characteristics. The radium-226 decay chain was simplified using weighted emission probabilities rather than explicit full progeny transport. Furthermore, only selected tunnel geometries and scale configurations were evaluated, and air composition was assumed spatially homogeneous.

An additional modeling consideration involves the F5 point-detector tally. The F5 tally is computationally intensive and limited to discrete spatial locations rather than volumetric regions. In this study, this limitation was acceptable because the F5 tally was used exclusively as a verification benchmark for corresponding F4 node locations, which were also evaluated at discrete coordinates. In contrast, F4 mesh tallies provided volumetric coverage of the full tunnel domain and enabled spatial mapping of dose-rate distributions. Implementation of the F5 tally required manual coordinate specification within the MCNP input file, increasing modeling effort but not affecting numerical validity.

These limitations establish the context within which the results should be interpreted; however, they do not diminish the internal consistency or comparative validity of the modeling framework or the physical trends identified in this study. Future work may incorporate heterogeneous tunnel environments, time-dependent source behavior, and coupled particle transport to further refine operational dose predictions.

6.11 - Implications for First Responder Radiation Protection in Subterranean Environments:

The hypothesis-driven results of this investigation provide important insight into radiation-protection challenges associated with emergency response operations in confined underground infrastructure. Operational exposure assessment in radiological response is often conceptualized using simplified free-field geometric attenuation assumptions. However, the findings of this study demonstrate that subterranean environments systematically modify expected spatial effective-dose behavior through the combined effects of geometric confinement, structural material properties, and scatter-mediated photon transport. These confinement-driven processes influence both the magnitude and spatial persistence of radiation fields and therefore represent critical considerations for responder exposure assessment and hazard characterization in complex built environments.

Across approximately forty modeled configurations, effective-dose attenuation trends in air-reference geometries reproduced classical inverse-square behavior, with log–log regression slopes converging near −2.01 and low variability across configurations. Agreement between F4 volume fluence tallies and F5 point-detector estimates remained within approximately five percent across evaluated locations. These quantitative indicators establish a physically credible baseline for interpreting confinement-driven deviations and demonstrate that observed dose-field modification arises from real photon transport behavior rather than numerical artifacts.

Beyond the specific findings, this work demonstrates how Monte Carlo radiation transport modeling can be systematically applied to complex confined environments by linking physical transport mechanisms, numerical discretization, and operational dose metrics within a unified framework. These results support the use of geometry-informed assessment strategies to improve exposure estimation, guide measurement prioritization, and enhance decision-making for responders operating in subterranean radiological scenarios. In particular, these findings indicate that reliance on distance-based or line-of-sight assumptions alone may lead to systematic underestimation of effective dose in confined environments.

6.11.1 Operational Interpretation of Attenuation Behavior

In contrast to air-reference conditions, confined tunnel configurations exhibited a consistent reduction in attenuation slope magnitude, with pooled behavior approaching approximately −1.98. Although this deviation from ideal geometric attenuation is modest, it reflects a systematic flattening of the dose–distance response that may influence exposure estimation during extended underground response operations. From an operational perspective, this behavior indicates that effective dose may persist at higher-than-expected levels over longer travel distances in confined infrastructure compared with open environments.

These results suggest that simplified inverse-square approximations may not fully characterize radiation exposure conditions in subterranean response scenarios. While distance-based estimation may remain reasonable in sufficiently large, air-filled environments, its reliability decreases as geometric confinement and structural complexity increase. Incorporating geometry-informed transport modeling into decision-support frameworks can improve situational awareness and support more effective dose-management strategies for responders operating in confined environments.

6.11.2 Implications for Survey Strategy and Hazard Zoning

Material-dependent photon interaction processes were observed to influence effective-dose magnitude and spatial distribution. Integrated pathway analysis demonstrated measurable deviations from air-reference conditions associated with tunnel wall composition, with higher-density materials sustaining increased scattered-photon contributions relative to free-field behavior. These results indicate that boundary interactions and scatter can maintain localized dose conditions beyond those predicted by geometric spreading alone.

From a radiation-protection planning perspective, these findings suggest that survey strategies based solely on increasing distance from a suspected source location may not adequately characterize exposure potential in confined environments. Geometry-informed monitoring approaches that prioritize structural transition regions—including corridor intersections, access shafts, and changes in tunnel cross-section—can improve hazard delineation and support more effective responder route selection.

Recognition of confinement-modified dose behavior, therefore, supports improved hazard-zoning practices and more reliable exposure-control planning during subterranean response scenarios. In particular, measurement strategies that account for structural connectivity and potential photon streaming pathways may reduce the likelihood of underestimating localized exposure risk.

6.11.3 Non-Line-of-Sight Exposure Risk Considerations

A particularly significant operational observation of this study is the reproducible presence of measurable effective dose in non-line-of-sight tunnel locations. Structural connectivity enables preferential photon transport pathways that redistribute radiation into geometrically obstructed regions, producing streaming enhancement ratios exceeding a factor of two in multiple modeled configurations. Across evaluated layouts, the mean ratio of non-line-of-sight to line-of-sight effective dose was approximately 0.29, indicating sustained exposure potential even where direct source visibility is absent.

These findings demonstrate that responder exposure risk in subterranean environments cannot be reliably inferred solely from visual shielding conditions or assumed geometric protection. Instead, interpretation of field radiation-detector measurements must explicitly account for scattered-photon contributions and potential streaming pathways that create spatially anisotropic dose distributions. Incorporating these considerations into survey planning, tactical movement decisions, and hazard-zone establishment can improve exposure control and support safer responder operations in confined infrastructure. In particular, reliance on line-of-sight assumptions alone may lead to systematic underestimation of exposure risk in confined environments

6.11.4 Integration into Radiation Protection Decision Frameworks

The hypothesis-driven results collectively support a conceptual model in which confined tunnel radiation fields exhibit spatially structured attenuation behavior governed by interacting transport mechanisms. Near the source, dose distributions are influenced by confinement-driven boundary scatter and geometric effects that elevate and redistribute effective dose. At intermediate distances, attenuation behavior transitions toward distance-controlled geometric spreading as the relative contribution of scattered photons decreases. At sufficiently large separations, effective-dose trends progressively converge toward classical inverse-square behavior, although the distance at which this occurs depends on tunnel scale, photon energy, and material interaction characteristics.

By quantitatively linking environmental structure to effective-dose behavior, the modeling framework developed in this study provides a basis for integrating confinement effects into responder exposure-assessment methodologies. In confined or structurally complex tunnel environments, transport-based modeling approaches can improve predictive reliability and support development of decision-support tools for hazard characterization, survey prioritization, and route planning. When implemented within a validated modeling framework, such approaches may strengthen operational application of the as-low-as-reasonably-achievable principle in response scenarios where traditional free-field assumptions are insufficient.

Taken together, these results demonstrate that radiation fields in confined environments exhibit structured and reproducible transport behavior that can be quantitatively characterized and operationally interpreted. Recognition of this predictability enables more informed hazard characterization, improved responder safety planning, and more effective radiation-protection decision-making in subterranean response scenarios. This framework provides a foundation for extending geometry-informed radiation protection practices to a broader range of confined and built environments.

6.12 - Broader Scientific Contribution:

This investigation contributes to the broader scientific understanding of photon radiation transport in spatially confined built environments. While classical analytic formulations such as inverse-square attenuation provide a well-established foundation for describing geometric dose reduction in open conditions, the results of this study demonstrate that confinement introduces systematic and quantifiable deviations from idealized behavior. Through high-fidelity Monte Carlo transport modeling, this work provides a quantitative characterization of effective-dose attenuation trends in large-scale subterranean geometries and establishes a physically interpretable framework for evaluating confinement-modified radiation fields.

A principal contribution of this study is the controlled evaluation of photon attenuation behavior across representative tunnel configurations and structural materials. By comparing transport outcomes for multiple photon energies and material compositions, the research demonstrates how material density, interaction probability, and scattered-photon persistence collectively influence spatial dose behavior. These findings extend traditional attenuation concepts by showing that environmental boundary conditions modify not only local dose magnitude but also broader field-scale attenuation gradients and dose persistence.

The investigation further contributes methodological insight through comparison of effective-dose conversion approaches aligned with modern radiation-protection guidance. Application of ICRP 116 fluence-to-dose coefficients enabled evaluation of operationally relevant exposure quantities while maintaining rigorous transport-physics fidelity. This integration strengthens the connection between fundamental radiation-transport modeling and applied health-physics practice, supporting more meaningful interpretation of simulated dose fields in real-world response contexts.

Additionally, the study provides a structured framework for evaluating material influence within confined geometries under controlled conditions of source placement, geometry scale, and transport modeling. By isolating the coupled effects of geometry, material composition, and photon energy, the work establishes a reproducible approach for investigating radiation transport in complex infrastructure environments. Although focused on tunnel systems, these insights are broadly applicable to other confined radiation scenarios, including underground facilities, shielded industrial structures, and similar built environments where boundary interactions govern dose behavior.

Collectively, these contributions advance understanding of how environmental structure governs photon radiation transport and provide a foundation for future interdisciplinary research integrating radiation physics, infrastructure design, and operational exposure-risk assessment. This work demonstrates that confined radiation fields can be systematically characterized and predicted, providing a pathway toward more accurate and operationally relevant radiation-protection strategies in complex environments.

6.13 - Summary of Discussion:

The results of this investigation confirm that spatial confinement modifies photon effective-dose distributions relative to idealized free-field expectations. While inverse-square attenuation behavior was reproduced in sufficiently large air-filled tunnel geometries, systematic deviations were observed in material-filled configurations due to boundary scatter, geometric confinement, and non-line-of-sight photon transport processes. Collectively, these findings demonstrate that radiation fields in subterranean environments exhibit structured attenuation behavior governed by interacting physical mechanisms rather than geometric spreading alone.

Accurate characterization of confinement-modified radiation fields requires a rigorous transport-modeling approach. Key factors influencing predictive reliability include appropriate spatial mesh resolution, correct implementation of transport tallies, selection of suitable fluence-to-dose conversion coefficients, and validation of model performance against analytic reference behavior. When these methodological elements are properly implemented, Monte Carlo transport modeling provides a robust and defensible framework for predicting effective-dose behavior in complex underground infrastructure.

Overall, the analysis presented in this chapter demonstrates that confined environments introduce reproducible and operationally meaningful modifications to radiation transport behavior. Recognition of these effects enhances interpretation of spatial dose distributions and establishes a quantitative foundation for applying transport-based modeling to responder exposure assessment and radiation-protection decision-making in confined built environments.

Chapter 7 - Conclusion and Future Work:

7.1 - Summary of Research Objectives:

This research investigated photon radiation transport behavior in confined subterranean tunnel environments using hypothesis-driven Monte Carlo modeling and structured quantitative evaluation. The results demonstrate that environmental confinement systematically modifies effective-dose distributions relative to idealized free-field expectations through interacting geometric, material, and scattering processes. These findings confirm that spatial radiation-field behavior in complex underground infrastructure is governed not only by geometric distance from the source but also by boundary interactions and structural connectivity that influence photon persistence and redistribution.

The first hypothesis evaluated whether photon dose attenuation in sufficiently large tunnel geometries converges toward classical inverse-square behavior. Modeling results confirmed that air-filled reference configurations reproduced expected geometric attenuation trends, with log–log dose–distance slopes converging near −2 with low variability across configurations. However, confined tunnel conditions exhibited consistent attenuation-slope flattening, indicating that convergence toward free-field behavior occurs progressively with increasing distance and is influenced by tunnel scale and environmental boundary conditions. This result indicates that inverse-square assumptions may be conditionally applicable in large, minimally confined environments but require careful interpretation in structurally complex subterranean settings.

The second hypothesis examined the influence of tunnel wall composition on photon dose distributions. Comparative modeling across representative construction materials showed that density-dependent interaction probability and scattered-photon persistence measurably modify spatial dose magnitude and attenuation gradients. Integrated pathway analyses confirmed that material properties contribute to sustained effective-dose conditions relative to air baseline geometries, highlighting the importance of environmental composition in determining radiation-field behavior within confined infrastructure.

The third hypothesis evaluated whether confined geometries produce measurable non-line-of-sight dose persistence beyond direct line-of-sight regions. Results demonstrated reproducible non-line-of-sight effective-dose behavior associated with structural streaming pathways, including corridor intersections and connected passageways. Quantified enhancement ratios and non-line-of-sight dose fractions confirmed that geometric connectivity redistributes radiation in ways not predicted by simple shielding or distance-based assumptions. These findings establish that subterranean radiation fields exhibit spatially anisotropic behavior that must be considered in exposure assessment and hazard characterization.

Methodologically, this investigation demonstrates that high-fidelity Monte Carlo transport modeling provides a robust and defensible framework for evaluating radiation behavior in complex built environments when supported by appropriate mesh resolution, correct tally implementation, modern fluence-to-dose conversion methodology, and validation against analytic reference conditions. Agreement between independent tally approaches and consistent attenuation trends across multiple modeled configurations supports the reliability of the predictive framework developed in this work.

Overall, the results confirm that radiation transport in confined subterranean environments exhibits structured and reproducible spatial behavior that can be quantitatively characterized and operationally interpreted. By linking environmental geometry, material composition, and photon interaction processes to effective-dose outcomes, this research advances understanding of radiation-field behavior in complex infrastructure and provides a foundation for improved radiation-protection assessment and decision-making in underground response scenarios.

7.2 - Principal Scientific Findings and Integrated Interpretation:

7.2.1 Conditional Applicability of Inverse-Square Attenuation:

Modeling results demonstrated that photon effective-dose attenuation in air-filled tunnel geometries with centrally located point sources follows classical inverse-square behavior within engineering tolerance over short to intermediate distances. Agreement between Monte Carlo–derived dose rates and free-field gamma-constant calculations was typically within approximately 1–10% when appropriate spatial mesh refinement and modern dose-conversion methodology were applied.

However, systematic deviation from ideal inverse-square response was observed at larger distances in confined geometries. This behavior arises from finite boundary conditions and wall-induced scattered-photon persistence, indicating that inverse-square assumptions are conditionally valid rather than universally applicable in subterranean environments. The degree of conformity to free-field attenuation depends on the relationship between tunnel cross-sectional scale and photon interaction length. When tunnel dimensions are large relative to the dominant mean free path, geometric attenuation behavior is approximately recovered. As confinement increases, attenuation gradients become progressively modified by environmental structure. These findings reinforce that inverse-square–based estimation methods must be applied with consideration of geometric scale and confinement conditions in subterranean environments.

7.2.2 Influence of Structural Material Composition:

Tunnel wall composition influences spatial dose distributions through competing attenuation and scattering mechanisms. Higher-density structural materials increase photon interaction probability, resulting in both reduction of direct fluence and enhancement of scattered-photon contributions to the total effective dose. The net impact of material composition depends on source placement, tunnel scale, and photon energy spectrum.

Modeling results demonstrate that structural materials produce measurable and reproducible modification of effective-dose distributions relative to matched air configurations. Increased interaction probability within denser media alters both attenuation gradients and scattered-photon persistence, resulting in spatial dose behavior that deviates from idealized free-field expectations. Although the magnitude of this effect varies with geometry and source conditions, the underlying behavior remains consistent across modeled scenarios.

These findings indicate that environmental composition systematically influences radiation-field evolution in confined infrastructure and should be incorporated into operational exposure assessment and interpretation of field measurements. Accordingly, the results support the use of geometry- and material-informed radiation survey strategies in subterranean response environments. This behavior reinforces that material properties must be considered alongside geometry when interpreting dose behavior in confined radiation fields.

7.2.3 Scatter-Driven Redistribution and Non-Line-of-Sight Dose Persistence:

A key finding of this research is the reproducible presence of a measurable effective dose in regions without direct line-of-sight to the radiation source. Compton-scattered photons originating from tunnel boundaries contribute to dose in geometrically obstructed locations, demonstrating that confinement alters angular photon distributions and spatial transport pathways.

The magnitude of non-line-of-sight dose persistence depends on photon energy and material interaction characteristics but remains consistently observable across modeled configurations. These results demonstrate that simplified geometric shielding assumptions may underestimate exposure potential in confined environments and that radiation fields in subterranean infrastructure exhibit spatially anisotropic behavior governed by structural connectivity. In particular, reliance on line-of-sight assumptions alone may lead to systematic underestimation of exposure risk in confined environments.

7.2.4 Sensitivity of Volume-Averaged Tallies to Spatial Resolution:

This investigation demonstrated the importance of spatial discretization in accurately representing confinement-modified radiation fields. Large tetrahedral mesh elements in regions of steep dose gradients produced artificial smoothing and underestimation of localized peak effective dose. Progressive mesh refinement near the source reduced discrepancies between F4 volume fluence tallies and F5 point-detector estimates from approximately 20% in coarse configurations to below approximately 2% in refined models.

These findings highlight that appropriate mesh design is essential for reliable representation of spatial dose behavior in confined environments and that transport-model fidelity depends not only on physical modeling assumptions but also on numerical implementation choices. This sensitivity underscores the importance of resolution-aware modeling when using simulation results to inform operational decision-making in confined environments.

7.2.5 Model Validation Through Independent Tally Comparison:

Independent verification of transport-model performance was achieved through comparison of point-detector tallies with analytic dose predictions derived from gamma-constant formulations. When source definition, energy binning, geometry construction, and dose-conversion methodology were implemented consistently, F5 tallies demonstrated agreement with analytic expectations within approximately 1–10%.

This validation provides confidence that the modeling framework accurately represents photon transport behavior in both free-field and confined conditions and supports the defensibility of the predictive results presented in this research. This agreement confirms both the physical consistency and numerical reliability of the modeling framework.

7.2.6 Importance of Effective-Dose Conversion Methodology:

Selection of appropriate fluence-to-effective-dose conversion coefficients was found to exert a measurable influence on comparison outcomes between analytic reference predictions and modeled tunnel dose distributions. Application of geometry-appropriate ICRP 116 anteroposterior coefficients produced improved agreement relative to ISO-based conversion frameworks, indicating that dose-conversion methodology can introduce systematic bias comparable to or greater than differences arising from transport-model implementation.

This finding underscores the importance of aligning dosimetric interpretation approaches with the physical exposure scenario being evaluated. Adoption of modern external effective-dose conversion coefficients was therefore essential for ensuring that modeled radiation-field behavior remains both physically consistent and operationally interpretable. These results demonstrate that dosimetric interpretation is a critical component of accurate radiation-field assessment, not merely a post-processing step.

7.3 - Study Limitations and Future Research Needs:

Although this investigation provides quantitative insight into photon radiation transport behavior in confined subterranean environments, several modeling assumptions and scope constraints should be recognized when interpreting the results. The tunnel geometries evaluated in this study were intentionally idealized to isolate fundamental transport mechanisms associated with environmental confinement, structural material composition, and scattered-photon persistence. Real-world underground infrastructure may exhibit greater geometric irregularity, variable surface roughness, heterogeneous construction materials, ventilation-driven transport pathways, and the presence of operational clutter or shielding objects. These factors could further influence spatial radiation-field behavior, angular photon redistribution, and localized dose variability beyond that represented in the modeled configurations.

The source representations used in this work were limited to centrally located point-source scenarios selected to enable controlled hypothesis evaluation. While this approach supports clear interpretation of confinement-driven attenuation behavior, actual radiological incidents may involve distributed source terms, shielded sources, or complex energy spectra that evolve over time. Radionuclide representations, including simplified treatment of decay chains such as radium-226 progeny, were selected to support comparative transport analysis and may not fully capture all spectral and temporal complexities present in operational environments. Future investigations could expand upon the present modeling framework by incorporating alternative source geometries, time-dependent release conditions, and mixed radionuclide inventories.

Another limitation relates to the exclusive reliance on computational transport modeling. Although Monte Carlo methods provide high-fidelity representation of photon interaction physics, empirical field validation in representative underground settings would further strengthen confidence in predicted dose-field behavior. Controlled measurement campaigns in test tunnels or accessible subterranean facilities could support verification of non-line-of-sight dose persistence, assessment of scatter-driven enhancement mechanisms, and evaluation of detector-specific response characteristics under realistic operational conditions.

The spatial resolution requirements identified in this research also highlight opportunities for methodological advancement. While localized mesh refinement improved predictive accuracy near steep dose gradients, the computational cost associated with large-scale high-resolution transport modeling remains significant. Future work may explore hybrid modeling approaches, variance-reduction techniques, and machine-learning-assisted surrogate models to enable rapid estimation of confinement-modified radiation fields while maintaining acceptable accuracy for decision-support applications.

In addition, this study focused primarily on external effective-dose assessment using contemporary fluence-to-dose conversion coefficients. Further research could extend the present framework to evaluate additional operational exposure metrics, including organ-specific dose, cumulative exposure along responder movement pathways, and the influence of protective equipment, partial shielding, and detector geometry. Integration of transport modeling with human performance considerations and tactical movement constraints may also provide more comprehensive exposure-risk assessment tools.

A particularly promising research direction involves the integration of the structured radiation-field datasets generated in this study with statistical learning and artificial intelligence methodologies. These datasets provide a foundation for developing predictive models capable of estimating source characteristics and spatial dose distributions from limited measurement inputs. Future work should evaluate the robustness, generalizability, and operational applicability of physics-informed machine learning approaches across varying tunnel geometries, material compositions, and radionuclide spectra. Such approaches have the potential to reduce measurement density requirements while improving situational awareness during time-critical response scenarios.

Despite these limitations, the structured and reproducible transport behavior observed across modeled configurations demonstrates that confinement-modified radiation fields can be reliably characterized using rigorous computational methods. Continued investigation of radiation transport in complex built environments will support development of predictive frameworks that bridge fundamental radiation physics with applied health-physics decision making in underground response scenarios. This work establishes a foundation for future efforts to integrate physics-based modeling with operational decision-support tools for complex radiological response environments.

7.4 - Operational Implications:

The results of this investigation have direct relevance for radiation-protection planning and exposure assessment in subterranean response environments. Emergency response operations in underground infrastructure are often conducted under conditions of limited situational awareness, constrained mobility, and complex structural geometry. Traditional exposure-estimation approaches based on simple inverse-square attenuation may underestimate responder effective dose in confined environments. This study demonstrates that structural geometry and scatter-mediated transport can sustain dose levels beyond those predicted by free-field models, highlighting the need for geometry-informed survey strategies during underground response operations. Recognition of confinement-driven effects—including boundary scatter, structural connectivity, and photon transport persistence—is essential for improving operational radiation-protection decision-making in subterranean scenarios.

Inverse-square assumptions should therefore be applied cautiously when interpreting radiation measurements in confined infrastructure. While simplified geometric models may provide reasonable first-order estimates in large air-filled tunnel geometries, increasing confinement and structural complexity can sustain effective-dose levels at distances where free-field behavior would predict more rapid attenuation. Incorporating confinement-aware interpretation strategies into responder training and survey protocols may improve hazard characterization and reduce the potential for underestimation of exposure risk.

The presence of measurable non-line-of-sight dose persistence has important implications for tactical movement and hazard zoning. Structural features such as intersecting corridors, ventilation shafts, and changes in tunnel cross-section can facilitate photon streaming pathways that redistribute radiation into geometrically obstructed regions. As a result, visually shielded locations cannot be assumed to represent areas of negligible exposure potential. Survey strategies that prioritize measurements near structural transition zones and along anticipated responder travel routes may improve spatial characterization of radiation fields and support more effective exposure-control measures.

Material-dependent transport behavior further indicates that environmental composition influences the spatial distribution and persistence of radiation dose. In confined spaces with dense structural materials, increased scattered-photon contributions may alter attenuation gradients and sustain localized dose conditions relative to air-filled environments. Awareness of these material effects may assist responders and radiation-protection personnel in interpreting field measurements and selecting monitoring approaches appropriate to the infrastructure being assessed.

From a methodological perspective, these findings demonstrate that transport-based modeling provides valuable decision-support capability for radiological response planning in complex underground settings. When implemented with appropriate spatial resolution, validated source definitions, and modern fluence-to-dose conversion methodology, Monte Carlo modeling enables quantitative prediction of effective-dose behavior under conditions that are difficult to represent using simplified analytic approaches. Integration of such modeling tools into pre-incident planning, training exercises, and scenario analysis may enhance preparedness for radiological events in confined infrastructure.

Ultimately, this research reinforces the importance of applying the as-low-as-reasonably-achievable principle in a manner that accounts for environmental structure and transport physics. By improving understanding of confinement-modified radiation behavior, these results support more informed survey strategies, responder route planning, and hazard-zone establishment. Collectively, these contributions strengthen the scientific basis for operational radiation-protection practice in subterranean environments and provide a framework for translating advanced transport-modeling insights into practical exposure-management decision-making. This work provides a foundation for extending geometry-informed radiation protection practices to a wide range of confined and structurally complex environments.

7.5 - Final Conclusions:

This research demonstrates that confined subterranean geometries systematically modify photon effective-dose distributions in ways that cannot be reliably approximated using free-field inverse-square assumptions alone. While geometric attenuation remains the dominant governing principle at sufficiently large distances, boundary interactions, material-dependent scattering processes, and structural photon streaming introduce quantifiable and reproducible deviations that are operationally significant. The magnitude and spatial persistence of these effects depend on photon energy spectrum, tunnel scale, and transport-model implementation, highlighting the necessity of geometry-aware radiation assessment in confined environments.

These findings provide quantitative confirmation and extension of earlier confined-geometry radiation transport observations reported in small-scale tunnel studies, demonstrating that similar scatter-mediated persistence and structural streaming behavior occur in infrastructure-scale subterranean environments. Through structured hypothesis evaluation, comparison with analytic dose-rate constants, and controlled assessment of mesh resolution and dosimetric methodology, this investigation establishes a defensible computational framework for evaluating effective dose in complex photon transport scenarios. The results clarify the conditions under which simplified analytic approaches may provide reasonable exposure estimates and identify situations in which transport-based modeling is required to avoid systematic bias in dose interpretation.

As subterranean infrastructure continues to expand across transportation, defense, and urban development applications, radiological response planning must account for the influence of environmental structure on radiation-field behavior. By quantitatively linking geometric confinement, material composition, and scattered-photon transport mechanisms to operational dose outcomes, this research advances understanding of radiation behavior in shielded built environments and supports development of improved decision-support methodologies for responder exposure assessment. Incorporation of confinement-aware dose assessment approaches into responder training, hazard zoning, and measurement strategy development can improve exposure control and situational awareness during radiological incidents in complex built environments.

Future extension of this work toward dynamic source conditions, mixed radionuclide inventories, and predictive modeling tools offers a pathway toward enhanced situational awareness and risk-informed planning for radiological incidents in confined infrastructure.

Collectively, these findings establish that geometry-aware radiation transport modeling is not simply advantageous but necessary for accurate dose assessment in confined subterranean environments, representing a substantive advancement beyond traditional free-field approximation methods used in operational radiation protection.

WORKS CITED

ALMisned, G., Zakaly, H. M. H., Ali, F. T., Issa, S. A. M., Ene, A., Kilic, G., Ivanov, V., & Tekin, H. O. (2022). A closer look at the efficiency calibration of LaBr3(Ce) and NaI(Tl) scintillation detectors using MCNPX for various types of nuclear investigations. *Heliyon*, *8*(10). https://doi.org/10.1016/j.heliyon.2022.e10839

Ansys. (2024, April). *Ansys SpaceClaim 3D Modeling Software*. https://www.ansys.com/products/3d-design/ansys-spaceclaim

Bang, J. Y., Hough, M., Hawes, R. H., & Varadarajulu, S. (2020). Use of Artificial Intelligence to Reduce Radiation Exposure at Fluoroscopy-Guided Endoscopic Procedures. *Official Journal of the American College of Gastroenterology | ACG*, *115*(4). https://journals.lww.com/ajg/fulltext/2020/04000/use_of_artificial_intelligence_to_reduce_radiation.14.aspx

Bland, J., Potter, C. "Gus," & Homann, S. (2018). *Radiological Exposure Devices (RED) Technical Basis for Threat Profile*. https://classic.ntis.gov/help/order-methods/

Burr, W., & Kornbluh, P. (2022, September 22). The Moscow Signals Declassified: Irradiating Richard Nixon. *NationalSecurityArchive*. https://nsarchive.gwu.edu/briefing-book/intelligence-nuclear-vault-russia-programs/2022-09-22/moscow-signals-declassified#:~:text=Washington%20D.C.%20September%2022%2C%202022,first%20days%20of%20his%20trip.

Calibration of Survey Instruments, Pub. L. 35.61 (2017). https://www.nrc.gov/reading-rm/doc-collections/cfr/part035/part035-0061.html

Chao, N. J. (2007). Accidental or intentional exposure to ionizing radiation: Biodosimetry and treatment options. *Experimental Hematology*, *35*(4 SUPPL.), 24–27. https://doi.org/10.1016/j.exphem.2007.01.008

Colorado Department of Transportation. (2023, March 8). *More than 434 million vehicles have traveled through the I-70 Eisenhower-Johnson Memorial Tunnel since it opened 50 years ago*. Https://Www.Codot.Gov/News/2023/March/I70-Eisenhower-Tunnel-50-Years-Event.

Friedrich, S., Süss, U., & Gustmann, M. (2024). KHG: The German Emergency Response Organization for Nuclear Accidents. *Journal of Robotics and Mechatronics*, *36*(1), 134–138. https://doi.org/10.20965/jrm.2024.p0134

Gollnick, D. A. (2018). *Basic Radiation Protection Technology* (6th ed.).

International Atomic Energy Agency. (2006). *IAEA Safety Reports Series No. 47 – Radiation Protection and Shielding in Accelerator Facilities*.

International Commission on Radiological Protection. (1983). ICRP 38 Radionuclide Transformations Energy and Intensity of Emissions. *International Commission on Radiological Protection*, *11–13*.

International Commission on Radiological Protection. (2010). *ICRP Publication 116: Conversion Coefficients for Radiological Protection Quantities for External Radiation Exposures*.

International Commission on Radiation Units and Measurements. (1998). ICRU Report 57, Conversion Coefficients for use in Radiological Protection against External Radiation. *International Commission on Radiation Units and Measurements*.

International Atomic Energy Agency. (2006). *Dangerous quantities of radioactive material (D-values)*. http://www-ns.iaea.org/standards/

International Atomic Energy Agency. (2024). *Incidents of nuclear and other radioactive material out of regulatory control*. https://www.iaea.org/sites/default/files/24/05/itdb_factsheet_2024.pdf

Johnson, T. E. (2017). *Introduction to Health Physics* (5th ed.). McGrall Hill Education.
Johnson, T. E., & Birky, B. K. (2012). *Health Physics and Radiological Health Handbook* (Fourth). Lippincott Williams & Wilkins.
Knoll, G. F. (2010). *Radiation Detection and Measurement* (4th ed.). Wiley.
Los Alamos National Laboratory. (2024, February 21). *The MCNP Code.* https://mcnp.lanl.gov/index.html
Merriam-Webster. (2024, July 1). *Tunnel.* https://www.merriam-webster.com/dictionary/tunnel
Montan Universitat - Leoben. (n.d.). *Zentrum am Burg: The Facility*. Retrieved September 9, 2024, from https://www.zab.at/en/ueber-uns/die-anlage#:~:text=The%20test%20and%20research%20facility,underground%20testing%20and%20training%20areas.
Norman Coleman, C., Bader, J. L., Koerner, J. F., Hrdina, C., Cliffer, K. D., Hick, J. L., James, J. J., Mansoura, M. K., Livinski, A. A., Nystrom, S. V., Dicarlo-Cohen, A., Marinissen, M. J., Wathen, L., Appler, J. M., Buddemeier, B., Casagrande, R., Estes, D., Byrne, P., Kennedy, E. M., … Hatchett, R. (2019). Chemical, Biological, Radiological, Nuclear, and Explosive (CBRNE) Science and the CBRNE Science Medical Operations Science Support Expert (CMOSSE). *Disaster Medicine and Public Health Preparedness*, *13*(5–6), 995–1010. https://doi.org/10.1017/dmp.2018.163
Parker, A. R., (2022). *Characteristics Of Gamma Radiation Fields In Subterranean Structures For Radiation Protection And Decision-Making.*
Petersen, L., Havârneanu, G. M., Arnold, A., Carbon, D., Görgen, T., Gavel, A., Kroupa, T., & Kardel, D. (2023). Applicability of PROACTIVE recommendations on CBRNe risks and threats to passenger rail and metro sectors. *Journal of Transportation Security*, *16*(1). https://doi.org/10.1007/s12198-023-00263-3
Sen, S., Chandra, A., Pramanik, D., & Sarkar, Ms. (2013). *Study of Intrinsic Photo peak Efficiency of NaI(Tl) Detectors at 662 KeV*. www.sympnp.org/proceedings
Silver Fir. (n.d.). *Attila4MC*. Retrieved September 17, 2024, from https://www.silverfirsoftware.com/Pages/Products/Attila4MC.php
Turner, J. E. (2010). *Atoms, Radiation, and Radiation Protection*.
University of Maryland. (2024, July 5). *Global Terrorism Database.* https://www.start.umd.edu/gtd/search/Results.aspx?chart=casualties&search=tunnel
US Environmental Protection Agency. (2024, July 5). *Transportation of Radioactive Material*. https://www.epa.gov/radtown/transportation-radioactive-material#:~:text=Radioactive%20material%20can%20be%20transported,if%20there%20is%20an%20accident.
US Nuclear Regulatory Commission. (2023, May 6). *Materials Transportation*. https://www.nrc.gov/materials/transportation.html
Werner, C. J. (2017). *MCNP6 users guide.*
Zavala, M. (2016). *Autonomous Detection and Characterization of Nuclear Materials Using Co-Robot* [Georgia Institute of Technology]. https://repository.gatech.edu/server/api/core/bitstreams/613d6a70-16bb-4965-a4fd-5ef892b7a8aa/content

Appendix A Excerpt from Table A.1 ICRP Publication 116

This is applied to the F4 and F5 MCNP tallies to determine the effective dose per fluence in units of Sv cm^2 for monoenergetic particles incident on the Anterior-Posterior (AP) geometry.

Energy Bin (embde4) in MeV	Effective dose per Fluence (embdf4) in Sv cm^2
0.01	0
0.015	6.85E-14
0.02	1.56E-13
0.03	2.25E-13
0.04	3.13E-13
0.05	3.51E-13
0.06	3.70E-13
0.07	3.90E-13
0.08	4.13E-13
0.1	4.44E-13
0.15	5.19E-13
0.2	7.48E-13
0.3	1.00E-12
0.4	1.51E-12
0.5	2.00E-12
0.511	2.47E-12
0.6	2.52E-12
0.662	2.91E-12
0.8	3.17E-12
1	3.73E-12
1.117	4.49E-12
1.33	4.90E-12
1.5	5.59E-12
2	6.12E-12
3	7.48E-12
4	9.75E-12
5	1.17E-11
6	1.34E-11
6.129	1.50E-11
8	1.51E-11
10	1.78E-11
15	2.05E-11
20	2.61E-11
30	3.08E-11
40	3.79E-11
50	4.31E-11

Appendix B MCNP Input Code

```
run9xc
c
c Attila calculation "Run9xc"
c Run7xc rerun with new mesh around point
c added ICRP 116 AP in F4 tally
c concrete for mountain
c add F5 tally manually
c Road tunnel 55 geometry with 3113k cells
c 1E7 histories point 3 (x) centered in the pedestrian tunnel of the road tunnel
c -------------------------- Input Information ------------------------------ 80
c Attila GUI created MCNP6 Input
c Attila Version (not available)
c Input File Creation Date: Tue Jan 6 12:24:57 2026
c RxMesher version          : 1.0.0
c Simmetrix MeshSim version : 14.0-200321
c Global mesh size          : 5 m
c Generated                 : 2026-01-05T19:01:47-07:00
c Solid Geometry :
c   Filename     : Road Tunnel 50.x_t
c   Last changed : 2025-09-21T14:02:51-07:00
c   MD5 checksum : dbde909fe7be1afef164890b9898c1c1
c Note: RTT Mesh has added cell flags for MCNP Abaqus part and pseudo-cell.
c Associated Abaqus Unstructured Mesh :
c   Filename     : road_tunnel_55.mesh.abaq
c   Generated    : 2026-01-06T12:24:57
c   MD5 checksum : 499875a57daef01384fbec73a3f37906
c n_points = 569407
c n_sides  = 178828
c n_cells  = 3113097
c Mesh Bounding Box (cm):
c  x: 8007.732 - 17691.969
c  y: -9013.606 - -1441.325
c  z: -1855.985 - 1330.657
c
c Number of Attila Regions                : 19
c Number of Abaqus Parts/MCNP Pseudo-Cells : 30
c Number of Materials                     : 2
c
c  Mesh Region/Pseudo-Cell Information
c   Attila Region #    : 1
c   Attila Region Name : "Tunnel_A5"
c   Abaqus Part #      : 1
c   Abaqus Part Name   : "Tunnel_A5"
c   MCNP Pseudo-cell # : 1
c   Material           : "Air-(Dry,-Near-Sea-Level)_1"
```

```
c    MCNP Material     : m1
c    Density           : 4.988e-05 atoms/b-cm
c   Mesh Data
c     Meshed Volume    : 2.54254e+09 cm**3
c     # Cells          : 13857
c     % of Total Cells : 0.45%
c
c   Attila Region #    : 2
c   Attila Region Name : "Mountain"
c   Abaqus Part #      : 2
c   Abaqus Part Name   : "Mountain_sub1"
c   MCNP Pseudo-cell # : 2
c   Material           : "Concrete,-Los-Alamos-(MCNP)_2"
c    MCNP Material     : m2
c    Density           : 0.07186 atoms/b-cm
c   Mesh Data
c     Meshed Volume    : 1.81527e+11 cm**3
c     # Cells          : 152055
c     % of Total Cells : 4.88%
c
c   Attila Region #    : 2
c   Attila Region Name : "Mountain"
c   Abaqus Part #      : 3
c   Abaqus Part Name   : "Mountain_sub2"
c   MCNP Pseudo-cell # : 3
c   Material           : "Concrete,-Los-Alamos-(MCNP)_2"
c    MCNP Material     : m2
c    Density           : 0.07186 atoms/b-cm
c   Mesh Data
c     Meshed Volume    : 3.99372e+10 cm**3
c     # Cells          : 147114
c     % of Total Cells : 4.73%
c
c   Attila Region #    : 3
c   Attila Region Name : "Pedestrian_Tunnel_a"
c   Abaqus Part #      : 4
c   Abaqus Part Name   : "Pedestrian_Tunnel_a"
c   MCNP Pseudo-cell # : 4
c   Material           : "Air-(Dry,-Near-Sea-Level)_1"
c    MCNP Material     : m1
c    Density           : 4.988e-05 atoms/b-cm
c   Mesh Data
c     Meshed Volume    : 6.1786e+07 cm**3
c     # Cells          : 49459
c     % of Total Cells : 1.59%
c
c   Attila Region #    : 4
c   Attila Region Name : "Pedestrian_Tunnel_d"
```

```
c  Abaqus Part #      : 5
c  Abaqus Part Name   : "Pedestrian_Tunnel_d"
c  MCNP Pseudo-cell # : 5
c  Material           : "Air-(Dry,-Near-Sea-Level)_1"
c   MCNP Material     : m1
c   Density           : 4.988e-05 atoms/b-cm
c  Mesh Data
c    Meshed Volume    : 7.51224e+07 cm**3
c    # Cells          : 2413
c    % of Total Cells : 0.08%
c
c  Attila Region #    : 5
c  Attila Region Name : "Pedestrian_Tunnel_b"
c  Abaqus Part #      : 6
c  Abaqus Part Name   : "Pedestrian_Tunnel_b_sub1"
c  MCNP Pseudo-cell # : 6
c  Material           : "Air-(Dry,-Near-Sea-Level)_1"
c   MCNP Material     : m1
c   Density           : 4.988e-05 atoms/b-cm
c  Mesh Data
c    Meshed Volume    : 6.35125e+06 cm**3
c    # Cells          : 221081
c    % of Total Cells : 7.10%
c
c  Attila Region #    : 5
c  Attila Region Name : "Pedestrian_Tunnel_b"
c  Abaqus Part #      : 7
c  Abaqus Part Name   : "Pedestrian_Tunnel_b_sub2"
c  MCNP Pseudo-cell # : 7
c  Material           : "Air-(Dry,-Near-Sea-Level)_1"
c   MCNP Material     : m1
c   Density           : 4.988e-05 atoms/b-cm
c  Mesh Data
c    Meshed Volume    : 6.31639e+06 cm**3
c    # Cells          : 221096
c    % of Total Cells : 7.10%
c
c  Attila Region #    : 5
c  Attila Region Name : "Pedestrian_Tunnel_b"
c  Abaqus Part #      : 8
c  Abaqus Part Name   : "Pedestrian_Tunnel_b_sub3"
c  MCNP Pseudo-cell # : 8
c  Material           : "Air-(Dry,-Near-Sea-Level)_1"
c   MCNP Material     : m1
c   Density           : 4.988e-05 atoms/b-cm
c  Mesh Data
c    Meshed Volume    : 6.38886e+06 cm**3
c    # Cells          : 221067
```

```
c    % of Total Cells : 7.10%
c
c  Attila Region #    : 5
c  Attila Region Name : "Pedestrian_Tunnel_b"
c  Abaqus Part #      : 9
c  Abaqus Part Name   : "Pedestrian_Tunnel_b_sub4"
c  MCNP Pseudo-cell # : 9
c  Material           : "Air-(Dry,-Near-Sea-Level)_1"
c   MCNP Material     : m1
c   Density           : 4.988e-05 atoms/b-cm
c  Mesh Data
c    Meshed Volume    : 6.32098e+06 cm**3
c    # Cells          : 221099
c    % of Total Cells : 7.10%
c
c  Attila Region #    : 5
c  Attila Region Name : "Pedestrian_Tunnel_b"
c  Abaqus Part #      : 10
c  Abaqus Part Name   : "Pedestrian_Tunnel_b_sub5"
c  MCNP Pseudo-cell # : 10
c  Material           : "Air-(Dry,-Near-Sea-Level)_1"
c   MCNP Material     : m1
c   Density           : 4.988e-05 atoms/b-cm
c  Mesh Data
c    Meshed Volume    : 6.31817e+06 cm**3
c    # Cells          : 220960
c    % of Total Cells : 7.10%
c
c  Attila Region #    : 6
c  Attila Region Name : "Pedestrian_Tunnel_c"
c  Abaqus Part #      : 11
c  Abaqus Part Name   : "Pedestrian_Tunnel_c"
c  MCNP Pseudo-cell # : 11
c  Material           : "Air-(Dry,-Near-Sea-Level)_1"
c   MCNP Material     : m1
c   Density           : 4.988e-05 atoms/b-cm
c  Mesh Data
c    Meshed Volume    : 3.82518e+07 cm**3
c    # Cells          : 50506
c    % of Total Cells : 1.62%
c
c  Attila Region #    : 7
c  Attila Region Name : "Tunnel_A4"
c  Abaqus Part #      : 12
c  Abaqus Part Name   : "Tunnel_A4"
c  MCNP Pseudo-cell # : 12
c  Material           : "Air-(Dry,-Near-Sea-Level)_1"
c   MCNP Material     : m1
```

```
c   Density          : 4.988e-05 atoms/b-cm
c  Mesh Data
c    Meshed Volume    : 5.12969e+08 cm**3
c    # Cells          : 3878
c    % of Total Cells : 0.12%
c
c  Attila Region #    : 8
c  Attila Region Name : "Tunnel_A3"
c  Abaqus Part #      : 13
c  Abaqus Part Name   : "Tunnel_A3"
c  MCNP Pseudo-cell # : 13
c  Material           : "Air-(Dry,-Near-Sea-Level)_1"
c   MCNP Material     : m1
c   Density          : 4.988e-05 atoms/b-cm
c  Mesh Data
c    Meshed Volume    : 5.29723e+08 cm**3
c    # Cells          : 4896
c    % of Total Cells : 0.16%
c
c  Attila Region #    : 9
c  Attila Region Name : "Tunnel_A2"
c  Abaqus Part #      : 14
c  Abaqus Part Name   : "Tunnel_A2"
c  MCNP Pseudo-cell # : 14
c  Material           : "Air-(Dry,-Near-Sea-Level)_1"
c   MCNP Material     : m1
c   Density          : 4.988e-05 atoms/b-cm
c  Mesh Data
c    Meshed Volume    : 5.08604e+08 cm**3
c    # Cells          : 3400
c    % of Total Cells : 0.11%
c
c  Attila Region #    : 10
c  Attila Region Name : "Tunnel_A1"
c  Abaqus Part #      : 15
c  Abaqus Part Name   : "Tunnel_A1"
c  MCNP Pseudo-cell # : 15
c  Material           : "Air-(Dry,-Near-Sea-Level)_1"
c   MCNP Material     : m1
c   Density          : 4.988e-05 atoms/b-cm
c  Mesh Data
c    Meshed Volume    : 1.52562e+09 cm**3
c    # Cells          : 8657
c    % of Total Cells : 0.28%
c
c  Attila Region #    : 11
c  Attila Region Name : "Tunnel_A52"
c  Abaqus Part #      : 16
```

```
c  Abaqus Part Name   : "Tunnel_A52"
c  MCNP Pseudo-cell # : 16
c  Material           : "Air-(Dry,-Near-Sea-Level)_1"
c   MCNP Material     : m1
c   Density           : 4.988e-05 atoms/b-cm
c  Mesh Data
c    Meshed Volume    : 5.08526e+08 cm**3
c    # Cells          : 3302
c    % of Total Cells : 0.11%
c
c  Attila Region #    : 12
c  Attila Region Name : "Tunnel_B1"
c  Abaqus Part #      : 17
c  Abaqus Part Name   : "Tunnel_B1"
c  MCNP Pseudo-cell # : 17
c  Material           : "Air-(Dry,-Near-Sea-Level)_1"
c   MCNP Material     : m1
c   Density           : 4.988e-05 atoms/b-cm
c  Mesh Data
c    Meshed Volume    : 8.36004e+08 cm**3
c    # Cells          : 2158
c    % of Total Cells : 0.07%
c
c  Attila Region #    : 13
c  Attila Region Name : "Tunnel_B2"
c  Abaqus Part #      : 18
c  Abaqus Part Name   : "Tunnel_B2"
c  MCNP Pseudo-cell # : 18
c  Material           : "Air-(Dry,-Near-Sea-Level)_1"
c   MCNP Material     : m1
c   Density           : 4.988e-05 atoms/b-cm
c  Mesh Data
c    Meshed Volume    : 8.18194e+08 cm**3
c    # Cells          : 2060
c    % of Total Cells : 0.07%
c
c  Attila Region #    : 14
c  Attila Region Name : "Tunnel_B3"
c  Abaqus Part #      : 19
c  Abaqus Part Name   : "Tunnel_B3"
c  MCNP Pseudo-cell # : 19
c  Material           : "Air-(Dry,-Near-Sea-Level)_1"
c   MCNP Material     : m1
c   Density           : 4.988e-05 atoms/b-cm
c  Mesh Data
c    Meshed Volume    : 8.28163e+08 cm**3
c    # Cells          : 4148
c    % of Total Cells : 0.13%
```

```
c
c   Attila Region #    : 15
c   Attila Region Name : "Tunnel_B4"
c   Abaqus Part #      : 20
c   Abaqus Part Name   : "Tunnel_B4"
c   MCNP Pseudo-cell # : 20
c   Material           : "Air-(Dry,-Near-Sea-Level)_1"
c    MCNP Material     : m1
c    Density           : 4.988e-05 atoms/b-cm
c   Mesh Data
c     Meshed Volume    : 8.23439e+08 cm**3
c     # Cells          : 2090
c     % of Total Cells : 0.07%
c
c   Attila Region #    : 16
c   Attila Region Name : "Tunnel_B5"
c   Abaqus Part #      : 21
c   Abaqus Part Name   : "Tunnel_B5"
c   MCNP Pseudo-cell # : 21
c   Material           : "Air-(Dry,-Near-Sea-Level)_1"
c    MCNP Material     : m1
c    Density           : 4.988e-05 atoms/b-cm
c   Mesh Data
c     Meshed Volume    : 8.0928e+08 cm**3
c     # Cells          : 1822
c     % of Total Cells : 0.06%
c
c   Attila Region #    : 17
c   Attila Region Name : "Tunnel_B6"
c   Abaqus Part #      : 22
c   Abaqus Part Name   : "Tunnel_B6"
c   MCNP Pseudo-cell # : 22
c   Material           : "Air-(Dry,-Near-Sea-Level)_1"
c    MCNP Material     : m1
c    Density           : 4.988e-05 atoms/b-cm
c   Mesh Data
c     Meshed Volume    : 1.67694e+09 cm**3
c     # Cells          : 3956
c     % of Total Cells : 0.13%
c
c   Attila Region #    : 18
c   Attila Region Name : "Pedestrian_Tunnel_c1"
c   Abaqus Part #      : 23
c   Abaqus Part Name   : "Pedestrian_Tunnel_c1"
c   MCNP Pseudo-cell # : 23
c   Material           : "Air-(Dry,-Near-Sea-Level)_1"
c    MCNP Material     : m1
c    Density           : 4.988e-05 atoms/b-cm
```

```
c   Mesh Data
c     Meshed Volume    : 4.72747e+07 cm**3
c     # Cells          : 1450
c     % of Total Cells : 0.05%
c
c   Attila Region #    : 19
c   Attila Region Name : "Pedestrian_Tunnel_b1"
c   Abaqus Part #      : 24
c   Abaqus Part Name   : "Pedestrian_Tunnel_b1_sub1"
c   MCNP Pseudo-cell # : 24
c   Material           : "Air-(Dry,-Near-Sea-Level)_1"
c    MCNP Material     : m1
c    Density           : 4.988e-05 atoms/b-cm
c   Mesh Data
c     Meshed Volume    : 6.41161e+06 cm**3
c     # Cells          : 221556
c     % of Total Cells : 7.12%
c
c   Attila Region #    : 19
c   Attila Region Name : "Pedestrian_Tunnel_b1"
c   Abaqus Part #      : 25
c   Abaqus Part Name   : "Pedestrian_Tunnel_b1_sub2"
c   MCNP Pseudo-cell # : 25
c   Material           : "Air-(Dry,-Near-Sea-Level)_1"
c    MCNP Material     : m1
c    Density           : 4.988e-05 atoms/b-cm
c   Mesh Data
c     Meshed Volume    : 6.34579e+06 cm**3
c     # Cells          : 221556
c     % of Total Cells : 7.12%
c
c   Attila Region #    : 19
c   Attila Region Name : "Pedestrian_Tunnel_b1"
c   Abaqus Part #      : 26
c   Abaqus Part Name   : "Pedestrian_Tunnel_b1_sub3"
c   MCNP Pseudo-cell # : 26
c   Material           : "Air-(Dry,-Near-Sea-Level)_1"
c    MCNP Material     : m1
c    Density           : 4.988e-05 atoms/b-cm
c   Mesh Data
c     Meshed Volume    : 6.35786e+06 cm**3
c     # Cells          : 221526
c     % of Total Cells : 7.12%
c
c   Attila Region #    : 19
c   Attila Region Name : "Pedestrian_Tunnel_b1"
c   Abaqus Part #      : 27
c   Abaqus Part Name   : "Pedestrian_Tunnel_b1_sub4"
```

```
c  MCNP Pseudo-cell # : 27
c  Material          : "Air-(Dry,-Near-Sea-Level)_1"
c   MCNP Material     : m1
c   Density           : 4.988e-05 atoms/b-cm
c  Mesh Data
c    Meshed Volume    : 6.34373e+06 cm**3
c    # Cells          : 221540
c    % of Total Cells : 7.12%
c
c  Attila Region #    : 19
c  Attila Region Name : "Pedestrian_Tunnel_b1"
c  Abaqus Part #      : 28
c  Abaqus Part Name   : "Pedestrian_Tunnel_b1_sub5"
c  MCNP Pseudo-cell # : 28
c  Material          : "Air-(Dry,-Near-Sea-Level)_1"
c   MCNP Material     : m1
c   Density           : 4.988e-05 atoms/b-cm
c  Mesh Data
c    Meshed Volume    : 6.3303e+06 cm**3
c    # Cells          : 221514
c    % of Total Cells : 7.12%
c
c  Attila Region #    : 19
c  Attila Region Name : "Pedestrian_Tunnel_b1"
c  Abaqus Part #      : 29
c  Abaqus Part Name   : "Pedestrian_Tunnel_b1_sub6"
c  MCNP Pseudo-cell # : 29
c  Material          : "Air-(Dry,-Near-Sea-Level)_1"
c   MCNP Material     : m1
c   Density           : 4.988e-05 atoms/b-cm
c  Mesh Data
c    Meshed Volume    : 6.23194e+06 cm**3
c    # Cells          : 221514
c    % of Total Cells : 7.12%
c
c  Attila Region #    : 19
c  Attila Region Name : "Pedestrian_Tunnel_b1"
c  Abaqus Part #      : 30
c  Abaqus Part Name   : "Pedestrian_Tunnel_b1_sub7"
c  MCNP Pseudo-cell # : 30
c  Material          : "Air-(Dry,-Near-Sea-Level)_1"
c   MCNP Material     : m1
c   Density           : 4.988e-05 atoms/b-cm
c  Mesh Data
c    Meshed Volume    : 6.27113e+06 cm**3
c    # Cells          : 221367
c    % of Total Cells : 7.11%
c
```

```
c ------------------------ End Input Information ---------------------------- 80
c
c ----------------------------- Cell Cards --------------------------------- 80
1    1    4.988e-05    0                  u=1
2    2    0.07186      0                  u=1
3    2    0.07186      0                  u=1
4    1    4.988e-05    0                  u=1
5    1    4.988e-05    0                  u=1
6    1    4.988e-05    0                  u=1
7    1    4.988e-05    0                  u=1
8    1    4.988e-05    0                  u=1
9    1    4.988e-05    0                  u=1
10   1    4.988e-05    0                  u=1
11   1    4.988e-05    0                  u=1
12   1    4.988e-05    0                  u=1
13   1    4.988e-05    0                  u=1
14   1    4.988e-05    0                  u=1
15   1    4.988e-05    0                  u=1
16   1    4.988e-05    0                  u=1
17   1    4.988e-05    0                  u=1
18   1    4.988e-05    0                  u=1
19   1    4.988e-05    0                  u=1
20   1    4.988e-05    0                  u=1
21   1    4.988e-05    0                  u=1
22   1    4.988e-05    0                  u=1
23   1    4.988e-05    0                  u=1
24   1    4.988e-05    0                  u=1
25   1    4.988e-05    0                  u=1
26   1    4.988e-05    0                  u=1
27   1    4.988e-05    0                  u=1
28   1    4.988e-05    0                  u=1
29   1    4.988e-05    0                  u=1
30   1    4.988e-05    0                  u=1
31   0              0                     u=1 $ background
32   0              100 -101 102 -103 104 -105   fill=1 $ fill cell
33   0              (-100:101:-102:103:-104:105)
c --------------------------- End Cell Cards ------------------------------- 80

c ---------------------------- Surface Cards ------------------------------- 80
c
100 px 8002.73
101 px 17697
102 py -9018.61
103 py -1436.33
104 pz -1860.99
105 pz 1335.66
c ------------------------- End Surface Cards ----------------------------- 80
```

```
c ----------------------------- Data Cards ---------------------------------- 80
c Embedded Geometry Specification
embed1 meshgeo=abaqus mgeoin=road_tunnel_55.mesh.abaq
      meeout=run9xc.mcnp.eeout
      filetype=ascii
      background=31
      matcell= 1 1 2 2 3 3 4 4 5 5 6 6 7 7 8 8 9 9 10 10 11 11 12 12 13 13 &
      14 14 15 15 16 16 17 17 18 18 19 19 20 20 21 21 22 22 23 23 24 24 25 &
      25 26 26 27 27 28 28 29 29 30 30
c
c Materials
c
c  Material 1: "Air-(Dry,-Near-Sea-Level)_1"
c  Constituents (atom %):
c c12-6012 (0.00014841) c13-6013 (1.59e-06) n14-7014 (0.784431)
c o16-8016 (0.210748) ar36-18036 (1.55825e-05) ar38-18038 (2.93806e-06)
c ar40-18040 (0.00465248)
m1  6012 0.00014841 6013 1.59e-06 7014 0.784431 8016 0.210748 18036 &
1.55825e-05 18038 2.93806e-06 18040 0.00465248
c
c  Material 2: "Concrete,-Los-Alamos-(MCNP)_2"
c  Constituents (atom %):
c h1-1001 (0.084739) o16-8016 (0.604079) na23-11023 (0.012523)
c al27-13027 (0.024842) si28-14028 (0.223183) si29-14029 (0.0113025)
c si30-14030 (0.00743544) ca40-20040 (0.0264106) ca42-20042 (0.000176269)
c ca43-20043 (3.67794e-05) ca44-20044 (0.00056831) ca46-20046 (1.08976e-06)
c ca48-20048 (5.09463e-05) fe54-26054 (0.000271909) fe56-26056 (0.0042684)
c fe57-26057 (9.85759e-05) fe58-26058 (1.31186e-05)
m2  1001 0.084739 8016 0.604079 11023 0.012523 13027 0.024842 14028 &
0.223183 14029 0.0113025 14030 0.00743544 20040 0.0264106 20042 &
0.000176269 20043 3.67794e-05 20044 0.00056831 20046 1.08976e-06 20048 &
5.09463e-05 26054 0.000271909 26056 0.0042684 26057 9.85759e-05 26058 &
1.31186e-05
c
c Mode (Only n and/or p Currently Accepted)
mode p
c
c Cell Importances
imp:p 1 1 1 1 1 1 1 1 1 1 1 1 1 1 1 1 1 1 1 1 1 1 1 1 1 1 1 1 1 1 0
c
c Source Definition
sdef pos=13900 -5450 -400 erg=d1 par=p wgt=2
c      Spectrum "Co60"
si1 L  1.17 1.33
sp1 d  1    1
c
c Histories (or Computer Time Cutoff)
nps 1E7
```

```
c ctme 1
c
c
c Tallies or embee cards
c embee4 tally "Dose"
embee4:p embed=1 errors=yes
c embde/embdf4 user-defined response function "Gamma":  ICRP 116
c            AP dose response
embde4  0.01             0.015            0.02             &
      0.03             0.04             0.05             &
      0.06             0.07000000000000001 0.08             &
      0.1              0.15             0.2              &
      0.3              0.4              0.5              &
      0.511            0.6              0.662            &
      0.8              1                1.117            &
      1.33             1.5              2                &
      3                4                5                &
      6                6.129            8                &
      10               15               20               &
      30               40               50
embdf4  0                6.85e-14         1.56e-13         &
      2.25e-13         3.13e-13         3.51e-13         &
      3.7e-13          3.9e-13          4.13e-13         &
      4.44e-13         5.19e-13         7.48e-13         &
      1e-12            1.51e-12         2e-12            &
      2.47e-12         2.52e-12         2.91e-12         &
      3.17e-12         3.73e-12         4.49e-12         &
      4.9e-12          5.59e-12         6.12e-12         &
      7.48e-12         9.75e-12         1.17e-11         &
      1.34e-11         1.5e-11          1.51e-11         &
      1.78e-11         2.05e-11         2.61e-11         &
      3.08e-11         3.79e-11         4.31e-11
c
f5:p 13899.5          -5440.54         -396.249         1.0
e5 0.01             0.015            0.02             &
     0.03             0.04             0.05             &
     0.06             0.07                 0.08             &
     0.1              0.15             0.2              &
     0.3              0.4              0.5              &
     0.511            0.6              0.662            &
     0.8              1                1.117            &
     1.33             1.5              2                &
     3                4                5                &
     6                6.129            8                &
     10               15               20               &
     30               40               50               &
     60               80               100              &
     150              200              300              &
```

```
     400            500            600            &
     800            1000           1500           &
     2000           3000           4000           &
     5000           6000           8000           &
     10000
de5  0.01           0.015          0.02           &
     0.03           0.04           0.05           &
     0.06           0.07                  0.08           &
     0.1            0.15           0.2            &
     0.3            0.4            0.5            &
     0.511          0.6            0.662          &
     0.8            1              1.117          &
     1.33           1.5            2              &
     3              4              5              &
     6              6.129          8              &
     10             15             20             &
     30             40             50             &
     60             80             100            &
     150            200            300            &
     400            500            600            &
     800            1000           1500           &
     2000           3000           4000           &
     5000           6000           8000           &
     10000
df5 0.0685                0.156          0.225          &
     0.313          0.351          0.37           &
     0.39           0.413          0.444          &
     0.519          0.748          1              &
     1.51           2              2.47           &
     2.52           2.91           3.17           &
     3.73           4.49           4.9            &
     5.59           6.12           7.48           &
     9.75           11.7           13.4           &
     15             15.1           17.8           &
     20.5           26.1           30.8           &
     37.9           43.1           47.1           &
     50.1           54.5           57.8           &
     63.3           67.3           72.3           &
     75.5           77.5           78.9     &
     80.5           81.7           83.8           &
     85.2           86.9                  88.1           &
     88.9    89.5          90.2           &
     90.7
fm5 1.0
f15:p 13877        -5427.02999999999        -438.067        1.0
e15 0.01           0.015          0.02           &
     0.03           0.04           0.05           &
     0.06           0.07                  0.08           &
```

```
     0.1          0.15          0.2          &
     0.3          0.4           0.5          &
     0.511        0.6           0.662        &
     0.8          1             1.117        &
     1.33         1.5           2            &
     3            4             5            &
     6            6.129         8            &
     10           15            20           &
     30           40            50           &
     60           80            100          &
     150          200           300          &
     400          500           600          &
     800          1000          1500         &
     2000         3000          4000         &
     5000         6000          8000         &
     10000
de15  0.01           0.015         0.02         &
     0.03         0.04          0.05         &
     0.06         0.07          0.08         &
     0.1          0.15          0.2          &
     0.3          0.4           0.5          &
     0.511        0.6           0.662        &
     0.8          1             1.117        &
     1.33         1.5           2            &
     3            4             5            &
     6            6.129         8            &
     10           15            20           &
     30           40            50           &
     60           80            100          &
     150          200           300          &
     400          500           600          &
     800          1000          1500         &
     2000         3000          4000         &
     5000         6000          8000         &
     10000
df15 0.0685          0.156         0.225        &
     0.313        0.351         0.37         &
     0.39         0.413         0.444        &
     0.519        0.748         1            &
     1.51         2             2.47         &
     2.52         2.91          3.17         &
     3.73         4.49          4.9          &
     5.59         6.12          7.48         &
     9.75         11.7          13.4         &
     15           15.1          17.8         &
     20.5         26.1          30.8         &
     37.9         43.1          47.1         &
     50.1         54.5          57.8         &
```

```
     63.3            67.3            72.3            &
     75.5            77.5            78.9     &
     80.5            81.7            83.8            &
     85.2            86.9                   88.1            &
     88.9   89.5           90.2           &
     90.7
fm15 1.0
f25:p 13818.1         -5410.79        -441.92        1.0
e25 0.01             0.015           0.02            &
     0.03            0.04            0.05            &
     0.06            0.07                   0.08            &
     0.1             0.15            0.2             &
     0.3             0.4             0.5             &
     0.511            0.6            0.662           &
     0.8             1               1.117           &
     1.33             1.5            2               &
     3               4               5               &
     6               6.129           8               &
     10              15              20              &
     30              40              50              &
     60              80              100             &
     150             200             300             &
     400             500             600             &
     800             1000            1500            &
     2000            3000            4000            &
     5000            6000            8000            &
     10000
de25  0.01           0.015           0.02            &
     0.03            0.04            0.05            &
     0.06            0.07                   0.08            &
     0.1             0.15            0.2             &
     0.3             0.4             0.5             &
     0.511            0.6            0.662           &
     0.8             1               1.117           &
     1.33             1.5            2               &
     3               4               5               &
     6               6.129           8               &
     10              15              20              &
     30              40              50              &
     60              80              100             &
     150             200             300             &
     400             500             600             &
     800             1000            1500            &
     2000            3000            4000            &
     5000            6000            8000            &
     10000
df25 0.0685            0.156           0.225           &
     0.313            0.351           0.37            &
```

```
     0.39          0.413         0.444         &
     0.519         0.748         1             &
     1.51          2             2.47          &
     2.52          2.91          3.17          &
     3.73          4.49          4.9           &
     5.59          6.12          7.48          &
     9.75          11.7          13.4          &
     15            15.1          17.8          &
     20.5          26.1          30.8          &
     37.9          43.1          47.1          &
     50.1          54.5          57.8          &
     63.3          67.3          72.3          &
     75.5          77.5          78.9     &
     80.5          81.7          83.8          &
     85.2          86.9                88.1          &
     88.9   89.5        90.2          &
     90.7
fm25 1.0
f35:p 13834         -5319.10999999999         -433.992          1.0
e35 0.01           0.015         0.02          &
     0.03          0.04          0.05          &
     0.06          0.07                0.08          &
     0.1           0.15          0.2           &
     0.3           0.4           0.5           &
     0.511         0.6           0.662         &
     0.8           1             1.117         &
     1.33          1.5           2             &
     3             4             5             &
     6             6.129         8             &
     10            15            20            &
     30            40            50            &
     60            80            100           &
     150           200           300           &
     400           500           600           &
     800           1000          1500          &
     2000          3000          4000          &
     5000          6000          8000          &
     10000
de35  0.01          0.015         0.02          &
     0.03          0.04          0.05          &
     0.06          0.07                0.08          &
     0.1           0.15          0.2           &
     0.3           0.4           0.5           &
     0.511         0.6           0.662         &
     0.8           1             1.117         &
     1.33          1.5           2             &
     3             4             5             &
     6             6.129         8             &
```

```
     10              15              20              &
     30              40              50              &
     60              80              100             &
     150             200             300             &
     400             500             600             &
     800             1000            1500            &
     2000            3000            4000            &
     5000            6000            8000            &
     10000
df35 0.0685          0.156           0.225           &
     0.313           0.351           0.37            &
     0.39            0.413           0.444           &
     0.519           0.748           1               &
     1.51            2               2.47            &
     2.52            2.91            3.17            &
     3.73            4.49            4.9             &
     5.59            6.12            7.48            &
     9.75            11.7            13.4            &
     15              15.1            17.8            &
     20.5            26.1            30.8            &
     37.9            43.1            47.1            &
     50.1            54.5            57.8            &
     63.3            67.3            72.3            &
     75.5            77.5            78.9      &
     80.5            81.7            83.8            &
     85.2            86.9                  88.1            &
     88.9   89.5           90.2            &
     90.7
fm35 1.0
f45:p 13726.4         -5354.97         -366.257999999999         1.0
e45 0.01             0.015           0.02            &
     0.03            0.04            0.05            &
     0.06            0.07                  0.08            &
     0.1             0.15            0.2             &
     0.3             0.4             0.5             &
     0.511           0.6             0.662           &
     0.8             1               1.117           &
     1.33            1.5             2               &
     3               4               5               &
     6               6.129           8               &
     10              15              20              &
     30              40              50              &
     60              80              100             &
     150             200             300             &
     400             500             600             &
     800             1000            1500            &
     2000            3000            4000            &
     5000            6000            8000            &
```

```
     10000
de45  0.01       0.015      0.02       &
     0.03       0.04       0.05       &
     0.06       0.07       0.08       &
     0.1        0.15       0.2        &
     0.3        0.4        0.5        &
     0.511      0.6        0.662      &
     0.8        1          1.117      &
     1.33       1.5        2          &
     3          4          5          &
     6          6.129      8          &
     10         15         20         &
     30         40         50         &
     60         80         100        &
     150        200        300        &
     400        500        600        &
     800        1000       1500       &
     2000       3000       4000       &
     5000       6000       8000       &
     10000
df45 0.0685       0.156      0.225      &
     0.313      0.351      0.37       &
     0.39       0.413      0.444      &
     0.519      0.748      1          &
     1.51       2          2.47       &
     2.52       2.91       3.17       &
     3.73       4.49       4.9        &
     5.59       6.12       7.48       &
     9.75       11.7       13.4       &
     15         15.1       17.8       &
     20.5       26.1       30.8       &
     37.9       43.1       47.1       &
     50.1       54.5       57.8       &
     63.3       67.3       72.3       &
     75.5       77.5       78.9    &
     80.5       81.7       83.8       &
     85.2       86.9       88.1       &
     88.9  89.5       90.2       &
     90.7
fm45 1.0
f55:p 13889.7999999999       -5223.47999999999       -294.538999999999       1.0
e55 0.01       0.015      0.02       &
     0.03       0.04       0.05       &
     0.06       0.07       0.08       &
     0.1        0.15       0.2        &
     0.3        0.4        0.5        &
     0.511      0.6        0.662      &
     0.8        1          1.117      &
```

```
     1.33      1.5       2         &
     3         4         5         &
     6         6.129     8         &
     10        15        20        &
     30        40        50        &
     60        80        100       &
     150       200       300       &
     400       500       600       &
     800       1000      1500      &
     2000      3000      4000      &
     5000      6000      8000      &
     10000
de55 0.01      0.015     0.02      &
     0.03      0.04      0.05      &
     0.06      0.07      0.08      &
     0.1       0.15      0.2       &
     0.3       0.4       0.5       &
     0.511     0.6       0.662     &
     0.8       1         1.117     &
     1.33      1.5       2         &
     3         4         5         &
     6         6.129     8         &
     10        15        20        &
     30        40        50        &
     60        80        100       &
     150       200       300       &
     400       500       600       &
     800       1000      1500      &
     2000      3000      4000      &
     5000      6000      8000      &
     10000
df55 0.0685    0.156     0.225     &
     0.313     0.351     0.37      &
     0.39      0.413     0.444     &
     0.519     0.748     1         &
     1.51      2         2.47      &
     2.52      2.91      3.17      &
     3.73      4.49      4.9       &
     5.59      6.12      7.48      &
     9.75      11.7      13.4      &
     15        15.1      17.8      &
     20.5      26.1      30.8      &
     37.9      43.1      47.1      &
     50.1      54.5      57.8      &
     63.3      67.3      72.3      &
     75.5      77.5      78.9      &
     80.5      81.7      83.8      &
     85.2      86.9      88.1      &
```

```
     88.9    89.5                90.2                &
     90.7
fm55 1.0
f65:p 14152.7            -5287.22999999999           -398.132999999999            1.0
e65 0.01                 0.015               0.02                &
     0.03                0.04                0.05                &
     0.06                0.07                      0.08                &
     0.1                 0.15                0.2                 &
     0.3                 0.4                 0.5                 &
     0.511               0.6                 0.662               &
     0.8                 1                   1.117               &
     1.33                1.5                 2                   &
     3                   4                   5                   &
     6                   6.129               8                   &
     10                  15                  20                  &
     30                  40                  50                  &
     60                  80                  100                 &
     150                 200                 300                 &
     400                 500                 600                 &
     800                 1000                1500                &
     2000                3000                4000                &
     5000                6000                8000                &
     10000
de65  0.01               0.015               0.02                &
     0.03                0.04                0.05                &
     0.06                0.07                      0.08                &
     0.1                 0.15                0.2                 &
     0.3                 0.4                 0.5                 &
     0.511               0.6                 0.662               &
     0.8                 1                   1.117               &
     1.33                1.5                 2                   &
     3                   4                   5                   &
     6                   6.129               8                   &
     10                  15                  20                  &
     30                  40                  50                  &
     60                  80                  100                 &
     150                 200                 300                 &
     400                 500                 600                 &
     800                 1000                1500                &
     2000                3000                4000                &
     5000                6000                8000                &
     10000
df65 0.0685              0.156               0.225               &
     0.313               0.351               0.37                &
     0.39                0.413               0.444               &
     0.519               0.748               1                   &
     1.51                2                   2.47                &
     2.52                2.91                3.17                &
```

```
     3.73        4.49        4.9        &
     5.59        6.12        7.48       &
     9.75        11.7        13.4       &
     15          15.1        17.8       &
     20.5        26.1        30.8       &
     37.9        43.1        47.1       &
     50.1        54.5        57.8       &
     63.3        67.3        72.3       &
     75.5        77.5        78.9   &
     80.5        81.7        83.8       &
     85.2        86.9             88.1          &
     88.9   89.5         90.2         &
     90.7
fm65 1.0
f75:p 13652       -5596.25       -602.21      1.0
e75 0.01          0.015        0.02        &
     0.03        0.04        0.05       &
     0.06        0.07             0.08         &
     0.1         0.15        0.2        &
     0.3         0.4         0.5        &
     0.511        0.6        0.662      &
     0.8         1          1.117       &
     1.33        1.5         2          &
     3           4          5          &
     6           6.129       8          &
     10          15          20         &
     30          40          50         &
     60          80          100        &
     150         200         300        &
     400         500         600        &
     800         1000        1500       &
     2000        3000        4000       &
     5000        6000        8000       &
     10000
de75  0.01          0.015        0.02        &
     0.03        0.04        0.05       &
     0.06        0.07             0.08         &
     0.1         0.15        0.2        &
     0.3         0.4         0.5        &
     0.511        0.6        0.662      &
     0.8         1          1.117       &
     1.33        1.5         2          &
     3           4          5          &
     6           6.129       8          &
     10          15          20         &
     30          40          50         &
     60          80          100        &
     150         200         300        &
```

```
     400             500             600             &
     800             1000            1500            &
     2000            3000            4000            &
     5000            6000            8000            &
     10000
df75 0.0685          0.156           0.225           &
     0.313           0.351           0.37            &
     0.39            0.413           0.444           &
     0.519           0.748           1               &
     1.51            2               2.47            &
     2.52            2.91            3.17            &
     3.73            4.49            4.9             &
     5.59            6.12            7.48            &
     9.75            11.7            13.4            &
     15              15.1            17.8            &
     20.5            26.1            30.8            &
     37.9            43.1            47.1            &
     50.1            54.5            57.8            &
     63.3            67.3            72.3            &
     75.5            77.5            78.9      &
     80.5            81.7            83.8            &
     85.2            86.9                   88.1            &
     88.9    89.5            90.2            &
     90.7
fm75 1.0
f85:p 13786.2            -5072.06999999999           -334.382999999999            1.0
e85 0.01             0.015           0.02            &
     0.03            0.04            0.05            &
     0.06            0.07                   0.08            &
     0.1             0.15            0.2             &
     0.3             0.4             0.5             &
     0.511           0.6             0.662           &
     0.8             1               1.117           &
     1.33            1.5             2               &
     3               4               5               &
     6               6.129           8               &
     10              15              20              &
     30              40              50              &
     60              80              100             &
     150             200             300             &
     400             500             600             &
     800             1000            1500            &
     2000            3000            4000            &
     5000            6000            8000            &
     10000
de85  0.01             0.015           0.02            &
     0.03            0.04            0.05            &
     0.06            0.07                   0.08            &
```

```
     0.1               0.15              0.2              &
     0.3               0.4               0.5              &
     0.511             0.6               0.662            &
     0.8               1                 1.117            &
     1.33              1.5               2                &
     3                 4                 5                &
     6                 6.129             8                &
     10                15                20               &
     30                40                50               &
     60                80                100              &
     150               200               300              &
     400               500               600              &
     800               1000              1500             &
     2000              3000              4000             &
     5000              6000              8000             &
     10000
df85 0.0685                  0.156             0.225            &
     0.313             0.351             0.37             &
     0.39              0.413             0.444            &
     0.519             0.748             1                &
     1.51              2                 2.47             &
     2.52              2.91              3.17             &
     3.73              4.49              4.9              &
     5.59              6.12              7.48             &
     9.75              11.7              13.4             &
     15                15.1              17.8             &
     20.5              26.1              30.8             &
     37.9              43.1              47.1             &
     50.1              54.5              57.8             &
     63.3              67.3              72.3             &
     75.5              77.5              78.9       &
     80.5              81.7              83.8             &
     85.2              86.9                      88.1                &
     88.9    89.5              90.2              &
     90.7
fm85 1.0
f95:p 13809.2          -4975.81          -530.188999999999          1.0
e95 0.01               0.015             0.02             &
     0.03              0.04              0.05             &
     0.06              0.07                      0.08             &
     0.1               0.15              0.2              &
     0.3               0.4               0.5              &
     0.511             0.6               0.662            &
     0.8               1                 1.117            &
     1.33              1.5               2                &
     3                 4                 5                &
     6                 6.129             8                &
     10                15                20               &
```

```
     30          40          50          &
     60          80          100         &
     150         200         300         &
     400         500         600         &
     800         1000        1500        &
     2000        3000        4000        &
     5000        6000        8000        &
     10000
de95  0.01         0.015        0.02        &
     0.03        0.04        0.05        &
     0.06        0.07              0.08        &
     0.1         0.15        0.2         &
     0.3         0.4         0.5         &
     0.511        0.6        0.662       &
     0.8         1           1.117       &
     1.33        1.5         2           &
     3           4           5           &
     6           6.129       8           &
     10          15          20          &
     30          40          50          &
     60          80          100         &
     150         200         300         &
     400         500         600         &
     800         1000        1500        &
     2000        3000        4000        &
     5000        6000        8000        &
     10000
df95 0.0685          0.156        0.225        &
     0.313        0.351       0.37        &
     0.39        0.413       0.444       &
     0.519        0.748       1           &
     1.51        2           2.47        &
     2.52        2.91        3.17        &
     3.73        4.49        4.9         &
     5.59        6.12        7.48        &
     9.75        11.7        13.4        &
     15          15.1        17.8        &
     20.5        26.1        30.8        &
     37.9        43.1        47.1        &
     50.1        54.5        57.8        &
     63.3        67.3        72.3        &
     75.5        77.5        78.9    &
     80.5        81.7        83.8        &
     85.2        86.9              88.1        &
     88.9   89.5        90.2        &
     90.7
fm95 1.0
c
```

```
c Write the MCTAL file
prdmp j j 1
c
c L'Ecuyer 63-bit random number generator (period=9.2E18)
rand gen=2
c
print -85 -86 -87 -98
c
c --------------------------- End Data Cards -------------------------------- 80
c End MCNP Input
```

Appendix C Sample Microsoft Excel File Used in the data compilation and evaluation.

x	y	z	Dose from F4 Tally (in Sv cm^2)	Rel Std Error	Distance from source (cm)	Gamma Constant Calculated Dose Rate	Raw Diff between calc & modeled value with ICRP 38 Gamma constant	Percent difference Between F4 tally and ICRP 38 Calc	Percent Difference (symmetry) Between F4 tally and ICRP 38 Calc	Raw Diff between calc & modeled value with RHHB Gamma constant	Percent difference between calc & modeled value with RHHB Gamma constant	Percent Difference (symmetry)between calc & modeled value with RHHB Gamma constant	Calculated dose rate using RHHB gamma constant
13899.4	-5446.02	-399.17	3.478E-14	0.0017	4.109256	5.03E-14	30.91%	36.57%	30.91%	42.91%	54.63%	42.91%	6.09E-14
13895.8	-5453.49	-401.03	2.887E-14	0.00144	5.55781	2.75E-14	-4.93%	4.81%	4.93%	13.29%	14.24%	13.29%	3.33E-14
13894.5	-5447.34	-399.26	2.204E-14	0.00203	6.154603	2.24E-14	1.77%	1.78%	1.77%	18.82%	20.78%	18.82%	2.72E-14
13901.7	-5450.59	-390.16	1.502E-14	0.00235	9.99925	8.50E-15	-76.72%	55.45%	76.72%	-46.03%	37.42%	46.03%	1.03E-14
13902.4	-5450.15	-407.87	1.464E-14	0.00249	8.22918	1.26E-14	-16.63%	15.35%	16.63%	3.62%	3.69%	3.62%	1.52E-14
13895.5	-5445.54	-394.46	1.338E-14	0.003	8.412956	1.20E-14	-11.39%	10.77%	11.39%	7.95%	8.28%	7.95%	1.45E-14
13894.1	-5448.45	-406.01	1.244E-14	0.00231	8.564849	1.16E-14	-7.36%	7.10%	7.36%	11.28%	11.96%	11.28%	1.40E-14
13904.3	-5441.83	-396.40	1.238E-14	0.00211	9.908083	8.66E-15	-43.00%	35.39%	43.00%	-18.17%	16.66%	18.17%	1.05E-14
13906	-5442.09	-401.08	1.127E-14	0.00237	9.986824	8.52E-15	-32.22%	27.75%	32.22%	-9.26%	8.85%	9.26%	1.03E-14
13896.6	-5439.56	-400.81	1.055E-14	0.00287	11.0096	7.01E-15	-50.43%	40.28%	50.43%	-24.31%	21.68%	24.31%	8.49E-15
13899.5	-5440.54	-396.25	9.963E-15	0.00283	10.1888	8.19E-15	-21.68%	19.56%	21.68%	-0.55%	0.55%	0.55%	9.91E-15
13909.6	-5449.87	-398.24	9.948E-15	0.00277	9.760685	8.92E-15	-11.50%	10.87%	11.50%	7.86%	8.18%	7.86%	1.08E-14
13903.3	-5441.14	-405.74	8.016E-15	0.00277	11.06113	6.95E-15	-15.38%	14.28%	15.38%	4.65%	4.76%	4.65%	8.41E-15
13893.3	-5442.66	-398.48	7.879E-15	0.00377	10.05366	8.41E-15	6.31%	6.52%	6.31%	22.58%	25.45%	22.58%	1.02E-14

Mesh Geometry:	Road Tunnel 55
Source location	Point 3
x / y / z	13900 / -5450 / -400
Isotope:	Co-60
histories	1.00E+07
using ICRP 116 AP DCF	
mountain material is:	concrete
RHHB gamma dose rate constant in Gy m^2/s Bq	1.03E-16
NCRP 38 Specific Gamma Dose Rate Constant	8.50E-17

Appendix D Python Script used to evaluate Excel spreadsheets

```
#!/usr/bin/env python3
"""
analyze_pl_icrp_compare.py

Goal
----
For every workbook and every "PL <letter>" sheet:
1) Extract F4 modeled dose and the "ICRP gamma-constant calculated dose" column.
2) Compute per-sheet statistics of agreement: |% diff| between F4 and ICRP calc.
3) Compare each material run against the AIR tunnel for the *same variation*
   (same isotope, source location, PL letter), producing:
   - % change in F4 dose vs air at each distance
   - change in |% diff(F4 vs ICRP)| vs air at each distance
   - summary tables you can cite (mean/median changes)

Outputs (in --output_dir)
-------------------------
- pl_long.csv
- pl_run_summary.csv
- pl_comparison_to_air_long.csv
- pl_comparison_to_air_summary.csv
- pl_icrp_results.xlsx (all of the above as tabs)
- errors.txt (if any sheets fail)

How "same variation" is defined
-------------------------------
Key = (isotope, source_location, pl_id)
where pl_id is the letter a/b/c/... from the sheet name ",Ä¶ PL a".

Air baseline:
- material == "Air" (found from metadata text in the PL sheet)
- If multiple air runs exist for the same key, the script uses the first one
  after sorting by filename. (You can change this behavior if needed.)

Assumptions about your PL sheet columns
--------------------------------------
The script is robust to exact column titles and searches by substring for:
- Distance: contains "Distance from source"
- F4 dose: contains "Dose from F4"
- ICRP calc dose: prefers "Gamma Constant Calculated Dose Rate" (your current layout)
  but will fall back to any column containing "ICRP" if needed.
- % diff vs ICRP: prefers "Percent difference Between F4 tally and ICRP 38 Calc"
  (if present). Otherwise computes (F4 - calc)/calc.

Run
---
python3 analyze_pl_icrp_compare.py \
  --input_dir "/path/to/Python/Final Results" \
  --output_dir "/path/to/Python/PL_ICRP_Out"
"""
from __future__ import annotations
```

```
import argparse
import glob
import os
import re
from typing import Dict, List, Optional, Tuple

import numpy as np
import pandas as pd


RUN_RE = re.compile(r"(run\d+[a-z]*\d*)", re.IGNORECASE)


def run_id_from_filename(fn: str) -> str:
    m = RUN_RE.search(fn)
    return m.group(1) if m else os.path.splitext(os.path.basename(fn))[0]


def to_num(s: pd.Series) -> pd.Series:
    return pd.to_numeric(s, errors="coerce")


def find_col(df: pd.DataFrame, needle: str) -> Optional[str]:
    needle_l = needle.lower()
    for c in df.columns:
        if isinstance(c, str) and needle_l in c.lower():
            return c
    return None


def find_col_any(df: pd.DataFrame, needles: List[str]) -> Optional[str]:
    for n in needles:
        c = find_col(df, n)
        if c is not None:
            return c
    return None


def extract_metadata_generic(df_raw: pd.DataFrame) -> Dict[str, Optional[str]]:
    """
    Scans the entire sheet (including footer text blocks) to find metadata labels
    like "Isotope:", "Source location", "Material is", etc.
    """
    keys = {
        "mesh_geometry": ["mesh geometry"],
        "source_location": ["source location", "point"],
        "isotope": ["isotope"],
        "material": ["material is", "mountain material", "material"],
    }
    meta: Dict[str, Optional[str]] = {k: None for k in keys}

    df = df_raw.copy()
    for c in df.columns:
        df[c] = df[c].astype("string")
```

```python
    nrows, ncols = df.shape

    def set_if_empty(k: str, v):
        if meta[k] is None and v is not None and not pd.isna(v):
            vv = str(v).strip()
            if vv and vv.lower() != "nan":
                meta[k] = vv

    for r in range(nrows):
        for c in range(ncols):
            cell = df.iat[r, c]
            if cell is None or pd.isna(cell):
                continue
            sl = str(cell).strip().lower()
            for k, needles in keys.items():
                if any(nd in sl for nd in needles):
                    right = df.iat[r, c + 1] if c + 1 < ncols else None
                    below = df.iat[r + 1, c] if r + 1 < nrows else None
                    cand = right
                    if cand is None or pd.isna(cand) or str(cand).strip().lower() in ["", "nan"]:
                        cand = below
                    set_if_empty(k, cand)

    # normalize isotope labels
    if meta["isotope"]:
        iso = meta["isotope"].replace(" ", "").replace("_", "-").upper()
        iso = iso.replace("CS137", "CS-137").replace("CO60", "CO-60").replace("RA226", "RA-226")
        meta["isotope"] = iso

    # normalize material labels
    if meta["material"]:
        ml = meta["material"].strip().lower()
        if "air" in ml:
            meta["material"] = "Air"
        elif "concrete" in ml:
            meta["material"] = "Concrete"
        elif "granite" in ml:
            meta["material"] = "Granite"
        elif "rock" in ml or "mountain" in ml:
            meta["material"] = "Rock"

    # normalize source location to "Point X" when possible
    if meta["source_location"]:
        m = re.search(r"(point\s*\d+)", meta["source_location"], re.I)
        if m:
            meta["source_location"] = m.group(1).title().replace("  ", " ")

    return meta


def extract_pl_sheet(path: str, sheet: str) -> Tuple[pd.DataFrame, Dict[str, Optional[str]]]:
    df_raw = pd.read_excel(path, sheet_name=sheet, engine="openpyxl")
    meta = extract_metadata_generic(df_raw)
```

```
    # identify columns
    col_dist = find_col_any(df_raw, ["distance from source (cm)", "distance from source"])
    if col_dist is None:
        raise ValueError("Missing distance column")

    col_f4 = find_col_any(df_raw, ["dose from f4 tally", "dose from f4"])
    if col_f4 is None:
        raise ValueError("Missing F4 dose column")

    # Prefer your current explicit calc column title:
    col_icrp_calc = find_col_any(df_raw, ["gamma constant calculated dose rate"])
    # Fallback: some sheets might name it differently but include ICRP
    if col_icrp_calc is None:
        col_icrp_calc = find_col_any(df_raw, ["icrp", "icrp 38"])

    # Prefer the percent-diff column if present (already precomputed in sheet)
    col_pct = find_col_any(df_raw, ["percent difference between f4 tally and icrp 38 calc",
                                    "percent difference between f4 tally and icrp",
                                    "percent difference between f4 tally and icrp 38 calc"])

    dist = to_num(df_raw[col_dist])
    keep = dist.notna()
    df = df_raw.loc[keep].copy()

    out = pd.DataFrame({
        "distance_cm": dist.loc[keep].astype(float),
        "dose_f4": to_num(df[col_f4]).astype(float),
        "dose_icrp_calc": to_num(df[col_icrp_calc]).astype(float) if col_icrp_calc else np.nan,
    })

    if col_pct:
        out["pct_diff_f4_vs_icrp"] = to_num(df[col_pct]).astype(float)
    else:
        out["pct_diff_f4_vs_icrp"] = (out["dose_f4"] - out["dose_icrp_calc"]) / out["dose_icrp_calc"]

    out["abs_pct_diff_f4_vs_icrp"] = np.abs(out["pct_diff_f4_vs_icrp"])

    return out, meta


def main() -> None:
    ap = argparse.ArgumentParser()
    ap.add_argument("--input_dir", required=True, help="Folder containing RT Results run*.xlsx")
    ap.add_argument("--output_dir", required=True, help="Output folder")
    ap.add_argument("--glob", default="RT Results run*.xlsx", help="Glob pattern (default: RT Results
run*.xlsx)")
    args = ap.parse_args()

    os.makedirs(args.output_dir, exist_ok=True)

    paths = sorted(glob.glob(os.path.join(args.input_dir, args.glob)))
    if not paths:
        raise SystemExit(f"No files matched: {os.path.join(args.input_dir, args.glob)}")
```

```
pl_long_frames: List[pd.DataFrame] = []
pl_summary_rows: List[Dict[str, object]] = []
issues: List[Tuple[str, str, str]] = []

for fp in paths:
    rid = run_id_from_filename(os.path.basename(fp))
    try:
        xls = pd.ExcelFile(fp, engine="openpyxl")
    except Exception as e:
        issues.append((os.path.basename(fp), "ExcelFile", str(e)))
        continue

    pl_sheets = [s for s in xls.sheet_names if re.search(r"\bPL\s+[a-z]\b", s, re.I)]
    for sh in pl_sheets:
        m = re.search(r"\bPL\s+([a-z])\b", sh, re.I)
        pl_id = m.group(1).lower() if m else None

        try:
            df, meta = extract_pl_sheet(fp, sh)
        except Exception as e:
            issues.append((os.path.basename(fp), sh, str(e)))
            continue

        df.insert(0, "run_id", rid)
        df["pl_id"] = pl_id
        df["sheet"] = sh
        for k, v in meta.items():
            df[k] = v

        pl_long_frames.append(df)

        vals = df["abs_pct_diff_f4_vs_icrp"].to_numpy(dtype=float)
        vals = vals[np.isfinite(vals)]
        pl_summary_rows.append({
            "run_id": rid,
            "pl_id": pl_id,
            "sheet": sh,
            "isotope": meta.get("isotope"),
            "material": meta.get("material"),
            "source_location": meta.get("source_location"),
            "mesh_geometry": meta.get("mesh_geometry"),
            "n_points": int(df.shape[0]),
            "mean_abs_pct_diff_f4_vs_icrp": float(np.mean(vals)) if vals.size else np.nan,
            "median_abs_pct_diff_f4_vs_icrp": float(np.median(vals)) if vals.size else np.nan,
            "max_abs_pct_diff_f4_vs_icrp": float(np.max(vals)) if vals.size else np.nan,
        })

if issues:
    with open(os.path.join(args.output_dir, "errors.txt"), "w", encoding="utf-8") as f:
        for fn, sh, msg in issues:
            f.write(f"{fn} | {sh}: {msg}\n")

if not pl_long_frames:
```

```
        raise SystemExit("No PL sheets processed successfully.")

    pl_long = pd.concat(pl_long_frames, ignore_index=True)
    pl_summary = pd.DataFrame(pl_summary_rows)

    # Comparison to AIR baseline for same variation: (isotope, source_location, pl_id)
    key_cols = ["isotope", "source_location", "pl_id"]
    pl_long["dist_key"] = pl_long["distance_cm"].round(6)

    air = pl_long[pl_long["material"] == "Air"].copy()
    nonair = pl_long[pl_long["material"] != "Air"].copy()

    if air.empty:
        raise SystemExit("No AIR runs found (material == 'Air'). Cannot compute comparisons to air.")

    # One air baseline per key/distance (if duplicates exist, keep first)
    air_m = (
        air[key_cols + ["dist_key", "dose_f4", "dose_icrp_calc", "abs_pct_diff_f4_vs_icrp", "run_id"]]
        .rename(columns={
            "dose_f4": "dose_f4_air",
            "dose_icrp_calc": "dose_icrp_air",
            "abs_pct_diff_f4_vs_icrp": "abs_pct_diff_air",
            "run_id": "run_id_air",
        })
        .sort_values(["run_id_air"])
        .drop_duplicates(subset=key_cols + ["dist_key"], keep="first")
    )

    comp_long = nonair.merge(air_m, on=key_cols + ["dist_key"], how="inner")

    comp_long["pct_change_f4_vs_air"] = (comp_long["dose_f4"] - comp_long["dose_f4_air"]) /
comp_long["dose_f4_air"]
    # ICRP calc typically depends only on distance + isotope, so this often is ~0; kept for completeness
    comp_long["pct_change_icrp_calc_vs_air"] = (comp_long["dose_icrp_calc"] - comp_long["dose_icrp_air"]) /
comp_long["dose_icrp_air"]
    comp_long["delta_abs_pctdiff_vs_air"] = comp_long["abs_pct_diff_f4_vs_icrp"] -
comp_long["abs_pct_diff_air"]

    comp_summary = (
        comp_long
        .groupby(key_cols + ["material", "run_id", "run_id_air"], observed=True, dropna=False)
        .agg(
            n=("dist_key", "count"),
            mean_pct_change_f4_vs_air=("pct_change_f4_vs_air", "mean"),
            median_pct_change_f4_vs_air=("pct_change_f4_vs_air", "median"),
            mean_delta_abs_pctdiff_vs_air=("delta_abs_pctdiff_vs_air", "mean"),
            mean_abs_pctdiff_f4_vs_icrp=("abs_pct_diff_f4_vs_icrp", "mean"),
            mean_abs_pctdiff_air=("abs_pct_diff_air", "mean"),
        )
        .reset_index()
        .sort_values(key_cols + ["material", "run_id"])
    )

    # write outputs
```

```python
    pl_long.to_csv(os.path.join(args.output_dir, "pl_long.csv"), index=False)
    pl_summary.to_csv(os.path.join(args.output_dir, "pl_run_summary.csv"), index=False)
    comp_long.to_csv(os.path.join(args.output_dir, "pl_comparison_to_air_long.csv"), index=False)
    comp_summary.to_csv(os.path.join(args.output_dir, "pl_comparison_to_air_summary.csv"), index=False)

    xlsx_path = os.path.join(args.output_dir, "pl_icrp_results.xlsx")
    with pd.ExcelWriter(xlsx_path, engine="openpyxl") as w:
        pl_long.to_excel(w, sheet_name="PL_Long", index=False)
        pl_summary.to_excel(w, sheet_name="PL_RunSummary", index=False)
        comp_long.to_excel(w, sheet_name="CompareToAir_Long", index=False)
        comp_summary.to_excel(w, sheet_name="CompareToAir_Summary", index=False)

    print("DONE. Outputs written to:", args.output_dir)


if __name__ == "__main__":
    main()
```

Appendix E Pooled F4 vs F5 Comparison N=400

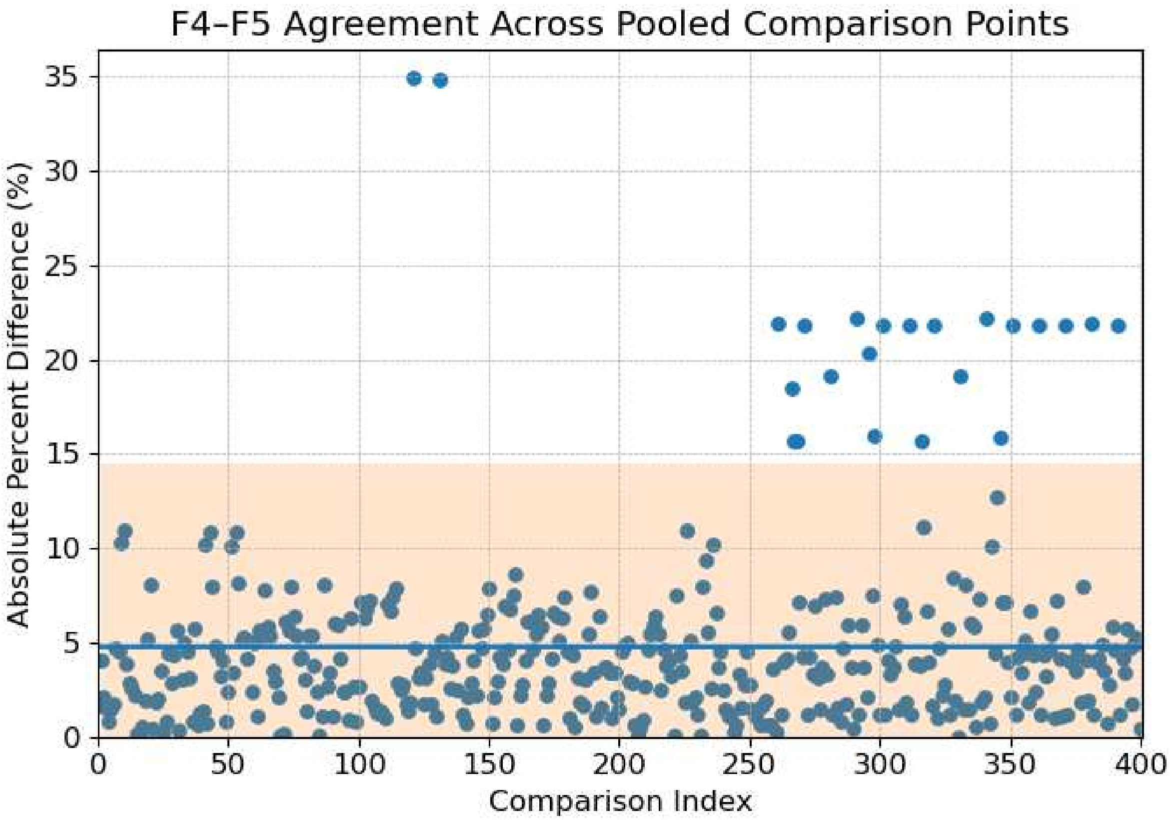

Figure E-1: Distribution of absolute percent differences between F4 and F5 effective dose estimates across all pooled comparison points (N = 400). Points represent individual F4–F5 comparisons. The solid line indicates the overall mean, and the shaded region represents mean ± 2 standard deviations, illustrating variability across pooled comparison points.

Appendix F MCNP Output File

```
          Code Name & Version = MCNP_6.20, 6.2.0

     _/      _/        _/_/_/       _/      _/       _/_/_/         _/_/_/
    _/_/  _/_/      _/             _/_/    _/       _/    _/     _/
   _/  _/  _/      _/             _/  _/  _/       _/_/_/       _/_/_/
  _/      _/      _/             _/    _/_/       _/           _/    _/
 _/      _/        _/_/_/       _/      _/       _/             _/_/
```



```
1mcnp     version 6.mpi ld=07/01/21                    01/06/26 18:06:59
 *************************************************************************                    probid =
01/06/26 18:06:59
 i=run9xc.mcnp.i o=run9xc.mcnp.o
xsdir=/home/dbo/MY_MCNP/MCNP_DATA/xsdir_mcnp6.2
```

comment. Physics models disabled.

```
run9xc
c
c Attila calculation "Run9xc"
c Run7xc rerun with new mesh around point
c added ICRP 116 AP in F4 tally
c concrete for mountain
c add F5 tally manually
c Road tunnel 55 geometry with 3113k cells
c 1E7 histories point 3 (x) centered in the pedestrian tunnel of the road tunnel
c -------------------------- Input Information ------------------------------ 80
c Attila GUI created MCNP6 Input
c Attila Version (not available)
c Input File Creation Date: Tue Jan 6 12:24:57 2026
c RxMesher version          : 1.0.0
c Simmetrix MeshSim version : 14.0-200321
c Global mesh size          : 5 m
c Generated                 : 2026-01-05T19:01:47-07:00
c Solid Geometry :
c   Filename     : Road Tunnel 50.x_t
c   Last changed : 2025-09-21T14:02:51-07:00
c   MD5 checksum : dbde909fe7be1afef164890b9898c1c1
c Note: RTT Mesh has added cell flags for MCNP Abaqus part and pseudo-cell.
c Associated Abaqus Unstructured Mesh :
c   Filename     : road_tunnel_55.mesh.abaq
c   Generated    : 2026-01-06T12:24:57
c   MD5 checksum : 499875a57daef01384fbec73a3f37906
c n_points = 569407
c n_sides  = 178828
c n_cells  = 3113097
c Mesh Bounding Box (cm):
c  x: 8007.732 - 17691.969
c  y: -9013.606 - -1441.325
c  z: -1855.985 - 1330.657
c
c Number of Attila Regions                  : 19
c Number of Abaqus Parts/MCNP Pseudo-Cells : 30
c Number of Materials                       : 2
c
c  Mesh Region/Pseudo-Cell Information
c   Attila Region #    : 1
c   Attila Region Name : "Tunnel_A5"
c   Abaqus Part #      : 1
```

```
c  Abaqus Part Name   : "Tunnel_A5"
c  MCNP Pseudo-cell # : 1
c  Material           : "Air-(Dry,-Near-Sea-Level)_1"
c   MCNP Material     : m1
c   Density           : 4.988e-05 atoms/b-cm
c  Mesh Data
c    Meshed Volume    : 2.54254e+09 cm**3
c    # Cells          : 13857
c    % of Total Cells : 0.45%
c
c  Attila Region #    : 2
c  Attila Region Name : "Mountain"
c  Abaqus Part #      : 2
c  Abaqus Part Name   : "Mountain_sub1"
c  MCNP Pseudo-cell # : 2
c  Material           : "Concrete,-Los-Alamos-(MCNP)_2"
c   MCNP Material     : m2
c   Density           : 0.07186 atoms/b-cm
c  Mesh Data
c    Meshed Volume    : 1.81527e+11 cm**3
c    # Cells          : 152055
c    % of Total Cells : 4.88%
c
c  Attila Region #    : 2
c  Attila Region Name : "Mountain"
c  Abaqus Part #      : 3
c  Abaqus Part Name   : "Mountain_sub2"
c  MCNP Pseudo-cell # : 3
c  Material           : "Concrete,-Los-Alamos-(MCNP)_2"
c   MCNP Material     : m2
c   Density           : 0.07186 atoms/b-cm
c  Mesh Data
c    Meshed Volume    : 3.99372e+10 cm**3
c    # Cells          : 147114
c    % of Total Cells : 4.73%
c
c  Attila Region #    : 3
c  Attila Region Name : "Pedestrian_Tunnel_a"
c  Abaqus Part #      : 4
c  Abaqus Part Name   : "Pedestrian_Tunnel_a"
c  MCNP Pseudo-cell # : 4
c  Material           : "Air-(Dry,-Near-Sea-Level)_1"
c   MCNP Material     : m1
c   Density           : 4.988e-05 atoms/b-cm
c  Mesh Data
c    Meshed Volume    : 6.1786e+07 cm**3
```

```
c     # Cells          : 49459
c     % of Total Cells : 1.59%
c
c   Attila Region #    : 4
c   Attila Region Name : "Pedestrian_Tunnel_d"
c   Abaqus Part #      : 5
c   Abaqus Part Name   : "Pedestrian_Tunnel_d"
c   MCNP Pseudo-cell # : 5
c   Material           : "Air-(Dry,-Near-Sea-Level)_1"
c    MCNP Material     : m1
c    Density           : 4.988e-05 atoms/b-cm
c   Mesh Data
c     Meshed Volume    : 7.51224e+07 cm**3
c     # Cells          : 2413
c     % of Total Cells : 0.08%
c
c   Attila Region #    : 5
c   Attila Region Name : "Pedestrian_Tunnel_b"
c   Abaqus Part #      : 6
c   Abaqus Part Name   : "Pedestrian_Tunnel_b_sub1"
c   MCNP Pseudo-cell # : 6
c   Material           : "Air-(Dry,-Near-Sea-Level)_1"
c    MCNP Material     : m1
c    Density           : 4.988e-05 atoms/b-cm
c   Mesh Data
c     Meshed Volume    : 6.35125e+06 cm**3
c     # Cells          : 221081
c     % of Total Cells : 7.10%
c
c   Attila Region #    : 5
c   Attila Region Name : "Pedestrian_Tunnel_b"
c   Abaqus Part #      : 7
c   Abaqus Part Name   : "Pedestrian_Tunnel_b_sub2"
c   MCNP Pseudo-cell # : 7
c   Material           : "Air-(Dry,-Near-Sea-Level)_1"
c    MCNP Material     : m1
c    Density           : 4.988e-05 atoms/b-cm
c   Mesh Data
c     Meshed Volume    : 6.31639e+06 cm**3
c     # Cells          : 221096
c     % of Total Cells : 7.10%
c
c   Attila Region #    : 5
c   Attila Region Name : "Pedestrian_Tunnel_b"
c   Abaqus Part #      : 8
c   Abaqus Part Name   : "Pedestrian_Tunnel_b_sub3"
```

```
c  MCNP Pseudo-cell # : 8
c  Material          : "Air-(Dry,-Near-Sea-Level)_1"
c   MCNP Material     : m1
c   Density           : 4.988e-05 atoms/b-cm
c  Mesh Data
c    Meshed Volume    : 6.38886e+06 cm**3
c    # Cells          : 221067
c    % of Total Cells : 7.10%
c
c  Attila Region #    : 5
c  Attila Region Name : "Pedestrian_Tunnel_b"
c  Abaqus Part #      : 9
c  Abaqus Part Name   : "Pedestrian_Tunnel_b_sub4"
c  MCNP Pseudo-cell # : 9
c  Material          : "Air-(Dry,-Near-Sea-Level)_1"
c   MCNP Material     : m1
c   Density           : 4.988e-05 atoms/b-cm
c  Mesh Data
c    Meshed Volume    : 6.32098e+06 cm**3
c    # Cells          : 221099
c    % of Total Cells : 7.10%
c
c  Attila Region #    : 5
c  Attila Region Name : "Pedestrian_Tunnel_b"
c  Abaqus Part #      : 10
c  Abaqus Part Name   : "Pedestrian_Tunnel_b_sub5"
c  MCNP Pseudo-cell # : 10
c  Material          : "Air-(Dry,-Near-Sea-Level)_1"
c   MCNP Material     : m1
c   Density           : 4.988e-05 atoms/b-cm
c  Mesh Data
c    Meshed Volume    : 6.31817e+06 cm**3
c    # Cells          : 220960
c    % of Total Cells : 7.10%
c
c  Attila Region #    : 6
c  Attila Region Name : "Pedestrian_Tunnel_c"
c  Abaqus Part #      : 11
c  Abaqus Part Name   : "Pedestrian_Tunnel_c"
c  MCNP Pseudo-cell # : 11
c  Material          : "Air-(Dry,-Near-Sea-Level)_1"
c   MCNP Material     : m1
c   Density           : 4.988e-05 atoms/b-cm
c  Mesh Data
c    Meshed Volume    : 3.82518e+07 cm**3
c    # Cells          : 50506
```

```
c    % of Total Cells : 1.62%
c
c  Attila Region #    : 7
c  Attila Region Name : "Tunnel_A4"
c  Abaqus Part #      : 12
c  Abaqus Part Name   : "Tunnel_A4"
c  MCNP Pseudo-cell # : 12
c  Material           : "Air-(Dry,-Near-Sea-Level)_1"
c   MCNP Material     : m1
c   Density           : 4.988e-05 atoms/b-cm
c  Mesh Data
c    Meshed Volume    : 5.12969e+08 cm**3
c    # Cells          : 3878
c    % of Total Cells : 0.12%
c
c  Attila Region #    : 8
c  Attila Region Name : "Tunnel_A3"
c  Abaqus Part #      : 13
c  Abaqus Part Name   : "Tunnel_A3"
c  MCNP Pseudo-cell # : 13
c  Material           : "Air-(Dry,-Near-Sea-Level)_1"
c   MCNP Material     : m1
c   Density           : 4.988e-05 atoms/b-cm
c  Mesh Data
c    Meshed Volume    : 5.29723e+08 cm**3
c    # Cells          : 4896
c    % of Total Cells : 0.16%
c
c  Attila Region #    : 9
c  Attila Region Name : "Tunnel_A2"
c  Abaqus Part #      : 14
c  Abaqus Part Name   : "Tunnel_A2"
c  MCNP Pseudo-cell # : 14
c  Material           : "Air-(Dry,-Near-Sea-Level)_1"
c   MCNP Material     : m1
c   Density           : 4.988e-05 atoms/b-cm
c  Mesh Data
c    Meshed Volume    : 5.08604e+08 cm**3
c    # Cells          : 3400
c    % of Total Cells : 0.11%
c
c  Attila Region #    : 10
c  Attila Region Name : "Tunnel_A1"
c  Abaqus Part #      : 15
c  Abaqus Part Name   : "Tunnel_A1"
c  MCNP Pseudo-cell # : 15
```

```
c  Material          : "Air-(Dry,-Near-Sea-Level)_1"
c   MCNP Material     : m1
c   Density           : 4.988e-05 atoms/b-cm
c  Mesh Data
c    Meshed Volume    : 1.52562e+09 cm**3
c    # Cells          : 8657
c    % of Total Cells : 0.28%
c
c  Attila Region #    : 11
c  Attila Region Name : "Tunnel_A52"
c  Abaqus Part #      : 16
c  Abaqus Part Name   : "Tunnel_A52"
c  MCNP Pseudo-cell # : 16
c  Material          : "Air-(Dry,-Near-Sea-Level)_1"
c   MCNP Material     : m1
c   Density           : 4.988e-05 atoms/b-cm
c  Mesh Data
c    Meshed Volume    : 5.08526e+08 cm**3
c    # Cells          : 3302
c    % of Total Cells : 0.11%
c
c  Attila Region #    : 12
c  Attila Region Name : "Tunnel_B1"
c  Abaqus Part #      : 17
c  Abaqus Part Name   : "Tunnel_B1"
c  MCNP Pseudo-cell # : 17
c  Material          : "Air-(Dry,-Near-Sea-Level)_1"
c   MCNP Material     : m1
c   Density           : 4.988e-05 atoms/b-cm
c  Mesh Data
c    Meshed Volume    : 8.36004e+08 cm**3
c    # Cells          : 2158
c    % of Total Cells : 0.07%
c
c  Attila Region #    : 13
c  Attila Region Name : "Tunnel_B2"
c  Abaqus Part #      : 18
c  Abaqus Part Name   : "Tunnel_B2"
c  MCNP Pseudo-cell # : 18
c  Material          : "Air-(Dry,-Near-Sea-Level)_1"
c   MCNP Material     : m1
c   Density           : 4.988e-05 atoms/b-cm
c  Mesh Data
c    Meshed Volume    : 8.18194e+08 cm**3
c    # Cells          : 2060
c    % of Total Cells : 0.07%
```

```
c
c   Attila Region #    : 14
c   Attila Region Name : "Tunnel_B3"
c   Abaqus Part #      : 19
c   Abaqus Part Name   : "Tunnel_B3"
c   MCNP Pseudo-cell # : 19
c   Material           : "Air-(Dry,-Near-Sea-Level)_1"
c    MCNP Material     : m1
c    Density           : 4.988e-05 atoms/b-cm
c   Mesh Data
c     Meshed Volume    : 8.28163e+08 cm**3
c     # Cells          : 4148
c     % of Total Cells : 0.13%
c
c   Attila Region #    : 15
c   Attila Region Name : "Tunnel_B4"
c   Abaqus Part #      : 20
c   Abaqus Part Name   : "Tunnel_B4"
c   MCNP Pseudo-cell # : 20
c   Material           : "Air-(Dry,-Near-Sea-Level)_1"
c    MCNP Material     : m1
c    Density           : 4.988e-05 atoms/b-cm
c   Mesh Data
c     Meshed Volume    : 8.23439e+08 cm**3
c     # Cells          : 2090
c     % of Total Cells : 0.07%
c
c   Attila Region #    : 16
c   Attila Region Name : "Tunnel_B5"
c   Abaqus Part #      : 21
c   Abaqus Part Name   : "Tunnel_B5"
c   MCNP Pseudo-cell # : 21
c   Material           : "Air-(Dry,-Near-Sea-Level)_1"
c    MCNP Material     : m1
c    Density           : 4.988e-05 atoms/b-cm
c   Mesh Data
c     Meshed Volume    : 8.0928e+08 cm**3
c     # Cells          : 1822
c     % of Total Cells : 0.06%
c
c   Attila Region #    : 17
c   Attila Region Name : "Tunnel_B6"
c   Abaqus Part #      : 22
c   Abaqus Part Name   : "Tunnel_B6"
c   MCNP Pseudo-cell # : 22
c   Material           : "Air-(Dry,-Near-Sea-Level)_1"
```

```
c   MCNP Material     : m1
c   Density           : 4.988e-05 atoms/b-cm
c  Mesh Data
c    Meshed Volume    : 1.67694e+09 cm**3
c    # Cells          : 3956
c    % of Total Cells : 0.13%
c
c  Attila Region #    : 18
c  Attila Region Name : "Pedestrian_Tunnel_c1"
c  Abaqus Part #      : 23
c  Abaqus Part Name   : "Pedestrian_Tunnel_c1"
c  MCNP Pseudo-cell # : 23
c  Material           : "Air-(Dry,-Near-Sea-Level)_1"
c   MCNP Material     : m1
c   Density           : 4.988e-05 atoms/b-cm
c  Mesh Data
c    Meshed Volume    : 4.72747e+07 cm**3
c    # Cells          : 1450
c    % of Total Cells : 0.05%
c
c  Attila Region #    : 19
c  Attila Region Name : "Pedestrian_Tunnel_b1"
c  Abaqus Part #      : 24
c  Abaqus Part Name   : "Pedestrian_Tunnel_b1_sub1"
c  MCNP Pseudo-cell # : 24
c  Material           : "Air-(Dry,-Near-Sea-Level)_1"
c   MCNP Material     : m1
c   Density           : 4.988e-05 atoms/b-cm
c  Mesh Data
c    Meshed Volume    : 6.41161e+06 cm**3
c    # Cells          : 221556
c    % of Total Cells : 7.12%
c
c  Attila Region #    : 19
c  Attila Region Name : "Pedestrian_Tunnel_b1"
c  Abaqus Part #      : 25
c  Abaqus Part Name   : "Pedestrian_Tunnel_b1_sub2"
c  MCNP Pseudo-cell # : 25
c  Material           : "Air-(Dry,-Near-Sea-Level)_1"
c   MCNP Material     : m1
c   Density           : 4.988e-05 atoms/b-cm
c  Mesh Data
c    Meshed Volume    : 6.34579e+06 cm**3
c    # Cells          : 221556
c    % of Total Cells : 7.12%
c
```

```
c  Attila Region #    : 19
c  Attila Region Name : "Pedestrian_Tunnel_b1"
c  Abaqus Part #      : 26
c  Abaqus Part Name   : "Pedestrian_Tunnel_b1_sub3"
c  MCNP Pseudo-cell # : 26
c  Material           : "Air-(Dry,-Near-Sea-Level)_1"
c   MCNP Material     : m1
c   Density           : 4.988e-05 atoms/b-cm
c  Mesh Data
c    Meshed Volume    : 6.35786e+06 cm**3
c    # Cells          : 221526
c    % of Total Cells : 7.12%
c
c  Attila Region #    : 19
c  Attila Region Name : "Pedestrian_Tunnel_b1"
c  Abaqus Part #      : 27
c  Abaqus Part Name   : "Pedestrian_Tunnel_b1_sub4"
c  MCNP Pseudo-cell # : 27
c  Material           : "Air-(Dry,-Near-Sea-Level)_1"
c   MCNP Material     : m1
c   Density           : 4.988e-05 atoms/b-cm
c  Mesh Data
c    Meshed Volume    : 6.34373e+06 cm**3
c    # Cells          : 221540
c    % of Total Cells : 7.12%
c
c  Attila Region #    : 19
c  Attila Region Name : "Pedestrian_Tunnel_b1"
c  Abaqus Part #      : 28
c  Abaqus Part Name   : "Pedestrian_Tunnel_b1_sub5"
c  MCNP Pseudo-cell # : 28
c  Material           : "Air-(Dry,-Near-Sea-Level)_1"
c   MCNP Material     : m1
c   Density           : 4.988e-05 atoms/b-cm
c  Mesh Data
c    Meshed Volume    : 6.3303e+06 cm**3
c    # Cells          : 221514
c    % of Total Cells : 7.12%
c
c  Attila Region #    : 19
c  Attila Region Name : "Pedestrian_Tunnel_b1"
c  Abaqus Part #      : 29
c  Abaqus Part Name   : "Pedestrian_Tunnel_b1_sub6"
c  MCNP Pseudo-cell # : 29
c  Material           : "Air-(Dry,-Near-Sea-Level)_1"
c   MCNP Material     : m1
```

```
c   Density           : 4.988e-05 atoms/b-cm
c  Mesh Data
c    Meshed Volume    : 6.23194e+06 cm**3
c    # Cells          : 221514
c    % of Total Cells : 7.12%
c
c  Attila Region #    : 19
c  Attila Region Name : "Pedestrian_Tunnel_b1"
c  Abaqus Part #      : 30
c  Abaqus Part Name   : "Pedestrian_Tunnel_b1_sub7"
c  MCNP Pseudo-cell # : 30
c  Material           : "Air-(Dry,-Near-Sea-Level)_1"
c   MCNP Material     : m1
c   Density           : 4.988e-05 atoms/b-cm
c  Mesh Data
c    Meshed Volume    : 6.27113e+06 cm**3
c    # Cells          : 221367
c    % of Total Cells : 7.11%
c
c ------------------------ End Input Information ---------------------------- 80
c
c ----------------------------- Cell Cards ---------------------------------- 80
1   1   4.988e-05   0                        u=1
2   2   0.07186     0                        u=1
3   2   0.07186     0                        u=1
4   1   4.988e-05   0                        u=1
5   1   4.988e-05   0                        u=1
6   1   4.988e-05   0                        u=1
7   1   4.988e-05   0                        u=1
8   1   4.988e-05   0                        u=1
9   1   4.988e-05   0                        u=1
10   1   4.988e-05   0                       u=1
11   1   4.988e-05   0                       u=1
12   1   4.988e-05   0                       u=1
13   1   4.988e-05   0                       u=1
14   1   4.988e-05   0                       u=1
15   1   4.988e-05   0                       u=1
16   1   4.988e-05   0                       u=1
17   1   4.988e-05   0                       u=1
18   1   4.988e-05   0                       u=1
19   1   4.988e-05   0                       u=1
20   1   4.988e-05   0                       u=1
21   1   4.988e-05   0                       u=1
22   1   4.988e-05   0                       u=1
23   1   4.988e-05   0                       u=1
24   1   4.988e-05   0                       u=1
```

```
25   1    4.988e-05   0                         u=1
26   1    4.988e-05   0                         u=1
27   1    4.988e-05   0                         u=1
28   1    4.988e-05   0                         u=1
29   1    4.988e-05   0                         u=1
30   1    4.988e-05   0                         u=1
31   0              0                       u=1 $ background
32   0              100 -101 102 -103 104 -105   fill=1 $ fill cell
33   0              (-100:101:-102:103:-104:105)
c -------------------------- End Cell Cards -------------------------------- 80

c ---------------------------- Surface Cards -------------------------------- 80
c
100 px 8002.73
101 px 17697
102 py -9018.61
103 py -1436.33
104 pz -1860.99
105 pz 1335.66
c ------------------------- End Surface Cards ------------------------------ 80

c ---------------------------- Data Cards ---------------------------------- 80
c Embedded Geometry Specification
embed1 meshgeo=abaqus mgeoin=road_tunnel_55.mesh.abaq
      meeout=run9xc.mcnp.eeout
      filetype=ascii
      background=31
      matcell= 1 1 2 2 3 3 4 4 5 5 6 6 7 7 8 8 9 9 10 10 11 11 12 12 13 13 &
      14 14 15 15 16 16 17 17 18 18 19 19 20 20 21 21 22 22 23 23 24 24 25 &
      25 26 26 27 27 28 28 29 29 30 30
c
c Materials
c
c  Material 1: "Air-(Dry,-Near-Sea-Level)_1"
c  Constituents (atom %):
c c12-6012 (0.00014841) c13-6013 (1.59e-06) n14-7014 (0.784431)
c o16-8016 (0.210748) ar36-18036 (1.55825e-05) ar38-18038 (2.93806e-06)
c ar40-18040 (0.00465248)
m1  6012 0.00014841 6013 1.59e-06 7014 0.784431 8016 0.210748 18036 &
1.55825e-05 18038 2.93806e-06 18040 0.00465248
c
c  Material 2: "Concrete,-Los-Alamos-(MCNP)_2"
c  Constituents (atom %):
```

```
c h1-1001 (0.084739) o16-8016 (0.604079) na23-11023 (0.012523)
c al27-13027 (0.024842) si28-14028 (0.223183) si29-14029 (0.0113025)
c si30-14030 (0.00743544) ca40-20040 (0.0264106) ca42-20042 (0.000176269)
c ca43-20043 (3.67794e-05) ca44-20044 (0.00056831) ca46-20046 (1.08976e-06)
c ca48-20048 (5.09463e-05) fe54-26054 (0.000271909) fe56-26056 (0.0042684)
c fe57-26057 (9.85759e-05) fe58-26058 (1.31186e-05)
m2  1001 0.084739 8016 0.604079 11023 0.012523 13027 0.024842 14028 &
0.223183 14029 0.0113025 14030 0.00743544 20040 0.0264106 20042 &
0.000176269 20043 3.67794e-05 20044 0.00056831 20046 1.08976e-06 20048 &
5.09463e-05 26054 0.000271909 26056 0.0042684 26057 9.85759e-05 26058 &
1.31186e-05
c
c Mode (Only n and/or p Currently Accepted)
mode p
c
c Cell Importances
imp:p 1 1 1 1 1 1 1 1 1 1 1 1 1 1 1 1 1 1 1 1 1 1 1 1 1 1 1 1 1 1 1 1 0
c
c Source Definition
sdef pos=13900 -5450 -400 erg=d1 par=p wgt=2
c     Spectrum "Co60"
si1 L  1.17 1.33
sp1 d  1    1
c
c Histories (or Computer Time Cutoff)
nps 1E7
c ctme 1
c
c
c Tallies or embee cards
c embee4 tally "Dose"
embee4:p embed=1 errors=yes
c embde/embdf4 user-defined response function "Gamma":  ICRP 116
c            AP dose response
embde4  0.01              0.015              0.02              &
     0.03              0.04              0.05              &
     0.06              0.07000000000000001 0.08              &
     0.1               0.15              0.2               &
     0.3               0.4               0.5               &
     0.511              0.6               0.662              &
```

```
         0.8        1         1.117       &
         1.33       1.5       2           &
         3          4         5           &
         6          6.129     8           &
         10         15        20          &
         30         40        50
    embdf4  0          6.85e-14     1.56e-13      &
         2.25e-13    3.13e-13    3.51e-13     &
         3.7e-13     3.9e-13     4.13e-13     &
         4.44e-13    5.19e-13    7.48e-13     &
         1e-12       1.51e-12    2e-12        &
         2.47e-12    2.52e-12    2.91e-12     &
         3.17e-12    3.73e-12    4.49e-12     &
         4.9e-12     5.59e-12    6.12e-12     &
         7.48e-12    9.75e-12    1.17e-11     &
         1.34e-11    1.5e-11     1.51e-11     &
         1.78e-11    2.05e-11    2.61e-11     &
         3.08e-11    3.79e-11    4.31e-11
    c
    c
    c Write the MCTAL file
    prdmp j j 1
    c
    c L'Ecuyer 63-bit random number generator (period=9.2E18)
    rand gen=2
    c
    print -85 -86 -87 -98
    c
    c --------------------------- End Data Cards -------------------------------- 80
    c End MCNP Input
```

```
***************************************************
* Random Number Generator  =                    2 *
* Random Number Seed       =                    1 *
* Random Number Multiplier =  9219741426499971445 *
* Random Number Adder      =                    1 *
* Random Number Bits Used  =                   63 *
* Random Number Stride     =               152917 *
***************************************************
```

```
***************************************
***** ABAQUS Input File Statistics *****
***************************************
```

File: road_tunnel_55.mesh.abaq

Number of Parts	30
Number of Assemblies	1
Number of Instances	30
Number of Materials	2

Number of Parts with 1st Order Tets	30
Number of Parts with 1st Order Pents	0
Number of Parts with 1st Order Hexs	0
Number of Parts with 2nd Order Tets	0
Number of Parts with 2nd Order Pents	0
Number of Parts with 2nd Order Hexs	0

UNASSEMBLED Maximums

Total Number of 1st Order Tets	3113097
Total Number of 1st Order Pents	0
Total Number of 1st Order Hexs	0
Total Number of 2nd Order Tets	0
Total Number of 2nd Order Pents	0
Total Number of 2nd Order Hexs	0
Total Number of Elements	3113097
Total Number of Nodes	618113
Max Number of Pseudo-Cells	60

PART Maximums

Maximum Number of Nodes	44043
Maximum Number of 1st Order Tets	221556
Maximum Number of 1st Order Pents	0
Maximum Number of 1st Order Hexs	0
Maximum Number of 2nd Order Tets	0
Maximum Number of 2nd Order Pents	0
Maximum Number of 2nd Order Hexs	0
Maximum Number of Elements	221556
Maximum Number of Materials	1
Maximum Number of Volume Source Sets	0
Maximum Number of Statistical Regions	1
Maximum Number of Material Elements	221556
Maximum Number of Statistical Region Elements	221556

ASSEMBLED Maximums

Total Number of Pseudo-Cells	30
Total Number of Elements	3113097
Total Number of Nodes	618113

****
***** PART DATA *****
****

***** PART # 1 tunnel_a5

Number of 1st Order Tets	13857
Number of 1st Order Pents	0
Number of 1st Order Hexs	0
Number of 2nd Order Tets	0
Number of 2nd Order Pents	0
Number of 2nd Order Hexs	0
Number of Nodes	3372
Number of Materials	1
Number of Statistical Regions	1
Number of Source Sets	0
Maximum Number in any Part Set	
Material Elements	13857
Statistical Elements	13857

***** PART # 2 mountain_sub1

Number of 1st Order Tets	152055
Number of 1st Order Pents	0
Number of 1st Order Hexs	0
Number of 2nd Order Tets	0
Number of 2nd Order Pents	0
Number of 2nd Order Hexs	0
Number of Nodes	36889
Number of Materials	1
Number of Statistical Regions	1
Number of Source Sets	0
Maximum Number in any Part Set	
Material Elements	152055
Statistical Elements	152055

***** PART # 3 mountain_sub2

Number of 1st Order Tets	147114
Number of 1st Order Pents	0
Number of 1st Order Hexs	0
Number of 2nd Order Tets	0
Number of 2nd Order Pents	0
Number of 2nd Order Hexs	0

Number of Nodes 40060
Number of Materials 1
Number of Statistical Regions 1
Number of Source Sets 0
Maximum Number in any Part Set
Material Elements 147114
Statistical Elements 147114

***** PART # 4 pedestrian_tunnel_a

Number of 1st Order Tets 49459
Number of 1st Order Pents 0
Number of 1st Order Hexs 0
Number of 2nd Order Tets 0
Number of 2nd Order Pents 0
Number of 2nd Order Hexs 0
Number of Nodes 11835
Number of Materials 1
Number of Statistical Regions 1
Number of Source Sets 0
Maximum Number in any Part Set
Material Elements 49459
Statistical Elements 49459

***** PART # 5 pedestrian_tunnel_d

Number of 1st Order Tets 2413
Number of 1st Order Pents 0
Number of 1st Order Hexs 0
Number of 2nd Order Tets 0
Number of 2nd Order Pents 0
Number of 2nd Order Hexs 0
Number of Nodes 700
Number of Materials 1
Number of Statistical Regions 1
Number of Source Sets 0
Maximum Number in any Part Set
Material Elements 2413
Statistical Elements 2413

***** PART # 6 pedestrian_tunnel_b_sub1

Number of 1st Order Tets 221081
Number of 1st Order Pents 0
Number of 1st Order Hexs 0
Number of 2nd Order Tets 0

Number of 2nd Order Pents	0
Number of 2nd Order Hexs	0
Number of Nodes	40775
Number of Materials	1
Number of Statistical Regions	1
Number of Source Sets	0
Maximum Number in any Part Set	
Material Elements	221081
Statistical Elements	221081

***** PART # 7 pedestrian_tunnel_b_sub2

Number of 1st Order Tets	221096
Number of 1st Order Pents	0
Number of 1st Order Hexs	0
Number of 2nd Order Tets	0
Number of 2nd Order Pents	0
Number of 2nd Order Hexs	0
Number of Nodes	41096
Number of Materials	1
Number of Statistical Regions	1
Number of Source Sets	0
Maximum Number in any Part Set	
Material Elements	221096
Statistical Elements	221096

***** PART # 8 pedestrian_tunnel_b_sub3

Number of 1st Order Tets	221067
Number of 1st Order Pents	0
Number of 1st Order Hexs	0
Number of 2nd Order Tets	0
Number of 2nd Order Pents	0
Number of 2nd Order Hexs	0
Number of Nodes	40727
Number of Materials	1
Number of Statistical Regions	1
Number of Source Sets	0
Maximum Number in any Part Set	
Material Elements	221067
Statistical Elements	221067

***** PART # 9 pedestrian_tunnel_b_sub4

Number of 1st Order Tets	221099
Number of 1st Order Pents	0

Number of 1st Order Hexs	0
Number of 2nd Order Tets	0
Number of 2nd Order Pents	0
Number of 2nd Order Hexs	0
Number of Nodes	41441
Number of Materials	1
Number of Statistical Regions	1
Number of Source Sets	0
Maximum Number in any Part Set	
Material Elements	221099
Statistical Elements	221099

***** PART # 10 pedestrian_tunnel_b_sub5

Number of 1st Order Tets	220960
Number of 1st Order Pents	0
Number of 1st Order Hexs	0
Number of 2nd Order Tets	0
Number of 2nd Order Pents	0
Number of 2nd Order Hexs	0
Number of Nodes	44043
Number of Materials	1
Number of Statistical Regions	1
Number of Source Sets	0
Maximum Number in any Part Set	
Material Elements	220960
Statistical Elements	220960

***** PART # 11 pedestrian_tunnel_c

Number of 1st Order Tets	50506
Number of 1st Order Pents	0
Number of 1st Order Hexs	0
Number of 2nd Order Tets	0
Number of 2nd Order Pents	0
Number of 2nd Order Hexs	0
Number of Nodes	11867
Number of Materials	1
Number of Statistical Regions	1
Number of Source Sets	0
Maximum Number in any Part Set	
Material Elements	50506
Statistical Elements	50506

***** PART # 12 tunnel_a4

Number of 1st Order Tets	3878
Number of 1st Order Pents	0
Number of 1st Order Hexs	0
Number of 2nd Order Tets	0
Number of 2nd Order Pents	0
Number of 2nd Order Hexs	0
Number of Nodes	1092
Number of Materials	1
Number of Statistical Regions	1
Number of Source Sets	0
Maximum Number in any Part Set	
Material Elements	3878
Statistical Elements	3878

***** PART # 13 tunnel_a3

Number of 1st Order Tets	4896
Number of 1st Order Pents	0
Number of 1st Order Hexs	0
Number of 2nd Order Tets	0
Number of 2nd Order Pents	0
Number of 2nd Order Hexs	0
Number of Nodes	1318
Number of Materials	1
Number of Statistical Regions	1
Number of Source Sets	0
Maximum Number in any Part Set	
Material Elements	4896
Statistical Elements	4896

***** PART # 14 tunnel_a2

Number of 1st Order Tets	3400
Number of 1st Order Pents	0
Number of 1st Order Hexs	0
Number of 2nd Order Tets	0
Number of 2nd Order Pents	0
Number of 2nd Order Hexs	0
Number of Nodes	959
Number of Materials	1
Number of Statistical Regions	1
Number of Source Sets	0
Maximum Number in any Part Set	
Material Elements	3400
Statistical Elements	3400

***** PART # 15 tunnel_a1

Number of 1st Order Tets	8657
Number of 1st Order Pents	0
Number of 1st Order Hexs	0
Number of 2nd Order Tets	0
Number of 2nd Order Pents	0
Number of 2nd Order Hexs	0
Number of Nodes	2173
Number of Materials	1
Number of Statistical Regions	1
Number of Source Sets	0
Maximum Number in any Part Set	
Material Elements	8657
Statistical Elements	8657

***** PART # 16 tunnel_a52

Number of 1st Order Tets	3302
Number of 1st Order Pents	0
Number of 1st Order Hexs	0
Number of 2nd Order Tets	0
Number of 2nd Order Pents	0
Number of 2nd Order Hexs	0
Number of Nodes	929
Number of Materials	1
Number of Statistical Regions	1
Number of Source Sets	0
Maximum Number in any Part Set	
Material Elements	3302
Statistical Elements	3302

***** PART # 17 tunnel_b1

Number of 1st Order Tets	2158
Number of 1st Order Pents	0
Number of 1st Order Hexs	0
Number of 2nd Order Tets	0
Number of 2nd Order Pents	0
Number of 2nd Order Hexs	0
Number of Nodes	648
Number of Materials	1
Number of Statistical Regions	1
Number of Source Sets	0
Maximum Number in any Part Set	
Material Elements	2158

Statistical Elements 2158

***** PART # 18 tunnel_b2

Number of 1st Order Tets 2060
Number of 1st Order Pents 0
Number of 1st Order Hexs 0
Number of 2nd Order Tets 0
Number of 2nd Order Pents 0
Number of 2nd Order Hexs 0
Number of Nodes 589
Number of Materials 1
Number of Statistical Regions 1
Number of Source Sets 0
Maximum Number in any Part Set
Material Elements 2060
Statistical Elements 2060

***** PART # 19 tunnel_b3

Number of 1st Order Tets 4148
Number of 1st Order Pents 0
Number of 1st Order Hexs 0
Number of 2nd Order Tets 0
Number of 2nd Order Pents 0
Number of 2nd Order Hexs 0
Number of Nodes 1079
Number of Materials 1
Number of Statistical Regions 1
Number of Source Sets 0
Maximum Number in any Part Set
Material Elements 4148
Statistical Elements 4148

***** PART # 20 tunnel_b4

Number of 1st Order Tets 2090
Number of 1st Order Pents 0
Number of 1st Order Hexs 0
Number of 2nd Order Tets 0
Number of 2nd Order Pents 0
Number of 2nd Order Hexs 0
Number of Nodes 603
Number of Materials 1
Number of Statistical Regions 1
Number of Source Sets 0

Maximum Number in any Part Set
Material Elements 2090
Statistical Elements 2090

***** PART # 21 tunnel_b5

Number of 1st Order Tets 1822
Number of 1st Order Pents 0
Number of 1st Order Hexs 0
Number of 2nd Order Tets 0
Number of 2nd Order Pents 0
Number of 2nd Order Hexs 0
Number of Nodes 539
Number of Materials 1
Number of Statistical Regions 1
Number of Source Sets 0
Maximum Number in any Part Set
Material Elements 1822
Statistical Elements 1822

***** PART # 22 tunnel_b6

Number of 1st Order Tets 3956
Number of 1st Order Pents 0
Number of 1st Order Hexs 0
Number of 2nd Order Tets 0
Number of 2nd Order Pents 0
Number of 2nd Order Hexs 0
Number of Nodes 1127
Number of Materials 1
Number of Statistical Regions 1
Number of Source Sets 0
Maximum Number in any Part Set
Material Elements 3956
Statistical Elements 3956

***** PART # 23 pedestrian_tunnel_c1

Number of 1st Order Tets 1450
Number of 1st Order Pents 0
Number of 1st Order Hexs 0
Number of 2nd Order Tets 0
Number of 2nd Order Pents 0
Number of 2nd Order Hexs 0
Number of Nodes 433
Number of Materials 1

Number of Statistical Regions 1
Number of Source Sets 0
Maximum Number in any Part Set
Material Elements 1450
Statistical Elements 1450

***** PART # 24 pedestrian_tunnel_b1_sub1

Number of 1st Order Tets 221556
Number of 1st Order Pents 0
Number of 1st Order Hexs 0
Number of 2nd Order Tets 0
Number of 2nd Order Pents 0
Number of 2nd Order Hexs 0
Number of Nodes 41138
Number of Materials 1
Number of Statistical Regions 1
Number of Source Sets 0
Maximum Number in any Part Set
Material Elements 221556
Statistical Elements 221556

***** PART # 25 pedestrian_tunnel_b1_sub2

Number of 1st Order Tets 221556
Number of 1st Order Pents 0
Number of 1st Order Hexs 0
Number of 2nd Order Tets 0
Number of 2nd Order Pents 0
Number of 2nd Order Hexs 0
Number of Nodes 41790
Number of Materials 1
Number of Statistical Regions 1
Number of Source Sets 0
Maximum Number in any Part Set
Material Elements 221556
Statistical Elements 221556

***** PART # 26 pedestrian_tunnel_b1_sub3

Number of 1st Order Tets 221526
Number of 1st Order Pents 0
Number of 1st Order Hexs 0
Number of 2nd Order Tets 0
Number of 2nd Order Pents 0
Number of 2nd Order Hexs 0

Number of Nodes	42102
Number of Materials	1
Number of Statistical Regions	1
Number of Source Sets	0
Maximum Number in any Part Set	
Material Elements	221526
Statistical Elements	221526

***** PART # 27 pedestrian_tunnel_b1_sub4

Number of 1st Order Tets	221540
Number of 1st Order Pents	0
Number of 1st Order Hexs	0
Number of 2nd Order Tets	0
Number of 2nd Order Pents	0
Number of 2nd Order Hexs	0
Number of Nodes	41516
Number of Materials	1
Number of Statistical Regions	1
Number of Source Sets	0
Maximum Number in any Part Set	
Material Elements	221540
Statistical Elements	221540

***** PART # 28 pedestrian_tunnel_b1_sub5

Number of 1st Order Tets	221514
Number of 1st Order Pents	0
Number of 1st Order Hexs	0
Number of 2nd Order Tets	0
Number of 2nd Order Pents	0
Number of 2nd Order Hexs	0
Number of Nodes	41571
Number of Materials	1
Number of Statistical Regions	1
Number of Source Sets	0
Maximum Number in any Part Set	
Material Elements	221514
Statistical Elements	221514

***** PART # 29 pedestrian_tunnel_b1_sub6

Number of 1st Order Tets	221514
Number of 1st Order Pents	0
Number of 1st Order Hexs	0
Number of 2nd Order Tets	0

Number of 2nd Order Pents 0
Number of 2nd Order Hexs 0
Number of Nodes 43147
Number of Materials 1
Number of Statistical Regions 1
Number of Source Sets 0
Maximum Number in any Part Set
Material Elements 221514
Statistical Elements 221514

***** PART # 30 pedestrian_tunnel_b1_sub7

Number of 1st Order Tets 221367
Number of 1st Order Pents 0
Number of 1st Order Hexs 0
Number of 2nd Order Tets 0
Number of 2nd Order Pents 0
Number of 2nd Order Hexs 0
Number of Nodes 42555
Number of Materials 1
Number of Statistical Regions 1
Number of Source Sets 0
Maximum Number in any Part Set
Material Elements 221367
Statistical Elements 221367

****
***** MATERIAL DATA *****
****

***** MATERIAL # 1 air-(dry,-near-sea-level)_1
***** MATERIAL # 2 concrete,-los-alamos-(mcnp)_2

****
***** INSTANCE DATA *****
****

***** INSTANCE # 1 tunnel_a5P1 tunnel_a5P1
***** INSTANCE # 2 mountain_sub1P1 mountain_sub1P1
***** INSTANCE # 3 mountain_sub2P1 mountain_sub2P1
***** INSTANCE # 4 pedestrian_tunnel_aP1 pedestrian_tunnel_aP1
***** INSTANCE # 5 pedestrian_tunnel_dP1 pedestrian_tunnel_dP1
***** INSTANCE # 6 pedestrian_tunnel_b_sub1P1
pedestrian_tunnel_b_sub1P1

***** INSTANCE #   7   pedestrian_tunnel_b_sub2P1
pedestrian_tunnel_b_sub2P1
***** INSTANCE #   8   pedestrian_tunnel_b_sub3P1
pedestrian_tunnel_b_sub3P1
***** INSTANCE #   9   pedestrian_tunnel_b_sub4P1
pedestrian_tunnel_b_sub4P1
***** INSTANCE # 10   pedestrian_tunnel_b_sub5P1
pedestrian_tunnel_b_sub5P1
***** INSTANCE # 11   pedestrian_tunnel_cP1   pedestrian_tunnel_cP1
***** INSTANCE # 12   tunnel_a4P1   tunnel_a4P1
***** INSTANCE # 13   tunnel_a3P1   tunnel_a3P1
***** INSTANCE # 14   tunnel_a2P1   tunnel_a2P1
***** INSTANCE # 15   tunnel_a1P1   tunnel_a1P1
***** INSTANCE # 16   tunnel_a52P1   tunnel_a52P1
***** INSTANCE # 17   tunnel_b1P1   tunnel_b1P1
***** INSTANCE # 18   tunnel_b2P1   tunnel_b2P1
***** INSTANCE # 19   tunnel_b3P1   tunnel_b3P1
***** INSTANCE # 20   tunnel_b4P1   tunnel_b4P1
***** INSTANCE # 21   tunnel_b5P1   tunnel_b5P1
***** INSTANCE # 22   tunnel_b6P1   tunnel_b6P1
***** INSTANCE # 23   pedestrian_tunnel_c1P1   pedestrian_tunnel_c1P1
***** INSTANCE # 24   pedestrian_tunnel_b1_sub1P1
pedestrian_tunnel_b1_sub1P1
***** INSTANCE # 25   pedestrian_tunnel_b1_sub2P1
pedestrian_tunnel_b1_sub2P1
***** INSTANCE # 26   pedestrian_tunnel_b1_sub3P1
pedestrian_tunnel_b1_sub3P1
***** INSTANCE # 27   pedestrian_tunnel_b1_sub4P1
pedestrian_tunnel_b1_sub4P1
***** INSTANCE # 28   pedestrian_tunnel_b1_sub5P1
pedestrian_tunnel_b1_sub5P1
***** INSTANCE # 29   pedestrian_tunnel_b1_sub6P1
pedestrian_tunnel_b1_sub6P1
***** INSTANCE # 30   pedestrian_tunnel_b1_sub7P1
pedestrian_tunnel_b1_sub7P1

****
****
* Building the Global Tracking Model
*
****
****

Adding Instance #   1   : tunnel_a5P1   [Part:]   tunnel_a5P1

First 1st Order TET element number: 1 Last 1st Order TET element number: 13857
First 1st Order PENT element number: 0 Last 1st Order PENT element number: 0
First 1st Order HEX element number: 0 Last 1st Order HEX element number: 0
First 2nd Order TET element number: 0 Last 2nd Order TET element number: 0
First 2nd Order PENT element number: 0 Last 2nd Order PENT element number: 0
First 2nd Order HEX element number: 0 Last 2nd Order HEX element number: 0

Last GLOBAL element : 13857
Last GLOBAL node : 3372

Translate: 0.000000000000000 0.000000000000000 0.000000000000000
Rotate : 0.000000000000000 0.000000000000000 0.000000000000000
0.000000000000000 0.000000000000000 0.000000000000000
0.000000000000000

Adding Instance # 2 : mountain_sub1P1 [Part:] mountain_sub1P1

First 1st Order TET element number: 13858 Last 1st Order TET element number: 165912
First 1st Order PENT element number: 0 Last 1st Order PENT element number: 0
First 1st Order HEX element number: 0 Last 1st Order HEX element number: 0
First 2nd Order TET element number: 0 Last 2nd Order TET element number: 0
First 2nd Order PENT element number: 0 Last 2nd Order PENT element number: 0
First 2nd Order HEX element number: 0 Last 2nd Order HEX element number: 0

Last GLOBAL element : 165912
Last GLOBAL node : 40261

Translate: 0.000000000000000 0.000000000000000 0.000000000000000
Rotate : 0.000000000000000 0.000000000000000 0.000000000000000
0.000000000000000 0.000000000000000 0.000000000000000
0.000000000000000

Adding Instance # 3 : mountain_sub2P1 [Part:] mountain_sub2P1

First 1st Order TET element number: 165913 Last 1st Order TET element number: 313026
First 1st Order PENT element number: 0 Last 1st Order PENT element number: 0
First 1st Order HEX element number: 0 Last 1st Order HEX element number: 0
First 2nd Order TET element number: 0 Last 2nd Order TET element number: 0
First 2nd Order PENT element number: 0 Last 2nd Order PENT element number: 0
First 2nd Order HEX element number: 0 Last 2nd Order HEX element number: 0
Last GLOBAL element : 313026
Last GLOBAL node : 80321

Translate: 0.000000000000000 0.000000000000000 0.000000000000000
Rotate : 0.000000000000000 0.000000000000000 0.000000000000000
0.000000000000000 0.000000000000000 0.000000000000000
0.000000000000000

Adding Instance # 4 : pedestrian_tunnel_aP1 [Part:] pedestrian_tunnel_aP1

First 1st Order TET element number: 313027 Last 1st Order TET element number: 362485
First 1st Order PENT element number: 0 Last 1st Order PENT element number: 0
First 1st Order HEX element number: 0 Last 1st Order HEX element number: 0
First 2nd Order TET element number: 0 Last 2nd Order TET element number: 0
First 2nd Order PENT element number: 0 Last 2nd Order PENT element number: 0
First 2nd Order HEX element number: 0 Last 2nd Order HEX element number: 0

Last GLOBAL element : 362485
Last GLOBAL node : 92156

Translate: 0.000000000000000 0.000000000000000 0.000000000000000
Rotate : 0.000000000000000 0.000000000000000 0.000000000000000
0.000000000000000 0.000000000000000 0.000000000000000

0.000000000000000

Adding Instance # 5 : pedestrian_tunnel_dP1 [Part:] pedestrian_tunnel_dP1

First 1st Order TET element number: 362486 Last 1st Order TET element number: 364898
First 1st Order PENT element number: 0 Last 1st Order PENT element number: 0
First 1st Order HEX element number: 0 Last 1st Order HEX element number: 0
First 2nd Order TET element number: 0 Last 2nd Order TET element number: 0
First 2nd Order PENT element number: 0 Last 2nd Order PENT element number: 0
First 2nd Order HEX element number: 0 Last 2nd Order HEX element number: 0

Last GLOBAL element : 364898
Last GLOBAL node : 92856

Translate: 0.000000000000000 0.000000000000000 0.000000000000000
Rotate : 0.000000000000000 0.000000000000000 0.000000000000000
0.000000000000000 0.000000000000000 0.000000000000000
0.000000000000000

Adding Instance # 6 : pedestrian_tunnel_b_sub1P1 [Part:] pedestrian_tunnel_b_sub1P1

First 1st Order TET element number: 364899 Last 1st Order TET element number: 585979
First 1st Order PENT element number: 0 Last 1st Order PENT element number: 0
First 1st Order HEX element number: 0 Last 1st Order HEX element number: 0
First 2nd Order TET element number: 0 Last 2nd Order TET element number: 0
First 2nd Order PENT element number: 0 Last 2nd Order PENT element number: 0
First 2nd Order HEX element number: 0 Last 2nd Order HEX element number: 0
Last GLOBAL element : 585979
Last GLOBAL node : 133631

Translate: 0.000000000000000 0.000000000000000 0.000000000000000
Rotate : 0.000000000000000 0.000000000000000 0.000000000000000

0.000000000000000 0.000000000000000 0.000000000000000
0.000000000000000

Adding Instance # 7 : pedestrian_tunnel_b_sub2P1 [Part:]
pedestrian_tunnel_b_sub2P1

First 1st Order TET element number: 585980 Last 1st Order TET element number: 807075
First 1st Order PENT element number: 0 Last 1st Order PENT element number: 0
First 1st Order HEX element number: 0 Last 1st Order HEX element number: 0
First 2nd Order TET element number: 0 Last 2nd Order TET element number: 0
First 2nd Order PENT element number: 0 Last 2nd Order PENT element number: 0
First 2nd Order HEX element number: 0 Last 2nd Order HEX element number: 0
Last GLOBAL element : 807075
Last GLOBAL node : 174727

Translate: 0.000000000000000 0.000000000000000 0.000000000000000
Rotate : 0.000000000000000 0.000000000000000 0.000000000000000
0.000000000000000 0.000000000000000 0.000000000000000
0.000000000000000

Adding Instance # 8 : pedestrian_tunnel_b_sub3P1 [Part:]
pedestrian_tunnel_b_sub3P1

First 1st Order TET element number: 807076 Last 1st Order TET element number: 1028142
First 1st Order PENT element number: 0 Last 1st Order PENT element number: 0
First 1st Order HEX element number: 0 Last 1st Order HEX element number: 0
First 2nd Order TET element number: 0 Last 2nd Order TET element number: 0
First 2nd Order PENT element number: 0 Last 2nd Order PENT element number: 0
First 2nd Order HEX element number: 0 Last 2nd Order HEX element number: 0

Last GLOBAL element : 1028142
Last GLOBAL node : 215454

Translate: 0.000000000000000 0.000000000000000 0.000000000000000

Rotate : 0.000000000000000 0.000000000000000 0.000000000000000
0.000000000000000 0.000000000000000 0.000000000000000
0.000000000000000

Adding Instance # 9 : pedestrian_tunnel_b_sub4P1 [Part:] pedestrian_tunnel_b_sub4P1

First 1st Order TET element number: 1028143 Last 1st Order TET element number: 1249241
First 1st Order PENT element number: 0 Last 1st Order PENT element number: 0
First 1st Order HEX element number: 0 Last 1st Order HEX element number: 0
First 2nd Order TET element number: 0 Last 2nd Order TET element number: 0
First 2nd Order PENT element number: 0 Last 2nd Order PENT element number: 0
First 2nd Order HEX element number: 0 Last 2nd Order HEX element number: 0

Last GLOBAL element : 1249241
Last GLOBAL node : 256895

Translate: 0.000000000000000 0.000000000000000 0.000000000000000
Rotate : 0.000000000000000 0.000000000000000 0.000000000000000
0.000000000000000 0.000000000000000 0.000000000000000
0.000000000000000

Adding Instance # 10 : pedestrian_tunnel_b_sub5P1 [Part:] pedestrian_tunnel_b_sub5P1

First 1st Order TET element number: 1249242 Last 1st Order TET element number: 1470201
First 1st Order PENT element number: 0 Last 1st Order PENT element number: 0
First 1st Order HEX element number: 0 Last 1st Order HEX element number: 0
First 2nd Order TET element number: 0 Last 2nd Order TET element number: 0
First 2nd Order PENT element number: 0 Last 2nd Order PENT element number: 0
First 2nd Order HEX element number: 0 Last 2nd Order HEX element number: 0

Last GLOBAL element : 1470201
Last GLOBAL node : 300938

Translate: 0.000000000000000 0.000000000000000 0.000000000000000
Rotate : 0.000000000000000 0.000000000000000 0.000000000000000
0.000000000000000 0.000000000000000 0.000000000000000
0.000000000000000

Adding Instance # 11 : pedestrian_tunnel_cP1 [Part:] pedestrian_tunnel_cP1

First 1st Order TET element number: 1470202 Last 1st Order TET element number: 1520707
First 1st Order PENT element number: 0 Last 1st Order PENT element number: 0
First 1st Order HEX element number: 0 Last 1st Order HEX element number: 0
First 2nd Order TET element number: 0 Last 2nd Order TET element number: 0
First 2nd Order PENT element number: 0 Last 2nd Order PENT element number: 0
First 2nd Order HEX element number: 0 Last 2nd Order HEX element number: 0
Last GLOBAL element : 1520707
Last GLOBAL node : 312805

Translate: 0.000000000000000 0.000000000000000 0.000000000000000
Rotate : 0.000000000000000 0.000000000000000 0.000000000000000
0.000000000000000 0.000000000000000 0.000000000000000
0.000000000000000

Adding Instance # 12 : tunnel_a4P1 [Part:] tunnel_a4P1

First 1st Order TET element number: 1520708 Last 1st Order TET element number: 1524585
First 1st Order PENT element number: 0 Last 1st Order PENT element number: 0
First 1st Order HEX element number: 0 Last 1st Order HEX element number: 0
First 2nd Order TET element number: 0 Last 2nd Order TET element number: 0
First 2nd Order PENT element number: 0 Last 2nd Order PENT element number: 0
First 2nd Order HEX element number: 0 Last 2nd Order HEX element number: 0
Last GLOBAL element : 1524585
Last GLOBAL node : 313897

Translate: 0.000000000000000 0.000000000000000 0.000000000000000
Rotate : 0.000000000000000 0.000000000000000 0.000000000000000
0.000000000000000 0.000000000000000 0.000000000000000
0.000000000000000

Adding Instance # 13 : tunnel_a3P1 [Part:] tunnel_a3P1

First 1st Order TET element number: 1524586 Last 1st Order TET element number: 1529481
First 1st Order PENT element number: 0 Last 1st Order PENT element number: 0
First 1st Order HEX element number: 0 Last 1st Order HEX element number: 0
First 2nd Order TET element number: 0 Last 2nd Order TET element number: 0
First 2nd Order PENT element number: 0 Last 2nd Order PENT element number: 0
First 2nd Order HEX element number: 0 Last 2nd Order HEX element number: 0

Last GLOBAL element : 1529481
Last GLOBAL node : 315215

Translate: 0.000000000000000 0.000000000000000 0.000000000000000
Rotate : 0.000000000000000 0.000000000000000 0.000000000000000
0.000000000000000 0.000000000000000 0.000000000000000
0.000000000000000

Adding Instance # 14 : tunnel_a2P1 [Part:] tunnel_a2P1

First 1st Order TET element number: 1529482 Last 1st Order TET element number: 1532881
First 1st Order PENT element number: 0 Last 1st Order PENT element number: 0
First 1st Order HEX element number: 0 Last 1st Order HEX element number: 0
First 2nd Order TET element number: 0 Last 2nd Order TET element number: 0
First 2nd Order PENT element number: 0 Last 2nd Order PENT element number: 0
First 2nd Order HEX element number: 0 Last 2nd Order HEX element number: 0

Last GLOBAL element : 1532881
Last GLOBAL node : 316174

Translate: 0.000000000000000 0.000000000000000 0.000000000000000
Rotate : 0.000000000000000 0.000000000000000 0.000000000000000
0.000000000000000 0.000000000000000 0.000000000000000
0.000000000000000

Adding Instance # 15 : tunnel_a1P1 [Part:] tunnel_a1P1

First 1st Order TET element number: 1532882 Last 1st Order TET element number: 1541538
First 1st Order PENT element number: 0 Last 1st Order PENT element number: 0
First 1st Order HEX element number: 0 Last 1st Order HEX element number: 0
First 2nd Order TET element number: 0 Last 2nd Order TET element number: 0
First 2nd Order PENT element number: 0 Last 2nd Order PENT element number: 0
First 2nd Order HEX element number: 0 Last 2nd Order HEX element number: 0

Last GLOBAL element : 1541538
Last GLOBAL node : 318347

Translate: 0.000000000000000 0.000000000000000 0.000000000000000
Rotate : 0.000000000000000 0.000000000000000 0.000000000000000
0.000000000000000 0.000000000000000 0.000000000000000
0.000000000000000

Adding Instance # 16 : tunnel_a52P1 [Part:] tunnel_a52P1

First 1st Order TET element number: 1541539 Last 1st Order TET element number: 1544840
First 1st Order PENT element number: 0 Last 1st Order PENT element number: 0
First 1st Order HEX element number: 0 Last 1st Order HEX element number: 0
First 2nd Order TET element number: 0 Last 2nd Order TET element number: 0
First 2nd Order PENT element number: 0 Last 2nd Order PENT element number: 0
First 2nd Order HEX element number: 0 Last 2nd Order HEX element number: 0

Last GLOBAL element : 1544840
Last GLOBAL node : 319276

Translate: 0.000000000000000 0.000000000000000 0.000000000000000
Rotate : 0.000000000000000 0.000000000000000 0.000000000000000
0.000000000000000 0.000000000000000 0.000000000000000
0.000000000000000

Adding Instance # 17 : tunnel_b1P1 [Part:] tunnel_b1P1

First 1st Order TET element number: 1544841 Last 1st Order TET element number: 1546998
First 1st Order PENT element number: 0 Last 1st Order PENT element number: 0
First 1st Order HEX element number: 0 Last 1st Order HEX element number: 0
First 2nd Order TET element number: 0 Last 2nd Order TET element number: 0
First 2nd Order PENT element number: 0 Last 2nd Order PENT element number: 0
First 2nd Order HEX element number: 0 Last 2nd Order HEX element number: 0

Last GLOBAL element : 1546998
Last GLOBAL node : 319924

Translate: 0.000000000000000 0.000000000000000 0.000000000000000
Rotate : 0.000000000000000 0.000000000000000 0.000000000000000
0.000000000000000 0.000000000000000 0.000000000000000
0.000000000000000

Adding Instance # 18 : tunnel_b2P1 [Part:] tunnel_b2P1

First 1st Order TET element number: 1546999 Last 1st Order TET element number: 1549058
First 1st Order PENT element number: 0 Last 1st Order PENT element number: 0
First 1st Order HEX element number: 0 Last 1st Order HEX element number: 0
First 2nd Order TET element number: 0 Last 2nd Order TET element number: 0
First 2nd Order PENT element number: 0 Last 2nd Order PENT element number: 0
First 2nd Order HEX element number: 0 Last 2nd Order HEX element number: 0

Last GLOBAL element : 1549058
Last GLOBAL node : 320513

Translate: 0.000000000000000 0.000000000000000 0.000000000000000
Rotate : 0.000000000000000 0.000000000000000 0.000000000000000
0.000000000000000 0.000000000000000 0.000000000000000
0.000000000000000

Adding Instance # 19 : tunnel_b3P1 [Part:] tunnel_b3P1

First 1st Order TET element number: 1549059 Last 1st Order TET element number: 1553206
First 1st Order PENT element number: 0 Last 1st Order PENT element number: 0
First 1st Order HEX element number: 0 Last 1st Order HEX element number: 0
First 2nd Order TET element number: 0 Last 2nd Order TET element number: 0
First 2nd Order PENT element number: 0 Last 2nd Order PENT element number: 0
First 2nd Order HEX element number: 0 Last 2nd Order HEX element number: 0

Last GLOBAL element : 1553206
Last GLOBAL node : 321592

Translate: 0.000000000000000 0.000000000000000 0.000000000000000
Rotate : 0.000000000000000 0.000000000000000 0.000000000000000
0.000000000000000 0.000000000000000 0.000000000000000
0.000000000000000

Adding Instance # 20 : tunnel_b4P1 [Part:] tunnel_b4P1

First 1st Order TET element number: 1553207 Last 1st Order TET element number: 1555296
First 1st Order PENT element number: 0 Last 1st Order PENT element number: 0
First 1st Order HEX element number: 0 Last 1st Order HEX element number: 0
First 2nd Order TET element number: 0 Last 2nd Order TET element number: 0

First 2nd Order PENT element number: 0 Last 2nd Order PENT element number: 0
First 2nd Order HEX element number: 0 Last 2nd Order HEX element number: 0

Last GLOBAL element : 1555296
Last GLOBAL node : 322195

Translate: 0.000000000000000 0.000000000000000 0.000000000000000
Rotate : 0.000000000000000 0.000000000000000 0.000000000000000
0.000000000000000 0.000000000000000 0.000000000000000
0.000000000000000

Adding Instance # 21 : tunnel_b5P1 [Part:] tunnel_b5P1

First 1st Order TET element number: 1555297 Last 1st Order TET element number: 1557118
First 1st Order PENT element number: 0 Last 1st Order PENT element number: 0
First 1st Order HEX element number: 0 Last 1st Order HEX element number: 0
First 2nd Order TET element number: 0 Last 2nd Order TET element number: 0
First 2nd Order PENT element number: 0 Last 2nd Order PENT element number: 0
First 2nd Order HEX element number: 0 Last 2nd Order HEX element number: 0

Last GLOBAL element : 1557118
Last GLOBAL node : 322734

Translate: 0.000000000000000 0.000000000000000 0.000000000000000
Rotate : 0.000000000000000 0.000000000000000 0.000000000000000
0.000000000000000 0.000000000000000 0.000000000000000
0.000000000000000

Adding Instance # 22 : tunnel_b6P1 [Part:] tunnel_b6P1

First 1st Order TET element number: 1557119 Last 1st Order TET element number: 1561074
First 1st Order PENT element number: 0 Last 1st Order PENT element number: 0

First 1st Order HEX element number: 0 Last 1st Order HEX element number: 0
First 2nd Order TET element number: 0 Last 2nd Order TET element number: 0
First 2nd Order PENT element number: 0 Last 2nd Order PENT element number: 0
First 2nd Order HEX element number: 0 Last 2nd Order HEX element number: 0

Last GLOBAL element : 1561074
Last GLOBAL node : 323861

Translate: 0.000000000000000 0.000000000000000 0.000000000000000
Rotate : 0.000000000000000 0.000000000000000 0.000000000000000
0.000000000000000 0.000000000000000 0.000000000000000
0.000000000000000

Adding Instance # 23 : pedestrian_tunnel_c1P1 [Part:] pedestrian_tunnel_c1P1

First 1st Order TET element number: 1561075 Last 1st Order TET element number: 1562524
First 1st Order PENT element number: 0 Last 1st Order PENT element number: 0
First 1st Order HEX element number: 0 Last 1st Order HEX element number: 0
First 2nd Order TET element number: 0 Last 2nd Order TET element number: 0
First 2nd Order PENT element number: 0 Last 2nd Order PENT element number: 0
First 2nd Order HEX element number: 0 Last 2nd Order HEX element number: 0

Last GLOBAL element : 1562524
Last GLOBAL node : 324294

Translate: 0.000000000000000 0.000000000000000 0.000000000000000
Rotate : 0.000000000000000 0.000000000000000 0.000000000000000
0.000000000000000 0.000000000000000 0.000000000000000
0.000000000000000

Adding Instance # 24 : pedestrian_tunnel_b1_sub1P1 [Part:] pedestrian_tunnel_b1_sub1P1

First 1st Order TET element number: 1562525 Last 1st Order TET element number: 1784080
First 1st Order PENT element number: 0 Last 1st Order PENT element number: 0
First 1st Order HEX element number: 0 Last 1st Order HEX element number: 0
First 2nd Order TET element number: 0 Last 2nd Order TET element number: 0
First 2nd Order PENT element number: 0 Last 2nd Order PENT element number: 0
First 2nd Order HEX element number: 0 Last 2nd Order HEX element number: 0

Last GLOBAL element : 1784080
Last GLOBAL node : 365432

Translate: 0.000000000000000 0.000000000000000 0.000000000000000
Rotate : 0.000000000000000 0.000000000000000 0.000000000000000
0.000000000000000 0.000000000000000 0.000000000000000
0.000000000000000

Adding Instance # 25 : pedestrian_tunnel_b1_sub2P1 [Part:] pedestrian_tunnel_b1_sub2P1

First 1st Order TET element number: 1784081 Last 1st Order TET element number: 2005636
First 1st Order PENT element number: 0 Last 1st Order PENT element number: 0
First 1st Order HEX element number: 0 Last 1st Order HEX element number: 0
First 2nd Order TET element number: 0 Last 2nd Order TET element number: 0
First 2nd Order PENT element number: 0 Last 2nd Order PENT element number: 0
First 2nd Order HEX element number: 0 Last 2nd Order HEX element number: 0

Last GLOBAL element : 2005636
Last GLOBAL node : 407222

Translate: 0.000000000000000 0.000000000000000 0.000000000000000
Rotate : 0.000000000000000 0.000000000000000 0.000000000000000
0.000000000000000 0.000000000000000 0.000000000000000
0.000000000000000

Adding Instance # 26 : pedestrian_tunnel_b1_sub3P1 [Part:]
pedestrian_tunnel_b1_sub3P1

First 1st Order TET element number: 2005637 Last 1st Order TET element number: 2227162
First 1st Order PENT element number: 0 Last 1st Order PENT element number: 0
First 1st Order HEX element number: 0 Last 1st Order HEX element number: 0
First 2nd Order TET element number: 0 Last 2nd Order TET element number: 0
First 2nd Order PENT element number: 0 Last 2nd Order PENT element number: 0
First 2nd Order HEX element number: 0 Last 2nd Order HEX element number: 0

Last GLOBAL element : 2227162
Last GLOBAL node : 449324

Translate: 0.000000000000000 0.000000000000000 0.000000000000000
Rotate : 0.000000000000000 0.000000000000000 0.000000000000000
0.000000000000000 0.000000000000000 0.000000000000000
0.000000000000000

Adding Instance # 27 : pedestrian_tunnel_b1_sub4P1 [Part:]
pedestrian_tunnel_b1_sub4P1

First 1st Order TET element number: 2227163 Last 1st Order TET element number: 2448702
First 1st Order PENT element number: 0 Last 1st Order PENT element number: 0
First 1st Order HEX element number: 0 Last 1st Order HEX element number: 0
First 2nd Order TET element number: 0 Last 2nd Order TET element number: 0
First 2nd Order PENT element number: 0 Last 2nd Order PENT element number: 0

First 2nd Order HEX element number: 0 Last 2nd Order HEX element number: 0

Last GLOBAL element : 2448702
Last GLOBAL node : 490840

Translate: 0.000000000000000 0.000000000000000 0.000000000000000
Rotate : 0.000000000000000 0.000000000000000 0.000000000000000
0.000000000000000 0.000000000000000 0.000000000000000
0.000000000000000

Adding Instance # 28 : pedestrian_tunnel_b1_sub5P1 [Part:] pedestrian_tunnel_b1_sub5P1

First 1st Order TET element number: 2448703 Last 1st Order TET element number: 2670216
First 1st Order PENT element number: 0 Last 1st Order PENT element number: 0
First 1st Order HEX element number: 0 Last 1st Order HEX element number: 0
First 2nd Order TET element number: 0 Last 2nd Order TET element number: 0
First 2nd Order PENT element number: 0 Last 2nd Order PENT element number: 0
First 2nd Order HEX element number: 0 Last 2nd Order HEX element number: 0

Last GLOBAL element : 2670216
Last GLOBAL node : 532411

Translate: 0.000000000000000 0.000000000000000 0.000000000000000
Rotate : 0.000000000000000 0.000000000000000 0.000000000000000
0.000000000000000 0.000000000000000 0.000000000000000
0.000000000000000

Adding Instance # 29 : pedestrian_tunnel_b1_sub6P1 [Part:] pedestrian_tunnel_b1_sub6P1

First 1st Order TET element number: 2670217 Last 1st Order TET element number: 2891730
First 1st Order PENT element number: 0 Last 1st Order PENT element number: 0

First 1st Order HEX element number: 0 Last 1st Order HEX element number: 0
First 2nd Order TET element number: 0 Last 2nd Order TET element number: 0
First 2nd Order PENT element number: 0 Last 2nd Order PENT element number: 0
First 2nd Order HEX element number: 0 Last 2nd Order HEX element number: 0

Last GLOBAL element : 2891730
Last GLOBAL node : 575558

Translate: 0.000000000000000 0.000000000000000 0.000000000000000
Rotate : 0.000000000000000 0.000000000000000 0.000000000000000
0.000000000000000 0.000000000000000 0.000000000000000
0.000000000000000

Adding Instance # 30 : pedestrian_tunnel_b1_sub7P1 [Part:] pedestrian_tunnel_b1_sub7P1

First 1st Order TET element number: 2891731 Last 1st Order TET element number: 3113097
First 1st Order PENT element number: 0 Last 1st Order PENT element number: 0
First 1st Order HEX element number: 0 Last 1st Order HEX element number: 0
First 2nd Order TET element number: 0 Last 2nd Order TET element number: 0
First 2nd Order PENT element number: 0 Last 2nd Order PENT element number: 0
First 2nd Order HEX element number: 0 Last 2nd Order HEX element number: 0

Last GLOBAL element : 3113097
Last GLOBAL node : 618113

Translate: 0.000000000000000 0.000000000000000 0.000000000000000
Rotate : 0.000000000000000 0.000000000000000 0.000000000000000
0.000000000000000 0.000000000000000 0.000000000000000
0.000000000000000

Global Model Extents
Min X: 8.00773E+03 Max X: 1.76920E+04

```
   Min Y: -9.01361E+03   Max Y: -1.44133E+03
   Min Z: -1.85599E+03   Max Z:  1.33066E+03


*************************************************************************************************
******************
  * Pseudo-Cell Cross Reference Table
*

*************************************************************************************************
******************
```

Pseudo-Cell #	MCNP6 Cell #	Instance #	Part #	Material #	Material Name
1	1	1	1	1	air-(dry,-near-sea-level)_1
2	2	2	2	2	concrete,-los-alamos-(mcnp)_2
3	3	3	3	2	concrete,-los-alamos-(mcnp)_2
4	4	4	4	1	air-(dry,-near-sea-level)_1
5	5	5	5	1	air-(dry,-near-sea-level)_1
6	6	6	6	1	air-(dry,-near-sea-level)_1
7	7	7	7	1	air-(dry,-near-sea-level)_1
8	8	8	8	1	air-(dry,-near-sea-level)_1
9	9	9	9	1	air-(dry,-near-sea-level)_1
10	10	10	10	1	air-(dry,-near-sea-level)_1
11	11	11	11	1	air-(dry,-near-sea-level)_1
12	12	12	12	1	air-(dry,-near-sea-level)_1
13	13	13	13	1	air-(dry,-near-sea-level)_1
14	14	14	14	1	air-(dry,-near-sea-level)_1
15	15	15	15	1	air-(dry,-near-sea-level)_1
16	16	16	16	1	air-(dry,-near-sea-level)_1
17	17	17	17	1	air-(dry,-near-sea-level)_1
18	18	18	18	1	air-(dry,-near-sea-level)_1
19	19	19	19	1	air-(dry,-near-sea-level)_1
20	20	20	20	1	air-(dry,-near-sea-level)_1
21	21	21	21	1	air-(dry,-near-sea-level)_1
22	22	22	22	1	air-(dry,-near-sea-level)_1
23	23	23	23	1	air-(dry,-near-sea-level)_1
24	24	24	24	1	air-(dry,-near-sea-level)_1
25	25	25	25	1	air-(dry,-near-sea-level)_1
26	26	26	26	1	air-(dry,-near-sea-level)_1
27	27	27	27	1	air-(dry,-near-sea-level)_1
28	28	28	28	1	air-(dry,-near-sea-level)_1
29	29	29	29	1	air-(dry,-near-sea-level)_1
30	30	30	30	1	air-(dry,-near-sea-level)_1

```
****************************************************************************************************
*******************
 * Global Tracking Model Complete
*

****************************************************************************************************
*******************

 ***** Estimated Memory Usage for Temporary Mesh Arrays *****

                              Bytes          MB
     Character Arrays :           15360           0
     Integer Arrays   :       1232834572        1232
     Real Arrays      :         31713360          31
     Total            :       1264563292        1264


 ***** Estimated Memory Usage for Permanent Mesh Arrays *****

                              Bytes          MB
     Character Arrays :               0           0
     Integer Arrays   :        314724270         314
     Real Arrays      :       1155102200        1155
     Total            :       1469826470        1469

1source                                                                         print table 10

 values of defaulted or explicitly defined source variables

   cel      0.0000E+00
   sur      0.0000E+00
   tme      0.0000E+00
   dir      isotropic
   pos      1.3900E+04  -5.4500E+03  -4.0000E+02
   x        0.0000E+00
   y        0.0000E+00
   z        0.0000E+00
   rad      0.0000E+00
   ext      0.0000E+00
   axs      0.0000E+00   0.0000E+00   0.0000E+00
   vec      0.0000E+00   0.0000E+00   0.0000E+00
   ccc      0.0000E+00
   nrm      1.0000E+00
   ara      0.0000E+00
   wgt      2.0000E+00
```

```
   eff       1.0000E-02
   par        2.0000E+00
   tr        0.0000E+00
   bem        0.0000E+00   0.0000E+00   0.0000E+00
   bap       0.0000E+00   0.0000E+00   0.0000E+00
   loc       0.0000E+00   0.0000E+00   0.0000E+00
   dat       0.0000E+00   0.0000E+00   0.0000E+00


 probability distribution       1 for source variable erg
 unbiased discrete  distribution

 source       source          cumulative         probability
  entry        value          probability          of bin

    1      1.17000E+00       5.000000E-01       5.000000E-01
    2      1.33000E+00       1.000000E+00       5.000000E-01

     the mean of source distribution       1 is  1.2500E+00


 order of sampling source variables.
 par pos erg tme wgt

  warning.  there are no tallies in this problem.
1material composition                                                       print table 40

 material
  number     component nuclide, atom fraction

        1          6012, 1.48410E-04      6013, 1.59000E-06       7014, 7.84431E-01
8016, 2.10748E-01
                  18036, 1.55825E-05     18038, 2.93806E-06      18040, 4.65248E-03
        2          1001, 8.47390E-02      8016, 6.04079E-01      11023, 1.25230E-02
13027, 2.48420E-02
                  14028, 2.23183E-01     14029, 1.13025E-02      14030, 7.43544E-03
20040, 2.64106E-02
                  20042, 1.76269E-04     20043, 3.67794E-05      20044, 5.68310E-04
20046, 1.08976E-06
                  20048, 5.09463E-05     26054, 2.71909E-04      26056, 4.26840E-03
26057, 9.85759E-05
                  26058, 1.31186E-05
```

```
 material
  number     component nuclide, mass fraction

       1           6012, 1.22453E-04      6013, 1.42160E-06      7014, 7.55270E-01
8016, 2.31776E-01
                  18036, 3.85365E-05     18038, 7.66906E-06     18040, 1.27838E-02
       2           1001, 4.53018E-03      8016, 5.12534E-01     11023, 1.52718E-02
13027, 3.55550E-02
                  14028, 3.31214E-01     14029, 1.73727E-02     14030, 1.18221E-02
20040, 5.59860E-02
                  20042, 3.92324E-04     20043, 8.38115E-05     20044, 1.32509E-03
20046, 2.65643E-06
                  20048, 1.29590E-04     26054, 7.77998E-04     26056, 1.26647E-02
26057, 2.97715E-04
                  26058, 4.03146E-05
1cell volumes and masses                                                          print table
50

             cell     atom         gram        input      calculated                     reason
volume
                   density      density      volume       volume        mass       pieces    not
calculated

       1        1  4.98800E-05   1.20464E-03   0.00000E+00   2.54254E+09   3.06286E+06
0
       2        2  7.18600E-02   2.24955E+00   0.00000E+00   1.81527E+11
4.08354E+11      0
       3        3  7.18600E-02   2.24955E+00   0.00000E+00   3.99372E+10
8.98408E+10      0
       4        4  4.98800E-05   1.20464E-03   0.00000E+00   6.17860E+07   7.44301E+04
0
       5        5  4.98800E-05   1.20464E-03   0.00000E+00   7.51224E+07   9.04957E+04
0
       6        6  4.98800E-05   1.20464E-03   0.00000E+00   6.35125E+06   7.65099E+03
0
       7        7  4.98800E-05   1.20464E-03   0.00000E+00   6.31639E+06   7.60900E+03
0
       8        8  4.98800E-05   1.20464E-03   0.00000E+00   6.38886E+06   7.69630E+03
0
       9        9  4.98800E-05   1.20464E-03   0.00000E+00   6.32098E+06   7.61453E+03
0
      10       10  4.98800E-05   1.20464E-03   0.00000E+00   6.31817E+06
7.61114E+03      0
```

11	11	4.98800E-05	1.20464E-03	0.00000E+00	3.82518E+07	4.60798E+04	0
12	12	4.98800E-05	1.20464E-03	0.00000E+00	5.12969E+08	6.17945E+05	0
13	13	4.98800E-05	1.20464E-03	0.00000E+00	5.29723E+08	6.38128E+05	0
14	14	4.98800E-05	1.20464E-03	0.00000E+00	5.08604E+08	6.12687E+05	0
15	15	4.98800E-05	1.20464E-03	0.00000E+00	1.52562E+09	1.83783E+06	0
16	16	4.98800E-05	1.20464E-03	0.00000E+00	5.08526E+08	6.12593E+05	0
17	17	4.98800E-05	1.20464E-03	0.00000E+00	8.36004E+08	1.00709E+06	0
18	18	4.98800E-05	1.20464E-03	0.00000E+00	8.18194E+08	9.85633E+05	0
19	19	4.98800E-05	1.20464E-03	0.00000E+00	8.28163E+08	9.97641E+05	0
20	20	4.98800E-05	1.20464E-03	0.00000E+00	8.23439E+08	9.91950E+05	0
21	21	4.98800E-05	1.20464E-03	0.00000E+00	8.09280E+08	9.74894E+05	0
22	22	4.98800E-05	1.20464E-03	0.00000E+00	1.67694E+09	2.02011E+06	0
23	23	4.98800E-05	1.20464E-03	0.00000E+00	4.72747E+07	5.69492E+04	0
24	24	4.98800E-05	1.20464E-03	0.00000E+00	6.41161E+06	7.72371E+03	0
25	25	4.98800E-05	1.20464E-03	0.00000E+00	6.34579E+06	7.64442E+03	0
26	26	4.98800E-05	1.20464E-03	0.00000E+00	6.35786E+06	7.65896E+03	0
27	27	4.98800E-05	1.20464E-03	0.00000E+00	6.34373E+06	7.64193E+03	0
28	28	4.98800E-05	1.20464E-03	0.00000E+00	6.33030E+06	7.62576E+03	0
29	29	4.98800E-05	1.20464E-03	0.00000E+00	6.23194E+06	7.50727E+03	0
30	30	4.98800E-05	1.20464E-03	0.00000E+00	6.27113E+06	7.55448E+03	0
31	31	0.00000E+00	0.00000E+00	0.00000E+00	0.00000E+00	0.00000E+00	0
32	32	0.00000E+00	0.00000E+00	0.00000E+00	2.34969E+11	0.00000E+00	0
33	33	0.00000E+00	0.00000E+00	0.00000E+00	0.00000E+00	0.00000E+00	0 infinite

1surface areas print table 50

surface		input area	calculated area	reason area not calculated
1	100	0.00000E+00	2.42379E+07	
2	101	0.00000E+00	2.42379E+07	
3	102	0.00000E+00	3.09892E+07	
4	103	0.00000E+00	3.09892E+07	
5	104	0.00000E+00	7.35047E+07	
6	105	0.00000E+00	7.35047E+07	

1cells print table 60

	cell	mat	atom density	gram density	volume	mass	photon pieces	importance
1	1	1	4.98800E-05	1.20464E-03	2.54254E+09	3.06286E+06	0	1.0000E+00
2	2	2	7.18600E-02	2.24955E+00	1.81527E+11	4.08354E+11	0	1.0000E+00
3	3	2	7.18600E-02	2.24955E+00	3.99372E+10	8.98408E+10	0	1.0000E+00
4	4	1	4.98800E-05	1.20464E-03	6.17860E+07	7.44301E+04	0	1.0000E+00
5	5	1	4.98800E-05	1.20464E-03	7.51224E+07	9.04957E+04	0	1.0000E+00
6	6	1	4.98800E-05	1.20464E-03	6.35125E+06	7.65099E+03	0	1.0000E+00
7	7	1	4.98800E-05	1.20464E-03	6.31639E+06	7.60900E+03	0	1.0000E+00
8	8	1	4.98800E-05	1.20464E-03	6.38886E+06	7.69630E+03	0	1.0000E+00
9	9	1	4.98800E-05	1.20464E-03	6.32098E+06	7.61453E+03	0	1.0000E+00
10	10	1	4.98800E-05	1.20464E-03	6.31817E+06	7.61114E+03	0	1.0000E+00
11	11	1	4.98800E-05	1.20464E-03	3.82518E+07	4.60798E+04	0	1.0000E+00
12	12	1	4.98800E-05	1.20464E-03	5.12969E+08	6.17945E+05	0	1.0000E+00
13	13	1	4.98800E-05	1.20464E-03	5.29723E+08	6.38128E+05	0	1.0000E+00
14	14	1	4.98800E-05	1.20464E-03	5.08604E+08	6.12687E+05	0	1.0000E+00
15	15	1	4.98800E-05	1.20464E-03	1.52562E+09	1.83783E+06	0	1.0000E+00

```
    16      16       1  4.98800E-05 1.20464E-03 5.08526E+08 6.12593E+05          0
1.0000E+00
    17      17       1  4.98800E-05 1.20464E-03 8.36004E+08 1.00709E+06          0
1.0000E+00
    18      18       1  4.98800E-05 1.20464E-03 8.18194E+08 9.85633E+05          0
1.0000E+00
    19      19       1  4.98800E-05 1.20464E-03 8.28163E+08 9.97641E+05          0
1.0000E+00
    20      20       1  4.98800E-05 1.20464E-03 8.23439E+08 9.91950E+05          0
1.0000E+00
    21      21       1  4.98800E-05 1.20464E-03 8.09280E+08 9.74894E+05          0
1.0000E+00
    22      22       1  4.98800E-05 1.20464E-03 1.67694E+09 2.02011E+06          0
1.0000E+00
    23      23       1  4.98800E-05 1.20464E-03 4.72747E+07 5.69492E+04          0
1.0000E+00
    24      24       1  4.98800E-05 1.20464E-03 6.41161E+06 7.72371E+03          0
1.0000E+00
    25      25       1  4.98800E-05 1.20464E-03 6.34579E+06 7.64442E+03          0
1.0000E+00
    26      26       1  4.98800E-05 1.20464E-03 6.35786E+06 7.65896E+03          0
1.0000E+00
    27      27       1  4.98800E-05 1.20464E-03 6.34373E+06 7.64193E+03          0
1.0000E+00
    28      28       1  4.98800E-05 1.20464E-03 6.33030E+06 7.62576E+03          0
1.0000E+00
    29      29       1  4.98800E-05 1.20464E-03 6.23194E+06 7.50727E+03          0
1.0000E+00
    30      30       1  4.98800E-05 1.20464E-03 6.27113E+06 7.55448E+03          0
1.0000E+00
    31      31       0  0.00000E+00 0.00000E+00 0.00000E+00 0.00000E+00          0
1.0000E+00
    32      32       0  0.00000E+00 0.00000E+00 2.34969E+11 0.00000E+00          0
1.0000E+00
    33      33       0  0.00000E+00 0.00000E+00 0.00000E+00 0.00000E+00          0
0.0000E+00

 total                                  4.68651E+11 4.98210E+11
1surfaces                                                            print table 70

        surface        trans  type   surface coefficients

     1      100              px    8.0027300E+03
     2      101              px    1.7697000E+04
     3      102              py   -9.0186100E+03
     4      103              py   -1.4363300E+03
```

```
      5      104              pz   -1.8609900E+03
      6      105              pz    1.3356600E+03

   minimum source weight = 2.0000E+00    maximum source weight = 2.0000E+00

        1 warning message so far.
1cross-section tables                                                          print table 100
    XSDIR used: /home/dbo/MY_MCNP/MCNP_DATA/xsdir_mcnp6.2

    table    length

                      tables from file xdata/mcplib84

   1000.84p    1974  Update of MCPLIB04 Photon Compton Broadening Data For
MCNP5 see LA-UR-    12-00018        01/03/12
                 Energy range:   1.00000E-03  to  1.00000E+05 MeV.
   6000.84p    3228  Update of MCPLIB04 Photon Compton Broadening Data For
MCNP5 see LA-UR-    12-00018        01/03/12
                 Energy range:   1.00000E-03  to  1.00000E+05 MeV.
   7000.84p    3270  Update of MCPLIB04 Photon Compton Broadening Data For
MCNP5 see LA-UR-    12-00018        01/03/12
                 Energy range:   1.00000E-03  to  1.00000E+05 MeV.
   8000.84p    3348  Update of MCPLIB04 Photon Compton Broadening Data For
MCNP5 see LA-UR-    12-00018        01/03/12
                 Energy range:   1.00000E-03  to  1.00000E+05 MeV.
  11000.84p    4071  Update of MCPLIB04 Photon Compton Broadening Data For
MCNP5 see LA-UR-    12-00018        01/03/12
                 Energy range:   1.00000E-03  to  1.00000E+05 MeV.
  13000.84p    4922  Update of MCPLIB04 Photon Compton Broadening Data For
MCNP5 see LA-UR-    12-00018        01/03/12
                 Energy range:   1.00000E-03  to  1.00000E+05 MeV.
  14000.84p    4868  Update of MCPLIB04 Photon Compton Broadening Data For
MCNP5 see LA-UR-    12-00018        01/03/12
                 Energy range:   1.00000E-03  to  1.00000E+05 MeV.
  18000.84p    4772  Update of MCPLIB04 Photon Compton Broadening Data For
MCNP5 see LA-UR-    12-00018        01/03/12
                 Energy range:   1.00000E-03  to  1.00000E+05 MeV.
  20000.84p    5089  Update of MCPLIB04 Photon Compton Broadening Data For
MCNP5 see LA-UR-    12-00018        01/03/12
                 Energy range:   1.00000E-03  to  1.00000E+05 MeV.
  26000.84p    5794  Update of MCPLIB04 Photon Compton Broadening Data For
MCNP5 see LA-UR-    12-00018        01/03/12
                 Energy range:   1.00000E-03  to  1.00000E+05 MeV.

  total      41336
```

maximum photon energy set to 100.0 mev (maximum electron energy)

tables from file xdata/el03

```
  1000.03e   2329                                                           6/6/98
             Energy range:  1.00000E-03  to  1.00000E+03 MeV.
  6000.03e   2333                                                           6/6/98
             Energy range:  1.00000E-03  to  1.00000E+03 MeV.
  7000.03e   2333                                                           6/6/98
             Energy range:  1.00000E-03  to  1.00000E+03 MeV.
  8000.03e   2333                                                           6/6/98
             Energy range:  1.00000E-03  to  1.00000E+03 MeV.
 11000.03e   2337                                                           6/6/98
             Energy range:  1.00000E-03  to  1.00000E+03 MeV.
 13000.03e   2337                                                           6/6/98
             Energy range:  1.00000E-03  to  1.00000E+03 MeV.
 14000.03e   2339                                                           6/6/98
             Energy range:  1.00000E-03  to  1.00000E+03 MeV.
 18000.03e   2341                                                           6/6/98
             Energy range:  1.00000E-03  to  1.00000E+03 MeV.
 20000.03e   2343                                                           6/6/98
             Energy range:  1.00000E-03  to  1.00000E+03 MeV.
 26000.03e   2345                                                           6/6/98
             Energy range:  1.00000E-03  to  1.00000E+03 MeV.

1particles and energy limits                                                print table
101

                    particle    maximum    smallest    largest    always      always
                    cutoff      particle   table       table      use table   use model
  particle type     energy      energy     maximum     maximum    below
above

   2  p   photon    1.0000E-03  1.0000E+02  1.0000E+05  1.0000E+05
1.0000E+36  1.0000E+36
   3  e   electron  1.0000E-03  1.0000E+02  1.0000E+02  1.0000E+02
1.0000E+36  1.0000E+36


*************************************************************************************************
******************

 dump no.   1 on file runtpe    nps =         0    coll =           0    ctm =      0.00   nrn
=
   0
```

```
         1 warning message so far.
1starting mcrun.      cp0 = 17.14                                              print table
110

     run9xc
 master starting      79 MPI slave tasks with       1 threads each  01/06/26 18:24:21
 master set rendezvous nps =    10000000,  work chunks =    79    01/06/26 18:24:30


    nps    x          y          z          cell       surf     u          v          w        energy    weight
time

     1  1.390E+04 -5.450E+03 -4.000E+02       32            -7.956E-01  4.901E-01 -
3.562E-01  1.170E+00  2.000E+00  0.000E+00
        1.390E+04 -5.450E+03 -4.000E+02       11          0 -7.956E-01  4.901E-01 -
3.562E-01
     2  1.390E+04 -5.450E+03 -4.000E+02       32            -9.998E-01 -1.904E-03 -
2.108E-02  1.330E+00  2.000E+00  0.000E+00
        1.390E+04 -5.450E+03 -4.000E+02       11          0 -9.998E-01 -1.904E-03 -
2.108E-02
     3  1.390E+04 -5.450E+03 -4.000E+02       32             7.446E-01  6.290E-01 -
2.234E-01  1.330E+00  2.000E+00  0.000E+00
        1.390E+04 -5.450E+03 -4.000E+02       11          0  7.446E-01  6.290E-01 -
2.234E-01
     4  1.390E+04 -5.450E+03 -4.000E+02       32            -6.649E-01  5.702E-01 -
4.824E-01  1.330E+00  2.000E+00  0.000E+00
        1.390E+04 -5.450E+03 -4.000E+02       11          0 -6.649E-01  5.702E-01 -
4.824E-01
     5  1.390E+04 -5.450E+03 -4.000E+02       32             1.055E-01  2.754E-01 -
9.555E-01  1.330E+00  2.000E+00  0.000E+00
        1.390E+04 -5.450E+03 -4.000E+02       11          0  1.055E-01  2.754E-01 -
9.555E-01
     6  1.390E+04 -5.450E+03 -4.000E+02       32            -8.926E-01 -4.119E-01 -
1.831E-01  1.330E+00  2.000E+00  0.000E+00
        1.390E+04 -5.450E+03 -4.000E+02       11          0 -8.926E-01 -4.119E-01 -
1.831E-01
     7  1.390E+04 -5.450E+03 -4.000E+02       32            -7.242E-01 -3.003E-01 -
6.208E-01  1.170E+00  2.000E+00  0.000E+00
        1.390E+04 -5.450E+03 -4.000E+02       11          0 -7.242E-01 -3.003E-01 -
6.208E-01
     8  1.390E+04 -5.450E+03 -4.000E+02       32            -5.122E-01  2.020E-01 -
8.348E-01  1.170E+00  2.000E+00  0.000E+00
        1.390E+04 -5.450E+03 -4.000E+02       11          0 -5.122E-01  2.020E-01 -
8.348E-01
```

9 1.390E+04 -5.450E+03 -4.000E+02 32 4.209E-01 7.432E-01
5.201E-01 1.170E+00 2.000E+00 0.000E+00
1.390E+04 -5.450E+03 -4.000E+02 11 0 4.209E-01 7.432E-01
5.201E-01
10 1.390E+04 -5.450E+03 -4.000E+02 32 -1.166E-03 2.845E-01 -
9.587E-01 1.330E+00 2.000E+00 0.000E+00
1.390E+04 -5.450E+03 -4.000E+02 11 0 -1.166E-03 2.845E-01 -
9.587E-01
11 1.390E+04 -5.450E+03 -4.000E+02 32 -4.094E-01 -8.958E-01 -
1.728E-01 1.330E+00 2.000E+00 0.000E+00
1.390E+04 -5.450E+03 -4.000E+02 11 0 -4.094E-01 -8.958E-01 -
1.728E-01
12 1.390E+04 -5.450E+03 -4.000E+02 32 4.934E-01 4.610E-01 -
7.376E-01 1.330E+00 2.000E+00 0.000E+00
1.390E+04 -5.450E+03 -4.000E+02 11 0 4.934E-01 4.610E-01 -
7.376E-01
13 1.390E+04 -5.450E+03 -4.000E+02 32 2.457E-01 2.132E-02 -
9.691E-01 1.330E+00 2.000E+00 0.000E+00
1.390E+04 -5.450E+03 -4.000E+02 11 0 2.457E-01 2.132E-02 -
9.691E-01
14 1.390E+04 -5.450E+03 -4.000E+02 32 3.158E-01 4.844E-01 -
8.159E-01 1.330E+00 2.000E+00 0.000E+00
1.390E+04 -5.450E+03 -4.000E+02 11 0 3.158E-01 4.844E-01 -
8.159E-01
15 1.390E+04 -5.450E+03 -4.000E+02 32 -1.987E-01 5.844E-01 -
7.868E-01 1.170E+00 2.000E+00 0.000E+00
1.390E+04 -5.450E+03 -4.000E+02 11 0 -1.987E-01 5.844E-01 -
7.868E-01
16 1.390E+04 -5.450E+03 -4.000E+02 32 7.805E-01 -1.370E-01
6.099E-01 1.330E+00 2.000E+00 0.000E+00
1.390E+04 -5.450E+03 -4.000E+02 11 0 7.805E-01 -1.370E-01
6.099E-01
17 1.390E+04 -5.450E+03 -4.000E+02 32 4.403E-01 -6.222E-01
6.473E-01 1.170E+00 2.000E+00 0.000E+00
1.390E+04 -5.450E+03 -4.000E+02 11 0 4.403E-01 -6.222E-01
6.473E-01
18 1.390E+04 -5.450E+03 -4.000E+02 32 8.715E-01 -2.737E-01
4.070E-01 1.170E+00 2.000E+00 0.000E+00
1.390E+04 -5.450E+03 -4.000E+02 11 0 8.715E-01 -2.737E-01
4.070E-01
19 1.390E+04 -5.450E+03 -4.000E+02 32 -3.264E-01 5.364E-01
7.783E-01 1.330E+00 2.000E+00 0.000E+00
1.390E+04 -5.450E+03 -4.000E+02 11 0 -3.264E-01 5.364E-01
7.783E-01
20 1.390E+04 -5.450E+03 -4.000E+02 32 -5.180E-01 1.299E-01 -
8.455E-01 1.170E+00 2.000E+00 0.000E+00

1.390E+04 -5.450E+03 -4.000E+02 11 0 -5.180E-01 1.299E-01 -
8.455E-01
21 1.390E+04 -5.450E+03 -4.000E+02 32 -6.475E-01 -6.276E-02 -
7.595E-01 1.330E+00 2.000E+00 0.000E+00
1.390E+04 -5.450E+03 -4.000E+02 11 0 -6.475E-01 -6.276E-02 -
7.595E-01
22 1.390E+04 -5.450E+03 -4.000E+02 32 -2.463E-01 -8.282E-01
5.033E-01 1.170E+00 2.000E+00 0.000E+00
1.390E+04 -5.450E+03 -4.000E+02 11 0 -2.463E-01 -8.282E-01
5.033E-01
23 1.390E+04 -5.450E+03 -4.000E+02 32 -1.164E-01 7.921E-02
9.900E-01 1.330E+00 2.000E+00 0.000E+00
1.390E+04 -5.450E+03 -4.000E+02 11 0 -1.164E-01 7.921E-02
9.900E-01
24 1.390E+04 -5.450E+03 -4.000E+02 32 -4.132E-02 3.121E-01 -
9.492E-01 1.330E+00 2.000E+00 0.000E+00
1.390E+04 -5.450E+03 -4.000E+02 11 0 -4.132E-02 3.121E-01 -
9.492E-01
25 1.390E+04 -5.450E+03 -4.000E+02 32 -5.385E-01 8.093E-01 -
2.348E-01 1.330E+00 2.000E+00 0.000E+00
1.390E+04 -5.450E+03 -4.000E+02 11 0 -5.385E-01 8.093E-01 -
2.348E-01
26 1.390E+04 -5.450E+03 -4.000E+02 32 7.710E-01 -5.041E-01
3.890E-01 1.170E+00 2.000E+00 0.000E+00
1.390E+04 -5.450E+03 -4.000E+02 11 0 7.710E-01 -5.041E-01
3.890E-01
27 1.390E+04 -5.450E+03 -4.000E+02 32 -4.866E-01 -8.057E-01 -
3.377E-01 1.330E+00 2.000E+00 0.000E+00
1.390E+04 -5.450E+03 -4.000E+02 11 0 -4.866E-01 -8.057E-01 -
3.377E-01
28 1.390E+04 -5.450E+03 -4.000E+02 32 -9.446E-02 6.576E-01
7.474E-01 1.170E+00 2.000E+00 0.000E+00
1.390E+04 -5.450E+03 -4.000E+02 11 0 -9.446E-02 6.576E-01
7.474E-01
29 1.390E+04 -5.450E+03 -4.000E+02 32 1.501E-01 9.856E-01 -
7.769E-02 1.330E+00 2.000E+00 0.000E+00
1.390E+04 -5.450E+03 -4.000E+02 11 0 1.501E-01 9.856E-01 -
7.769E-02
30 1.390E+04 -5.450E+03 -4.000E+02 32 8.858E-01 1.044E-01
4.522E-01 1.330E+00 2.000E+00 0.000E+00
1.390E+04 -5.450E+03 -4.000E+02 11 0 8.858E-01 1.044E-01
4.522E-01
31 1.390E+04 -5.450E+03 -4.000E+02 32 9.136E-01 -3.439E-01
2.171E-01 1.330E+00 2.000E+00 0.000E+00
1.390E+04 -5.450E+03 -4.000E+02 11 0 9.136E-01 -3.439E-01
2.171E-01

32 1.390E+04 -5.450E+03 -4.000E+02 32 -7.112E-01 4.219E-01 -
5.623E-01 1.170E+00 2.000E+00 0.000E+00
1.390E+04 -5.450E+03 -4.000E+02 11 0 -7.112E-01 4.219E-01 -
5.623E-01
33 1.390E+04 -5.450E+03 -4.000E+02 32 2.489E-01 -6.716E-01
6.978E-01 1.330E+00 2.000E+00 0.000E+00
1.390E+04 -5.450E+03 -4.000E+02 11 0 2.489E-01 -6.716E-01
6.978E-01
34 1.390E+04 -5.450E+03 -4.000E+02 32 -6.675E-01 -6.896E-01
2.810E-01 1.330E+00 2.000E+00 0.000E+00
1.390E+04 -5.450E+03 -4.000E+02 11 0 -6.675E-01 -6.896E-01
2.810E-01
35 1.390E+04 -5.450E+03 -4.000E+02 32 7.679E-01 -7.159E-02 -
6.366E-01 1.330E+00 2.000E+00 0.000E+00
1.390E+04 -5.450E+03 -4.000E+02 11 0 7.679E-01 -7.159E-02 -
6.366E-01
36 1.390E+04 -5.450E+03 -4.000E+02 32 -4.249E-01 -2.369E-01 -
8.737E-01 1.330E+00 2.000E+00 0.000E+00
1.390E+04 -5.450E+03 -4.000E+02 11 0 -4.249E-01 -2.369E-01 -
8.737E-01
37 1.390E+04 -5.450E+03 -4.000E+02 32 5.397E-01 -3.713E-01
7.556E-01 1.170E+00 2.000E+00 0.000E+00
1.390E+04 -5.450E+03 -4.000E+02 11 0 5.397E-01 -3.713E-01
7.556E-01
38 1.390E+04 -5.450E+03 -4.000E+02 32 3.649E-01 8.017E-01
4.734E-01 1.330E+00 2.000E+00 0.000E+00
1.390E+04 -5.450E+03 -4.000E+02 11 0 3.649E-01 8.017E-01
4.734E-01
39 1.390E+04 -5.450E+03 -4.000E+02 32 2.574E-01 9.641E-01 -
6.603E-02 1.330E+00 2.000E+00 0.000E+00
1.390E+04 -5.450E+03 -4.000E+02 11 0 2.574E-01 9.641E-01 -
6.603E-02
40 1.390E+04 -5.450E+03 -4.000E+02 32 9.948E-01 -1.008E-01 -
1.595E-02 1.170E+00 2.000E+00 0.000E+00
1.390E+04 -5.450E+03 -4.000E+02 11 0 9.948E-01 -1.008E-01 -
1.595E-02
41 1.390E+04 -5.450E+03 -4.000E+02 32 5.159E-01 -8.378E-01 -
1.786E-01 1.170E+00 2.000E+00 0.000E+00
1.390E+04 -5.450E+03 -4.000E+02 11 0 5.159E-01 -8.378E-01 -
1.786E-01
42 1.390E+04 -5.450E+03 -4.000E+02 32 -5.796E-01 -3.399E-01 -
7.407E-01 1.330E+00 2.000E+00 0.000E+00
1.390E+04 -5.450E+03 -4.000E+02 11 0 -5.796E-01 -3.399E-01 -
7.407E-01
43 1.390E+04 -5.450E+03 -4.000E+02 32 8.903E-01 -3.706E-01 -
2.647E-01 1.330E+00 2.000E+00 0.000E+00

```
      1.390E+04 -5.450E+03 -4.000E+02       11          0  8.903E-01 -3.706E-01 -
2.647E-01
    44  1.390E+04 -5.450E+03 -4.000E+02       32           -4.307E-01  5.509E-01 -
7.149E-01  1.330E+00  2.000E+00  0.000E+00
      1.390E+04 -5.450E+03 -4.000E+02       11          0 -4.307E-01  5.509E-01 -
7.149E-01
    45  1.390E+04 -5.450E+03 -4.000E+02       32            3.490E-01 -8.658E-01 -
3.585E-01  1.170E+00  2.000E+00  0.000E+00
      1.390E+04 -5.450E+03 -4.000E+02       11          0  3.490E-01 -8.658E-01 -
3.585E-01
    46  1.390E+04 -5.450E+03 -4.000E+02       32            2.083E-01  7.085E-01
6.743E-01  1.330E+00  2.000E+00  0.000E+00
      1.390E+04 -5.450E+03 -4.000E+02       11          0  2.083E-01  7.085E-01
6.743E-01
    47  1.390E+04 -5.450E+03 -4.000E+02       32           -2.466E-01 -1.684E-01
9.544E-01  1.330E+00  2.000E+00  0.000E+00
      1.390E+04 -5.450E+03 -4.000E+02       11          0 -2.466E-01 -1.684E-01
9.544E-01
    48  1.390E+04 -5.450E+03 -4.000E+02       32            6.602E-01 -7.084E-01
2.496E-01  1.330E+00  2.000E+00  0.000E+00
      1.390E+04 -5.450E+03 -4.000E+02       11          0  6.602E-01 -7.084E-01
2.496E-01
    49  1.390E+04 -5.450E+03 -4.000E+02       32            7.846E-01  3.339E-01
5.224E-01  1.170E+00  2.000E+00  0.000E+00
      1.390E+04 -5.450E+03 -4.000E+02       11          0  7.846E-01  3.339E-01
5.224E-01
    50  1.390E+04 -5.450E+03 -4.000E+02       32            6.707E-01 -4.055E-01 -
6.211E-01  1.170E+00  2.000E+00  0.000E+00
      1.390E+04 -5.450E+03 -4.000E+02       11          0  6.707E-01 -4.055E-01 -
6.211E-01
1problem summary

     run terminated when     10000000  particle histories were done.
+                                                                01/06/26 18:31:18

 =====>      88.32 M histories/hr    (based on wall-clock time in mcrun)


     run9xc     probid =  01/06/26 18:06:59

 photon creation     tracks      weight        energy           photon loss        tracks
weight        energy
                            (per source particle)                                    (per source particle)

 source            10000000    2.0000E+00    1.2500E+00         escape                221
4.4200E-05    3.6196E-06
```

nucl. interaction 0 0. 0. energy cutoff 0 0.
4.5838E-05
particle decay 0 0. 0. time cutoff 0 0. 0.
weight window 0 0. 0. weight window 0 0. 0.
cell importance 0 0. 0. cell importance 0 0. 0.
weight cutoff 0 0. 0. weight cutoff 0 0. 0.
e or t importance 0 0. 0. e or t importance 0 0. 0.
dxtran 0 0. 0. dxtran 0 0. 0.
forced collisions 0 0. 0. forced collisions 0 0. 0.
exp. transform 0 0. 0. exp. transform 0 0. 0.
from neutrons 0 0. 0. compton scatter 0 0.
1.1717E+00
bremsstrahlung 1702826 3.4057E-01 4.7496E-03 capture 12854145
2.5708E+00 8.3272E-02
p-annihilation 13078 2.6156E-03 6.6830E-04 pair production 6539
1.3078E-03 8.5441E-04
photonuclear 0 0. 0. photonuclear abs 0 0. 0.
electron x-rays 0 0. 0. loss to photofis 0 0. 0.
compton fluores 0 0. 0.
muon capt fluores 0 0. 0.
1st fluorescence 1145001 2.2900E-01 4.8768E-04
2nd fluorescence 0 0. 0.
cerenkov 0 0. 0.
(gamma,xgamma) 0 0. 0.
tabular sampling 0 0. 0.
prompt photofis 0 0. 0.
total 12860905 2.5722E+00 1.2559E+00 total 12860905
2.5722E+00 1.2559E+00

number of photons banked 1715904 average time of (shakes)
cutoffs
photon tracks per source particle 1.2861E+00 escape 1.0241E+01
tco 1.0000E+33
photon collisions per source particle 1.0458E+01 capture 1.7449E+00
eco 1.0000E-03
total photon collisions 104576852 capture or escape 1.7451E+00
wc1 -5.0000E-01
any termination 1.7448E+00 wc2 -
2.5000E-01

computer time so far in this run 568.61 minutes maximum number ever in bank
4
computer time in mcrun 508.06 minutes bank overflows to backup file
0
source particles per minute 1.9683E+04

random numbers generated 1557380446 most random numbers used was 624 in history 3099808

range of sampled source weights = 2.0000E+00 to 2.0000E+00

number of histories processed by each MPI task
0 126582 126582 126582 126583 126582 126582 126582
126583 126582
126582 126583 126582 126582 126582 126583 126582
126582 126583 126582
126582 126582 126583 126582 126582 126582 126583
126582 126582 126583
126582 126582 126582 126583 126582 126582 126583
126582 126582 126582
126583 126582 126582 126582 126583 126582 126582
126583 126582 126582
126582 126583 126582 126582 126583 126582 126582
126582 126583 126582
126582 126582 126583 126582 126582 126583 126582
126582 126582 126583
126582 126582 126583 126582 126582 126582 126583
126582 126582 126583

1source distribution frequency tables print table 170

the expected values below do not include the effect of the rejection loop which samples position.

source distribution 1 for erg

n	source value	number sampled	number expected	number sampled/expected	weight sampled	weight expected	weight sampled/expected
1	1.17000E+00	4.9988E-01	5.0000E-01	9.9976E-01	9.9976E-01	1.0000E+00	9.9976E-01
2	1.33000E+00	5.0012E-01	5.0000E-01	1.0002E+00	1.0002E+00	1.0000E+00	1.0002E+00
total		1.0000E+00	1.0000E+00	1.0000E+00	2.0000E+00	2.0000E+00	1.0000E+00

1the following cells are bounded by cells with photon importances print table 120
that may be different by more than a factor of four.

	maximum				minimum		
cell	importance	neighbor	importance	ratio	neighbor	importance	ratio
1	no data available yet for this cell.						
2	no data available yet for this cell.						
3	no data available yet for this cell.						
4	no data available yet for this cell.						
5	no data available yet for this cell.						
6	no data available yet for this cell.						
7	no data available yet for this cell.						
8	no data available yet for this cell.						
9	no data available yet for this cell.						
10	no data available yet for this cell.						
11	no data available yet for this cell.						
12	no data available yet for this cell.						
13	no data available yet for this cell.						
14	no data available yet for this cell.						
15	no data available yet for this cell.						
16	no data available yet for this cell.						
17	no data available yet for this cell.						
18	no data available yet for this cell.						
19	no data available yet for this cell.						
20	no data available yet for this cell.						
21	no data available yet for this cell.						
22	no data available yet for this cell.						
23	no data available yet for this cell.						
24	no data available yet for this cell.						
25	no data available yet for this cell.						
26	no data available yet for this cell.						
27	no data available yet for this cell.						
28	no data available yet for this cell.						
29	no data available yet for this cell.						
30	no data available yet for this cell.						
31	no data available yet for this cell.						

End of importance function analysis

1photon activity in each cell print table 126

tracks population collisions collisions number flux average average
cell entering * weight weighted weighted track weight track mfp
(per history) energy energy (relative) (cm)

1	1	14546	10310	1997	3.9940E-04	1.5529E-01	1.5529E-01	2.0000E+00	5.9313E+03
2	2	10164815	8722940	68782673	1.3757E+01	5.0230E-01	5.0230E-01	2.0000E+00	4.5966E+00
3	3	7294920	5770820	35204850	7.0410E+00	5.3777E-01	5.3777E-01	2.0000E+00	4.7518E+00
4	4	1176737	872300	35427	7.0854E-03	6.4977E-01	6.4977E-01	2.0000E+00	9.9998E+03
5	5	1060950	772478	34816	6.9632E-03	6.5533E-01	6.5533E-01	2.0000E+00	1.0050E+04
6	6	827217	536553	8595	1.7190E-03	7.1161E-01	7.1161E-01	2.0000E+00	1.0460E+04
7	7	926145	617412	8626	1.7252E-03	7.2339E-01	7.2339E-01	2.0000E+00	1.0545E+04
8	8	803110	516082	8173	1.6346E-03	7.0824E-01	7.0824E-01	2.0000E+00	1.0434E+04
9	9	858987	509409	7657	1.5314E-03	7.0219E-01	7.0219E-01	2.0000E+00	1.0382E+04
10	10	1297858	801503	7438	1.4876E-03	6.8622E-01	6.8622E-01	2.0000E+00	1.0264E+04
11	11	11609395	10015636	165901	3.3180E-02	1.0288E+00	1.0288E+00	2.0000E+00	1.2903E+04
12	12	201982	153311	13488	2.6976E-03	6.6088E-01	6.6088E-01	2.0000E+00	1.0088E+04
13	13	396348	304835	28014	5.6028E-03	7.4685E-01	7.4685E-01	2.0000E+00	1.0774E+04
14	14	66592	52528	4731	9.4620E-04	3.0193E-01	3.0193E-01	2.0000E+00	7.2399E+03
15	15	22046	15963	2635	5.2700E-04	1.6127E-01	1.6127E-01	2.0000E+00	5.9956E+03
16	16	32497	25611	2591	5.1820E-04	1.8774E-01	1.8774E-01	2.0000E+00	6.2762E+03
17	17	12383	8827	842	1.6840E-04	1.5872E-01	1.5872E-01	2.0000E+00	5.9838E+03
18	18	48406	36019	4593	9.1860E-04	2.0442E-01	2.0442E-01	2.0000E+00	6.4527E+03
19	19	391910	275124	34251	6.8502E-03	7.0257E-01	7.0257E-01	2.0000E+00	1.0430E+04
20	20	41996	31434	4050	8.1000E-04	1.9683E-01	1.9683E-01	2.0000E+00	6.3787E+03
21	21	7090	5337	758	1.5160E-04	1.6046E-01	1.6046E-01	2.0000E+00	5.9960E+03
22	22	6096	4417	315	6.3000E-05	1.6012E-01	1.6012E-01	2.0000E+00	6.0092E+03
23	23	2675086	2052852	62978	1.2596E-02	7.2754E-01	7.2754E-01	2.0000E+00	1.0581E+04

```
     24      24    2725824     1312931        22575    4.5150E-03   9.3735E-01
9.3735E-01   2.0000E+00   1.2196E+04
     25      25    6252710     4754662        48181    9.6362E-03   1.1327E+00
1.1327E+00   2.0000E+00   1.3707E+04
     26      26    2250557     1295682        15093    3.0186E-03   8.2078E-01
8.2078E-01   2.0000E+00   1.1294E+04
     27      27    2486251     1575902        18810    3.7620E-03   8.9200E-01
8.9200E-01   2.0000E+00   1.1842E+04
     28      28    2391040     1438727        17971    3.5942E-03   8.5018E-01
8.5018E-01   2.0000E+00   1.1523E+04
     29      29    2478203     1381888        13924    2.7848E-03   8.4958E-01
8.4958E-01   2.0000E+00   1.1515E+04
     30      30    2390821     1371755        14899    2.9798E-03   8.1232E-01
8.1232E-01   2.0000E+00   1.1229E+04
     31      31   14298258     7289973            0    0.0000E+00   4.5936E-01   4.5936E-
01   2.0000E+00   0.0000E+00
     32      32          0           0            0    0.0000E+00   0.0000E+00   0.0000E+00
0.0000E+00   0.0000E+00

          total     75210776     52533221    104576852    2.0915E+01
1photon   activity in each repeated structure / lattice element
print table 128

     source    entering  collisions       path

          0       14546       1997     1 <   32
          0    10164815   68782673     2 <   32
          0     7294920   35204850     3 <   32
          0     1176737      35427     4 <   32
          0     1060950      34816     5 <   32
          0      827217       8595     6 <   32
          0      926145       8626     7 <   32
          0      803110       8173     8 <   32
          0      858987       7657     9 <   32
          0     1297858       7438    10 <   32
   10000000    11609395     165901    11 <   32
          0      201982      13488    12 <   32
          0      396348      28014    13 <   32
          0       66592       4731    14 <   32
          0       22046       2635    15 <   32
          0       32497       2591    16 <   32
          0       12383        842    17 <   32
          0       48406       4593    18 <   32
          0      391910      34251    19 <   32
          0       41996       4050    20 <   32
          0        7090        758    21 <   32
```

```
     0       6096        315    22 <   32
     0    2675086      62978    23 <   32
     0    2725824      22575    24 <   32
     0    6252710      48181    25 <   32
     0    2250557      15093    26 <   32
     0    2486251      18810    27 <   32
     0    2391040      17971    28 <   32
     0    2478203      13924    29 <   32
     0    2390821      14899    30 <   32
     0   14298258          0    31 <   32
     0          0          0    33

  10000000    75210776   104576852


      print table 128 requires        365 decimal words of dynamically allocated storage.
1photon   weight balance in each cell                                                   print
table 130

     cell index      1         2         3         4         5         6         7         8         9
    cell number       1         2         3         4         5         6         7         8         9

 external events:
      entering  2.9092E-03  2.0330E+00  1.4590E+00  2.3535E-01  2.1219E-01
1.6544E-01  1.8523E-01  1.6062E-01  1.7180E-01
        source  0.0000E+00  0.0000E+00  0.0000E+00  0.0000E+00  0.0000E+00
0.0000E+00  0.0000E+00  0.0000E+00  0.0000E+00
   energy cutoff  0.0000E+00  0.0000E+00  0.0000E+00  0.0000E+00  0.0000E+00
0.0000E+00  0.0000E+00  0.0000E+00  0.0000E+00
     time cutoff  0.0000E+00  0.0000E+00  0.0000E+00  0.0000E+00  0.0000E+00
0.0000E+00  0.0000E+00  0.0000E+00  0.0000E+00
       exiting -2.8960E-03 -6.8982E-01 -8.0226E-01 -2.3527E-01 -2.1211E-01 -
1.6543E-01 -1.8521E-01 -1.6061E-01 -1.7178E-01
               ----------  ----------  ----------  ----------  ----------  ----------  ----------  ----------  -------
---
         total  1.3200E-05  1.3431E+00  6.5672E-01  8.1400E-05  7.6800E-05  9.2000E-
06  1.4400E-05  9.8000E-06  1.3200E-05

 variance reduction events:
   weight window  0.0000E+00  0.0000E+00  0.0000E+00  0.0000E+00  0.0000E+00
0.0000E+00  0.0000E+00  0.0000E+00  0.0000E+00
  cell importance  0.0000E+00  0.0000E+00  0.0000E+00  0.0000E+00  0.0000E+00
0.0000E+00  0.0000E+00  0.0000E+00  0.0000E+00
   weight cutoff  0.0000E+00  0.0000E+00  0.0000E+00  0.0000E+00  0.0000E+00
0.0000E+00  0.0000E+00  0.0000E+00  0.0000E+00
```

e or t importance 0.0000E+00 0.0000E+00 0.0000E+00 0.0000E+00 0.0000E+00
0.0000E+00 0.0000E+00 0.0000E+00 0.0000E+00
dxtran 0.0000E+00 0.0000E+00 0.0000E+00 0.0000E+00 0.0000E+00
0.0000E+00 0.0000E+00 0.0000E+00 0.0000E+00
forced collisions 0.0000E+00 0.0000E+00 0.0000E+00 0.0000E+00 0.0000E+00
0.0000E+00 0.0000E+00 0.0000E+00 0.0000E+00
exp. transform 0.0000E+00 0.0000E+00 0.0000E+00 0.0000E+00 0.0000E+00
0.0000E+00 0.0000E+00 0.0000E+00 0.0000E+00
---------- ---------- ---------- ---------- ---------- ---------- ---------- ---------- -------
---
total 0.0000E+00 0.0000E+00 0.0000E+00 0.0000E+00 0.0000E+00
0.0000E+00 0.0000E+00 0.0000E+00 0.0000E+00

physical events:
from neutrons 0.0000E+00 0.0000E+00 0.0000E+00 0.0000E+00 0.0000E+00
0.0000E+00 0.0000E+00 0.0000E+00 0.0000E+00
bremsstrahlung 4.0000E-07 2.1566E-01 1.2188E-01 1.1040E-04 1.1160E-04
2.9800E-05 3.3800E-05 3.0000E-05 2.6200E-05
capture -1.3800E-05 -1.7126E+00 -8.5501E-01 -1.9600E-04 -1.9320E-04 -
3.9400E-05 -4.9600E-05 -4.0600E-05 -4.0200E-05
p-annihilation 0.0000E+00 1.5856E-03 9.9240E-04 1.6000E-06 1.6000E-06
0.0000E+00 4.0000E-07 4.0000E-07 0.0000E+00
pair production 0.0000E+00 -7.9280E-04 -4.9620E-04 -8.0000E-07 -8.0000E-07
0.0000E+00 -2.0000E-07 -2.0000E-07 0.0000E+00
photonuclear 0.0000E+00 0.0000E+00 0.0000E+00 0.0000E+00 0.0000E+00
0.0000E+00 0.0000E+00 0.0000E+00 0.0000E+00
photonuclear abs 0.0000E+00 0.0000E+00 0.0000E+00 0.0000E+00 0.0000E+00
0.0000E+00 0.0000E+00 0.0000E+00 0.0000E+00
electron x-rays 0.0000E+00 0.0000E+00 0.0000E+00 0.0000E+00 0.0000E+00
0.0000E+00 0.0000E+00 0.0000E+00 0.0000E+00
compton fluores 0.0000E+00 0.0000E+00 0.0000E+00 0.0000E+00 0.0000E+00
0.0000E+00 0.0000E+00 0.0000E+00 0.0000E+00
muon capt fluores 0.0000E+00 0.0000E+00 0.0000E+00 0.0000E+00 0.0000E+00
0.0000E+00 0.0000E+00 0.0000E+00 0.0000E+00
fluorescence 2.0000E-07 1.5302E-01 7.5926E-02 3.4000E-06 4.0000E-06
4.0000E-07 1.2000E-06 2.0000E-07 8.0000E-07
cerenkov 0.0000E+00 0.0000E+00 0.0000E+00 0.0000E+00 0.0000E+00
0.0000E+00 0.0000E+00 0.0000E+00 0.0000E+00
decay gain 0.0000E+00 0.0000E+00 0.0000E+00 0.0000E+00 0.0000E+00
0.0000E+00 0.0000E+00 0.0000E+00 0.0000E+00
nucl. interaction 0.0000E+00 0.0000E+00 0.0000E+00 0.0000E+00 0.0000E+00
0.0000E+00 0.0000E+00 0.0000E+00 0.0000E+00
tabular sampling 0.0000E+00 0.0000E+00 0.0000E+00 0.0000E+00 0.0000E+00
0.0000E+00 0.0000E+00 0.0000E+00 0.0000E+00
photofission 0.0000E+00 0.0000E+00 0.0000E+00 0.0000E+00 0.0000E+00
0.0000E+00 0.0000E+00 0.0000E+00 0.0000E+00

loss to photofis 0.0000E+00 0.0000E+00 0.0000E+00 0.0000E+00 0.0000E+00
0.0000E+00 0.0000E+00 0.0000E+00 0.0000E+00
---------- ---------- ---------- ---------- ---------- ---------- ---------- ---------- -------
---
total -1.3200E-05 -1.3431E+00 -6.5671E-01 -8.1400E-05 -7.6800E-05 -
9.2000E-06 -1.4400E-05 -1.0200E-05 -1.3200E-05

---------- ---------- ---------- ---------- ---------- ---------- ---------- ---------- -------
---
total 0.0000E+00 4.0600E-05 9.4000E-06 0.0000E+00 0.0000E+00
0.0000E+00 0.0000E+00 -4.0000E-07 0.0000E+00

cell index 10 11 12 13 14 15 16 17
18
cell number 10 11 12 13 14 15 16 17
18

external events:
entering 2.5957E-01 3.2188E-01 4.0396E-02 7.9270E-02 1.3318E-02
4.4092E-03 6.4994E-03 2.4766E-03 9.6812E-03
source 0.0000E+00 2.0000E+00 0.0000E+00 0.0000E+00 0.0000E+00
0.0000E+00 0.0000E+00 0.0000E+00 0.0000E+00
energy cutoff 0.0000E+00 0.0000E+00 0.0000E+00 0.0000E+00 0.0000E+00
0.0000E+00 0.0000E+00 0.0000E+00 0.0000E+00
time cutoff 0.0000E+00 0.0000E+00 0.0000E+00 0.0000E+00 0.0000E+00
0.0000E+00 0.0000E+00 0.0000E+00 0.0000E+00
exiting -2.5956E-01 -2.3222E+00 -4.0363E-02 -7.9220E-02 -1.3297E-02 -
4.3906E-03 -6.4822E-03 -2.4700E-03 -9.6536E-03
---------- ---------- ---------- ---------- ---------- ---------- ---------- ---------- -------
---
total 1.4000E-05 -3.2740E-04 3.3000E-05 4.9600E-05 2.1200E-05 1.8600E-
05 1.7200E-05 6.6000E-06 2.7600E-05

variance reduction events:
weight window 0.0000E+00 0.0000E+00 0.0000E+00 0.0000E+00 0.0000E+00
0.0000E+00 0.0000E+00 0.0000E+00 0.0000E+00
cell importance 0.0000E+00 0.0000E+00 0.0000E+00 0.0000E+00 0.0000E+00
0.0000E+00 0.0000E+00 0.0000E+00 0.0000E+00
weight cutoff 0.0000E+00 0.0000E+00 0.0000E+00 0.0000E+00 0.0000E+00
0.0000E+00 0.0000E+00 0.0000E+00 0.0000E+00
e or t importance 0.0000E+00 0.0000E+00 0.0000E+00 0.0000E+00 0.0000E+00
0.0000E+00 0.0000E+00 0.0000E+00 0.0000E+00
dxtran 0.0000E+00 0.0000E+00 0.0000E+00 0.0000E+00 0.0000E+00
0.0000E+00 0.0000E+00 0.0000E+00 0.0000E+00

forced collisions 0.0000E+00 0.0000E+00 0.0000E+00 0.0000E+00 0.0000E+00 0.0000E+00 0.0000E+00 0.0000E+00 0.0000E+00
exp. transform 0.0000E+00 0.0000E+00 0.0000E+00 0.0000E+00 0.0000E+00 0.0000E+00 0.0000E+00 0.0000E+00 0.0000E+00
---------- ---------- ---------- ---------- ---------- ---------- ---------- ---------- ----------
total 0.0000E+00 0.0000E+00 0.0000E+00 0.0000E+00 0.0000E+00 0.0000E+00 0.0000E+00 0.0000E+00 0.0000E+00

physical events:
from neutrons 0.0000E+00 0.0000E+00 0.0000E+00 0.0000E+00 0.0000E+00 0.0000E+00 0.0000E+00 0.0000E+00 0.0000E+00
bremsstrahlung 2.5800E-05 1.1848E-03 3.9600E-05 1.1420E-04 3.8000E-06 1.0000E-06 2.2000E-06 2.0000E-07 2.8000E-06
capture -4.1000E-05 -8.7560E-04 -7.5000E-05 -1.6700E-04 -2.5400E-05 -2.0000E-05 -1.9800E-05 -7.0000E-06 -3.1600E-05
p-annihilation 0.0000E+00 1.5600E-05 8.0000E-07 2.4000E-06 0.0000E+00 0.0000E+00 0.0000E+00 0.0000E+00 0.0000E+00
pair production 0.0000E+00 -7.8000E-06 -4.0000E-07 -1.2000E-06 0.0000E+00 0.0000E+00 0.0000E+00 0.0000E+00 0.0000E+00
photonuclear 0.0000E+00 0.0000E+00 0.0000E+00 0.0000E+00 0.0000E+00 0.0000E+00 0.0000E+00 0.0000E+00 0.0000E+00
photonuclear abs 0.0000E+00 0.0000E+00 0.0000E+00 0.0000E+00 0.0000E+00 0.0000E+00 0.0000E+00 0.0000E+00 0.0000E+00
electron x-rays 0.0000E+00 0.0000E+00 0.0000E+00 0.0000E+00 0.0000E+00 0.0000E+00 0.0000E+00 0.0000E+00 0.0000E+00
compton fluores 0.0000E+00 0.0000E+00 0.0000E+00 0.0000E+00 0.0000E+00 0.0000E+00 0.0000E+00 0.0000E+00 0.0000E+00
muon capt fluores 0.0000E+00 0.0000E+00 0.0000E+00 0.0000E+00 0.0000E+00 0.0000E+00 0.0000E+00 0.0000E+00 0.0000E+00
fluorescence 1.2000E-06 1.0400E-05 1.8000E-06 2.0000E-06 4.0000E-07 4.0000E-07 4.0000E-07 2.0000E-07 1.2000E-06
cerenkov 0.0000E+00 0.0000E+00 0.0000E+00 0.0000E+00 0.0000E+00 0.0000E+00 0.0000E+00 0.0000E+00 0.0000E+00
decay gain 0.0000E+00 0.0000E+00 0.0000E+00 0.0000E+00 0.0000E+00 0.0000E+00 0.0000E+00 0.0000E+00 0.0000E+00
nucl. interaction 0.0000E+00 0.0000E+00 0.0000E+00 0.0000E+00 0.0000E+00 0.0000E+00 0.0000E+00 0.0000E+00 0.0000E+00
tabular sampling 0.0000E+00 0.0000E+00 0.0000E+00 0.0000E+00 0.0000E+00 0.0000E+00 0.0000E+00 0.0000E+00 0.0000E+00
photofission 0.0000E+00 0.0000E+00 0.0000E+00 0.0000E+00 0.0000E+00 0.0000E+00 0.0000E+00 0.0000E+00 0.0000E+00
loss to photofis 0.0000E+00 0.0000E+00 0.0000E+00 0.0000E+00 0.0000E+00 0.0000E+00 0.0000E+00 0.0000E+00 0.0000E+00
---------- ---------- ---------- ---------- ---------- ---------- ---------- ---------- ----------

total -1.4000E-05 3.2740E-04 -3.3200E-05 -4.9600E-05 -2.1200E-05 -1.8600E-05 -1.7200E-05 -6.6000E-06 -2.7600E-05

---------- ---------- ---------- ---------- ---------- ---------- ---------- ---------- ----------

total 0.0000E+00 0.0000E+00 -2.0000E-07 0.0000E+00 0.0000E+00 0.0000E+00 0.0000E+00 0.0000E+00 0.0000E+00

cell index 19 20 21 22 23 24 25 26 27

cell number 19 20 21 22 23 24 25 26 27

external events:

entering 7.8382E-02 8.3992E-03 1.4180E-03 1.2192E-03 5.3502E-01 5.4516E-01 1.2505E+00 4.5011E-01 4.9725E-01

source 0.0000E+00 0.0000E+00 0.0000E+00 0.0000E+00 0.0000E+00 0.0000E+00 0.0000E+00 0.0000E+00 0.0000E+00

energy cutoff 0.0000E+00 0.0000E+00 0.0000E+00 0.0000E+00 0.0000E+00 0.0000E+00 0.0000E+00 0.0000E+00 0.0000E+00

time cutoff 0.0000E+00 0.0000E+00 0.0000E+00 0.0000E+00 0.0000E+00 0.0000E+00 0.0000E+00 0.0000E+00 0.0000E+00

exiting -7.8309E-02 -8.3732E-03 -1.4114E-03 -1.2166E-03 -5.3492E-01 -5.4518E-01 -1.2507E+00 -4.5011E-01 -4.9725E-01

---------- ---------- ---------- ---------- ---------- ---------- ---------- ---------- ----------

total 7.3200E-05 2.6000E-05 6.6000E-06 2.6000E-06 9.3400E-05 -1.2400E-05 -1.6280E-04 3.0000E-06 -2.2000E-06

variance reduction events:

weight window 0.0000E+00 0.0000E+00 0.0000E+00 0.0000E+00 0.0000E+00 0.0000E+00 0.0000E+00 0.0000E+00 0.0000E+00

cell importance 0.0000E+00 0.0000E+00 0.0000E+00 0.0000E+00 0.0000E+00 0.0000E+00 0.0000E+00 0.0000E+00 0.0000E+00

weight cutoff 0.0000E+00 0.0000E+00 0.0000E+00 0.0000E+00 0.0000E+00 0.0000E+00 0.0000E+00 0.0000E+00 0.0000E+00

e or t importance 0.0000E+00 0.0000E+00 0.0000E+00 0.0000E+00 0.0000E+00 0.0000E+00 0.0000E+00 0.0000E+00 0.0000E+00

dxtran 0.0000E+00 0.0000E+00 0.0000E+00 0.0000E+00 0.0000E+00 0.0000E+00 0.0000E+00 0.0000E+00 0.0000E+00

forced collisions 0.0000E+00 0.0000E+00 0.0000E+00 0.0000E+00 0.0000E+00 0.0000E+00 0.0000E+00 0.0000E+00 0.0000E+00

exp. transform 0.0000E+00 0.0000E+00 0.0000E+00 0.0000E+00 0.0000E+00 0.0000E+00 0.0000E+00 0.0000E+00 0.0000E+00

---------- ---------- ---------- ---------- ---------- ---------- ---------- ---------- ----------
total 0.0000E+00 0.0000E+00 0.0000E+00 0.0000E+00 0.0000E+00 0.0000E+00 0.0000E+00 0.0000E+00 0.0000E+00

physical events:
from neutrons 0.0000E+00 0.0000E+00 0.0000E+00 0.0000E+00 0.0000E+00 0.0000E+00 0.0000E+00 0.0000E+00 0.0000E+00
bremsstrahlung 1.2580E-04 1.4000E-06 4.0000E-07 0.0000E+00 2.3940E-04 1.3580E-04 4.1600E-04 7.2200E-05 9.7400E-05
capture -2.0360E-04 -2.8200E-05 -7.0000E-06 -2.8000E-06 -3.3940E-04 -1.2620E-04 -2.5780E-04 -7.7200E-05 -9.7800E-05
p-annihilation 1.6000E-06 0.0000E+00 0.0000E+00 0.0000E+00 2.8000E-06 2.0000E-06 3.6000E-06 0.0000E+00 2.0000E-06
pair production -8.0000E-07 0.0000E+00 0.0000E+00 0.0000E+00 -1.4000E-06 -1.0000E-06 -1.8000E-06 0.0000E+00 -1.0000E-06
photonuclear 0.0000E+00 0.0000E+00 0.0000E+00 0.0000E+00 0.0000E+00 0.0000E+00 0.0000E+00 0.0000E+00 0.0000E+00
photonuclear abs 0.0000E+00 0.0000E+00 0.0000E+00 0.0000E+00 0.0000E+00 0.0000E+00 0.0000E+00 0.0000E+00 0.0000E+00
electron x-rays 0.0000E+00 0.0000E+00 0.0000E+00 0.0000E+00 0.0000E+00 0.0000E+00 0.0000E+00 0.0000E+00 0.0000E+00
compton fluores 0.0000E+00 0.0000E+00 0.0000E+00 0.0000E+00 0.0000E+00 0.0000E+00 0.0000E+00 0.0000E+00 0.0000E+00
muon capt fluores 0.0000E+00 0.0000E+00 0.0000E+00 0.0000E+00 0.0000E+00 0.0000E+00 0.0000E+00 0.0000E+00 0.0000E+00
fluorescence 3.8000E-06 8.0000E-07 0.0000E+00 2.0000E-07 5.2000E-06 1.8000E-06 2.8000E-06 1.6000E-06 1.6000E-06
cerenkov 0.0000E+00 0.0000E+00 0.0000E+00 0.0000E+00 0.0000E+00 0.0000E+00 0.0000E+00 0.0000E+00 0.0000E+00
decay gain 0.0000E+00 0.0000E+00 0.0000E+00 0.0000E+00 0.0000E+00 0.0000E+00 0.0000E+00 0.0000E+00 0.0000E+00
nucl. interaction 0.0000E+00 0.0000E+00 0.0000E+00 0.0000E+00 0.0000E+00 0.0000E+00 0.0000E+00 0.0000E+00 0.0000E+00
tabular sampling 0.0000E+00 0.0000E+00 0.0000E+00 0.0000E+00 0.0000E+00 0.0000E+00 0.0000E+00 0.0000E+00 0.0000E+00
photofission 0.0000E+00 0.0000E+00 0.0000E+00 0.0000E+00 0.0000E+00 0.0000E+00 0.0000E+00 0.0000E+00 0.0000E+00
loss to photofis 0.0000E+00 0.0000E+00 0.0000E+00 0.0000E+00 0.0000E+00 0.0000E+00 0.0000E+00 0.0000E+00 0.0000E+00
---------- ---------- ---------- ---------- ---------- ---------- ---------- ---------- ----------
total -7.3200E-05 -2.6000E-05 -6.6000E-06 -2.6000E-06 -9.3400E-05 1.2400E-05 1.6280E-04 -3.4000E-06 2.2000E-06

---------- ---------- ---------- ---------- ---------- ---------- ---------- ---------- -------
---
total 0.0000E+00 0.0000E+00 0.0000E+00 0.0000E+00 0.0000E+00
0.0000E+00 0.0000E+00 -4.0000E-07 0.0000E+00

cell index 28 29 30 31 32
cell number 28 29 30 31 32 total

external events:
entering 4.7821E-01 4.9564E-01 4.7816E-01 2.8597E+00 0.0000E+00
1.3042E+01
source 0.0000E+00 0.0000E+00 0.0000E+00 0.0000E+00 0.0000E+00
2.0000E+00
energy cutoff 0.0000E+00 0.0000E+00 0.0000E+00 0.0000E+00 0.0000E+00
0.0000E+00
time cutoff 0.0000E+00 0.0000E+00 0.0000E+00 0.0000E+00 0.0000E+00
0.0000E+00
exiting -4.7820E-01 -4.9563E-01 -4.7815E-01 -2.8597E+00 0.0000E+00 -
1.3042E+01
---------- ---------- ---------- ---------- ---------- ----------
total 8.0000E-06 8.6000E-06 1.6000E-05 -4.9000E-05 0.0000E+00
2.0000E+00

variance reduction events:
weight window 0.0000E+00 0.0000E+00 0.0000E+00 0.0000E+00 0.0000E+00
0.0000E+00
cell importance 0.0000E+00 0.0000E+00 0.0000E+00 0.0000E+00 0.0000E+00
0.0000E+00
weight cutoff 0.0000E+00 0.0000E+00 0.0000E+00 0.0000E+00 0.0000E+00
0.0000E+00
e or t importance 0.0000E+00 0.0000E+00 0.0000E+00 0.0000E+00 0.0000E+00
0.0000E+00
dxtran 0.0000E+00 0.0000E+00 0.0000E+00 0.0000E+00 0.0000E+00
0.0000E+00
forced collisions 0.0000E+00 0.0000E+00 0.0000E+00 0.0000E+00 0.0000E+00
0.0000E+00
exp. transform 0.0000E+00 0.0000E+00 0.0000E+00 0.0000E+00 0.0000E+00
0.0000E+00
---------- ---------- ---------- ---------- ---------- ----------
total 0.0000E+00 0.0000E+00 0.0000E+00 0.0000E+00 0.0000E+00
0.0000E+00

physical events:
from neutrons 0.0000E+00 0.0000E+00 0.0000E+00 0.0000E+00 0.0000E+00
0.0000E+00

bremsstrahlung 8.6400E-05 6.6400E-05 6.4600E-05 0.0000E+00 0.0000E+00
3.4057E-01
capture -9.6800E-05 -7.6800E-05 -8.2800E-05 0.0000E+00 0.0000E+00 -
2.5708E+00
p-annihilation 1.6000E-06 0.0000E+00 1.2000E-06 0.0000E+00 0.0000E+00
2.6156E-03
pair production -8.0000E-07 0.0000E+00 -6.0000E-07 0.0000E+00 0.0000E+00 -
1.3078E-03
photonuclear 0.0000E+00 0.0000E+00 0.0000E+00 0.0000E+00 0.0000E+00
0.0000E+00
photonuclear abs 0.0000E+00 0.0000E+00 0.0000E+00 0.0000E+00 0.0000E+00
0.0000E+00
electron x-rays 0.0000E+00 0.0000E+00 0.0000E+00 0.0000E+00 0.0000E+00
0.0000E+00
compton fluores 0.0000E+00 0.0000E+00 0.0000E+00 0.0000E+00 0.0000E+00
0.0000E+00
muon capt fluores 0.0000E+00 0.0000E+00 0.0000E+00 0.0000E+00 0.0000E+00
0.0000E+00
fluorescence 1.6000E-06 1.8000E-06 1.6000E-06 0.0000E+00 0.0000E+00
2.2900E-01
cerenkov 0.0000E+00 0.0000E+00 0.0000E+00 0.0000E+00 0.0000E+00
0.0000E+00
decay gain 0.0000E+00 0.0000E+00 0.0000E+00 0.0000E+00 0.0000E+00
0.0000E+00
nucl. interaction 0.0000E+00 0.0000E+00 0.0000E+00 0.0000E+00 0.0000E+00
0.0000E+00
tabular sampling 0.0000E+00 0.0000E+00 0.0000E+00 0.0000E+00 0.0000E+00
0.0000E+00
photofission 0.0000E+00 0.0000E+00 0.0000E+00 0.0000E+00 0.0000E+00
0.0000E+00
loss to photofis 0.0000E+00 0.0000E+00 0.0000E+00 0.0000E+00 0.0000E+00
0.0000E+00
---------- ---------- ---------- ---------- ---------- ----------
total -8.0000E-06 -8.6000E-06 -1.6000E-05 0.0000E+00 0.0000E+00 -
2.0000E+00

---------- ---------- ---------- ---------- ---------- ----------
total 0.0000E+00 0.0000E+00 0.0000E+00 -4.9000E-05 0.0000E+00
0.0000E+00

1photoatomic activity of each nuclide in each cell, per source particle
print table 140

cell cell nuclides atom total collisions wgt. lost weight of total
weight of total weight of

index name fraction collisions * weight to capture pair prod incoherent
incoherent coherent coherent

1 1 6000.84p 1.48E-04 2 4.0000E-07 0.0000E+00 0.0000E+00
2 4.0000E-07 0 0.0000E+00
6000.84p 1.59E-06 0 0.0000E+00 0.0000E+00 0.0000E+00
0 0.0000E+00 0 0.0000E+00
7000.84p 7.84E-01 1462 2.9240E-04 5.8000E-06 0.0000E+00
1382 2.7640E-04 51 1.0200E-05
8000.84p 2.11E-01 489 9.7800E-05 4.6000E-06 0.0000E+00
435 8.7000E-05 31 6.2000E-06
18000.84p 1.56E-05 0 0.0000E+00 0.0000E+00 0.0000E+00
0 0.0000E+00 0 0.0000E+00
18000.84p 2.94E-06 0 0.0000E+00 0.0000E+00 0.0000E+00
0 0.0000E+00 0 0.0000E+00
18000.84p 4.65E-03 44 8.8000E-06 3.4000E-06 0.0000E+00
24 4.8000E-06 3 6.0000E-07

2 2 1000.84p 8.47E-02 521785 1.0436E-01 1.0000E-06 6.0000E-07
521436 1.0429E-01 341 6.8200E-05
8000.84p 6.04E-01 31313360 6.2627E+00 2.0497E-01 2.8060E-04
29464994 5.8930E+00 822135 1.6443E-01
11000.84p 1.25E-02 961224 1.9224E-01 1.6687E-02 1.0400E-05
836329 1.6727E-01 41406 8.2812E-03
13000.84p 2.48E-02 2404918 4.8098E-01 6.5154E-02 2.8200E-05
1953220 3.9064E-01 125785 2.5157E-02
14000.84p 2.23E-01 23971180 4.7942E+00 7.4867E-01 3.2860E-04
18858916 3.7718E+00 1367269 2.7345E-01
14000.84p 1.13E-02 1214280 2.4286E-01 3.7972E-02 1.9000E-05
954921 1.9098E-01 69403 1.3881E-02
14000.84p 7.44E-03 796654 1.5933E-01 2.5014E-02 1.0400E-05
625682 1.2514E-01 45851 9.1702E-03
20000.84p 2.64E-02 5539677 1.1079E+00 3.9572E-01 8.4400E-05
3161179 6.3224E-01 399459 7.9892E-02
20000.84p 1.76E-04 37229 7.4458E-03 2.6752E-03 4.0000E-07
21212 4.2424E-03 2639 5.2780E-04
20000.84p 3.68E-05 7732 1.5464E-03 5.5160E-04 2.0000E-07
4433 8.8660E-04 540 1.0800E-04
20000.84p 5.68E-04 119705 2.3941E-02 8.5718E-03 1.2000E-06
68058 1.3612E-02 8782 1.7564E-03
20000.84p 1.09E-06 217 4.3400E-05 1.5600E-05 0.0000E+00
121 2.4200E-05 18 3.6000E-06
20000.84p 5.09E-05 10841 2.1682E-03 7.7000E-04 4.0000E-07
6211 1.2422E-03 778 1.5560E-04
26000.84p 2.72E-04 109784 2.1957E-02 1.1975E-02 1.2000E-06
41818 8.3636E-03 8087 1.6174E-03

26000.84p 4.27E-03 1728953 3.4579E-01 1.8889E-01 2.5800E-05
657994 1.3160E-01 126371 2.5274E-02
26000.84p 9.86E-05 39787 7.9574E-03 4.3600E-03 1.4000E-06
15078 3.0156E-03 2902 5.8040E-04
26000.84p 1.31E-05 5347 1.0694E-03 5.8500E-04 0.0000E+00
2023 4.0460E-04 399 7.9800E-05

3 3 1000.84p 8.47E-02 267573 5.3515E-02 6.0000E-07 6.0000E-07
267401 5.3480E-02 166 3.3200E-05
8000.84p 6.04E-01 16088461 3.2177E+00 1.0398E-01 1.7160E-04
15160411 3.0321E+00 407289 8.1458E-02
11000.84p 1.25E-02 491771 9.8354E-02 8.3958E-03 4.6000E-06
428970 8.5794E-02 20799 4.1598E-03
13000.84p 2.48E-02 1231565 2.4631E-01 3.2777E-02 2.0400E-05
1004983 2.0100E-01 62596 1.2519E-02
14000.84p 2.23E-01 12253954 2.4508E+00 3.7398E-01 2.0700E-04
9704134 1.9408E+00 678896 1.3578E-01
14000.84p 1.13E-02 621612 1.2432E-01 1.8965E-02 1.2400E-05
492206 9.8441E-02 34521 6.9042E-03
14000.84p 7.44E-03 408813 8.1763E-02 1.2441E-02 8.6000E-06
323988 6.4798E-02 22579 4.5158E-03
20000.84p 2.64E-02 2804022 5.6080E-01 1.9618E-01 5.3000E-05
1624794 3.2496E-01 198077 3.9615E-02
20000.84p 1.76E-04 18684 3.7368E-03 1.2992E-03 2.0000E-07
10932 2.1864E-03 1255 2.5100E-04
20000.84p 3.68E-05 3976 7.9520E-04 2.8520E-04 2.0000E-07
2255 4.5100E-04 294 5.8800E-05
20000.84p 5.68E-04 60613 1.2123E-02 4.2616E-03 1.4000E-06
34920 6.9840E-03 4378 8.7560E-04
20000.84p 1.09E-06 106 2.1200E-05 8.8000E-06 0.0000E+00
56 1.1200E-05 6 1.2000E-06
20000.84p 5.09E-05 5492 1.0984E-03 3.9860E-04 0.0000E+00
3123 6.2460E-04 376 7.5200E-05
26000.84p 2.72E-04 55802 1.1160E-02 6.0206E-03 8.0000E-07
21634 4.3268E-03 4061 8.1220E-04
26000.84p 4.27E-03 869736 1.7395E-01 9.3587E-02 1.5000E-05
338961 6.7792E-02 62766 1.2553E-02
26000.84p 9.86E-05 20115 4.0230E-03 2.1636E-03 4.0000E-07
7832 1.5664E-03 1463 2.9260E-04
26000.84p 1.31E-05 2555 5.1100E-04 2.7520E-04 0.0000E+00
983 1.9660E-04 196 3.9200E-05

4 4 6000.84p 1.48E-04 7 1.4000E-06 0.0000E+00 0.0000E+00
7 1.4000E-06 0 0.0000E+00
6000.84p 1.59E-06 0 0.0000E+00 0.0000E+00 0.0000E+00
0 0.0000E+00 0 0.0000E+00

7000.84p 7.84E-01 26483 5.2966E-03 1.0680E-04 6.0000E-07
25413 5.0826E-03 533 1.0660E-04
8000.84p 2.11E-01 8346 1.6692E-03 5.4800E-05 2.0000E-07
7869 1.5738E-03 202 4.0400E-05
18000.84p 1.56E-05 1 2.0000E-07 0.0000E+00 0.0000E+00
1 2.0000E-07 0 0.0000E+00
18000.84p 2.94E-06 0 0.0000E+00 0.0000E+00 0.0000E+00
0 0.0000E+00 0 0.0000E+00
18000.84p 4.65E-03 590 1.1800E-04 3.4400E-05 0.0000E+00
381 7.6200E-05 37 7.4000E-06

5 5 6000.84p 1.48E-04 4 8.0000E-07 2.0000E-07 0.0000E+00
3 6.0000E-07 0 0.0000E+00
6000.84p 1.59E-06 0 0.0000E+00 0.0000E+00 0.0000E+00
0 0.0000E+00 0 0.0000E+00
7000.84p 7.84E-01 26167 5.2334E-03 1.0640E-04 6.0000E-07
25122 5.0244E-03 510 1.0200E-04
8000.84p 2.11E-01 8059 1.6118E-03 5.0800E-05 2.0000E-07
7586 1.5172E-03 218 4.3600E-05
18000.84p 1.56E-05 3 6.0000E-07 2.0000E-07 0.0000E+00
2 4.0000E-07 0 0.0000E+00
18000.84p 2.94E-06 0 0.0000E+00 0.0000E+00 0.0000E+00
0 0.0000E+00 0 0.0000E+00
18000.84p 4.65E-03 583 1.1660E-04 3.5600E-05 0.0000E+00
355 7.1000E-05 50 1.0000E-05

6 6 6000.84p 1.48E-04 1 2.0000E-07 0.0000E+00 0.0000E+00
1 2.0000E-07 0 0.0000E+00
6000.84p 1.59E-06 0 0.0000E+00 0.0000E+00 0.0000E+00
0 0.0000E+00 0 0.0000E+00
7000.84p 7.84E-01 6455 1.2910E-03 2.2400E-05 0.0000E+00
6224 1.2448E-03 119 2.3800E-05
8000.84p 2.11E-01 2013 4.0260E-04 9.4000E-06 0.0000E+00
1923 3.8460E-04 43 8.6000E-06
18000.84p 1.56E-05 1 2.0000E-07 2.0000E-07 0.0000E+00
0 0.0000E+00 0 0.0000E+00
18000.84p 2.94E-06 0 0.0000E+00 0.0000E+00 0.0000E+00
0 0.0000E+00 0 0.0000E+00
18000.84p 4.65E-03 125 2.5000E-05 7.4000E-06 0.0000E+00
82 1.6400E-05 6 1.2000E-06

7 7 6000.84p 1.48E-04 0 0.0000E+00 0.0000E+00 0.0000E+00
0 0.0000E+00 0 0.0000E+00
6000.84p 1.59E-06 0 0.0000E+00 0.0000E+00 0.0000E+00
0 0.0000E+00 0 0.0000E+00

7000.84p 7.84E-01 6482 1.2964E-03 2.6800E-05 2.0000E-07
6237 1.2474E-03 110 2.2000E-05
8000.84p 2.11E-01 1994 3.9880E-04 1.3400E-05 0.0000E+00
1887 3.7740E-04 40 8.0000E-06
18000.84p 1.56E-05 1 2.0000E-07 0.0000E+00 0.0000E+00
1 2.0000E-07 0 0.0000E+00
18000.84p 2.94E-06 1 2.0000E-07 0.0000E+00 0.0000E+00
1 2.0000E-07 0 0.0000E+00
18000.84p 4.65E-03 148 2.9600E-05 9.4000E-06 0.0000E+00
91 1.8200E-05 10 2.0000E-06

8 8 6000.84p 1.48E-04 1 2.0000E-07 0.0000E+00 0.0000E+00
0 0.0000E+00 1 2.0000E-07
6000.84p 1.59E-06 0 0.0000E+00 0.0000E+00 0.0000E+00
0 0.0000E+00 0 0.0000E+00
7000.84p 7.84E-01 6144 1.2288E-03 2.2000E-05 2.0000E-07
5934 1.1868E-03 99 1.9800E-05
8000.84p 2.11E-01 1884 3.7680E-04 1.0800E-05 0.0000E+00
1782 3.5640E-04 48 9.6000E-06
18000.84p 1.56E-05 0 0.0000E+00 0.0000E+00 0.0000E+00
0 0.0000E+00 0 0.0000E+00
18000.84p 2.94E-06 0 0.0000E+00 0.0000E+00 0.0000E+00
0 0.0000E+00 0 0.0000E+00
18000.84p 4.65E-03 144 2.8800E-05 7.8000E-06 0.0000E+00
99 1.9800E-05 6 1.2000E-06

9 9 6000.84p 1.48E-04 0 0.0000E+00 0.0000E+00 0.0000E+00
0 0.0000E+00 0 0.0000E+00
6000.84p 1.59E-06 0 0.0000E+00 0.0000E+00 0.0000E+00
0 0.0000E+00 0 0.0000E+00
7000.84p 7.84E-01 5782 1.1564E-03 2.4200E-05 0.0000E+00
5558 1.1116E-03 103 2.0600E-05
8000.84p 2.11E-01 1761 3.5220E-04 1.0000E-05 0.0000E+00
1678 3.3560E-04 33 6.6000E-06
18000.84p 1.56E-05 0 0.0000E+00 0.0000E+00 0.0000E+00
0 0.0000E+00 0 0.0000E+00
18000.84p 2.94E-06 0 0.0000E+00 0.0000E+00 0.0000E+00
0 0.0000E+00 0 0.0000E+00
18000.84p 4.65E-03 114 2.2800E-05 6.0000E-06 0.0000E+00
75 1.5000E-05 9 1.8000E-06

10 10 6000.84p 1.48E-04 1 2.0000E-07 0.0000E+00 0.0000E+00
1 2.0000E-07 0 0.0000E+00
6000.84p 1.59E-06 0 0.0000E+00 0.0000E+00 0.0000E+00
0 0.0000E+00 0 0.0000E+00

7000.84p 7.84E-01 5538 1.1076E-03 2.0800E-05 0.0000E+00
5336 1.0672E-03 98 1.9600E-05
8000.84p 2.11E-01 1781 3.5620E-04 1.2400E-05 0.0000E+00
1673 3.3460E-04 46 9.2000E-06
18000.84p 1.56E-05 0 0.0000E+00 0.0000E+00 0.0000E+00
0 0.0000E+00 0 0.0000E+00
18000.84p 2.94E-06 0 0.0000E+00 0.0000E+00 0.0000E+00
0 0.0000E+00 0 0.0000E+00
18000.84p 4.65E-03 118 2.3600E-05 7.8000E-06 0.0000E+00
67 1.3400E-05 12 2.4000E-06

11 11 6000.84p 1.48E-04 19 3.8000E-06 0.0000E+00 0.0000E+00
19 3.8000E-06 0 0.0000E+00
6000.84p 1.59E-06 0 0.0000E+00 0.0000E+00 0.0000E+00
0 0.0000E+00 0 0.0000E+00
7000.84p 7.84E-01 124307 2.4861E-02 5.0760E-04 5.4000E-06
120511 2.4102E-02 1231 2.4620E-04
8000.84p 2.11E-01 39125 7.8250E-03 2.6040E-04 2.4000E-06
37345 7.4690E-03 466 9.3200E-05
18000.84p 1.56E-05 8 1.6000E-06 2.0000E-07 0.0000E+00
7 1.4000E-06 0 0.0000E+00
18000.84p 2.94E-06 1 2.0000E-07 0.0000E+00 0.0000E+00
1 2.0000E-07 0 0.0000E+00
18000.84p 4.65E-03 2441 4.8820E-04 1.0740E-04 0.0000E+00
1813 3.6260E-04 91 1.8200E-05

12 12 6000.84p 1.48E-04 5 1.0000E-06 0.0000E+00 0.0000E+00
5 1.0000E-06 0 0.0000E+00
6000.84p 1.59E-06 0 0.0000E+00 0.0000E+00 0.0000E+00
0 0.0000E+00 0 0.0000E+00
7000.84p 7.84E-01 10043 2.0086E-03 3.8200E-05 4.0000E-07
9643 1.9286E-03 207 4.1400E-05
8000.84p 2.11E-01 3193 6.3860E-04 2.2200E-05 0.0000E+00
3005 6.0100E-04 77 1.5400E-05
18000.84p 1.56E-05 2 4.0000E-07 0.0000E+00 0.0000E+00
2 4.0000E-07 0 0.0000E+00
18000.84p 2.94E-06 0 0.0000E+00 0.0000E+00 0.0000E+00
0 0.0000E+00 0 0.0000E+00
18000.84p 4.65E-03 245 4.9000E-05 1.4600E-05 0.0000E+00
156 3.1200E-05 16 3.2000E-06

13 13 6000.84p 1.48E-04 1 2.0000E-07 0.0000E+00 0.0000E+00
1 2.0000E-07 0 0.0000E+00
6000.84p 1.59E-06 0 0.0000E+00 0.0000E+00 0.0000E+00
0 0.0000E+00 0 0.0000E+00

7000.84p 7.84E-01 21073 4.2146E-03 9.5800E-05 1.2000E-06
20265 4.0530E-03 323 6.4600E-05
8000.84p 2.11E-01 6456 1.2912E-03 4.4600E-05 0.0000E+00
6071 1.2142E-03 162 3.2400E-05
18000.84p 1.56E-05 0 0.0000E+00 0.0000E+00 0.0000E+00
0 0.0000E+00 0 0.0000E+00
18000.84p 2.94E-06 0 0.0000E+00 0.0000E+00 0.0000E+00
0 0.0000E+00 0 0.0000E+00
18000.84p 4.65E-03 484 9.6800E-05 2.6600E-05 0.0000E+00
314 6.2800E-05 37 7.4000E-06

14 14 6000.84p 1.48E-04 0 0.0000E+00 0.0000E+00 0.0000E+00
0 0.0000E+00 0 0.0000E+00
6000.84p 1.59E-06 0 0.0000E+00 0.0000E+00 0.0000E+00
0 0.0000E+00 0 0.0000E+00
7000.84p 7.84E-01 3533 7.0660E-04 1.4800E-05 0.0000E+00
3360 6.7200E-04 99 1.9800E-05
8000.84p 2.11E-01 1107 2.2140E-04 6.0000E-06 0.0000E+00
1032 2.0640E-04 45 9.0000E-06
18000.84p 1.56E-05 0 0.0000E+00 0.0000E+00 0.0000E+00
0 0.0000E+00 0 0.0000E+00
18000.84p 2.94E-06 0 0.0000E+00 0.0000E+00 0.0000E+00
0 0.0000E+00 0 0.0000E+00
18000.84p 4.65E-03 91 1.8200E-05 4.6000E-06 0.0000E+00
60 1.2000E-05 8 1.6000E-06

15 15 6000.84p 1.48E-04 1 2.0000E-07 0.0000E+00 0.0000E+00
1 2.0000E-07 0 0.0000E+00
6000.84p 1.59E-06 0 0.0000E+00 0.0000E+00 0.0000E+00
0 0.0000E+00 0 0.0000E+00
7000.84p 7.84E-01 1948 3.8960E-04 1.0800E-05 0.0000E+00
1819 3.6380E-04 75 1.5000E-05
8000.84p 2.11E-01 637 1.2740E-04 6.0000E-06 0.0000E+00
585 1.1700E-04 22 4.4000E-06
18000.84p 1.56E-05 0 0.0000E+00 0.0000E+00 0.0000E+00
0 0.0000E+00 0 0.0000E+00
18000.84p 2.94E-06 0 0.0000E+00 0.0000E+00 0.0000E+00
0 0.0000E+00 0 0.0000E+00
18000.84p 4.65E-03 49 9.8000E-06 3.2000E-06 0.0000E+00
29 5.8000E-06 4 8.0000E-07

16 16 6000.84p 1.48E-04 0 0.0000E+00 0.0000E+00 0.0000E+00
0 0.0000E+00 0 0.0000E+00
6000.84p 1.59E-06 0 0.0000E+00 0.0000E+00 0.0000E+00
0 0.0000E+00 0 0.0000E+00

7000.84p 7.84E-01 1907 3.8140E-04 1.1000E-05 0.0000E+00
1792 3.5840E-04 60 1.2000E-05
8000.84p 2.11E-01 635 1.2700E-04 5.4000E-06 0.0000E+00
581 1.1620E-04 27 5.4000E-06
18000.84p 1.56E-05 0 0.0000E+00 0.0000E+00 0.0000E+00
0 0.0000E+00 0 0.0000E+00
18000.84p 2.94E-06 0 0.0000E+00 0.0000E+00 0.0000E+00
0 0.0000E+00 0 0.0000E+00
18000.84p 4.65E-03 49 9.8000E-06 3.4000E-06 0.0000E+00
24 4.8000E-06 8 1.6000E-06

17 17 6000.84p 1.48E-04 0 0.0000E+00 0.0000E+00 0.0000E+00
0 0.0000E+00 0 0.0000E+00
6000.84p 1.59E-06 0 0.0000E+00 0.0000E+00 0.0000E+00
0 0.0000E+00 0 0.0000E+00
7000.84p 7.84E-01 647 1.2940E-04 3.6000E-06 0.0000E+00
609 1.2180E-04 20 4.0000E-06
8000.84p 2.11E-01 179 3.5800E-05 2.2000E-06 0.0000E+00
161 3.2200E-05 7 1.4000E-06
18000.84p 1.56E-05 0 0.0000E+00 0.0000E+00 0.0000E+00
0 0.0000E+00 0 0.0000E+00
18000.84p 2.94E-06 0 0.0000E+00 0.0000E+00 0.0000E+00
0 0.0000E+00 0 0.0000E+00
18000.84p 4.65E-03 16 3.2000E-06 1.2000E-06 0.0000E+00
8 1.6000E-06 2 4.0000E-07

18 18 6000.84p 1.48E-04 0 0.0000E+00 0.0000E+00 0.0000E+00
0 0.0000E+00 0 0.0000E+00
6000.84p 1.59E-06 0 0.0000E+00 0.0000E+00 0.0000E+00
0 0.0000E+00 0 0.0000E+00
7000.84p 7.84E-01 3429 6.8580E-04 1.6000E-05 0.0000E+00
3250 6.5000E-04 99 1.9800E-05
8000.84p 2.11E-01 1064 2.1280E-04 8.0000E-06 0.0000E+00
978 1.9560E-04 46 9.2000E-06
18000.84p 1.56E-05 0 0.0000E+00 0.0000E+00 0.0000E+00
0 0.0000E+00 0 0.0000E+00
18000.84p 2.94E-06 0 0.0000E+00 0.0000E+00 0.0000E+00
0 0.0000E+00 0 0.0000E+00
18000.84p 4.65E-03 100 2.0000E-05 7.6000E-06 0.0000E+00
53 1.0600E-05 9 1.8000E-06

19 19 6000.84p 1.48E-04 7 1.4000E-06 0.0000E+00 0.0000E+00
7 1.4000E-06 0 0.0000E+00
6000.84p 1.59E-06 0 0.0000E+00 0.0000E+00 0.0000E+00
0 0.0000E+00 0 0.0000E+00

7000.84p 7.84E-01 25473 5.0946E-03 1.1100E-04 6.0000E-07
24466 4.8932E-03 449 8.9800E-05
8000.84p 2.11E-01 8143 1.6286E-03 5.5800E-05 2.0000E-07
7671 1.5342E-03 192 3.8400E-05
18000.84p 1.56E-05 0 0.0000E+00 0.0000E+00 0.0000E+00
0 0.0000E+00 0 0.0000E+00
18000.84p 2.94E-06 0 0.0000E+00 0.0000E+00 0.0000E+00
0 0.0000E+00 0 0.0000E+00
18000.84p 4.65E-03 628 1.2560E-04 3.6800E-05 0.0000E+00
407 8.1400E-05 37 7.4000E-06

20 20 6000.84p 1.48E-04 1 2.0000E-07 0.0000E+00 0.0000E+00
1 2.0000E-07 0 0.0000E+00
6000.84p 1.59E-06 0 0.0000E+00 0.0000E+00 0.0000E+00
0 0.0000E+00 0 0.0000E+00
7000.84p 7.84E-01 3022 6.0440E-04 1.5600E-05 0.0000E+00
2852 5.7040E-04 92 1.8400E-05
8000.84p 2.11E-01 957 1.9140E-04 6.2000E-06 0.0000E+00
890 1.7800E-04 36 7.2000E-06
18000.84p 1.56E-05 1 2.0000E-07 2.0000E-07 0.0000E+00
0 0.0000E+00 0 0.0000E+00
18000.84p 2.94E-06 0 0.0000E+00 0.0000E+00 0.0000E+00
0 0.0000E+00 0 0.0000E+00
18000.84p 4.65E-03 69 1.3800E-05 6.2000E-06 0.0000E+00
33 6.6000E-06 5 1.0000E-06

21 21 6000.84p 1.48E-04 0 0.0000E+00 0.0000E+00 0.0000E+00
0 0.0000E+00 0 0.0000E+00
6000.84p 1.59E-06 0 0.0000E+00 0.0000E+00 0.0000E+00
0 0.0000E+00 0 0.0000E+00
7000.84p 7.84E-01 569 1.1380E-04 3.6000E-06 0.0000E+00
532 1.0640E-04 19 3.8000E-06
8000.84p 2.11E-01 172 3.4400E-05 1.6000E-06 0.0000E+00
159 3.1800E-05 5 1.0000E-06
18000.84p 1.56E-05 0 0.0000E+00 0.0000E+00 0.0000E+00
0 0.0000E+00 0 0.0000E+00
18000.84p 2.94E-06 0 0.0000E+00 0.0000E+00 0.0000E+00
0 0.0000E+00 0 0.0000E+00
18000.84p 4.65E-03 17 3.4000E-06 1.8000E-06 0.0000E+00
4 8.0000E-07 4 8.0000E-07

22 22 6000.84p 1.48E-04 0 0.0000E+00 0.0000E+00 0.0000E+00
0 0.0000E+00 0 0.0000E+00
6000.84p 1.59E-06 0 0.0000E+00 0.0000E+00 0.0000E+00
0 0.0000E+00 0 0.0000E+00

7000.84p 7.84E-01 226 4.5200E-05 1.2000E-06 0.0000E+00
215 4.3000E-05 5 1.0000E-06
8000.84p 2.11E-01 80 1.6000E-05 8.0000E-07 0.0000E+00
75 1.5000E-05 1 2.0000E-07
18000.84p 1.56E-05 0 0.0000E+00 0.0000E+00 0.0000E+00
0 0.0000E+00 0 0.0000E+00
18000.84p 2.94E-06 0 0.0000E+00 0.0000E+00 0.0000E+00
0 0.0000E+00 0 0.0000E+00
18000.84p 4.65E-03 9 1.8000E-06 8.0000E-07 0.0000E+00
4 8.0000E-07 1 2.0000E-07

23 23 6000.84p 1.48E-04 12 2.4000E-06 2.0000E-07 0.0000E+00
11 2.2000E-06 0 0.0000E+00
6000.84p 1.59E-06 0 0.0000E+00 0.0000E+00 0.0000E+00
0 0.0000E+00 0 0.0000E+00
7000.84p 7.84E-01 47347 9.4694E-03 1.9240E-04 8.0000E-07
45563 9.1126E-03 818 1.6360E-04
8000.84p 2.11E-01 14582 2.9164E-03 9.0600E-05 6.0000E-07
13839 2.7678E-03 287 5.7400E-05
18000.84p 1.56E-05 5 1.0000E-06 0.0000E+00 0.0000E+00
5 1.0000E-06 0 0.0000E+00
18000.84p 2.94E-06 3 6.0000E-07 2.0000E-07 0.0000E+00
1 2.0000E-07 1 2.0000E-07
18000.84p 4.65E-03 1029 2.0580E-04 5.6000E-05 0.0000E+00
677 1.3540E-04 72 1.4400E-05

24 24 6000.84p 1.48E-04 0 0.0000E+00 0.0000E+00 0.0000E+00
0 0.0000E+00 0 0.0000E+00
6000.84p 1.59E-06 0 0.0000E+00 0.0000E+00 0.0000E+00
0 0.0000E+00 0 0.0000E+00
7000.84p 7.84E-01 17017 3.4034E-03 7.6600E-05 1.0000E-06
16412 3.2824E-03 217 4.3400E-05
8000.84p 2.11E-01 5206 1.0412E-03 3.3000E-05 0.0000E+00
4976 9.9520E-04 65 1.3000E-05
18000.84p 1.56E-05 2 4.0000E-07 2.0000E-07 0.0000E+00
1 2.0000E-07 0 0.0000E+00
18000.84p 2.94E-06 1 2.0000E-07 0.0000E+00 0.0000E+00
1 2.0000E-07 0 0.0000E+00
18000.84p 4.65E-03 349 6.9800E-05 1.6400E-05 0.0000E+00
250 5.0000E-05 17 3.4000E-06

25 25 6000.84p 1.48E-04 6 1.2000E-06 0.0000E+00 0.0000E+00
6 1.2000E-06 0 0.0000E+00
6000.84p 1.59E-06 0 0.0000E+00 0.0000E+00 0.0000E+00
0 0.0000E+00 0 0.0000E+00

7000.84p 7.84E-01 36330 7.2660E-03 1.6140E-04 1.6000E-06
35312 7.0624E-03 203 4.0600E-05
8000.84p 2.11E-01 11183 2.2366E-03 7.0000E-05 2.0000E-07
10749 2.1498E-03 83 1.6600E-05
18000.84p 1.56E-05 1 2.0000E-07 2.0000E-07 0.0000E+00
0 0.0000E+00 0 0.0000E+00
18000.84p 2.94E-06 2 4.0000E-07 4.0000E-07 0.0000E+00
0 0.0000E+00 0 0.0000E+00
18000.84p 4.65E-03 659 1.3180E-04 2.5800E-05 0.0000E+00
517 1.0340E-04 13 2.6000E-06

26 26 6000.84p 1.48E-04 1 2.0000E-07 0.0000E+00 0.0000E+00
1 2.0000E-07 0 0.0000E+00
6000.84p 1.59E-06 0 0.0000E+00 0.0000E+00 0.0000E+00
0 0.0000E+00 0 0.0000E+00
7000.84p 7.84E-01 11268 2.2536E-03 4.6400E-05 0.0000E+00
10856 2.1712E-03 180 3.6000E-05
8000.84p 2.11E-01 3590 7.1800E-04 1.9200E-05 0.0000E+00
3433 6.8660E-04 61 1.2200E-05
18000.84p 1.56E-05 0 0.0000E+00 0.0000E+00 0.0000E+00
0 0.0000E+00 0 0.0000E+00
18000.84p 2.94E-06 0 0.0000E+00 0.0000E+00 0.0000E+00
0 0.0000E+00 0 0.0000E+00
18000.84p 4.65E-03 234 4.6800E-05 1.1600E-05 0.0000E+00
166 3.3200E-05 10 2.0000E-06

27 27 6000.84p 1.48E-04 3 6.0000E-07 0.0000E+00 0.0000E+00
3 6.0000E-07 0 0.0000E+00
6000.84p 1.59E-06 0 0.0000E+00 0.0000E+00 0.0000E+00
0 0.0000E+00 0 0.0000E+00
7000.84p 7.84E-01 14127 2.8254E-03 5.5200E-05 8.0000E-07
13629 2.7258E-03 218 4.3600E-05
8000.84p 2.11E-01 4360 8.7200E-04 2.7800E-05 2.0000E-07
4141 8.2820E-04 79 1.5800E-05
18000.84p 1.56E-05 2 4.0000E-07 0.0000E+00 0.0000E+00
2 4.0000E-07 0 0.0000E+00
18000.84p 2.94E-06 0 0.0000E+00 0.0000E+00 0.0000E+00
0 0.0000E+00 0 0.0000E+00
18000.84p 4.65E-03 318 6.3600E-05 1.4800E-05 0.0000E+00
224 4.4800E-05 20 4.0000E-06

28 28 6000.84p 1.48E-04 0 0.0000E+00 0.0000E+00 0.0000E+00
0 0.0000E+00 0 0.0000E+00
6000.84p 1.59E-06 0 0.0000E+00 0.0000E+00 0.0000E+00
0 0.0000E+00 0 0.0000E+00

7000.84p 7.84E-01 13494 2.6988E-03 5.5400E-05 4.0000E-07
13020 2.6040E-03 195 3.9000E-05
8000.84p 2.11E-01 4187 8.3740E-04 2.8400E-05 2.0000E-07
3968 7.9360E-04 76 1.5200E-05
18000.84p 1.56E-05 0 0.0000E+00 0.0000E+00 0.0000E+00
0 0.0000E+00 0 0.0000E+00
18000.84p 2.94E-06 0 0.0000E+00 0.0000E+00 0.0000E+00
0 0.0000E+00 0 0.0000E+00
18000.84p 4.65E-03 290 5.8000E-05 1.3000E-05 2.0000E-07
215 4.3000E-05 9 1.8000E-06

29 29 6000.84p 1.48E-04 1 2.0000E-07 0.0000E+00 0.0000E+00
1 2.0000E-07 0 0.0000E+00
6000.84p 1.59E-06 0 0.0000E+00 0.0000E+00 0.0000E+00
0 0.0000E+00 0 0.0000E+00
7000.84p 7.84E-01 10464 2.0928E-03 4.3400E-05 0.0000E+00
10083 2.0166E-03 164 3.2800E-05
8000.84p 2.11E-01 3243 6.4860E-04 2.2400E-05 0.0000E+00
3075 6.1500E-04 56 1.1200E-05
18000.84p 1.56E-05 1 2.0000E-07 0.0000E+00 0.0000E+00
1 2.0000E-07 0 0.0000E+00
18000.84p 2.94E-06 0 0.0000E+00 0.0000E+00 0.0000E+00
0 0.0000E+00 0 0.0000E+00
18000.84p 4.65E-03 215 4.3000E-05 1.1000E-05 0.0000E+00
146 2.9200E-05 14 2.8000E-06

30 30 6000.84p 1.48E-04 1 2.0000E-07 0.0000E+00 0.0000E+00
1 2.0000E-07 0 0.0000E+00
6000.84p 1.59E-06 0 0.0000E+00 0.0000E+00 0.0000E+00
0 0.0000E+00 0 0.0000E+00
7000.84p 7.84E-01 11166 2.2332E-03 4.6600E-05 4.0000E-07
10744 2.1488E-03 187 3.7400E-05
8000.84p 2.11E-01 3500 7.0000E-04 2.3400E-05 2.0000E-07
3323 6.6460E-04 59 1.1800E-05
18000.84p 1.56E-05 1 2.0000E-07 2.0000E-07 0.0000E+00
0 0.0000E+00 0 0.0000E+00
18000.84p 2.94E-06 1 2.0000E-07 2.0000E-07 0.0000E+00
0 0.0000E+00 0 0.0000E+00
18000.84p 4.65E-03 230 4.6000E-05 1.2400E-05 0.0000E+00
151 3.0200E-05 17 3.4000E-06

total 104576852 2.0915E+01 2.5708E+00 1.3078E-03
87184759 1.7437E+01 4531409 9.0628E-01

total over all cells by nuclide total collisions wgt. lost weight of total
weight of total weight of

collisions * weight to capture pair prod incoherent
incoherent coherent coherent

1000.84p 789358 1.5787E-01 1.6000E-06 1.2000E-06
788837 1.5777E-01 507 1.0140E-04
6000.84p 74 1.4800E-05 4.0000E-07 0.0000E+00 71
1.4200E-05 1 2.0000E-07
7000.84p 441903 8.8381E-02 1.8418E-03 1.4200E-05
426139 8.5228E-02 6484 1.2968E-03
8000.84p 47539747 9.5079E+00 3.0985E-01 4.5660E-04
44756295 8.9513E+00 1231937 2.4639E-01
11000.84p 1452995 2.9060E-01 2.5083E-02 1.5000E-05
1265299 2.5306E-01 62205 1.2441E-02
13000.84p 3636483 7.2730E-01 9.7931E-02 4.8600E-05
2958203 5.9164E-01 188381 3.7676E-02
14000.84p 39266493 7.8533E+00 1.2170E+00 5.8600E-04
30959847 6.1920E+00 2218519 4.4370E-01
18000.84p 9426 1.8852E-03 4.8920E-04 2.0000E-07
6451 1.2902E-03 528 1.0560E-04
20000.84p 8608294 1.7217E+00 6.1074E-01 1.4140E-04
4937294 9.8746E-01 616602 1.2332E-01
26000.84p 2832079 5.6642E-01 3.0786E-01 4.4600E-05
1086323 2.1726E-01 206245 4.1249E-02

****
dump no. 2 on file runtpe nps = 10000000 coll = 104576852 ctm =
508.06 nrn =
1557380446
tally data written to file mctal

1 warning message so far.

run terminated when 10000000 particle histories were done.

computer time = 568.93 minutes

mcnp version 6.mpi 07/01/21 01/06/26 18:31:37 probid =
01/06/26 18:06:59